Summer 8-12-2011

Measurement of Inclusive Isolated Prompt Photon Production at $\sqrt{s} = 7$ TeV with the ATLAS Detector

Michael Hance
University of Pennsylvania, hance@sas.upenn.edu

Measurement of Inclusive Isolated Prompt Photon Production at $\sqrt{s} = 7$ TeV with the ATLAS Detector

Abstract
Prompt photons at hadron colliders are useful probes of perturbative quantum chromodynamics (pQCD), and are also found in signatures of new physics. A precise measurement of prompt photon production is both a useful test of theoretical models as well as an important step towards understanding final states that contain energetic photons. This thesis presents a measurement of the inclusive isolated prompt photon production cross section in proton-proton collisions at a center-of-mass energy of $\sqrt{s} = 7$ TeV. The data are collected with the ATLAS detector at the Large Hadron Collider, and correspond to 35 pb^{-1} of integrated luminosity. The measurement is made in four photon pseudorapidity (η) regions: $0 \leq \eta < 0.6$; $0.6 \leq \eta < 1.37$; $1.52 \leq \eta < 1.81$; and $1.81 \leq \eta < 2.37$; and covers photon transverse energies (E_T) in the range 15 GeV $\leq E_T <$ 400 GeV. Photon candidates are reconstructed and identif ied through the use of the ATLAS calorimeter and tracking systems. The residual background, primarily from neutral meson decays, is estimated using in-situ techniques based on observed distributions of the total transverse energy in a narrow cone around the photon candidate. The measurements are compared to predictions from next-to-leading order pQCD calculations, with good agreement for photon transverse energies greater than 25 GeV.

Degree Type
Dissertation

Degree Name
Doctor of Philosophy (PhD)

Graduate Group
Physics & Astronomy

First Advisor
H. H. Williams

Keywords
CERN, Large Hadron Collider, LHC, ATLAS, Prompt Photons

Subject Categories
Elementary Particles and Fields and String Theory

MEASUREMENT OF INCLUSIVE ISOLATED PROMPT PHOTON PRODUCTION AT $\sqrt{s} = 7$ TEV WITH THE ATLAS DETECTOR

Michael Hance

A DISSERTATION
in
Physics and Astronomy

Presented to the Faculties of the University of Pennsylvania
in Partial Fulfillment of the Requirements for the Degree of Doctor of Philosophy
2011

H.H. Williams, Professor, Physics
Supervisor of Dissertation

A. T. Charlie Johnson, Professor, Physics
Graduate Group Chairperson

Dissertation Committee
I. Joseph Kroll, Professor, Physics
Burt Ovrut, Professor, Physics
Masao Sako, Assistant Professor, Physics
Evelyn Thomson, Associate Professor, Physics
H.H. Williams, Professor, Physics

MEASUREMENT OF INCLUSIVE ISOLATED PROMPT PHOTON PRODUCTION AT $\sqrt{s} = 7$ TEV WITH THE ATLAS DETECTOR

Acknowledgements

I am fortunate to have had many mentors, colleagues, and friends who have helped me a great deal during my time at Penn. While it's impossible to list everyone who has helped me over the years, there are several people that deserve acknowledgement.

My parents, George and Lorraine Hance, and my sisters, Katie and Kristen, have been a source of incredible support for as long as I can remember. I would not be the person I am today without them, and I feel lucky beyond words to have them as my family.

Rob Carey, Lee Roberts, Jim Miller, and the Intermediate Energy Group at Boston University gave me my first taste of what experimental physics is like. I hope that someday I will be able to give the same guidance and enthusiasm to my own students.

During my first years at CERN, I learned a great deal from Ole Røhne and Ben LeGeyt, without whom neither I nor the TRT would have ever left SR1. The Penn instrumentation group: Mike Reilly, Godwin Mayers, Walt Kononenko, and especially Rick Van Berg and Mitch Newcomer, provided a great deal of support and instruction, and taught me a lot about what it means to build something that works. Paul Keener deserves special thanks for mentoring me in the dark arts of data acquisition, and for helping me to learn about, and cope with, all the frustrating aspects of merging (non-existent) hardware with (untested) software.

Fido Dittus, Christoph Rembser and Anatoli Romaniouk took no small risk in leaving so

much of the TRT in my hands, and I remain in their debt for the opportunities they have given me. Anatoli, in particular, taught me a great deal about the attention to detail that is needed to make a project like the TRT succeed. Zbyszek Hajduk, Elzbieta Banas, Jolanta Olszowska, and the rest of the Kraków group were a pleasure to work with. I am also indebted to Peter Lichard, Philippe Farthouat and the TRT electronics group at CERN, who were extremely patient in teaching me the finer details of data acquisition electronics.

Jack Fowler and Kirill Egorov chaired many Friday afternoon meetings that were on time, efficiently run, and always instructive. My education would be less complete without their help.

At Penn, I'd like to first thank Jean O'Boyle, whose patience with me in handling logistical issues in the US and abroad has been tested many times. I'd also like to thank Joe Kroll and Evelyn Thomson, and more recently Elliot Lipeles, for their advice and support, and for countless dinners on several continents. The group they have assembled over the past five years is incredible, and I feel very lucky to have been a part of it. The Penn graduate students and post-docs are among the best in ATLAS, and I'll have words with anyone who says otherwise. Jim Degenhardt and Saša Fratina are both friends and allies in the fight for the TRT's good name, and I hope that Saša will still have dinner with me if she goes to CMS. Peter Wagner and Jon Stahlman deserve special recognition for their years of service on the TRT DAQ, and for being so easy to work with even when I was not. While his graduate career is only just beginning, I've had the pleasure of working with Jamie Saxon since the earliest days of my own time at Penn, and I'm glad to know that the photon analyses will remain in good hands for the foreseeable future. John Alison and Ryan Reece were among the first students that I had the opportunity to work with at CERN, and I can easily say that I've learned more from them than they have from me (though I hear it was supposed to be the other way around). Dominick Olivito deserves my extra thanks, and my sympathies,

for consistently taking on my projects and making them more successful than I ever did. Dominick, I hope you'll be lucky enough to have someone like yourself to work with on your own projects, as I was lucky to work with you.

At CERN, I was privileged to work extensively with Kerstin Tackmann and Thomas Koffas, who taught me a lot about photon reconstruction and e/gamma performance. I was also fortunate to have had so much help from Mauro Donegà, who consistently supported and encouraged me through what ultimately became the material for this thesis. Within the photon group, I learned a lot from working with Martin Tripiana, Mark Stockton, and Francesca Bucci, in addition to everyone else who participated in the early photon analyses. I especially owe thanks to Giovanni Marchiori and Marcello Fanti for their patience with me as co-editors of ATLAS notes and papers. Brian Martin and Joey Huston provided us with some valuable insights on photon physics at the LHC, and I look forward to continuing our work together in the future. Leonardo Carminati was a consistent and strong advocate for me within the photon group, and I surely owe him far more than I will ever be able to repay for his confidence in me and my work.

The guidance and support that Brig Williams has given me over the years has had a profound influence on me, both as a physicist and as a person. I can't imagine a better colleague or friend. Thank you, Brig, for everything.

Finally, to Sarah: we made it. I love you.

ABSTRACT

MEASUREMENT OF INCLUSIVE ISOLATED PROMPT PHOTON PRODUCTION AT $\sqrt{s} = 7$ TEV WITH THE ATLAS DETECTOR

Michael Hance

H.H. Williams

Prompt photons at hadron colliders are useful probes of perturbative quantum chromodynamics (pQCD), and are also found in signatures of new physics. A precise measurement of prompt photon production is both a useful test of theoretical models as well as an important step towards understanding final states that contain energetic photons. This thesis presents a measurement of the inclusive isolated prompt photon production cross section in proton-proton collisions at a center-of-mass energy of $\sqrt{s} = 7$ TeV. The data are collected with the ATLAS detector at the Large Hadron Collider, and correspond to 35 pb^{-1} of integrated luminosity. The measurement is made in four photon pseudorapidity (η^{γ}) regions: $0 \leq |\eta^{\gamma}| < 0.6$; $0.6 \leq |\eta^{\gamma}| < 1.37$; $1.52 \leq |\eta^{\gamma}| < 1.81$; and $1.81 \leq |\eta^{\gamma}| < 2.37$; and covers photon transverse energies (E_{T}^{γ}) in the range 15 GeV $\leq E_{\mathrm{T}}^{\gamma} <$ 400 GeV. Photon candidates are reconstructed and identified through the use of the ATLAS calorimeter and tracking systems. The residual background, primarily from neutral meson decays, is estimated using *in-situ* techniques based on observed distributions of the total transverse energy in a narrow cone around the photon candidate. The measurements are compared to predictions from next-to-leading order pQCD calculations, with good agreement for photon transverse energies greater than 25 GeV.

Contents

List of Tables

List of Figures

Chapter 1

Introduction

This thesis presents two measurements of the inclusive isolated prompt photon cross section in proton-proton collisions at a center-of-mass energy of 7 TeV using data collected with the ATLAS detector at the Large Hadron Collider. Prompt photons are photons that are produced either directly in the hard scattering process or during final state parton fragmentation, and do not include photons from hadron decays. The measurements are made separately in four regions of pseudorapidity ($0 \leq |\eta^{\gamma}| < 0.6, 0.6 \leq |\eta^{\gamma}| < 1.37, 1.52 \leq |\eta^{\gamma}| < 1.81$, and $1.81 \leq |\eta^{\gamma}| < 2.37$), and are differential in the transverse energy of the photon, E_{T}^{γ}. The first measurement is made using a data sample with an integrated luminosity of 880 nb^{-1}, and covers 15 GeV $\leq E_{\mathrm{T}}^{\gamma} <$ 100 GeV, while the second measurement uses 35 pb^{-1} of data, and covers 45 GeV $\leq E_{\mathrm{T}}^{\gamma} <$ 400 GeV.

The thesis is arranged as follows. The first chapter covers the primary motivations for the study of prompt photon physics at hadron colliders. The second chapter describes the experimental apparatus, including the CERN accelerator complex and the ATLAS detector. The following six chapters describe the measurement of the cross section with the 880 nb^{-1} data sample, including the extraction of the reconstruction and identification efficiencies, background rates, and a comparison of the measured cross section with theoretical predictions. Chapter 10 describes the measurement of the cross section with the larger dataset. A

conclusion and bibliography complete the document.

Chapter 2

Theoretical Motivation

This chapter presents the theoretical motivation for the study of prompt photons at hadron colliders. A discussion of the physics of hadron colliders, including a brief description of perturbative quantum chromodynamics (pQCD), is followed by the phenomonology of prompt photon production and detection. The importance of prompt photon studies is illustrated with several examples of decay signatures of new physics that include photons in the final state. Finally, the currently available tools for predicting prompt photon production rates are reviewed, along with a summary of previous measurements at other experiments.

2.1 Physics at Hadron Colliders

The physics of the very small and very energetic is well described by the Standard Model of particle physics. [3, 4, 5] The Standard Model has either explained or predicted nearly every major discovery in particle physics for over four decades.[1] A full description of the Standard Model and its importance in (and beyond) particle physics is beyond the scope of this text, but some features of the Standard Model are central to the study of prompt photon physics, and are worth some review. As will be described in Section 2.3, the production of prompt

[1] One notable exception is the discovery of neutrino flavor oscillations [6, 7, 8], which was not predicted by the Standard Model.

photons at hadron colliders is dominated by QCD processes, primarily through the coupling of a photon to a quark line. The theories of parton scattering, and the tools developed to model such interactions, play a fundamental role in the understanding of prompt photon dynamics.

2.1.1 The Parton Model and Perturbative QCD

The Parton Model was proposed by Bjorken and Feynman to explain the results of deep inelastic scattering experiments in the 1960's.[9, 10] In the Parton Model, protons are modeled as small groups of loosely bound point-like particles. A high-momentum-transfer (large Q^2) process will cause the disintegration of the proton into its constituent partons, and a feature known as Bjorken Scaling predicts that the partons will not interact with each other during this hard scattering process, provided that the total energy transfer of the system is sufficiently high. This means that the parton-parton coupling must be small at high energies.

The parton model, however, was not sufficient to describe the dynamics of low energy systems, where the partons do not behave independently of each other. These dynamics required a new theory based on a new quantum number, color, called quantum chromodynamics (QCD). The bridge between these two energy regimes was provided by the proof, in 1973, of the existence of renormalizable gauge fields with asymptotic freedom.[11] Asymptotic freedom is the characteristic of non-Abelian gauge theories that allows the interactions between particles to become weak as the energy scale grows large.

The physical consequence of asymptotic freedom in the context of QCD is that quark (or gluon) scattering at high energies is well described by the parton model. Mathematically, it equates the parton model with a first-order perturbative expansion of QCD in powers of α_S, the coupling constant that defines the interactions between colored particles. Because α_S becomes small at high Q^2, accurate predictions of parton dynamics require an expansion to relatively few orders in α_S, allowing the parton model (with higher-order corrections) to

remain relevant over many orders of magnitude in Q^2.

The description of the parton model as the first part of a perturbative expansion in orders of α_S means that, like in quantum electrodynamics (QED), diagrams will appear that cause fixed-order calculations to diverge. The solution, also as in QED, is to renormalize the theory, *i.e.* re-parametrize it so as to absorb the divergences into terms that exactly cancel. The penalty associated with this prescription is the introduction of a renormalization scale, μ_R, which has no physical meaning - it is only a mathematical term needed to "sweep the infinities under the rug". [12] The value of μ_R is typically chosen to be of the order of Q^2, though the exact choice of scale is often a matter of some debate. (See Section 2.1.4 for more discussion on the choice of scale.)

2.1.2 The Factorization Theorem

The dynamics of short-range interactions are well described by the parton model, but the long-range interactions between partons (interactions characterized by longer time constants and lower energies) also play some role in determining observable cross sections. In this regime, however, QCD is no longer perturbative, and singularities associated with gluon emission and reabsorption between different partons give rise to a new set of divergences, ones which do not cancel with the renormalization of QCD at high Q^2. While these divergences cannot be eliminated, they can be hidden within quantities that are measurably finite, in this case the parton distribution functions (PDFs). As with the renormalization procedure, this comes at the cost of the introduction of an unphysical scale parameter, μ_F, which effectively corresponds to the distance scale at which an interaction goes from being "short range" to being "long range".[13]

This separation of short- and long-range interactions into two distinct pieces is the core of the factorization theorem, which states that the cross section for some process $AB \to X$, where

A is composed of constituents $a_1, a_2, ..., a_i$ and B is composed of constituents $b_1, b_2, ..., b_j$, can be written as:

$$\sigma_{AB\to X} = \int dx_{a_i} f_{A/a_i}(x_{a_i}, \mu_F^2) dx_{b_j} f_{B/b_j}(x_{b_j}, \mu_F^2) \sigma_{a_i b_j \to X}(\mu_F^2, \mu_R^2) \tag{2.1}$$

The PDFs in Eq. (2.1) (f_{A/a_i} and f_{B/b_j}) cannot be calculated analytically, but their dependence on Q^2 (or μ_F, which is typically chosen to be of the same order as Q^2) is predicted by the Dokshitzer-Gribov-Lipatov-Altarelli-Parisi (DGLAP) evolution equations.[14, 15, 16] This allows a measurement of the PDF at a fixed value of Q^2 to be used to predict the PDFs over a wide range of Q^2. Several different collaborations have constructed sets of PDFs based on experimental data from HERA, the Tevatron, and other sources, using a variety of different methods for combining the diverse experimental inputs to create global constraints. In the analyses presented here, the CTEQ 6.6 [17] PDFs are used as the baseline, while comparisons are also made to predictions using MSTW 2008 [18].

2.1.3 Non-Perturbative Effects

The factorization theorem describes the dynamics of two hadrons interacting via constituent partons, and evolving into some partonic final state. However, the interactions treated by the factorization theorem are only part of the activity in the typical proton-proton interaction. Two additional effects play an important role in the definition of final-state observables at hadron colliders, namely the underlying event and hadronization.

2.1.3.1 The Underlying Event

Protons are composed of three valence quarks (two up quarks and a $d$own quark), and a number of sea quarks and gluons that carry part of the proton momentum. When two bunches of protons cross in the LHC, and two of those protons have a hard interaction, the momentum

transfer usually occurs through a single parton from each proton, along with some exchange of color charge.[2] The remnants of the two protons will carry some momentum away from the hard scatter, and additional parton-parton interactions (called multiple-parton interactions, or MPI) can also occur. Both of these effects can lead to the deposition of additional energy in the detector surrounding the interaction point, primarily in the form of soft particles that are weakly correlated with the products of the hard interaction. The total of all activity not associated with the hard scattering process is called the underlying event.[3] These types of processes are all classified as long-range interactions, and cannot be calculated perturbatively. Models that describe the underlying event exist within different Monte Carlo generators (discussed in Section 2.5), and can often provide a reasonable estimate of the average impact of the underlying event on final-state observables.

2.1.3.2 Hadronization

In interactions that produce a final-state parton, the escape of the new parton from the local color field causes a process known as hadronization or fragmentation.[4] The parton effectively begins to radiate gluons, which then decompose into $q\bar{q}$ pairs, which radiate gluons, and so on, creating a shower of partons with progressively smaller momenta. Eventually the partons will cluster into colorless hadrons, the collection of which is called a "jet".

While the creation of a final-state parton can be treated within pQCD, the evolution of a parton into a shower of low-energy particles eventually crosses into the non-perturbative regime. The dynamics of this evolution are absorbed into fragmentation functions, which give the probability for a parton to produce a final-state hadron through fragmentation. The σ

[2] Events in which the protons interact without any exchange of quantum numbers are called "diffractive", and typically have most of their activity at large rapidities.

[3] The text here is left intentionally vague, as the underlying event is not precisely defined in terms of specific processes. It is best understood as "everything but the hard interaction". See, for instance, reference [19] for more discussion of this.

[4] The two terms are often used interchangeably in this context.

term in Eq. (2.1) can thus be further modified to compute the process $A + B \to C + X$:

$$\sigma_{a_i b_j \to C+X} = \int dz_C D_{c_k}(z_C, \mu_f^2) \sigma_{a_i b_j \to c_k + X}(\mu_F^2, \mu_R^2) \tag{2.2}$$

where C is a hadron, D_{c_k} is the fragmentation function that defines the probability of a parton c_k fragmenting into C with momentum fraction $z_C = p_C / p_{c_k}$. These fragmentation functions depend on a fragmentation scale, μ_f, and effectively remove the same singularities in the final state as those removed by the factorization theorem in the initial state. As with the PDFs, measurements of the fragmentation functions can be made at a fixed value of Q^2 and evolved through the DGLAP equations to extrapolate to larger Q^2.

The only physical observables accessible to collider experiments are those measured after hadronization, by which point they are said to be measured at the particle level. This means that any cross section computed at the parton level, *i.e.* before hadronization, is not something that can be observed directly. Monte Carlo programs are typically used to estimate the impact of hadronization on observables to allow theoretical predictions (almost always made at the parton level) to be meaningfully compared with experimental measurements (almost always made at the particle level).[5]

2.1.4 Renormalization, Factorization, and Fragmentation Scales

The unphysical scales μ_R, μ_F, and μ_f are usually set to be equal (with their common value called μ). In the case of prompt photons, where the photon momentum is usually balanced by a single jet in the transverse direction (see Section 2.3), a convenient choice for the scale is the transverse energy of the photon, E_{T}^{γ}. This, however, is a somewhat arbitrary choice, and there is some systematic uncertainty associated with the exact choice of scale. This uncertainty can

[5] For a good discussion of these, and many other issues, see [13].

be evaluated by varying the scales around their nominal values and observing the change in value of the observable; a common range for photon measurements is $0.5E_{\mathrm{T}}^{\gamma} < \mu < 2E_{\mathrm{T}}^{\gamma}$.

2.2 Photon Physics

The previous section focused on the physics of hadron colliders; this section will focus on those proton-proton collisions that produce photons in the final state. The study of these photons plays an important role at hadron colliders, from probing pQCD to providing evidence for new physics within and beyond the Standard Model.

2.2.1 Testing Perturbative QCD

The primary means of testing perturbative QCD is with measurements of jet observables: their number, energy, azimuthal (de)correlations, and so on. This is because hard $2 \rightarrow 2$ processes that produce jets are by far the most abundant events at hadron colliders, and they provide great statistical power out to very high transverse energies. However, jets are messy objects. The definition of a jet is algorithmic (and parametric), not absolute. The development of several infrared- and collinear-safe jet algorithms is a relatively recent achievement, and the current jet algorithm favored by the LHC experiments (called the anti-$k_{\perp}$ algorithm [20]) is roughly three years old.

Another way of directly probing the hard scattering process, and thus pQCD, is with direct photons. The direct production of photons, through either a quark-annihilation or QCD-Compton process (see Section 2.3 and Fig. 2.2), provide an extremely clean probe of parton-parton interactions. The photon emerges from the hard interaction without any effects from hadronization, making the photon well defined at both the parton and particle levels. Furthermore, the existence of the QCD Compton diagram means that their production rate

is sensitive to the gluon content of the proton. This value is constrained at low $x_{\mathrm{T}} = 2E_{\mathrm{T}}^{\gamma}/\sqrt{s}$ by measurements of deep inelastic scattering and photo-production at HERA; the LHC will probe a much wider range of x_{T} values, with the potential to provide valuable input to global fits of parton distribution functions.

2.2.2 The Search for the Higgs Boson

The search for a low-mass Higgs at the Tevatron usually focuses on the case where the Higgs decays into a $b\bar{b}$ pair. The detection of a resonance in a $b\bar{b}$ invariant mass spectrum is challenging, as the QCD backgrounds are substantial (and not necessarily well modeled). To remedy this, the Higgs is usually required to be produced via $q\bar{q}$ annihilation into a W or Z boson, which then radiates a Higgs. The vector boson is used to tag the event, which reduces the backgrounds to more managable levels. At the LHC, however, the absence of a valence anti-quark with which to produce a W or Z (that then radiates a Higgs) combined with the significantly larger QCD backgrounds make a search in the $b\bar{b}$ channel extremely challenging.

The Higgs boson does not couple directly to photons, or to any massless particles. However, it can produce two photons in the final state via an intermediate fermion or vector-boson loop (see Fig. 2.1).

As the Higgs does not couple directly to any massless objects, its production from two gluons and decay to two photons both proceed through loops. These loops contain other particles to which the Higgs does couple strongly. In Higgs production, there is a colored loop of bottom or top quarks that connects to the colliding gluons. In a Higgs decay, there is an electrically charged loop of W bosons or top quarks that connects to the photons. Such a diphoton signature is extremely clean, and represents one of the most powerful channels for observing the Higgs in the mass range between 100 and 140 GeV.

The Higgs search in this channel is complicated by a large irreducible background from

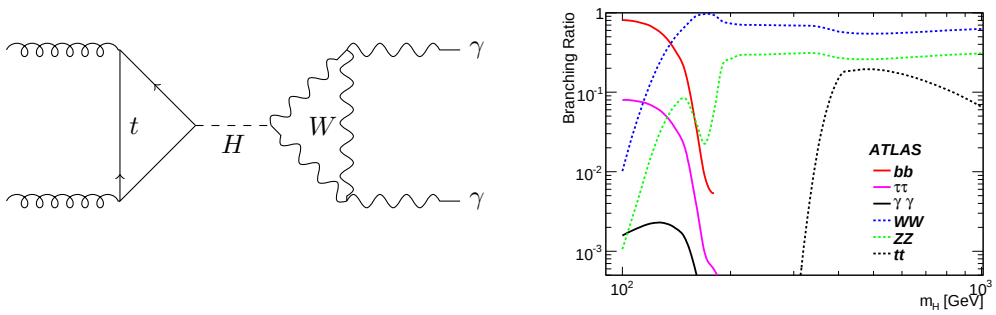

(a) Higgs Production/Decay (b) Higgs Branching Ratios

Figure 2.1: The Feynman diagram for the production of a Higgs boson and its decay into two photons (a), and the branching ratios of the Standard Model Higgs as a function of the Higgs mass (b). Standard Model Higgs production is dominated by the gluon-gluon channel (through a b or t quark loop), while the Higgs decay to photons can go through a loop of either W bosons or top quarks. The diphoton decay channel is most significant at Higgs masses of around 120 GeV. Despite the overall low branching ratio for $H \to \gamma\gamma$, it remains an important decay mode because of its clean signature.

Standard Model diphoton production, and by similarly large, but reducible, backgrounds from gamma+jet and dijet events (where one or more jets fake a photon). The gamma+jet background is exactly the direct component of Standard Model prompt photon production, and the jet-jet background is shared between the two analyses, allowing the development of the Higgs search to benefit from the high statistics samples of the inclusive photon measurement.

2.2.3 Physics Beyond the Standard Model

Looking beyond the Standard Model, photons are present in the final states of many signatures of new physics.

- **Randall-Sundrum Gravitons** The Randall-Sundrum (RS) model [21] was proposed in an attempt to solve the hierarchy problem, by postulating that the observable universe is a four-dimensional brane contained within a five-dimensional bulk space. In this model (and in other models containing large extra dimensions) gravity operates in five dimensions while the other known forces only operate within the brane, leading

to the apparent weakening of gravity within the brane. The warped geometry of the bulk space leads to a tower of excited resonances of the gravitational field, the first of which corresponds to the (normally massless) graviton, with charge=0 and spin=2. The massive graviton can then decay into Standard Model fermions or bosons, including into pairs of photons.

- **Large Extra Dimensions** In addition to the RS model, other theories with large extra dimensions (see, for instance, [22]) predict the production of di-photon pairs, this time in combination with missing transverse energy ($E_{\mathrm{T}}^{\mathrm{miss}}$) due to the escape of massless gravitons in a cascade decay from the first Kaluza-Klein (KK) excitation. In this case, the signal would appear as an excess in the $E_{\mathrm{T}}^{\mathrm{miss}}$ distribution for events containing two energetic photons.

- **Gauge-Mediated Supersymmetry Breaking** One model of symmetry breaking within Supersymmetry is called gauge-mediated supersymmetry breaking (GMSB) [23, 24, 25], where the lightest supersymmetric particle (LSP) is the gravitino, the supersymmetric partner to the graviton. The lightest neutralino then decays to a gravitino and a photon. When a pair of heavy supersymmetric particles are produced, they can cascade decay down to neutralinos (which then decay), producing jets, two photons, and two gravitinos (which appear as $E_{\mathrm{T}}^{\mathrm{miss}}$).

This is not an exhaustive list of new physics that can be probed with photons, but it illustrates the ability of photon physics to play a role in covering a broad range of theoretical models that extend beyond the Standard Model.

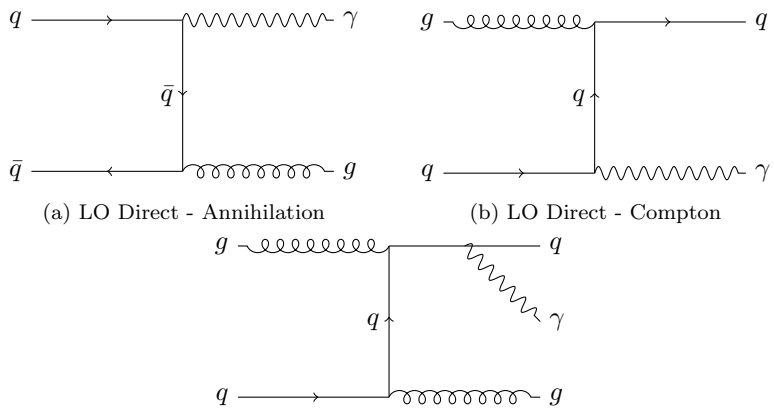

Figure 2.2: Leading order diagrams of direct photon production at hadron colliders. Direct photons are prompt photons that take part directly in the hard scattering process. The quark-gluon QCD-Compton diagram (b) dominates the direct production at the LHC, accounting for more than 90% of the total rate for all E_{T}^{γ}. The LO fragmentation diagram (c) has a large contribution at low E_{T}^{γ}.

2.3 Prompt Photon Production

Prompt photons are often separated into two categories: direct photons, which take place in the hard scattering process, and fragmentation photons, which are the products of the collinear fragmentation of a final-state parton.

At leading order, direct photons are produced through two Born-level processes: $q\bar{q} \rightarrow g\gamma$, (annihilation) and $qg \rightarrow q\gamma$ (Compton). Both diagrams are shown in Fig. 2.2. At the LHC, the Compton process dominates for all energies.[6]

At next-to-leading order, the direct component includes contributions from diagrams like $q\bar{q} \rightarrow \gamma\, gg$ and $qg \rightarrow \gamma\, qg$, where the photon is effectively produced via radiation off of an intermediate quark line. There are also virtual corrections to the annihilation and Compton processes that enter at next-to-leading order, including the leading-order component of the fragmentation contribution. These leading-order fragmentation diagrams can be thought of

[6] At the Tevatron, the presence of valence anti-quarks leads to the annihilation process dominating for photons with high transverse energies.

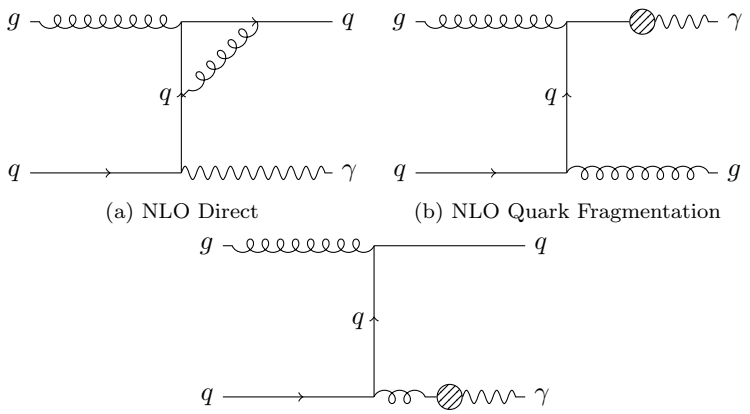

Figure 2.3: Next-to-leading order (NLO) diagrams of prompt photon production at hadron colliders. The NLO direct component (a) comes primarily from gluon loop corrections to the LO direct diagrams in Fig. 2.2. The fragmentation diagrams (b) and (c) represent all parton splittings that end in a single photon emitted from a quark line, and are encapsulated within the fragmentation functions D_k^γ.

as the hard radiation of a photon off of a final-state quark. The next-to-leading order fragmentation component goes on to include all processes in which a final-state parton fragments to produce a single photon (in association with other hadronic remnants of fragmentation), including the cases where the photon is produced collinear to the parton momentum.

The higher-order (in α_S) terms of the fragmentation process are factorized and absorbed into photon fragmentation functions, $D_k^\gamma(z, \mu_F)$, where k indicates either a quark or gluon, z the fraction of the parton momentum carried away by the photon, and μ_F the fragmentation scale used in the fixed-order calculation.

With this treatment of the diagrams at next-to-leading order (and beyond), the distinction between fragmentation and direct photons has no physical meaning beyond leading order. Only the sum of the direct and fragmentation components yields a physical observable.

2.4 Isolated Prompt Photons

The principle challenge of prompt photon studies at hadron colliders is the extraction of the signal in the presence large backgrounds, which are primarily composed of light mesons (π^0, η, ω) that decay to multiple photons. In order to separate the prompt photon signal from these backgrounds, photon candidates are typically required to be isolated from nearby hadronic activity characteristic of a jet with a leading light meson. One measure of this nearby hadronic activity is the transverse energy in a region around the photon candidate, called the transverse isolation energy. (In this document, it is abbreviated as $E_{\mathrm{T}}^{\mathrm{iso}}$.) It is the sum of the transverse momenta of all particles produced in a cone of radius ΔR around the photon axis.[7] The isolation cut usually takes one of two forms: either a cut relative to the photon E_{T} ($E_{\mathrm{T}}^{\mathrm{iso}}/E_{\mathrm{T}}^{\gamma} < \epsilon$), or an absolute cut independent of E_{T}^{γ} ($E_{\mathrm{T}}^{\mathrm{iso}} < E_{\mathrm{T}}^{\mathrm{max}}$).

Light mesons that fake prompt photons are produced as part of a jet, which will have additional nearby particles that lead to a large value of $E_{\mathrm{T}}^{\mathrm{iso}}$. Direct photons produced in a Born-level process are produced back-to-back (in azimuth) with a single jet, and will almost always have $E_{\mathrm{T}}^{\mathrm{iso}} = 0$. For fragmentation photons, the situation is slightly more complicated. In this case, the photon is produced as part of a fragmentation process that also has hadronic remnants. In cases where the cone radius is small and the photon is produced with large z, $E_{\mathrm{T}}^{\mathrm{iso}}$ can still be small (or zero), and the separation between signal and background is preserved. In cases when the cone radius is large, or when z is small, the value of $E_{\mathrm{T}}^{\mathrm{iso}}$ will increase. Thus, the application of an isolation requirement will remove some fraction of the fragmentation component as well as the background. When performing NLO calculations, the situation is further complicated by the presence of soft gluons, which emerge as part of the factorization scheme. An isolation cut on the photon will limit the allowable phase space for

[7] See Chapter 3 for a precise definition of the coordinate system for this quantity.

soft gluon emission.

These side-effects of the isolation requirement lead one to question whether the factorization theorem, as applied to inclusive photon production, is still valid in the case of *isolated* photon production. This question was first answered in [26], where the authors proved that an isolation requirement is collinear and infrared safe, and does not lead to divergences in the calculations. However, there are certain conditions in which the calculation can diverge at certain orders in perturbation theory, so the endorsement of an isolation prescription comes with the following caveats:

1. The cone radius, ΔR, should not be too small (to avoid large uncertainties in the fragmentation functions)

2. The $E_{\mathrm{T}}^{\mathrm{iso}}$ threshold, $E_{\mathrm{T}}^{\mathrm{max}}$, should be large enough that the phase space for soft gluon emission is not overly restricted.

To meet these constraints, while optimizing signal efficiency and background rejection in an experiment, a typical isolation prescription defines a cone of radius $\Delta R = 0.4$ and an absolute $E_{\mathrm{T}}^{\mathrm{iso}}$ threshold of a few GeV (or a relative threshold of around 10% of the photon E_{T}). The specific cuts used by the Tevatron experiments and by CMS are described in Section 2.6; the details of the ATLAS isolation prescription will be described in Section 5.3.

2.5 Predictive Tools

There are several tools available for making predictions of prompt photon production rates at hadron colliders.

2.5.1 JETPHOX

The JETPHOX generator [26] is a next-to-leading order Monte Carlo program. It calculates the double-differential cross-sections $d^2\sigma/(dE_{\mathrm{T}}^{\gamma}d\eta^{\gamma})$ for $A+B \rightarrow C+D+X$ processes, where either C or D (or both) can be photons, and A and B are partons with properties given by parton distribution functions. The program takes as inputs the definitions of the fragmentation functions, the parton distribution functions, and acceptance criteria that can be used to simulate common experimental constraints.

The default behavior in JETPHOX is to calculate a fully inclusive prompt photon cross section, with no regard for the isolation of the photon from additional hadronic activity. However, JETPHOX is also capable of estimating the isolation energy of prompt photons at the parton level, and can therefore provide a prediction of an isolated prompt photon cross section. The isolation cut can be applied either as a relative cut or as an absolute cut.

2.5.2 PYTHIA

The PYTHIA event generator is a leading-order parton-shower Monte Carlo program [27], and is widely used in collider physics to generate a broad range of QCD, electroweak, and more exotic events. It accounts for QED radiation emitted off quarks in the initial state (ISR) and final state (FSR). The underlying event is simulated using the MPI model, and the hadronization of partons is modeled with the Lund string model [28].

PYTHIA models the leading order direct photon contributions in roughly the same way as JETPHOX. The fragmentation component is modeled as FSR, with no knowledge of the fragmentation functions D_k^{γ}. The ATLAS configuration of PYTHIA uses the modified leading order MRST2007 [29] parton distribution functions, and the event generator parameters are set according to the ATLAS MC09 tune [30].

As PYTHIA is a parton-shower program, its output is passed into a detailed simulation of the ATLAS detector to enable studies of the detector response. The detector is simulated using the GEANT4 program [31]. These simulated samples are then reconstructed with the same algorithms used for data. More details on the event generation and simulation infrastructure of the ATLAS experiment are provided in [32].

2.5.3 HERWIG

The HERWIG event generator is also a leading-order parton-shower Monte Carlo program [33]. It differs from PYTHIA in its parton shower model (which is angle-ordered instead of p_{T}-ordered), its hadronization, (the cluster model instead of the Lund string model), and its treatment of the underlying event (modeled with a separate package, JIMMY [34]). Samples generated with HERWIG are used in the analyses presented in this document to derive systematic uncertainties related to the event generator, the hadronization model, and the impact of the underlying event on the measurement.

2.5.4 SHERPA

SHERPA is a relatively new multi-purpose event generator. [35] Its treatment of prompt photons differs from that of PYTHIA and HERWIG by modeling the fragmentation functions as a part of the parton shower, thus making predictions with NLO accuracy while still providing parton-shower merging that can be used to study the detector response. Future measurements of prompt photon, photon+jet, and diphoton production at the LHC will likely include comparisons to SHERPA as well as JETPHOX. At the time of this writing, however, its predictions of prompt photon production have not yet been fully validated by the authors. Thus it is listed here only for completeness.

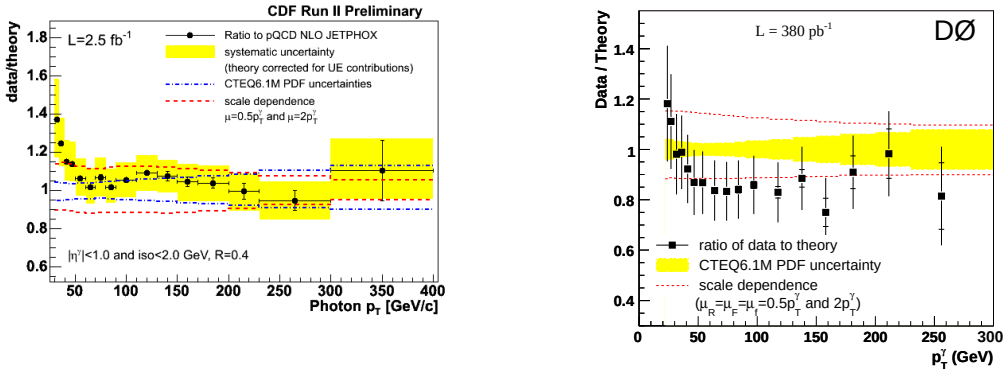

(a) CDF (b) DØ

Figure 2.4: Measurements of the inclusive isolated prompt photon production made at CDF (a) and DØ(b), presented as a ratio of the double ($E_{\mathrm{T}}$and η) differential cross-section with respect to the JETPHOX predictions.

2.6 Previous Results

The earliest studies of prompt photon production were carried out at the ISR collider at CERN. [36, 37] Subsequent studies, for example [38, 39, 40], further established prompt photons as a useful probe of parton interactions.

More recent measurements at hadron colliders were performed at the Tevatron, in $p\bar{p}$ collisions at a center-of-mass energy $\sqrt{s} = 1.96$ TeV. The measurement by the DØ Collaboration [41] is based on 326 pb^{-1} and covers a pseudorapidity range $|\eta^{\gamma}| < 0.9$, with a transverse energy range $23 < E_{\mathrm{T}}^{\gamma} < 300$ GeV. The measurement by the CDF Collaboration [42] is based on 2.5 fb^{-1} and covers a pseudorapidity range $|\eta^{\gamma}| < 1.0$, with a transverse energy range $30 < E_{\mathrm{T}}^{\gamma} < 400$ GeV. Both DØ and CDF measure an isolated prompt photon cross section in agreement with next-to-leading order pQCD calculations, with a slight excess seen in the CDF data between 30 and 50 GeV. Their measured cross sections, compared with JETPHOX predictions, are shown in Fig. 2.4.

The most recent measurement of the inclusive isolated prompt photon production was

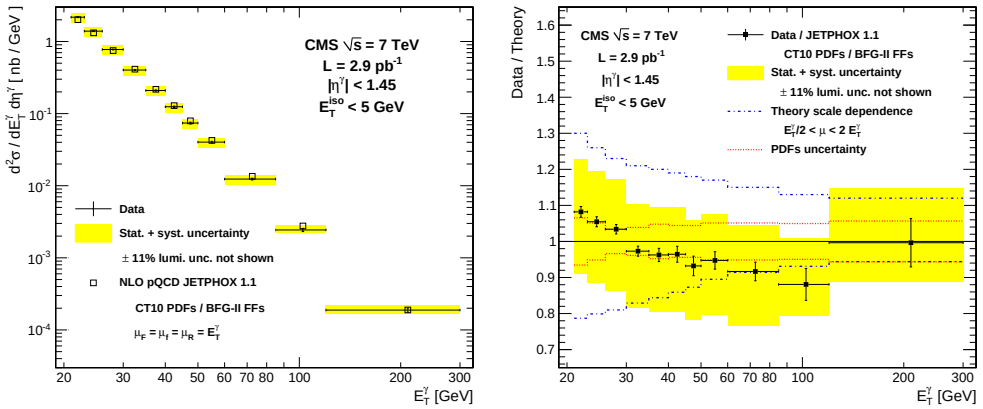

(a) (b)

Figure 2.5: A measurement of inclusive isolated prompt photon production made by the CMS collaboration, shown as (a) a double differential (in E_{T} and η) cross section, and (b) as the ratio of the cross section to the theoretical prediction from JETPHOX.

done with 2.9 pb^{-1} of proton-proton collisions at $\sqrt{s} = 7$ TeV by the CMS Collaboration [43]. That measurement, shown in Fig. 2.5, covers $21 < E_{\mathrm{T}}^{\gamma} < 300$ GeV and $|\eta^{\gamma}| < 1.45$, and shows good agreement with JETPHOX predictions over the full E_{T}^{γ} range.

The isolation prescriptions used by D∅, CDF, and CMS are all slightly different:

- D∅ defines isolation energy as $E_{total}(0.4) - E_{EM}(0.2)$, where $E_{total}(X)$ ($E_{EM}(X)$) is the total (electromagnetic) calorimeter energy in a cone of radius X. The isolation energy is required to be less than $0.1 \times E_{EM}(0.2)$.

- CDF defines isolation energy as $E_{\mathrm{T}}(0.4) - E_{\mathrm{T}}^{\gamma}$, where $E_{\mathrm{T}}(0.4)$ is the total calorimeter E_{T} in a cone of radius 0.4 around the cluster centroid. This isolation energy is further corrected to remove photon leakage contributions and pileup effects. The isolation energy is required to be less than 2 GeV.

- CMS defines separate track, EM, and hadronic isolation energies, and applies cuts on all three:

- Track Isolation: the sum of the transverse momenta of all tracks in an annulus of $0.04 < R < 0.40$ around the photon must be less than 2 GeV. The region also excludes a rectangular strip of $\Delta\eta \times \Delta\phi = 0.015 \times 0.400$ around the photon, to remove the energy from tracks associated with a photon conversion.
- EM Isolation: the sum of the transverse energy deposited in the ECAL in an annulus of $0.06 < R < 0.40$, excluding the strip $\Delta\eta \times \Delta\phi = 0.04 \times 0.400$, must be less than 4.2 GeV.
- Hadronic Isolation: the sum of the transverse energy deposited in the HCAL in an annulus of $0.15 < R < 0.40$ around the photon must be less than 2.2 GeV.

In the CDF and CMS measurements, the theoretical predictions from `JETPHOX` are scaled to take into account the contributions of underlying event and parton fragmentation, which tend to increase the energy in the isolation cone at the particle level. The scale factors are typically estimated using `PYTHIA` Monte Carlo samples with multiple-parton interactions and/or hadronization turned off, by comparing the measured cross section in such samples with the cross section measured in samples simulated under nominal conditions. For CDF, this results in an 8.7% correction, while for CMS the correction is 3%.

Chapter 3

The Large Hadron Collider and the ATLAS Detector

3.1 The Large Hadron Collider

The Large Hadron Collider (LHC) at CERN (the European Center for Nuclear Research) is a 26.7 kilometer long particle accelerator outside of Geneva, Switzerland. [44] It lies below-ground in the tunnel previously inhabited by the LEP machine. It is capable of colliding particles at four different experimental sites, which are occupied by the ATLAS, ALICE, CMS, and LHCb detectors.

There are several principal parameters used to define the physics potential of a particle accelerator:

- The center-of-mass energy, or $\sqrt{s}$, is the total energy of a proton-proton system at an interaction point (in the lab frame).

- A is the cross-sectional area of the beam at a collision point, and depends on the longitudinal and lateral spread of the proton bunches. It can be expressed as:

$$A = \frac{4\pi\varepsilon_n\beta^*}{\gamma_r F} \tag{3.1}$$

  where ε_n is the normalized transverse beam emittance, β^* is the beta function (a measure

of the beam width) at the collision point, γ_r is the Lorentz gamma factor, and F is a factor that accounts for the fact that the beams do not strike head-on, but rather cross with some angle.

- The luminosity, $\mathcal{L}$, is then defined as:

$$\mathcal{L} = \frac{f_{rev} n_b N_1 N_2}{A} \tag{3.2}$$

where f_{rev} is the revolution frequency of the beam, n_b is the number of bunches in the beam, and N_i is the number of particles in each bunch. (Their typical values will be discussed in the following section.)

As a proton-proton collider, the LHC has a designed center-of-mass energy of 14 TeV and a designed luminosity of 10^{34} cm^{-2}s^{-1}. It is also capable of colliding heavy ions (lead) at energies of 5.5 TeV per nucleon pair, with a peak luminosity of 10^{27} cm^{-2}s^{-1}.

3.1.1 Design

To achieve its ambitious goals for beam energy and luminosity, while meeting the physical constraints of the LEP tunnel, the LHC was designed as a two-ring superconducting accelerator. The superconducting elements are Niobium-Titanium (NbTi) coils, which are cooled to a temperature of 1.9 Kelvin through the use of 96 metric tons of superfluid liquid Helium. The two rings share a cryogenic and mechanical structure, and are coupled magnetically, each ring having a magnetic flux equal in magnitude (but opposite in direction) to the other. A cut-away view of an LHC dipole is shown in Fig. 3.1.

Protons are accelerated in stages in the CERN accelerator complex, culminating in their injection into the LHC at a beam energy of 450 GeV. The protons are injected in bunches, with a maximum bunch size of roughly 1.5×10^{11} protons (N_i). There can in principle be as

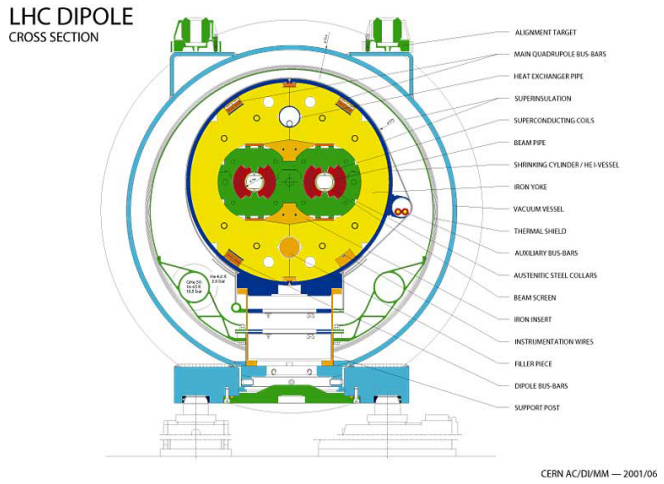

Figure 3.1: A cut-away view of an LHC dipole magnet. There sections of both LHC rings in each magnet, one for each beam. The rings are coupled magnetically, each having a flux of equal magnitude and opposite sign to the other, and share mechanical and cryogenic services.

many as 3564 bunches stored in each ring; in practice, not every bunch is filled, and there is an effective maximum of 2808 filled bunches (n_b). Each bunch orbits the ring with a frequency of 11 kHz (f_{rev}). Bunch crossings occur at each of the interaction points at a frequency of 40.08 MHz. At its design luminosity, each bunch crossing will have roughly 20 proton-proton interactions.

After injection and acceleration, protons are circulated and collided for a long period of time. This is known as a fill, and can last as long as 24 hours. Over this time the instantaneous luminosity will degrade as the protons collide and the proton bunches slowly lose their integrity. A typical fill can see a factor of two (or more) drop in instantaneous luminosity from beginning to end, depending on the length of the fill and the stability of the beam.[8]

Even at the highest instantaneous luminosities, most bunch crossings will contain only one hard (large Q^2) interaction. Additional proton-proton interactions in each crossing are referred to as in-time pileup, and will typically contribute energy (in the form of soft parti-

[8]The luminosity lifetime (τ) of the LHC beam is roughly 15 hours; depending on the down-time between fills, the optimal fill length is anywhere from 5 to 24 hours. [44]

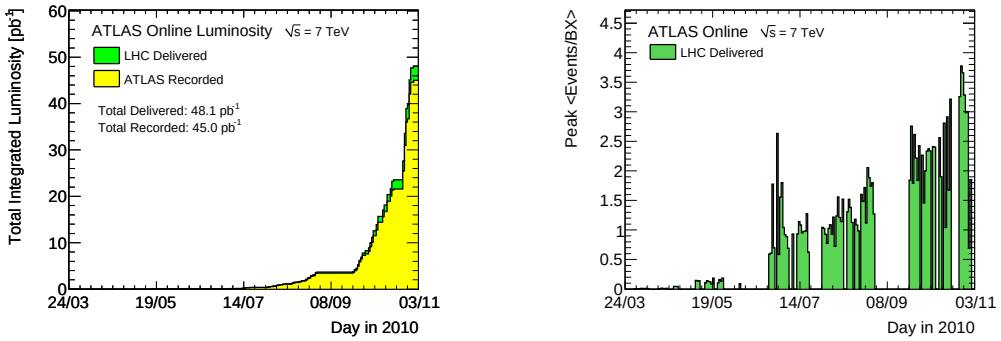

(a) Integrated Luminosity

(b) Peak Instantaneous Luminosity

Figure 3.2: The integrated luminosity (a) and the peak average interactions per crossing (b) delivered by the LHC in the 2010 run.

cles) homogenously throughout the detector. The effects of in-time pileup on prompt-photon identification will be discussed further in Section 5.3. In addition to in-time pileup, the short bunch-spacing of the LHC beams means that the detector response in a given bunch crossing can be influenced by the residual effects of previous bunch crossings. Such out-of-time pileup effects will also be discussed in Section 5.3.

3.1.2 Running Conditions in 2010

The LHC produced its first collisions at $\sqrt{s}$=7 TeV in the spring of 2010, and continued to run throughout the summer and fall at that energy. At first, there was a single bunch per beam, with an average of less than one interaction per bunch crossing. The beam conditions improved quickly over the summer and fall, and the instantaneous luminosity grew from 10^{27} cm^{-2}s^{-1} in April to over 2×10^{32} cm^{-2}s^{-1} in November. At the end of the 2010 run, the LHC was averaging over three interactions per crossing, with trains of filled bunches in each beam. The minimum bunch spacing was 150 ns. A plot of the integrated luminosity delivered by the LHC vs. time is shown in Fig. 3.2.

3.2 The ATLAS Detector

ATLAS (**A** **T**oroidal **L**HC **A**pparatu**S**) is one of two general-purpose detectors at the LHC - the other is the Compact Muon Solenoid (CMS) detector. As with other modern experiments, ATLAS was designed as a hermetic detector with the following elements:

- An inner tracking detector immersed in a solenoidal magnetic field, capable of providing precision momentum measurements for charged particles originating at (or near) the interaction point,
- A calorimetry system sensitive to both electromagnetic (EM) and hadronic interactions, which provide good particle identification capabilities as well as accurate measurements of object/jet energies and missing transverse energy ($E_{\mathrm{T}}^{\mathrm{miss}}$),
- A muon spectrometer, also immersed in a magnetic field, which provides muon identification and accurate momentum measurements over a wide range of muon momenta, and
- A tiered triggering system, composed of both hardware- and software-based decision making elements, to identify interesting events for a broad variety of physics goals.

ATLAS distinguishes itself from other, similar experiments in two important ways. First, in addition to silicon pixel and silicon strip sensors in the inner tracker, ATLAS uses a straw tracker with transition radiation detection capabilities for electron/pion discrimination. Second, the magnet system used for the muon spectrometer is composed of superconducting air-core toroids, rather than a second solenoidal field.

In this section, the features of the ATLAS detector relevant to photon physics will be reviewed. The primary focus will be on the inner tracker and the EM calorimeter, with some additional discussion of the hadronic calorimetry and trigger systems used in the prompt

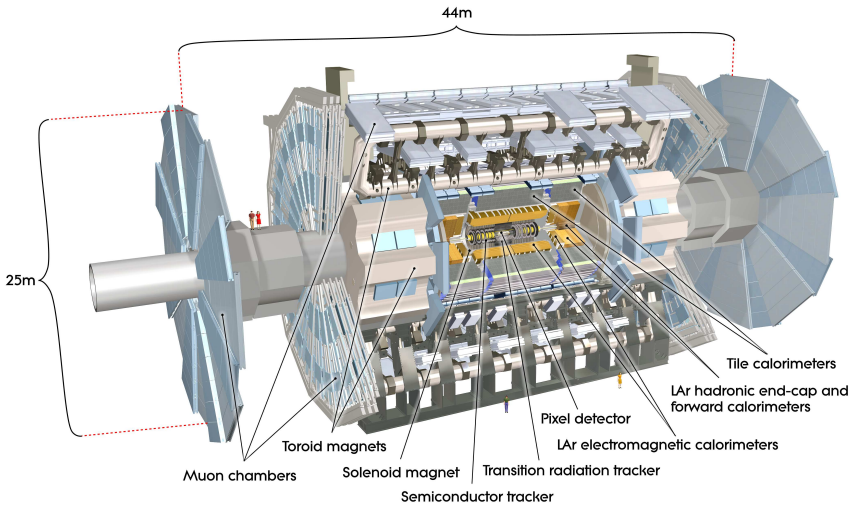

Figure 3.3: The ATLAS detector. The inner-most layers belong to the inner tracker, and include both silicon and straw tube sensors. Just outside of the inner tracker are the electromagnetic and hadronic calorimeters. The large air-core toroids and muon spectrometer define the outer envelope of the detector.

photon analysis. More detailed explanations and references for much of the material in this section can be found in [45].

3.2.1 Coordinate System

The ATLAS coordinate system defines the origin at the nominal proton-proton interaction point. The beam direction defines the z axis; positive values point counter-clockwise around the ring. The $x-y$ plane is perpendicular to the z axis, with positive x values pointing towards the center of the ring. The coordinate system is chosen to be right handed, so the positive y axis points away from the Earth's core. ATLAS is nominally symmetric across the $x-y$ plane at $z = 0$; the portion of the detector corresponding to $z > 0$ is sometimes called "Side A", while $z < 0$ is called "Side C". Many subsystems are composed of a barrel portion, which has detecting elements arranged parallel to the z axis, and two endcap portions, with detecting elements arranged in planes perpendicular to the beam axis. The endcaps may therefore be

referred to as "Endcap-A" and "Endcap-C".

Cylindrical and polar coordinate systems are frequently used to describe both detecting elements and the trajectories of particles through the apparatus. The radius R is defined as the perpendicular distance to the z axis. An azimuthal angle ϕ is defined around the z axis, while a polar angle θ is defined as the angle away from the z axis. The variable θ itself is rarely used; rather, a variable known as rapidity (y) is preferred:

$$y = \frac{1}{2}\ln\left(\frac{E + p_z}{E - p_z}\right) \tag{3.3}$$

where E represents the energy of an object, and p_Z its momentum along the z axis. In the case of massless objects, such as photons, the rapidity is equivalent to the pseudorapidity (η):

$$\eta = -\ln\,\tan\left(\frac{\theta}{2}\right) \tag{3.4}$$

As pseudorapidity is defined only with respect to θ, it has a well-defined and mass-independent interpretation in the lab frame, and is commonly used when discussing detector performance. It is also common to refer to the $\eta - \phi$ plane, in which the surfaces of the cylindrical detectors appear as flat sheets.

Colliding protons transfer momenta through constituent partons which carry unknown fractions of the proton momentum. Some of that momentum is exchanged in the hard interaction, and some of it lost to remnants that escape down the beam pipe. Thus, one cannot easily use total momentum conservation to place constraints on the kinematics of a single event. However, as the protons approach each other with trajectories that are nearly along the z axis, momentum *is* conserved in the plane transverse to the beam axis. Thus, in many cases, only the transverse component is used when describing object kinematics, *e.g.* $E_{\mathrm{T}}(= E\sin\theta)$ and $p_{\mathrm{T}}(= p\sin\theta)$.

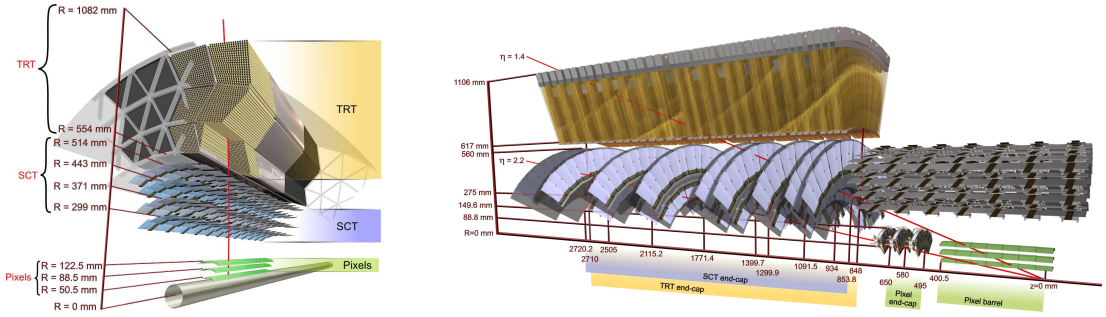

(a) ID Barrel (b) ID Endcap

Figure 3.4: The barrel (a) and endcap (b) inner tracking subsystems of the ATLAS detector. The pixel subsystem is closest to the beamline, followed by the SCT, and finally the TRT. Detecting elements in the barrel are arranged axially, while those in the endcap are arranged radially.

3.2.2 Inner Tracker

The inner tracker contains three subsystems. The subsystem closest to the interaction point is composed of silicon pixel sensors, and is commonly called the "pixel detector" (or just the "pixels"). Just outside of the pixels is a silicon microstrip detector, called the Semi-Conductor Tracker (SCT). The outermost system is a straw tube tracker with transition radiation inducing and detecting capabilities, called the Transition Radiation Tracker (TRT). Each subsystem is composed of a barrel and two endcaps, shown in Fig. 3.4.

Silicon-based trackers are used in all modern general-purpose particle detectors for their excellent position resolution, which is typically on the order of microns. The sensors are thin pieces of high-purity doped silicon, which produce electron-hole pairs when traversed by an ionizing particle. An electric field is applied to the sensor to prevent the pairs from recombining, and the subsequent drift and capture of the free charge carriers produces a current pulse that is read out by analog electronics.

The pixel and SCT subsystems each provide a small number of hits on track; the TRT, by contrast, is a straw-tracker that provides semi-continuous tracking out to large radii. An

typical charged particle traversing the TRT will produce approximately 36 hits on track, with a resolution of around 130 μm. The TRT is also unique in its ability to induce and detect transition radiation, which provides good electron/pion separation over a broad range of particle momenta.

3.2.2.1 The Pixel Detector

The pixel detector has a barrel section and two endcap sections. The barrel has three concentric layers, with distances of 50.5 mm, 88.5 mm, and 122.5 mm from the beam axis, and which cover the central region up to $|\eta| = 1.9$. The innermost layer is called the "B-layer", and is mechanically integrated with the beryllium beam pipe. There are three endcap disks on each side, extending the total coverage out to $|\eta| = 2.5$. A charged track originating at the interaction point will almost always produce three pixel hits; the single-hit efficiency ranges from 97% to 100%, depending on the layer, including acceptance losses.

There are 1744 "sensors" in the pixel subsystem, with each sensor composed of 47323 individual pixels. The sensors are 19×63 mm^2, while the nominal pixels dimensions are 50×400 μm^2. This leads to a total of over 80 million pixels, each with an intrinsic $R-\phi$ accuracy of 10 μm, and an intrinsic z (R) accuracy of 115 μm in the barrel (endcap).

3.2.2.2 The Semi-Conductor Tracker

The SCT is also composed of a barrel and two endcap sections. The barrel part has four concentric layers, ranging from an innermost radius of R=299 mm to the outermost layer at R=514 mm. It covers the central region, up to $|\eta| = 1.1$. The endcaps each have nine disks of varying sizes, extending the total coverage of the SCT out to $|\eta| = 2.5$. A charged track originating from the origin will almost always cross four separate SCT detecting elements; the single-hit efficiency is better than 99% in all regions of the detector.

The silicon sensors are designed as collections of thin strips; each of the 15912 sensors has 768 active strips, for a total of over 6 million channels. The strips are 12 cm in length, with a pitch of 80 μm. Each layer of the SCT has sensors on both sides, with a stereo angle of 40 mrad between back-to-back modules. This allows the nominally one-dimensional sensors to have a resolution in z (R) in the barrel (endcap) of roughly 580 μm, while the resolution in $R-\phi$ is 17 μm. The requirement of coincident hits on both sides of the module reduces the impact of noise to negligible levels.

3.2.2.3 Transition Radiation Tracker

3.2.2.3.1 The Physics of Straw Trackers When a charged particle passes through the TRT straws, Coulomb interactions between the charged particle and the valence electrons in the gas will result in the liberation of some of those electrons from their respective nuclei. In the TRT, the outer wall of the straw has a radius of 2 mm and acts as a cathode, held at a negative potential. A wire strung down the middle of the straw acts as an anode. The primary ionization electrons are move towards the anode; as they get close to the wire, the strong electric field allows the primary electrons to ionize more of the gas, inducing an avalanche of electrons that amplifies the signal at the wire. This characteristic "gas gain" in the TRT is of order 2×10^4.

If the electrons are liberated close to the wire, the electrons will be collected by the anode almost immediately. Electrons that are freed closer to the cathode will have a drift time that depends on the type of gas used - for a Xenon/CO_2 mixture, the drift time for electrons will be around 25 ns/mm. A particle passing through the straw will always ionize some of the gas close to the edge of the straw, so the "trailing edge" of the electronic pulse should be fixed with respect to the time at which the particle traverses the straw.

The electron drift towards the anode is balanced by an ion drift towards the cathode. The

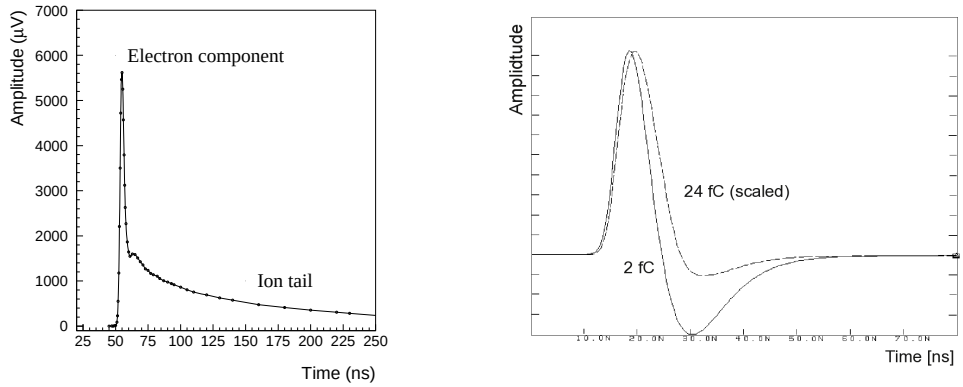

(a) Current Response (b) Baseline Restoration

Figure 3.5: (a) The current response on the TRT wires due to a point-like ionization in the gas. The component due to the avalanche electrons is roughly 5% of the total signal, and quickly gives way to a long tail due to the ion drift towards the cathode. (b) The result of the baseline restoration in the TRT front-end electronics for a 2 fC (solid) and 24 fC (dashed) input charge. The 24 fC pulse is scaled to have the same peak amplitude as the 2 fC pulse. (Images from [1].)

ion drift is largely composed of the ionized gas from the avalanche near the wire, and thus travels the full 2 mm to the straw wall. This ion drift occurs at significantly longer time scales (μs/mm) and induces a long tail of mirror current on the wire. An example of the total straw current response is shown in Fig. 3.5a. The tail is sufficiently long compared to the LHC bunch spacing that collecting all of the charge from the ions is not possible at the LHC, so some active cancellation is performed at the TRT front-end. This is illustrated in Fig. 3.5b, and explained in more detail in Section 3.2.2.3.4.

3.2.2.3.2 Mechanical Design Like the silicon trackers, the TRT has one barrel and two endcap sections. The barrel has straw tubes arranged coaxially with the beamline, while the endcaps have straws arranged radially in layers of constant z. The barrel part provides full coverage out to $|\eta| = .7$, and partial coverage up to $|\eta| \approx 1.0$, while the endcap extends the coverage to $|\eta| = 2$.

The straw tubes in the TRT are made of two layers of polyimide film, strengthened by

carbon fibers, surrounded by two thin layers of aluminum protected by a graphite-polyimide layer. The straws are 4 mm in diameter, and 1.4 m (0.35 m) long in the barrel (endcap). A gold-plated tungsten wire runs down the middle of the straw, attached to tension plates on either end. The straws are filled with a gas mixture of 70% Xe, 27% CO_2, and 3% O_2.[9] The Xenon provides efficient absorption of the transition radiation X-rays, while the CO_2 and O_2 help to prevent frequent discharges in the gas and increase the electron drift velocity. The straw wall is held at approximately -1530 Volts.[10] The gold/tungsten wire anode is connected to the analog readout electronics.

There are 298,304 straws in the TRT; 52,544 straws are in the barrel. The wires in these straws are separated at $|\eta| = 0$ with a glass bead, allowing the analog signals to be read out on both ends, and effectively doubling the total readout channels to 105,088.[11] The barrel is split into three concentric layers of 32 trapezoidal modules each, supported by a carbon-fiber space frame. On either end of each module are two triangular "active roof" boards, which hold the analog and digital electronics. A picture of the barrel TRT, taken in its surface assembly facility at CERN, is shown in Fig. 3.6a.

The remaining 245,760 straws are split evenly between both endcaps. Each endcap is composed of stacks of disks in z called wheels. The first six wheels in z are the "A" wheels; each A wheel has sixteen planes of straws. The outermost eight wheels are the "B" wheels; each B wheel has eight planes of straws.[12] Each plane has 768 straws, and the planes in all of the wheels are slightly offset from each other in ϕ (with a period of eight planes) to ensure good coverage. The readout electronics are connected to the straws at the outer radius of

[9] A 70% Ar/30% CO_2 mixture was used for much of the commissioning period, to avoid the cost of running with Xenon.

[10] The exact voltage is tuned in groups $\tilde{1}00$ straws to give a gas gain of 2.5×10^4.

[11] The innermost 10 layers in R have two glass beads, creating an uninstrumented gap in the middle of the straw; this was done to reduce the total occupancy of the innermost straws at high luminosities.

[12] The original design of the TRT called for "C" wheels that would extend the $|\eta|$ coverage out to almost 2.5; for a number of reasons, these wheels were never built.

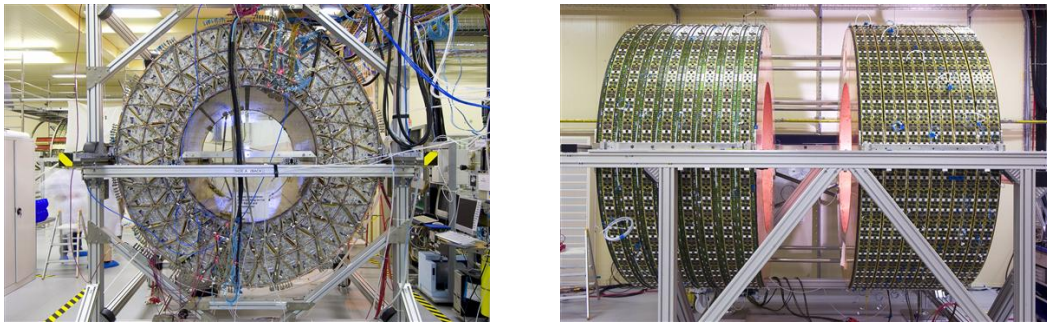

(a) Barrel (b) Endcap

Figure 3.6: The ATLAS TRT barrel (a) and endcap (b) in their assembly facility on the surface. The TRT barrel is shown during cosmic-ray testing, when 3/32 of the detector (in ϕ) were instrumented and read-out. The endcap is shown before the combination of the A (right) and B (left) wheels into the full endcap package.

the endcap. Each wheel has 32 slices in ϕ; each B-wheel has one front-end board per ϕ slice, while the A-wheels each have two boards, stacked in z. A picture of one of the TRT endcaps is shown in Fig. 3.6b.

3.2.2.3.3 Transition Radiation Transition Radiation (TR) is emitted by relativistic particles when they pass between media with different dielectric constants. The total TR energy emitted, per material transition, by a relativistic particle with unit charge is:

$$E = \frac{\alpha}{3}\gamma\hbar\omega_p \tag{3.5}$$

where γ is the Lorentz gamma factor ($\gamma = c/\sqrt{c^2 - v^2}$) and ω_p is the plasma frequency, which depends on the materials at the boundary region. A typical value of $\hbar\omega_p$ is roughly 20 eV. The transition radiation photons are produced with energies of several keV - more energy than that produced by minimum ionizing particles passing through a straw (around 1 keV). As electrons have masses that are 250 times smaller than pions, the γ factor for an electron with the same energy as a pion will be significantly larger, corresponding to a larger probability for emitting transition radiation. The TR photons are also emitted with small

angles ($\theta \approx 1/\gamma$) relative to the particle's direction. Unfortunately, the probability of a TR photon being emitted is low (from the factor of $\alpha/3 \approx 1/(3 \cdot 137)$), meaning many transition regions need to be encountered to ensure good TR emission efficiency.

In the barrel, the radiator material is a foam mat of polypropylene/polyethylene fibers. [46] The fibers have a diameter of 19 μm, and are molded into 3 mm-thick fabric sheets. The sheets are cut in the shape of the barrel modules and stamped with a hole pattern allowing the straws to be inserted perpendicular to the plane of the sheet. Around 500 sheets are needed to fill each barrel module. In the endcap, the radiator is made of layers of 15 μm-thick polypropylene foils. [47] The wheels are segmented into groups containing four straw-planes each; stacks of foils were placed at the outside edges of the four-plane wheels, and between each internal straw-plane. The number of foils in each stack ranges from 6 to 34, depending on the position of the stack in z. The emitted transition radiation photons are absorbed by the Xenon gas, producing a cluster of primary electrons.

3.2.2.3.4 Front-End Electronics The principle components of the front-end electronics are custom made, including the analog and digital application specific integrated circuits (ASICs) and the printed circuit boards on which they are mounted.

The analog chips are connected directly to the straw wires, and perform amplification, shaping, discrimination, and base-line restoration (ASDBLR) of the avalanche current from the wire. The ASDBLR is implemented as a custom ASIC in a radiation-hard process so as to withstand the high radiation background near the interaction point. Signals from the wire pass first through a pre-amplifier, which has a gain of 1.5 mV/fC and a peaking time of 1.5 ns. The signals are then shaped to isolate the electron peak of the ionization curve (see Fig. 3.5a). The ion-tail is canceled and the baseline output restored as the signal is passed into the discriminators. There are two independent discriminators; the first is for detecting the

currents from minimum ionizing particles, and the second is for detecting the larger currents from transition radiation photons. Each discriminator has an associated threshold, set by an externally-applied voltage level, and interpreted with respect to the analog ground reference. The "low" threshold is applied to the first discriminator, in the range of 250-300 eV, while a "high" threshold is applied to the transition-radiation discriminator, usually at 5-7 keV. The output of each channel is a ternary signal, indicating the firing of neither, one, or both of the discriminators (with the ambiguity in the second case broken by assuming that the low threshold is always lower than the high threshold). Each ASDBLR has eight channels, each corresponding to a single straw. The discriminator thresholds are shared by all channels in an ASDBLR.

The analog output from the ASDBLR feeds directly into a drift time measurement read-out chip (DTMROC), which digitizes the analog signals and synchronizes them to the 40 MHz clock. The DTMROC, like the ASDBLR, is also a custom ASIC implemented in a radiation-hard process. Each DTMROC takes the output of two ASDBLRs, and provides binary output for the low-level discriminator of each channel in eight time-bins every 25 ns (3.125 ns per bin). The high-level threshold information is encoded as a single bit per 25 ns. The digitized results, along with a counter indicating the bunch crossing associated with the straw data, are stored for up to 6 μs while waiting for a trigger decision. The DTMROCs also store the configuration for each of its ASDBLRs, and apply the low and high thresholds in the form of voltage levels with respect to the digital ground reference.

In the barrel, both the ASDBLRs and DTMROCs are mounted on the same active roof (AR) boards. The ASDBLRs occupy the low-z side of the board, while the DTMROCs are on the opposite side. Each of the three trapezoidal module types in the barrel have two unique triangular boards per side, for a total of twelve independent board designs.[13] Data to and

[13]While the boards that mirror each other across the $x-y$ plane are similar in size and shape, and have

from the chips pass through a connector on the outer (DTMROC) side of the AR board.

In the endcap, the ASDBLRs and DTMROCs are mounted on separate boards. The ASDBLR boards for the A wheels and B wheels are slightly different in design, to accommodate the larger gaps between the straw planes in the B-wheels. Each ASDBLR board connects to 64 straws through flexible integrated circuits. The DTMROC boards for the A-wheels and B-wheels are identical, and arranged in triplets. Each part of the three pieces corresponds to a single ASDBLR board, and all channels on a triplet share a common connection for signal and power transmission.

One of the principle challenges in the construction of a straw tracker like the TRT is the sensitivity of its detecting elements to high frequency noise. To reduce the impact of noise generated outside of the TRT volume, the digital ground planes of all AR boards in the barrel are electrically connected to the copper tape wrapping the carbon fiber space frame, completing a large Faraday shield. In the endcap, the analog ground plane completes an internal Faraday shield, while an external shield is created by cable trays between the endcap and the cryostat wall.

In addition to external noise, the close proximity of the signal traces carrying the 40 MHz clock to the preamplifiers in the ASDBLRs leads to significant clock pickup. This is especially true in the barrel, where the analog and digital circuits share a single printed circuit board. Extensive testing was done to ensure that the detector operated at or below its designed noise occupancy of 2.25%, while retaining a high tracking efficiency. This 2.25% noise occupancy is commonly expressed in terms of a noise hit rate, which for a 40 MHz clock (and a three bunch-crossing readout window) corresponds to 300 kHz. The amount of noise is quantified by the threshold at which this 300 kHz rate is reached. Figure 3.7 shows the 300 kHz rate threshold for all electronics channels before and after installation on the barrel modules. The left-hand

identical numbers of channels, they were designed and implemented separately.

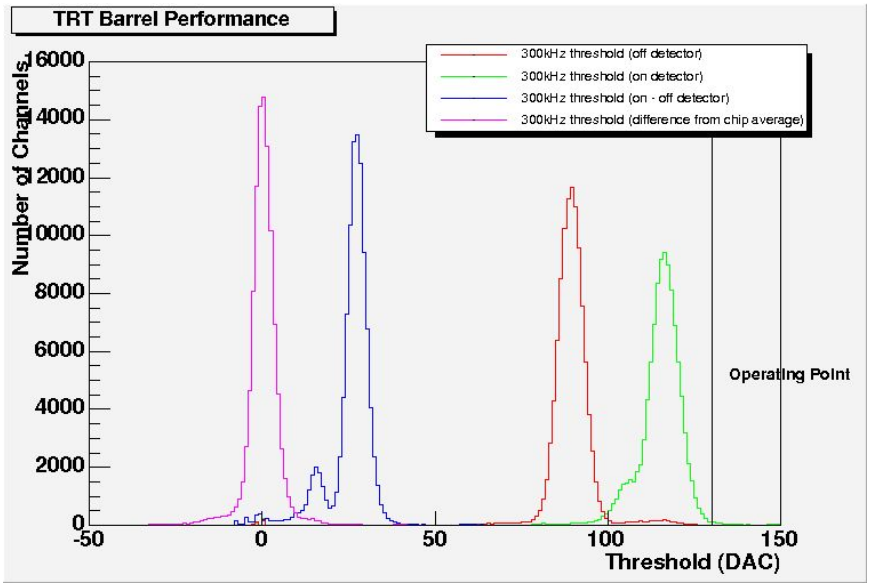

Figure 3.7: Per channel 300kHz threshold distributions for Barrel electronics on (green), off (red), on-off (blue) the detector and then difference from chip average (purple). Note that the increase in the 300 kHz threshold when the electronics are mounted in place is due to the detector capacitance which raises the equivalent noise charge figure for the ASDBLR. The smaller capacitance of the first nine layers of 'short' straws is clearly evident in the difference (blue) distribution. (Figure and caption from [2].)

shoulder in the "on detector" and "on-off detector" trends is due to the "short" straws at low R (which have an uninstrumented region in the middle of the wire) and indicates that the detector is operating at the thermal limit defined by the capacitance of the wires.

3.2.2.3.5 Back-End Electronics and Data Acquisition The interface between the TRT front-end electronics and the ATLAS data acquisition (DAQ) system is composed of a pair of custom 9U VME modules called the Timing and Trigger Controller (TTC) and Read-Out Driver (ROD). The TTC receives copies of the ATLAS clock and command signals, and distributes them to the front-end electronics through intermediate "patch panels" (physically located within the muon spectrometer). The RODs receive data from the front-end, package them, and either make them available over the VME backplane (for testing) or pass them to

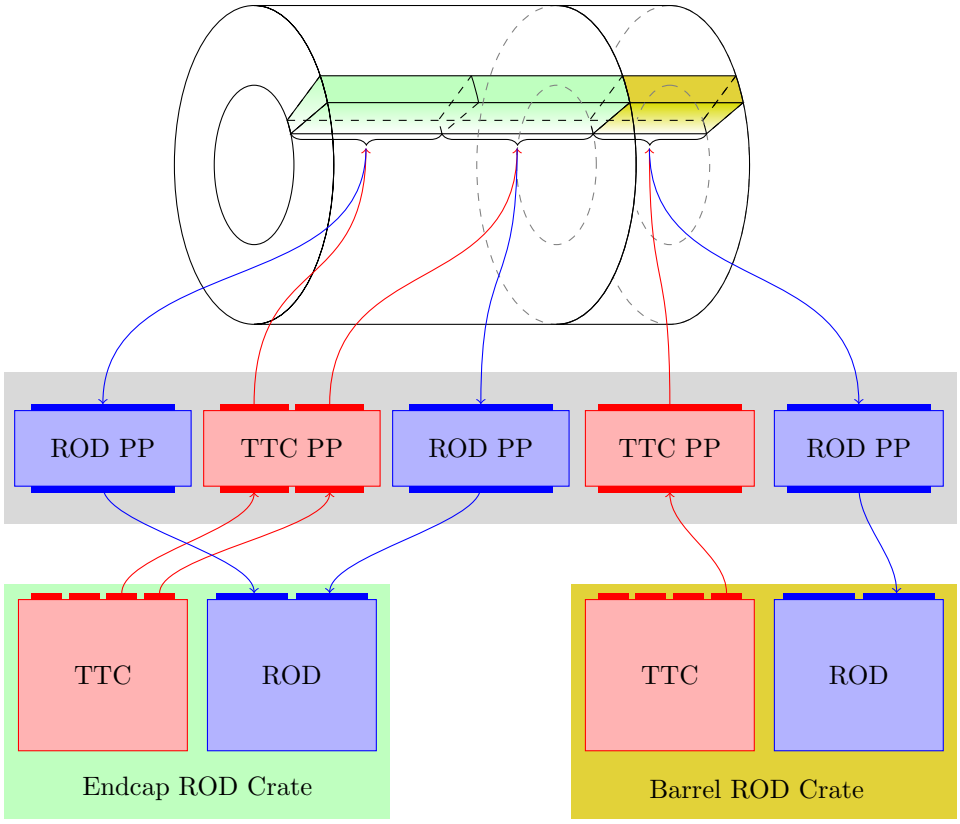

Figure 3.8: Half of 1/32nd of the TRT readout chain, from back end modules to the front-end electronics.

the ATLAS DAQ system over a fiberoptic link.

Upon receipt of a level-1 trigger accept from the TTC, a DTMROC bundles the hit information from three consecutive bunch crossings and transmits the data to the TRT backend electronics. The data are transmitted through thin twisted-pair cables to patch panels, which encode and multiplex the data in groups of 30 DTMROCs. The data are then transmitted over a 1.2 Gb/s fiberoptic link to the RODs. A graphical representation of the read-out chain, from front-end to back-end, is shown in Fig. 3.8.

In order to collect front-end data that correspond to the bunch crossing of interest, the system must be carefully tuned so that the digitized pulses for each straw are fully contained

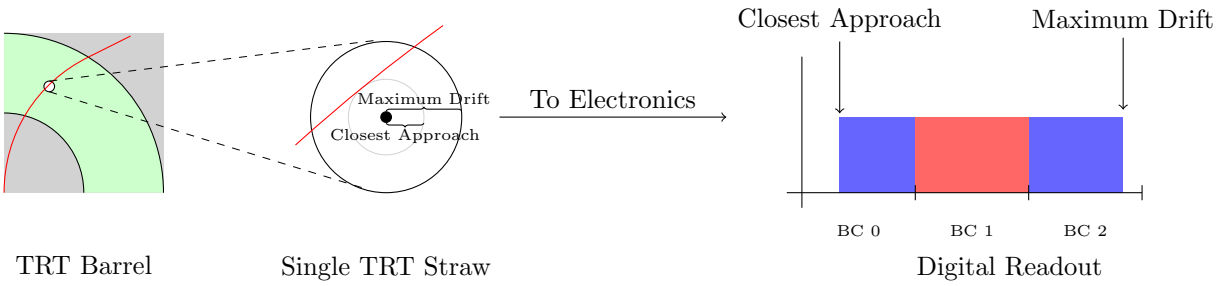

Figure 3.9: The passage of a charged particle through the straw ionizes gas, which causes electrons to drift into the anode. The resulting current is read out by the analog electronics, and then digitized. The pulse at the right shows the result of that digitization. The blue regions are where the low threshold was crossed - the red region is where both the low and the high threshold were crossed. The point of closest approach of the particle to the wire determines the leading edge of the digital pulse, while the size of the straw (and drift speed of the gas) determines the trailing edge.

in a 75ns window. This is accomplished by tuning the trailing edge of each digitized pulse to fall near the end of the readout window. As mentioned previously, a minimum-ionizing particle will always ionize some of the gas near the straw wall, meaning that the trailing edge of the pulse is primarily determined by the wire-to-wall distance. The time over threshold for the digital output is then determined by the point of closest approach of the track to the wire. Figure 3.9 has an illustration of this effect. An example of the effect of a charged particle track passing further away from the center of the wire is shown in Fig. 3.10.

3.2.2.3.6 Straw Hit Efficiency for Tracking The hit efficiency for the barrel and end-cap detectors are shown in Fig. 3.11 as a function of the distance of closest approach of the charged particle to the straw center. The total efficiency, excluding the 2% of channels known to be dead, is over 95% in the plateau region.

3.2.2.3.7 Transition Radiation Performance The primary purpose of transition radiation detection is to separate electrons from charged pions, which complements the separation

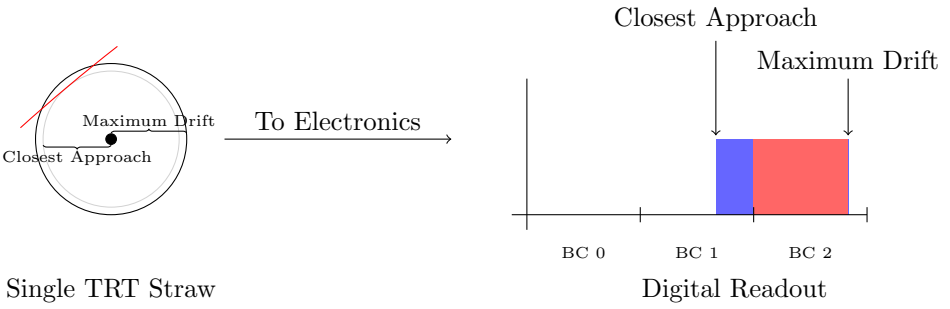

Figure 3.10: A scenario similar to that shown in Fig. 3.9. In this case, the straw is just barely hit by the charged particle, and the only gas ionized is near the cathode. The trailing edge of the distribution does not shift, as it is fixed by the size of the straw - the leading edge, however, moves later in time to reflect the drift radius of the track.

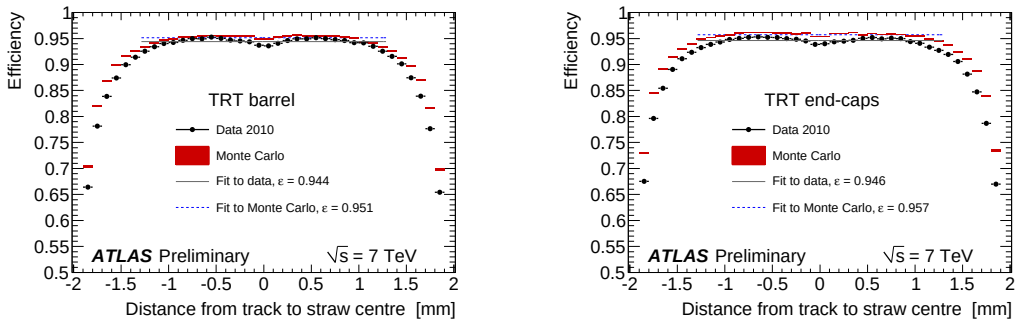

(a) Barrel (b) Endcap

Figure 3.11: Plots of the hit efficiencies for the barrel (a) and endcap (b) as a function of the distance of the track from the straw center. The 2% of channels known to be dead are not considered.

of electrons from pions based on the evolution of the shower in the electromagnetic calorimeter (especially at low particle energies). The different masses of electrons (0.5 MeV) and pions (140 MeV) mean that electrons and pions with similar momenta will have different Lorentz γ factors, and thus different probabilities for emitting transition radiation. The transition radiation turn-on curves measured with the TRT using 2010 data are shown in Fig. 3.12b, and show the good performance of the detector compared with Monte Carlo simulations.

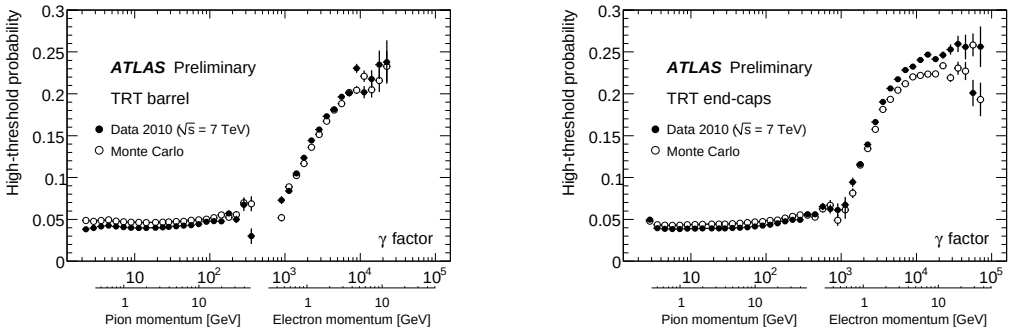

(a) Barrel (b) Endcap

Figure 3.12: A plot of the transition-radiation turn-on for electrons and pions, as a function of their Lorentz γ factor, in the barrel (a) and endcap (b). The y-axis is the probability of inducing a high-threshold hit in the straws. The electron sample is extracted from reconstructed photon conversions, while the pion sample includes all low-momentum tracks that do not fall in the electron sample.

3.2.3 Calorimetry

The barrel part of ATLAS calorimetry system is composed of a high-granularity lead/liquid-argon (LAr) electromagnetic (EM) sampling calorimeter and a steel/scintillating-tile hadronic sampling calorimeter. In the endcap, the hadronic calorimetry is implemented with a LAr design instead of with scintillating tiles. A cut-away view of the ATLAS calorimeter system is shown in Fig. 3.13.

The EM and hadronic calorimetry provide separate event data for full reconstruction, but a reduced form of their input is merged in hardware to make Level-1 trigger decisions with low latency. At Level-1, one speaks of trigger "towers", composed of both EM and hadronic components, which measure the energy deposited in an array of detecting elements pointing outwards from the interaction point.

3.2.3.1 Electromagnetic Calorimeter

The EM calorimeter is of principal importance to the study of photons. Except in the cases where a photon pair converts in the inner detector (discussed in more detail in Section 5.1.1),

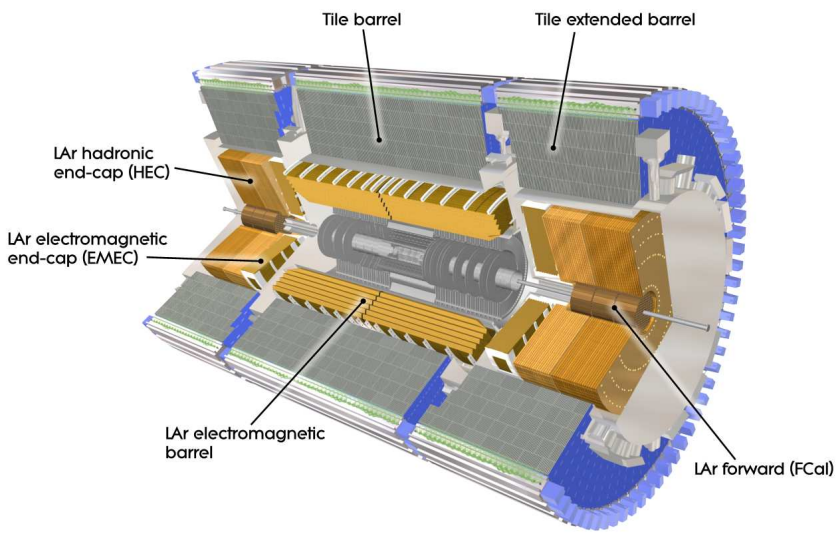

Figure 3.13: The ATLAS calorimeter subsystems. The EM calorimeter is a lead-LAr accordion sampling detector, while the hadronic calorimeter is composed of steel and scintillating tiles in the barrel, and copper/LAr in the endcaps.

the only sign of a photon's presence is a deposit of energy in the EM calorimeter.

The ATLAS electromagnetic calorimeter has a lead-LAr accordion design, seen in cross-section in Fig. 3.14. When a photon enters the detector, it interacts with the lead plates and pair-produces an electron and a positron. The electron and positron continue to interact with the material in the calorimeter, producing bremsstrahlung photons, which in turn pair-produce, creating a "shower" of electromagnetic activity. The LAr medium samples the energy of the shower, which is read out by analog electronics through capacitively-coupled copper sheets at the edges of the absorber.

An electron entering the LAr calorimeter will undergo the same chain reaction as a photon. Distinguishing between electrons and photons solely by the shower profile is difficult, and is not attempted at reconstruction level. Instead, the presence of a matching track in the inner detector is used to break the ambiguity. The situation is somewhat complicated in cases where a photon pair-produces before reaching the calorimeter; this will be discussed further

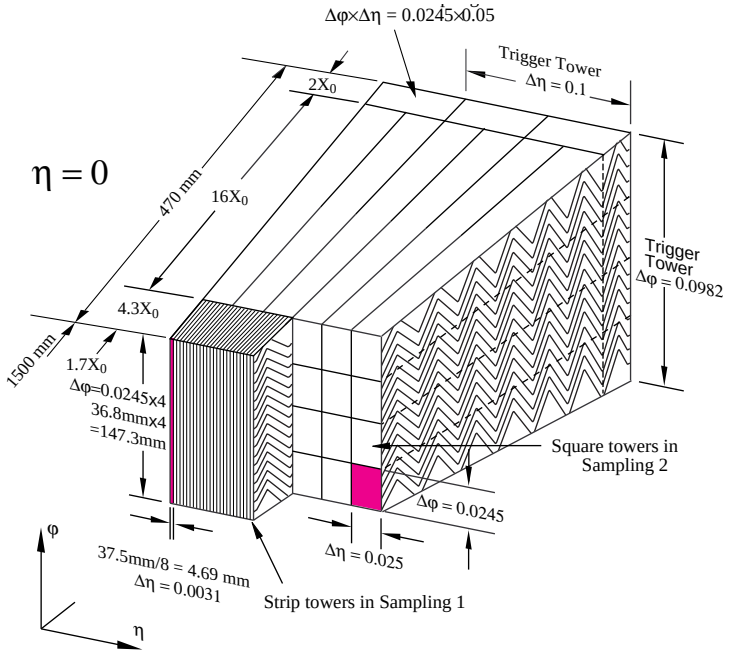

Figure 3.14: The granularity of the liquid argon electromagnetic barrel calorimeter, shown near $\eta = 0$. The innermost layer shown here is the 'strip' layer, with fine segmentation in η. The primary sampling layer makes up the bulk of the calorimeter volume and material, while the third (outer) layer has the coarsest granularity.

in Section 5.1.1.

The LAr calorimeter is separated longitudinally into four layers. The baseline granularity of the calorimeter cells in the barrel is 0.025×0.025 in $\Delta\eta \times \Delta\phi$; all cells have sizes that are even multiples (or fractions) of this baseline.[14]

- The first layer (at lowest R), called the pre-sampler, is a thin layer of active LAr that is designed to estimate and correct for losses of energy through a particle's interaction with material upstream of the calorimeter (*i.e.* in the inner tracker). It only extends to $|\eta| = 1.8$, and does not absorb a significant amount of a particle's energy. The detecting elements are 0.025×0.1 in size, with a coarser granularity in ϕ.

[14]The length in ϕ is sometimes quoted as 0.025 and sometimes as 0.0245; in reality, it is defined as $2\pi/256$ = 0.02454....

- The next layer out in radius is often called the "strip" layer, as it is composed of thin strips in η that provide excellent position resolution, as well as the ability to discriminate between single and double pulses (corresponding to single photon and diphoton objects, respectively). Each strip has a size of $0.025/8 \times 0.1$, in the barrel, and similar sizes in the endcap (that vary slightly with $|\eta|$).

- The following layer is the primary sampling layer, typically called "layer 2" (where the presampler is "layer 0"). Each cell in in the second layer is 0.025×0.025 in $\Delta\eta \times \Delta\phi$. The bulk of the energy of the shower is deposited in layer 2.

- The final layer, called "layer 3", is used to estimate the amount of energy that was not contained in the second layer, and has a coarser granularity of 0.050×0.025.

The fine segmentation of the EM calorimeter provides good position resolution for electron and photon reconstruction. After calibration, the η resolution in the strips is roughly 3×10^{-4}, while the resolution in ϕ is between 5×10^{-4} and 2×10^{-3} radians, depending on η.[15]

The design energy resolution of the EM calorimeter is $\sigma_E/E = 10\%/\sqrt{E} \oplus 0.7\%$, where the last term (0.7%) corresponds to the "constant term", and is independent of energy. A combination of studies using simulated data and test beam results indicate that the calorimeter is meeting its performance goals [48], and results with early collision data confirm this. [49]

The transition region between the barrel and endcap portions of the EM calorimeter contains an uninstrumented gap, needed to connect the inner tracker with services outside of the cryostat. Electron or photon candidates that fall within this gap will have reduced energy and position resolutions, and are excluded from most analyses. Furthermore, the strips in the first layer only extend to $|\eta| = 2.37$. Therefore, photon candidates are required to satisfy

[15] The precision in ϕ is degraded by the presence of material in the ID, which induces bremsstrahlung for electrons and pair production for photons.

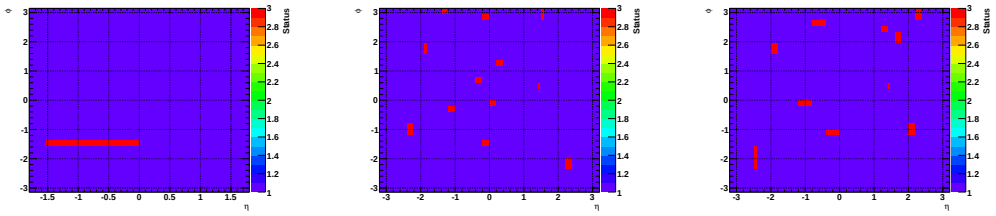

(a) Presampler (b) First Sampling (c) Second Sampling

Figure 3.15: Maps of the dead front-end board optical links for the presampler, first sampling, and second sampling of the LAr calorimeter. Photon candidates that fall into the red regions are ignored.

the fiducial requirement $|\eta_{S2}| < 1.37$ or $1.52 \leq |\eta_{S2}| < 2.37$, where η_{S2} is the η of the cluster barycenter in the second sampling layer.

Finally, a problem with the optical links that transmit data to and from the LAr front-end electronics prevented certain parts of the EM calorimeter from being properly read-out during the 2010 run.[16] The (η, ϕ) maps of the dead readout optical links for the presampler, first and second sampling layers are shown in Fig. 3.15. Events in which the leading photon is found within one of the red regions in those plots are excluded from the analysis; the effect of this acceptance loss is discussed in Chapter 6.

3.2.3.2 Hadronic Calorimeter

The hadronic calorimeter is composed of three independent pieces: the Tile Calorimeter (TileCal), which covers the central region up to $|\eta| = 1.7$; the liquid-argon hadronic endcap (HEC), which covers $1.5 < |\eta| < 3.2$; and the liquid-argon forward calorimeter (FCal), which extends the total acceptance beyond the HEC to $|\eta| < 4.9$. The acceptance for photons is driven by the EM calorimeter, so only the TileCal and the HEC are described in detail here. They are both sampling calorimeters, with nominal energy resolutions of $\sigma_E/E = 50\%/\sqrt{E} \oplus 3\%$ for $|\eta| < 3.2$.

[16] This problem has since been fixed, restoring the full acceptance in 2011.

The primary function of the hadronic calorimeter for photon studies is to provide a measurement of the hadronic activity behind the cluster in the EM calorimeter. Real photons will deposit very little energy in the hadronic calorimeter, having left most (if not all) of their energy in the liquid-argon calorimeter. Tight cuts on the allowed amount of hadronic energy associated with the photon cluster help to reduce the background contamination of the signal sample - these cuts are described in detail in Section 5.2.

3.2.3.2.1 TileCal The TileCal has a barrel region ($|\eta| < 1.0$) and two "extended barrel" regions ($0.8 < |\eta| < 1.7$). It has steel absorbers and active elements made from scintillating tiles. The radial thickness of the detector is roughly 7.4 nuclear interaction lengths.[17]

The tiles themselves have a granularity of 0.1×0.1 in $\Delta\eta \times \Delta\phi$. They are arranged in towers with a projective geometry in η, pointing towards the interaction point. The scintillators are read-out with photomultiplier tubes, which provide analog signals that are digitized on the front-end and made available for both triggering and readout.

3.2.3.2.2 Hadronic End Cap The HEC is an extension of the liquid-argon calorimeter, with copper-plate absorbers and a liquid-argon active medium. Each endcap is composed of two wheels, each divided into two segments in depth. Like the TileCal, the granularity of the detecting elements is 0.1×0.1 in $\Delta\eta \times \Delta\phi$ out to $|\eta| < 2.5$; for $2.5 < |\eta| < 3.2$, the detecting elements measure 0.2×0.2.

3.2.4 Trigger

ATLAS has a three-tiered trigger system, designed to select interesting events with a final output rate of roughly 200 Hz. It consists of a hardware trigger in the first tier (Level-1),

[17] The nuclear interaction length, λ, of some material defines the mean distance over which the number of relativistic charged particles is reduced by a factor of $1/e$ as they pass through that material.

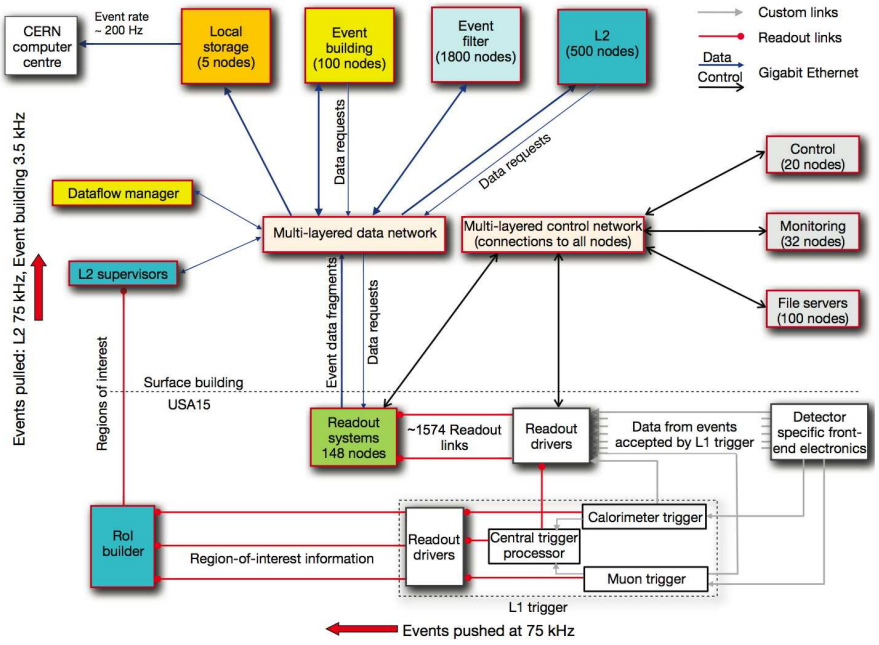

Figure 3.16: A schematic view of the ATLAS trigger and data-acquisition systems. Data flows from the bottom-right to the top-left.

followed by a software trigger that performs partial event reconstruction (Level-2). The final tier (the Event Filter) performs full event reconstruction using the same tools as used for offline analysis, albeit with a modified set of algorithms. The second and third tiers are collectively known as the High Level Trigger. A schematic view of the ATLAS trigger system is shown in Fig. 3.16.

Both Level-1 and Level-2 are Region of Interest (RoI) based triggers: they only consider the data from detecting elements in a limited region of η and ϕ. This allows them to make decisions before the data from all of the different subsystems and RoIs are built into a full event record, reducing the total internal bandwidth used by the system. The event filter operates after full events are built, and is the only place where the trigger can consider complicated

event topologies spanning multiple RoI's.[18]

3.2.4.1 Level-1 Hardware Trigger

The Level-1 trigger is a logical OR of many input trigger signals, combining information from the calorimeter and muon systems. Decisions are made by the individual trigger subsystems within 2.5 μs of the relevant bunch crossing, and are then propagated to the central trigger processor (CTP), which makes the final Level-1 trigger decision and distributes it to all ATLAS subsystems. After each Level-1 accept, there is a minimum dead-time of five bunch crossings (125ns). The total propagation delay, from a proton-proton collision to the readout of the detecting elements on the front-end, is less than 4 μs. The event data are then transmitted from the front-end to RODs, which package the event data for a large number of channels and transmit the formatted data into rack-mounted computers equipped with fiberoptic input cards (ROSs). The ROSs buffer the event data until it is requested by the Level-2 trigger or by the Event Building system.

The Level-1 accept rate is designed to be 75 kHz, almost three orders of magnitude below the 40 MHz bunch crossing rate. Operating under special conditions, all subsystems in ATLAS can accomodate up to a 100 kHz Level-1 accept rate (though this sometimes requires the truncation of some detector data in order to meet the bandwidth requirements).

3.2.4.2 Level-2 Software Trigger

The Level-2 trigger is seeded by the Level-1 trigger, and uses a modified set of offline reconstruction algorithms to refine the Level-1 selection criteria. Level-2 makes use of the same RoI flagged by Level-1, but takes advantage of the reduced event rate to run tracking algorithms for the first time, and to evaluate calorimeter quantities with greater precision. The

[18] Exceptions to this rule include triggers based on $E_{\mathrm{T}}^{\mathrm{miss}}$, which do exist at Level-1 and Level-2.

Level-2 accept rate is limited to 3.5 kHz, with a latency of roughly 40 ms. Events rejected at Level-2 are flushed from the ROS's, while events accepted by Level-2 are then collected by the event-building system, which merges the event data and passes it to the Event Filter.

3.2.4.3 Event Filter

At the Event Filter, events undergo full reconstruction. The Event Filter uses fast versions of offline reconstruction tools to look for diphoton and dilepton events, other multi-object events, and events with significant $E_{\mathrm{T}}^{\mathrm{miss}}$, in addition to the single-object topologies that are the focus of the first- and second-level triggers. The final output rate of the event filter is designed to be 200 Hz[19], with a total latency of roughly four seconds.

3.2.5 Luminosity

3.2.5.1 Luminosity Measurements

The integrated luminosity is a crucial component of a cross section measurement. ATLAS has several ways of measuring the luminosity of the LHC beams [50]; for the 2010 dataset, an event counting technique was used, with the absolute calibration provided by a series of van der Meer scans taken in April and May of 2010. The uncertainty on the measured luminosity for early data was 11%; this has since improved to 3.6% for the 2010 dataset. [51]

3.2.5.2 Luminosity Blocks

As an LHC fill progresses, the instantaneous luminosity slowly degrades, creating different conditions at the beginning and end of a fill. The concept of "luminosity blocks" allows ATLAS to subdivide a run into many separate chunks, within which all events have similar luminosity conditions.

[19] The limitation comes from the amount of data the collaboration is willing to keep for later analysis. In 2010, the nominal maximum output rate was often exceeded.

Chapter 4

Data Samples and Event Selection

The analyses presented in this document make use of the majority of the data collected by the ATLAS experiment in 2010, as well as using a number of simulated data samples used to study both signal and background processes. This chapter reviews the samples and event selection criteria used for the analyses.

4.1 Data Samples

The measurements presented here are based on proton-proton collision data collected at a center-of-mass energy of $\sqrt{s}$ =7 TeV with the ATLAS detector at the LHC. There are two distinct datasets used, depending on the specific measurement in question.

- The first measurement to be presented uses a sample corresponding to 880 nb^{-1} of integrated luminosity, collected between April and August of 2010.
- An extension of the first measurement is made with a significantly larger dataset, collected between August and November of 2010. This dataset corresponds to roughly 35 pb^{-1} of integrated luminosity.

The specifics of the 35 pb^{-1} sample will be revisited in Chapter 10; until then, any references to collision data will refer to the 880 nb^{-1} dataset (unless otherwise indicated).

4.2 Monte Carlo Samples

To study the characteristics of signal and background events, Monte Carlo samples are generated using PYTHIA 6.4.21 [27], a leading-order (LO) parton-shower MC generator, with the modified leading order MRST2007 [29] parton distribution functions (PDFs). The event generator parameters are set according to the ATLAS MC09 tune [30], and the ATLAS detector response is simulated using the GEANT4 program [31]. These samples are then reconstructed with the same algorithms used for data. More details on the event generation and simulation infrastructure of the ATLAS experiment are provided in [32]. For the study of systematic uncertainties related to the choice of the event generator and the parton shower model, alternative samples are also generated with HERWIG 6.5 [33].

To study background processes, two classes of samples are simulated. In the first, non-diffractive minimum bias events are generated and filtered by requiring at least 6 GeV of transverse energy in a 0.18×0.18 region in $\eta \times \phi$ at the truth particle level, which mimics a calorimetric Level-1 trigger requirement. The events passing this filter, whose efficiency is around 5.3% in inclusive dijet events, are then fully simulated. This filter is found to be unbiased for transverse energies above 10 GeV. The equivalent integrated luminosity of this sample, according to the effective production cross section returned by PYTHIA (including the filter efficiency) of $\sigma = 2.58$ mb, is 16 nb^{-1}.[20]

The E_{T} spectrum of reconstructed fake candidates decreases rapidly above the filter threshold. To ensure sufficient statistics for background studies a second class of samples, enriched in candidates with higher transverse energies, is used to study fake photon candidates with reconstructed $E_{\mathrm{T}} > 20$ GeV. In these samples, all relevant 2→2 QCD hard subprocesses are switched on, the transverse momentum of the hard-scattering products is required to be

[20] Within ATLAS, these are known as the "filtered min-bias" samples.

greater than 15 GeV, and the same filter used for the minimum bias sample is applied. The filter has a higher threshold than in the minimum bias sample, with cuts at 17 GeV and 35 GeV.[21] The sample with a 17 GeV minimum is found to be unbiased for transverse energies above 20 GeV. Its equivalent integrated luminosity, according to the effective production cross section $\sigma = 0.99$ mb computed with `PYTHIA` (taking into account also the filter efficiency, 8.6%), is 494 nb^{-1}. The sample with a parton-level p_{T} cut at 33 GeV and a truth-particle-jet filter cut at 35 GeV helps extend the reach to higher transverse energies, and corresponds to an integrated luminosities of 579 nb^{-1}.

All of these QCD background samples contain "fake" photon candidates (typically from π^0 and η decays), as well as prompt photon signals produced by QED radiation emitted off quarks. The higher energy samples also contain direct leading-order contributions, either from $q\ \bar{q}\ \rightarrow\ g\ \gamma$ or $q\ g\ \rightarrow\ q\ \gamma$. Reconstructed prompt photon candidates are matched to particles in the truth record of the event with a dedicated tool, which uses a combination of ancestry information from the generator and ΔR matching to determine whether a candidate is signal or background. All prompt photon contributions are removed from these samples when studying the background contribution.

For signal-only samples, two types of filters are used. The first class of prompt photon samples consists of simulated leading order γ-jet events, and contains only direct photons with generated transverse momenta above some threshold (7, 17, 35 and 70 GeV thresholds are used in these studies).[22] The equivalent luminosities of these samples range from 71 nb^{-1}(for the 7 GeV threshold) to 1 fb^{-1} (for the 70 GeV threshold). The box-diagram hard subprocess $gg \rightarrow g\gamma$ is part of the next-to-next-to-leading order (NNLO) cross section and gives a negligible contribution to the total prompt photon cross section compared to the other two subprocesses.

[21] Again, within ATLAS, these are known as JF17 and JF35.
[22] These are called "unbinned photon+jet samples".

It is not included in the generated samples.

The second class of signal samples contains both direct photons and photons from QED radiation off quarks. The events generated for this class of samples are similar to those generated for the study of the QCD backgrounds, but the filter applied before the full simulation only retains events that contain reconstructed photons matched to signal photons in the truth record, with generated transverse momenta above some threshold, either 7 GeV or 17 GeV.[23] The equivalent luminosities for those two samples are 206 nb^{-1} and 4.6 pb^{-1}, respectively. These samples are used to study the contribution to the prompt photon signal of photons from fragmentation or from the NLO part of the direct process and that are less isolated than those from the LO direct processes. In such studies, all direct LO photon contributions are removed from these samples in the analysis. The separation of the direct and brem/fragmentation components as described above is defined by the generator, and has no physical significance beyond leading order. In the analysis the LO-direct and NLO/brem contributions are typically used separately, without relying on the generator for implicit assumptions about their relative rates.

Finally, for the efficiency and purity studies involving electrons from W decays, a pure sample of $W \to e\nu$ events is used. The sample consists only of events with a final state W decaying leptonically to an electron and a neutrino.

4.3 Run and Event Selection

Only events where both the calorimeter and the inner detector are fully operational, and have good data quality, are used. In particular, events are required to belong to the $Z \to ee$ electron-photon "Good Runs List" (GRL). The GRL specifies both the run numbers and

[23] These are sometimes called "DP" samples - presumably for "direct photon", though they contain both the direct and fragmentation components.

luminosity blocks within each run that should be used in an analysis, and excludes events in which either the detector or the accelerator is not fully operational.

Each event is required to have a reconstructed primary vertex consistent with the average beam spot position, and with at least three associated tracks. These selection criteria are over 99.9% efficient for events containing photon candidates with $E_{\mathrm{T}}^{\gamma} > 15$ GeV.

4.4 Trigger Requirements

Events in the 880 nb^{-1} sample are triggered using the g10_loose high-level calorimeter trigger, based on the energy deposits in the electromagnetic and hadronic calorimeters. The g10_loose trigger is seeded by a Level-1 hardware trigger (L1_EM5), which searches for electromagnetic clusters with fixed size 0.2×0.2 and retains only those whose total transverse energy in two of their four trigger channels is greater than 5 GeV. The high level trigger exploits the full granularity and precision of the calorimeter to refine the Level-1 trigger selection.

The nominal transverse energy threshold of the g10_loose trigger is 10 GeV. The selection criteria that are applied by the trigger are looser than the photon identification criteria applied in the following analysis steps, and are chosen, together with the transverse energy threshold value, in order to reach a plateau of constant efficiency close to 100% for true photons with $E_{\mathrm{T}} > 15$ GeV.

4.5 Definition of the Measurement

The inclusive isolated prompt photon cross section is measured differentially in eight bins of E_{T}^{γ}: 15-20 GeV, 20-25 GeV, 25-30 GeV, 20-35 GeV, 35-40 GeV, 40-50 GeV, 50-60 GeV, and 60-100 GeV. The differential cross section is measured separately in four regions of pseudorapidity:

$0.00 \leq |\eta^{\gamma}| < 0.60$, $0.60 \leq |\eta^{\gamma}| < 1.37$, $1.52 \leq |\eta^{\gamma}| < 1.81$, and $1.81 \leq |\eta^{\gamma}| < 2.37$.[24] The value of η^{γ} is taken from the barycenter of the cluster energy in the second sampling layer of the EM calorimeter. The value of E_{T}^{γ} is determined from the calibrated energy of the photon cluster in the calorimeter and the η value of the barycenter of the cluster over all EM calorimeter layers, $\eta_{\mathrm{cluster}}^{\gamma}$:

$$E_{\mathrm{T}}^{\gamma} = \frac{E^{\gamma}}{\cosh(\eta_{\mathrm{cluster}}^{\gamma})} \tag{4.1}$$

[24] For reasons explained more thoroughly in Chapter 6, the first measurement will omit the last region in $|\eta^{\gamma}|$. It is recovered in the measurement presented in Chapter 10.

Chapter 5

Reconstruction and Identification of Prompt Photons

Reconstructed photons in ATLAS are seeded by clusters of energy in the EM calorimeter. They are distinguished from electrons, which are seeded by the same clusters, by the absence of a track whose trajectory is consistent with the candidate cluster. An example of such a cluster, without an associated track, is shown in Fig. 5.1a. A special case occurs when the photon pair-converts into an electron-positron system before reaching the EM calorimeter. In such cases, a separate reconstruction chain attempts to recover those photons from reconstructed electrons. An example of such a photon candidate is shown in Fig. 5.1b. After reconstruction, a series of selection criteria are used to separate single photons from backgrounds (primarily from light mesons decaying to multiple photons). This chapter will review the reconstruction of both converted and unconverted photons, and the identification criteria applied at the analysis level.

5.1 Photon Reconstruction

Clusters are formed in the calorimeter with a sliding window algorithm [52]. The algorithm forms rectangular regions of cells of fixed size, selected to maximize the contained energy by

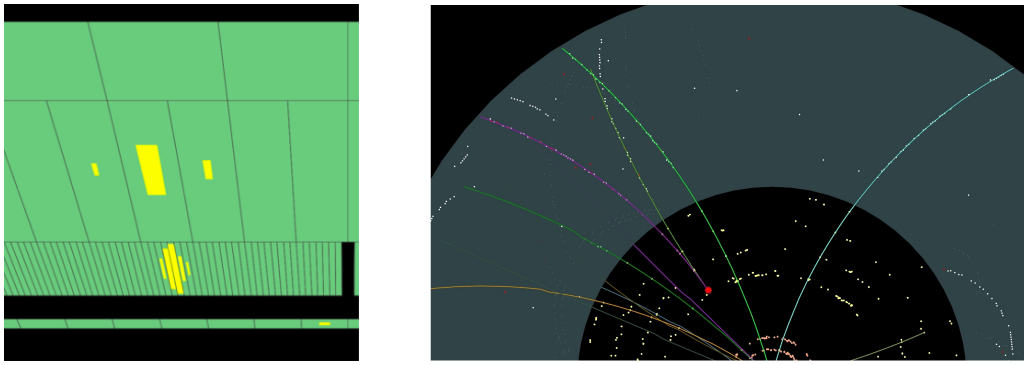

(a) Unconverted γ (b) Converted γ

Figure 5.1: Event displays of unconverted (a) and converted (b) prompt photon candidates. The left figure shows a slice in η of the EM calorimeter, showing the pre-sampler at the bottom, followed by the strip layer, the second sampling layer, and the third sampling layer. The unconverted photon candidate is well isolated in the calorimeter, and has a single peak in the first (strip) layer. The conversion candidate has two associated tracks, and a vertex in the first layer of the SCT.

adjusting the center of the window in η and ϕ. The clusters have an E_{T} threshold of 2.5 GeV, and a size in layer-2 of the EM calorimeter of 3×5 cells in $\eta \times \phi$.

To distinguish between photons and electrons, a track-matching procedure follows cluster finding. Tracks are required to be within a rectangular window in $\Delta\eta \times \Delta\phi$ of 0.05×0.10 of the cluster barycenter, and have a track momentum no less than 10% of the cluster energy. If such a track is found, the object is assumed to be an electron candidate, its position and energy is calibrated under that assumption, and the calibrated object is stored in the "electron container". The electron reconstruction efficiency at this stage is roughly 93%.

Clusters not matched to a track are classified as photons, and are stored in the "photon container". The reconstruction efficiency for photons which do not convert before the EM calorimeter is over 90%.

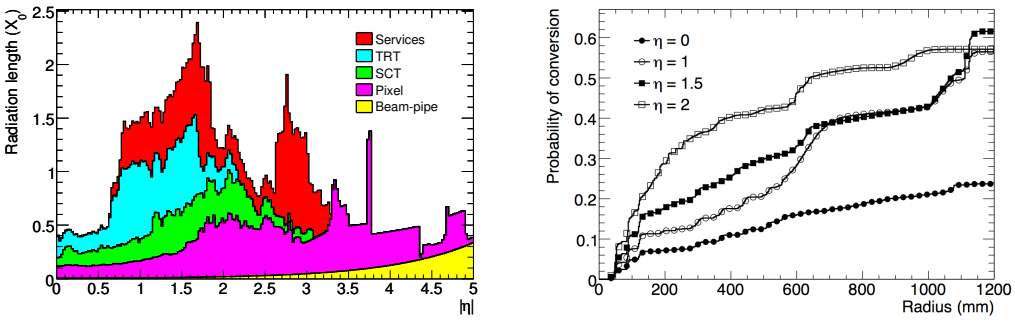

(a) Material Distribution

(b) Conversion Probability

Figure 5.2: (a): Material distribution of the ATLAS inner tracker, as a function of pseudo-rapidity. The large increase around $|\eta| \approx .7$ is due to the TRT and SCT services, which run between the barrel and endcap parts of the TRT. (b): The integrated probability of a photon converting as a function of the cylindrical radius R, for several values of pseudorapidity.

5.1.1 Photon Conversions

For photons that do convert in the inner tracker volume, the efficiency is significantly lower, and depends on the radius at which the photon converts. Conversions that occur late in the inner tracker are less likely to have a reconstructed track that is accurately matched to the calorimeter cluster, especially if the track is composed solely of TRT hits. Conversions that occur early in the ID volume, however, often produce a track that matches the cluster, and are reconstructed as an electron. The frequency of such conversions is driven by the amount of material, which depends strongly on η. A plot of the material profile for the inner tracker is shown in Fig. 5.2a. The mean free path for a photon to pair produce is $\frac{7}{9}X_0$; photons passing through the endcap of the inner detector (starting near $|\eta| = .7$) are almost as likely (or more likely) to convert as not convert (see Fig. 5.2b).

In order to increase the container-level efficiency for converted photons, converted photons are recovered from the electron container by searching for electron candidates consistent with being converted photons.

5.1.1.1 Recovery from Electrons

The recovery procedure begins with the track-cluster matching during the reconstruction of electron candidates. When a track is matched to a cluster, it is also checked to see if it is consistent with originating from a conversion vertex. Photons are massless particles[25], so their decay products have zero opening angle. A special secondary-vertexing algorithm has been developed to exploit this feature, and is documented thoroughly in [54]. It searches for all pairs of tracks that have opposite signs, and then applies several selection criteria to reduce the combinatorial background, including cuts on: the angle between the two tracks; their separation distance at the point of their closest approach (which should be zero); and the separation of the tracks at the reconstructed vertex (which should be identical to the distance of closest approach, and also zero). After these selection criteria are applied, the combinatorial background is reduced by more than a factor of 100. Some final selection criteria on the quality of the vertex fit, on the invariant mass of the track pair, and on the p_{T} of the photon candidate are applied, increasing the total rejection to a factor of almost 400.

Vertices which survive the selection above are matched to tracks associated with electron candidates, and used to identify possible photon conversions. Electron candidates with an associated vertex are copied from the electron container to the photon container, and can in principle be considered as either an electron or a photon at the analysis level.

The vertex-finding efficiency for photons that convert in the inner detector is shown as the solid line in Fig. 5.3. The total efficiency is over 80% at low R, where the track pairs typically have several precision silicon hits. At larger radii, the efficiency drops to less than 50%, and reaches zero at around R =800 mm.

The inefficiencies of the vertex-finding are due to several sources:

[25]The current upper limit on the photon mass is 1×10^{-18} eV. [53]

- **Asymmetric-track conversions**: the fractional momentum carried away by one of the tracks in the electron-positron pair can range from 0 to 1, and is roughly flat for photons in the energy ranges considered in this analysis. Thus, some non-trivial number of photons that convert produce one hard and one soft track, where the soft track may not be reconstructed (or may not be matched to its partner by the vertex-finding algorithm).

- **Merged-track conversions**: Extremely energetic photons that convert can produce electron-positron pairs whose tracks do not separate sufficiently in the magnetic field, and are reconstructed as a single track.

- **Late conversions**: photons that convert at large radii in the inner tracker produce tracks that are difficult to reconstruct, and whose track parameters may be mis-measured due to the lack of precision hits.

The default tracking algorithms, seeded by silicon hits, have poor efficiency for electrons from late conversions, and have zero efficiency for conversions that occur outside of the SCT. To improve the track-finding efficiency for late conversions, a tracking algorithm seeded by pattern-matched track segments in the TRT was developed.[54] This back-tracking algorithm restores good track-finding efficiency out to $R = 800$mm (beyond which photons that convert can be safely treated as unconverted).

To further reduce the total conversion-finding inefficiencies, the recovery algorithm also searches for electron candidates with tracks that are consistent with coming from a secondary vertex, but which are not matched with another track during vertex finding. The basic requirement for such tracks is that they not have a hit in the B-layer of the pixel detector. The lack of such a hit implies that the electron was not prompt, and may be due to a secondary (conversion) vertex. In this case, the vertex position is defined to be the first hit on the track.

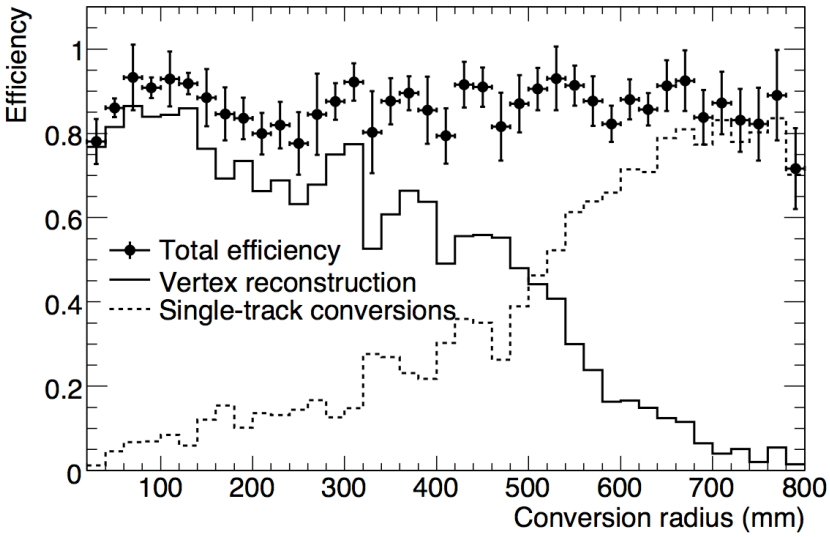

Figure 5.3: The conversion reconstruction efficiency for simulated photons that convert in the inner detector, as a function of the conversion radius.

After the inclusion of these "single-track" conversions, the total conversion reconstruction efficiency is improved to over 80% for most values of the conversion radius (see the black dots in Fig. 5.3).

5.1.2 Cluster Calibration

After the initial cluster-finding procedure, which is identical for photons and electrons, the objects reconstructed as photons are re-clustered, and their energies and positions are calibrated. Unconverted photons have a final cluster size of 3×5 cells (in $\eta \times \phi$) in the barrel calorimeter, while converted photons (like electrons) have a cluster size in the barrel of 3×7 cells (to allow for bremsstrahlung and bending in the magnetic field). In the endcap, all photons and electrons have cluster sizes of 5×5 cells.

The photons are calibrated using a longitudinal weighting method [54, 55], where the energy measured in each sampling layer of the EM calorimeter is scaled by a factor derived from

studies of test-beam and simulation data. The sum of those scaled energies is taken as the final cluster energy. The cluster position is similarly calibrated, taking into account the intrinsic resolution of each sampling layer. Converted and unconverted photons are calibrated using different calibration constants, to better account for the increased energy loss of converted photons due to interactions with the material in the inner detector.

5.2 Photon Identification

The contents of the photon container are dominated by background, especially at low energies. In order to reduce these backgrounds, selection criteria are applied on the shower profile of the photon candidate. The criteria are implemented as rectangular cuts on a set of discriminating variables, and are applied in menus labeled "loose" and "tight".

5.2.1 Discriminating Variables

There are three broad categories of discriminating variables for photon identification that are based on calorimeter information. The first category considers the amount of energy deposited in different layers of the EM and hadronic calorimeters relative to the total cluster energy; the second looks at the profile of the EM shower in the primary (second) sampling layer of the EM calorimeter; and the final looks at the shower profile in the strip layer. As seen in Fig. 3.14, the strips have very fine segmentation in η, which enables greater discrimination between single photons and the primary background from $\pi^0 \to \gamma\gamma$. All of the variables are defined in detail in reference [54, 56], but their definitions are included here for completeness.

5.2.1.1 Energy Ratios

Real prompt photons should be accompanied by a minimum of nearby hadronic activity, so the energy seen in the hadronic calorimeter should be small relative to the energy of the

photon cluster. There are two variables that measure this energy:

- R_{had}: the ratio of the total transverse energy in the hadronic calorimeter (in a $\Delta\eta \times \Delta\phi$ region of 0.24×0.24 behind the photon cluster) to the transverse energy of the photon cluster.

- $R_{\mathrm{had_1}}$: the ratio of the transverse energy in the first sampling layer of the hadronic calorimeter (in a $\Delta\eta \times \Delta\phi$ region of 0.24×0.24 behind the photon cluster) to the transverse energy of the photon cluster.

The variable R_{had} is only considered in the range $0.8 \leq |\eta| < 1.37$ (where the hadronic calorimeter transitions from the barrel to the extended barrel). $R_{\mathrm{had_1}}$ is considered for all other candidates.

In addition to looking at the energy in the hadronic calorimeter, the fractional energy in each of the layers of the EM calorimeter can also be considered. The variables f_0, f_1, f_2, and f_3 define the fraction of energy in the presampler, strips, second layer, and third layer, respectively. In practice only the cut on f_1 is used, and it is applied at a value that results in negligible efficiency losses.

5.2.1.2 Layer-2 Variables

Electromagnetic showers are typically narrower than hadronic clusters, allowing for discrimination between signal and background based on the lateral spread of the shower in the calorimeter. There are three variables that characterize the shower evolution in the second layer:

- w_2: This variable characterizes the lateral width of the shower in η, over a region of 3×5

cells in $\Delta\eta \times \Delta\phi$ around the center of the photon cluster. It is defined as:

$$w_2 = \sqrt{\frac{\sum E_i \eta_i^2}{\sum E_i} - \left[\frac{\sum E_i \eta_i}{\sum E_i}\right]^2} \tag{5.1}$$

where the subscript i indicates the cell index, ranging from 0 to 14.

- R_η: This variable measures the spread in η of the energy outside of the cluster. It is defined as:

$$R_\eta = \frac{E^{S2}_{3\times 7}}{E^{S2}_{7\times 7}} \tag{5.2}$$

where $E^{S2}_{x\times y}$ is the energy contained in $x \times y$ cells ($\eta \times \phi$) of the second layer, centered on the cluster used to define the photon.

- R_ϕ: This variable measures the spread in ϕ of the energy within (and outside of) the cluster. It is defined as:

$$R_\phi = \frac{E^{S2}_{3\times 3}}{E^{S2}_{3\times 7}} \tag{5.3}$$

where $E^{S2}_{x\times y}$ is defined as it is for R_η.

5.2.1.3 Strip Variables

Finally, there are five variables that characterize the shower profile in the strip layer. These variables exploit the good η resolution of the strips to distinguish between single photons, which should produce a single, well-defined peak, and pairs of photons (*e.g.* from π^0 decays), which can produce two separate peaks.

- F_{side}: This variable measures the lateral spread in η of the shower. It is defined as:

$$F_{\text{side}} = \frac{E^{S1}_{7\times 1} - E^{S1}_{3\times 1}}{E^{S1}_{7\times 1}} \tag{5.4}$$

where $E^{S1}_{x\times y}$ are the $x \times y$ ($\eta \times \phi$) strips surrounding the strip with the largest energy.

- $w_{s,3}$: This variable measures the weighted shower width in η in the three strips centered on the strip with the largest energy. It is defined as:

$$w_{s,3} = \sqrt{\frac{\sum E_i (i - i_{\max})^2}{\sum E_i}} \tag{5.5}$$

  where the index i corresponds to the strip number, and $i_{\max}$ is index of the strip with the largest energy.

- $w_{s,\mathrm{tot}}$: This variable is identical to $w_{s,3}$, except it is measured over all strips in a region of $\Delta\eta \times \Delta\phi$= .0625×.2 (20×2 strips).

- ΔE: This variable attempts to quantify the degree to which there are two peaks present in the energy profile. It is defined as:

$$\Delta E = \left[E^{S1}_{\mathrm{max2}} - E^{S1}_{\mathrm{min}}\right] \tag{5.6}$$

  where E^{S1}_{max2} is the energy of the strip that has the second-greatest energy, and E^{S1}_{min} is the energy of the strip with the least energy found between the strips with the greatest and second-greatest energies. For candidates without a distinguishable second peak, this value is close to zero, while candidates that have two peaks in the strips have some larger value.

- E_{ratio}: This variable looks at the size of the second maximum relative to the size of the first maximum. It is defined as:

$$E_{\mathrm{ratio}} = \frac{E^{S1}_{\mathrm{max1}} - E^{S1}_{\mathrm{max2}}}{E^{S1}_{\mathrm{max1}} + E^{S1}_{\mathrm{max2}}} \tag{5.7}$$

Distributions of all of the disciminating variables described above, for both signal and background photons from simulated photon+jet and dijet events, are shown in Fig. 5.4 (Fig. 5.5) for unconverted (converted) candidates. Comparisons of these simulated distributions with the same distributions from data will be shown in Chapter 6.

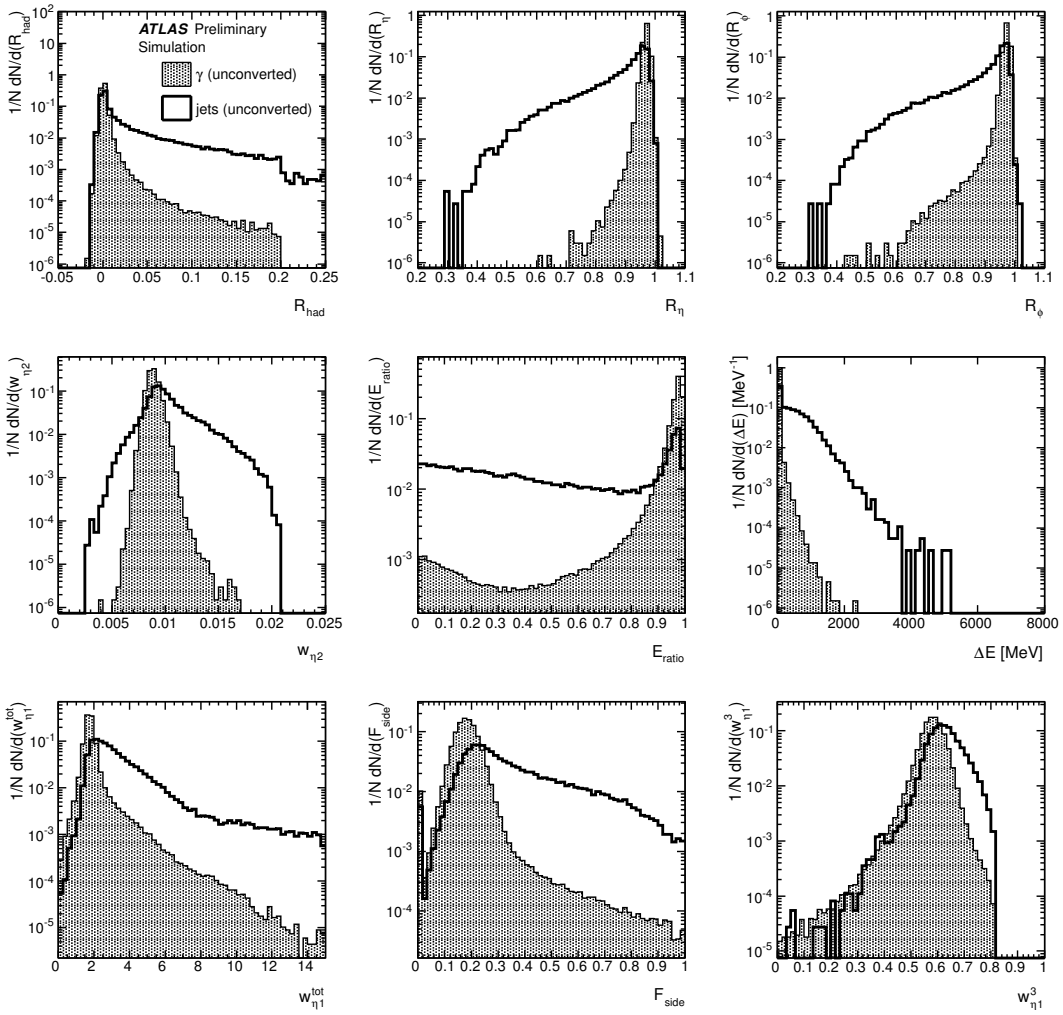

Figure 5.4: Distributions of the shower shape variables used in the identification of prompt photons. The photons and jets that populate these plots have $0 < |\eta| < 0.6$ and $E_{\mathrm{T}} > 20$ GeV, and include only unconverted photon candidates.

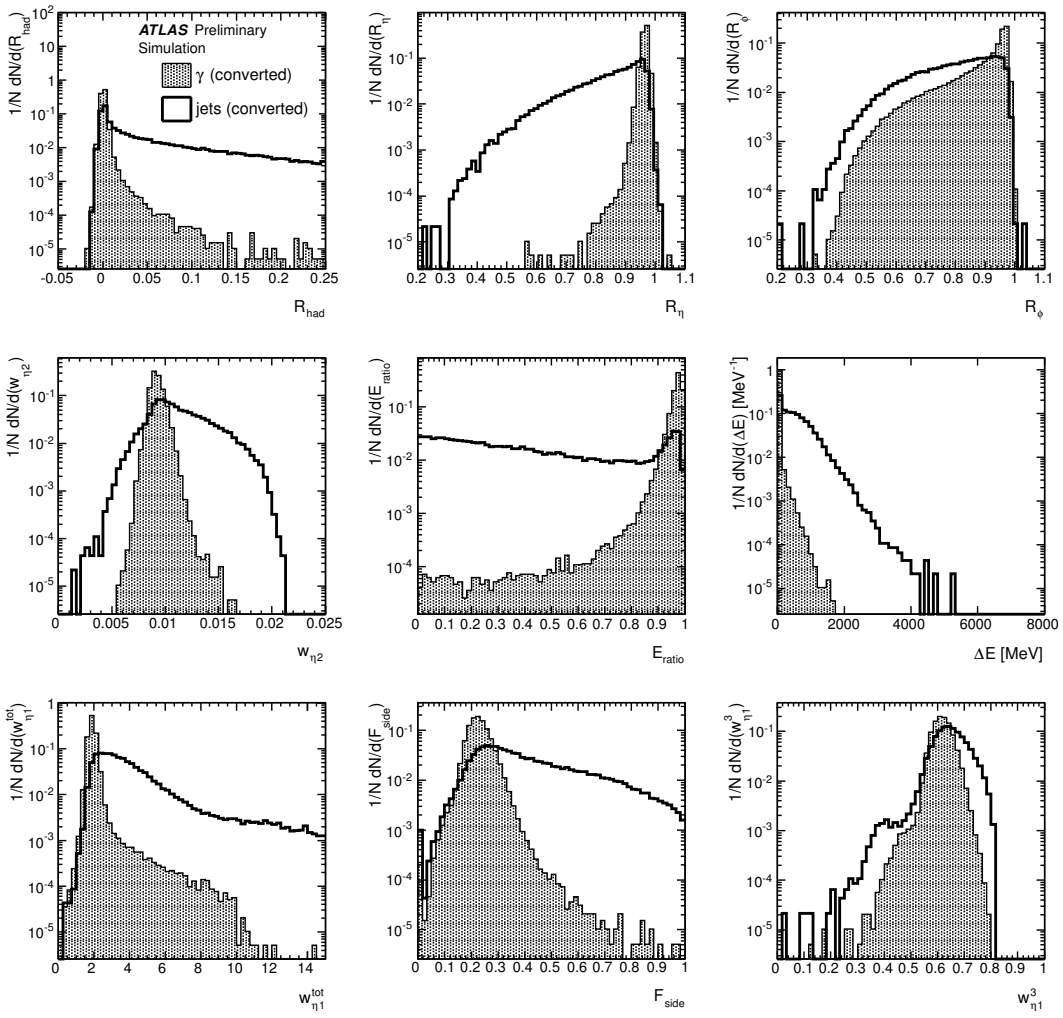

Figure 5.5: Distributions of the shower shape variables used in the identification of prompt photons. The photons and jets that populate these plots have $0 < |\eta| < 0.6$ and $E_{\mathrm{T}} > 20$ GeV, and include only converted photon candidates.

		$\lvert\eta\rvert$						
Variable	Cut	0-0.6	0.6-0.8	0.8-1.15	1.15-1.37	1.52-1.81	1.81-2.01	2.01-2.37
R_{had_1}, R_{had}	$<$	0.01	0.007	0.006	0.008	0.025	0.021	0.014
R_η	$>$	0.927	0.912	0.926	0.916	0.906	0.932	0.913
w_2	$<$	0.012	0.012	0.013	0.013	0.015	0.012	0.013

Table 5.1: Values of the photon loose selection cuts for the different discriminating variables in the different $|\eta|$ regions. R_{had} is used for $0.8 \leq |\eta| < 1.37$, R_{had_1} elsewhere.

5.2.2 Loose Selection Criteria

The "loose" cuts use only the variables based on the second sampling, as well as R_{had_1} (or R_{had}, depending on $|\eta|$). The values of the cuts were optimized for maximal background rejection, while requiring that the efficiency be at least 97% for photons with E_{T}^{γ}=20 GeV in simulation. The cuts are identical for converted and unconverted photons. The values of the cuts are shown in Table 5.1.

The photon triggers that rely on loose identification criteria use a variation on these loose critieria, which are always at least as loose as the cuts shown here.[26]

5.2.3 Tight Selection Criteria

The "tight" cuts use all of the discriminating variables listed above. The cuts were optimized to maximize the background rejection, while retaining a nominal average efficiency of 85% for true photons. Different cut values are used for converted and unconverted photons. The values of the tight cuts used in this analysis are listed in Table 5.2.

In all cases, the tight cuts are required to be at least as tight as the loose cuts. As will be shown in Chapter 6, this requirement has a significant impact in the region $|\eta^{\gamma}| > 1.81$.

[26] In almost all cases, the loose cuts offline are identical to the loose trigger cuts. However, the photon energy used in the computation of (for example) R_{had} is not necessarily the same after full reconstruction as it is for the trigger.

		$\|\eta\|$						
Variable	Cut	0-0.6	0.6-0.8	0.8-1.15	1.15-1.37	1.52-1.81	1.81-2.01	2.01-2.37
Unconverted photon candidates								
$R_{\mathrm{had}_{(1)}}$	$<$	0.0089	0.0070	0.0060	0.0080	0.0190	0.021	0.0137
R_η	$>$	0.951	0.940	0.942	0.946	0.932	0.939	0.926
R_ϕ	$>$	0.954	0.950	0.590	0.820	0.930	0.947	0.930
w_2	$<$	0.0107	0.0115	0.0108	0.0114	0.0114	0.0115	0.0129
F_{side}	$<$	0.284	0.360	0.360	0.514	0.670	0.211	0.191
$w_{s,3}$	$<$	0.660	0.690	0.697	0.810	0.730	0.631	0.57
$w_{s,\mathrm{tot}}$	$<$	2.95	4.40	3.26	3.40	3.80	3.5	1.99
ΔE	$<$	92	92	99	111	92	110	380
E_{ratio}	$>$	0.630	0.840	0.823	0.887	0.880	0.65	0.6
Converted photon candidates								
$R_{\mathrm{had}_{(1)}}$	$<$	0.00748	0.00700	0.00489	0.00800	0.01490	0.01440	0.01020
R_η	$>$	0.941	0.927	0.930	0.930	0.918	0.932	0.913
R_ϕ	$>$	0.400	0.426	0.493	0.437	0.535	0.479	0.692
w_2	$<$	0.0116	0.0114	0.0128	0.0126	0.0138	0.0120	0.0129
F_{side}	$<$	0.320	0.428	0.483	0.510	0.508	0.252	0.205
$w_{s,3}$	$<$	0.697	0.709	0.749	0.780	0.773	0.652	0.624
$w_{s,\mathrm{tot}}$	$<$	2.80	2.95	2.89	3.14	3.70	2.2	1.6
ΔE	$<$	200	200	122	86	123	300	300
E_{ratio}	$>$	0.908	0.911	0.808	0.803	0.670	0.922	0.962

Table 5.2: Values of the photon tight selection cuts for the different discriminating variables in the different $|\eta|$ regions, for unconverted and converted candidates. R_{had} is used for $0.8 \leq |\eta| < 1.37$, R_{had_1} elsewhere.

5.3 Isolation

The concept of isolation plays an important role in the measurements presented here, as explained in Section 2.4. Prompt photons are expected to be well isolated from nearby hadronic activity. The experimental challenge is to define a measure of this nearby activity that can be translated into a safe theoretical prescription, while still retaining good signal efficiency and background rejection.

5.3.1 Definition

The activity surrounding a photon candidate can be measured with either the inner tracker or the calorimeters. An implementation of a track-isolation variable is described in [54], where

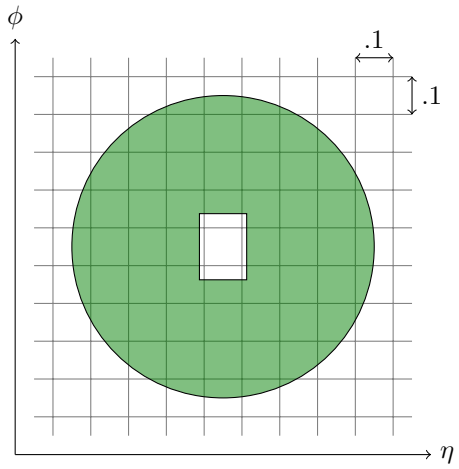

Figure 5.6: An illustration of the calculation of the EtCone40 variable in ATLAS. A circle is drawn around the photon in $\eta - \phi$ space, and the energy from all calorimeter cells inside of that circle are summed. The energy in a central rectangle of the cone is excluded, in an attempt to remove the electron or photon shower.

photon candidates are required to have tracks with a combined p_{T} of less than 4 GeV inside a cone of radius $R = 0.3$ centered on the photon axis. This selection is highly efficient for signal photons, and rejects roughly half of the background that remains after the tight identification criteria are applied. ATLAS has traditionally used the `EtCone` variables for a measurement of the calorimeter isolation energy. The `EtCone` variables are the scalar sums of the transverse energy in all calorimeter cells within a cone of some radius around the photon (or electron) axis. A rectangular core of cells (5×7 in $\eta \times \phi$) nearest to the photon is excluded from the sum, in an attempt to remove the photon energy from the sum. An illustration of the calculation of the `EtCone` variables is shown in Fig. 5.6.

The containment of an electromagnetic shower within the calorimeter is commonly characterized by the Molière radius: the radius of the circle (in the $\eta - \phi$ plane) containing (on average) 90% of the shower energy. For the ATLAS EM calorimeter, the Molière radius is approximately 4.8 cm [57], which corresponds to 1.3 cells in the LAr barrel. This means that over 90% of the photon energy should be contained in a grid of 3×3 cells, and over 95% of the

energy should be contained by the 5×7 cells excluded from the isolation sum. This implies that the leakage of the photon energy should be limited to the few-percent level, but that the energy of the photon is never perfectly contained within the subtracted central core.

In addition to contributions from the photon itself, two other effects play a large role in defining the isolation profile for isolated objects. The first is calorimeter noise at the cell level, which is centered at zero, with both positive and negative Gaussian fluctuations about the mean. The second is from physics not associated with the hard scattering process that produced the photon, *e.g.* from the underlying event and from pileup (both in-time and out-of-time).

Thus, there are four primary components of the final measurement of a given `EtCone`:

- Energy from the object itself that is not properly removed from the sum (I_{leakage})
- Energy from detector noise (I_{noise})
- Energy from the underlying event or pileup (I_{pileup}) (non-perturbative effects)
- Energy associated with the hard process that produced the photon candidate (I)

The measured isolation energy, I_{measured}, is the sum of these components:

$$I_{\text{measured}} = I_{\text{leakage}} + I_{\text{pileup}} + I_{\text{noise}} + I \tag{5.8}$$

The quantity I is the desired discriminating variable, *i.e.* the energy that comes from final state particles produced in the same hard-scattering process as the photon/electron candidate. So, one can reform equation (Eq. (5.8)) into:

$$I = I_{\text{measured}} - I_{\text{leakage}} - I_{\text{pileup}} - I_{\text{noise}} \tag{5.9}$$

Because the noise averages to zero, its only effect on the isolation profile is to induce a Gaussian smearing on I, with a total width proportional to the radius of the isolation cone. In practice, the noise component is difficult to remove in a straightforward way, so no attempt is made to estimate its effect.[27]

The final "corrected" `EtCone` variable is therefore calculated as follows:

$$I = I_{\text{measured}} - I_{\text{leakage}} - I_{\text{pileup}} \tag{5.10}$$

The following sections describe how the values of I_{leakage} and I_{pileup} are estimated.

5.3.2 Corrections for Lateral Leakage

The exclusion of the central core of cells can still leave a non-trivial fraction of the photon E_{T} left in the isolation cone, usually between 2% and 5% of the photon E_{T} (depending on η). For photons with large E_{T}, this residual leakge dominates the isolation profile. An example of the effect of this leakage on a simulated sample of photons from photon+jet events is shown in Fig. 5.7.

By fitting for the means of these isolation distributions for events containing a single photon (and nothing else), and plotting them as a function of E_{T}^{γ}, a clear trend emerges in Fig. 5.8b. The trend is different in different regions of η, most likely because of the material profile in the inner tracker. The slopes of linear fits to these distributions are listed in Table 5.3 (Table 5.4) for photons (electrons).

In many cases, the derived slopes for photons and electrons within the same region of $|\eta|$ are very similar, and they could almost be combined into a single set of corrections for all EM objects. However, the corrections for electrons are sensitive to effects like bremsstrahlung due

[27] There do exist isolation variables calculated after noise-suppression; such variables have narrower widths, but show little improvement in signal/background discrimination over non-noise-suppressed variables.

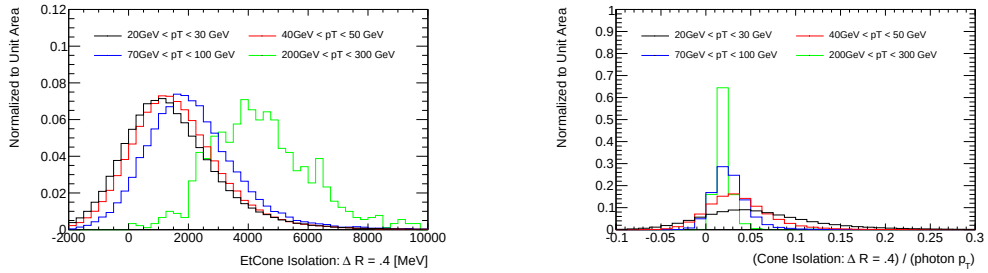

(a) Cone (b) Cone Over photon pT

Figure 5.7: The behavior of the cone isolation variable for different values of photon E_{T}^{γ}, for true photons from photon+jet Monte Carlo events. (All photons here have $|\eta| < .7$.) For the simple cone algorithm (a), the isolation energy increases with photon E_{T}^{γ}, even with the central core removed. When the cone isolation energy is divided by E_{T}^{γ} (b), the distributions shift towards smaller values (and smaller widths) with increasing photon E_{T}^{γ}.

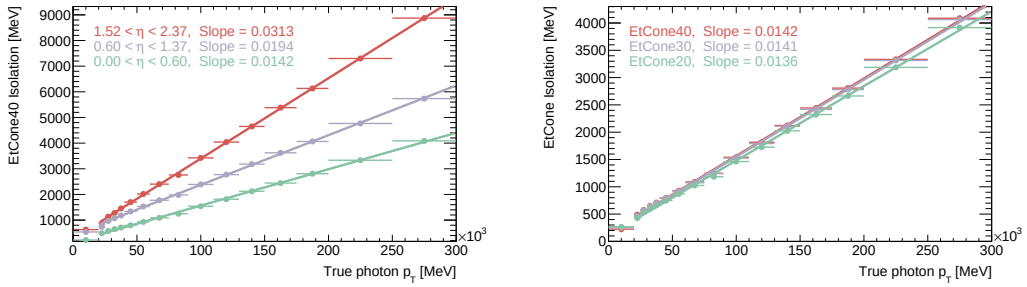

(a) E_{T} correction, η regions (b) E_{T} correction, different cone sizes

Figure 5.8: The behavior of the cone isolation variable as a function of the photon E_{T}. Figure A shows the EtCone40 distribution for three different η regions, while figure B shows different cone sizes (.20, .30, and .40) for $|\eta| < .6$. Similar plots have been produced for all $|\eta|$ regions and cone sizes, with slopes ranging from 1.4% at low $|\eta|$ to 4.5% at high $|\eta|$. The slope represents the transverse energy leakage of the photon outside of the central core, less the transverse leakage outside of the outer cone. The fit is performed for $E_{\mathrm{T}}^{\gamma} > 20$ GeV.

	Isolation Cone Radius						
	.10	.15	.20	.25	.30	.35	.40
$0.00 < \eta < 0.10$	.008	.013	.015	.015	.015	.015	.015
$0.10 < \eta < 0.60$	.008	.013	.014	.014	.014	.014	.014
$0.60 < \eta < 0.80$	.007	.012	.014	.014	.014	.014	.014
$0.80 < \eta < 1.15$	.008	.016	.018	.019	.019	.019	.019
$1.15 < \eta < 1.37$	.009	.018	.021	.022	.022	.022	.022
$1.37 < \eta < 1.52$	.010	.020	.023	.024	.025	.025	.026
$1.52 < \eta < 1.81$	.011	.020	.023	.024	.024	.025	.025
$1.81 < \eta < 2.01$	.012	.024	.027	.028	.029	.029	.029
$2.01 < \eta < 2.37$	.015	.030	.035	.036	.037	.038	.037
$2.37 < \eta < 2.47$	.018	.035	.041	.041	.044	.046	.046
$2.47 < \eta < 5.00$	.031	.040	.043	.044	.045	.045	.046

Table 5.3: Corrections applied to EtCone variables, for photons, to correct for E_{T} leakage outside of the subtracted core.

	Isolation Cone Radius						
	.10	.15	.20	.25	.30	.35	.40
$0.00 < \eta < 0.10$	.008	.013	.015	.015	.015	.015	.015
$0.10 < \eta < 0.60$	.008	.013	.014	.014	.015	.015	.015
$0.60 < \eta < 0.80$	.007	.013	.014	.015	.015	.015	.015
$0.80 < \eta < 1.15$	.009	.017	.019	.020	.020	.020	.020
$1.15 < \eta < 1.37$	.010	.021	.024	.025	.026	.026	.026
$1.37 < \eta < 1.52$	-.01	.019	.033	.038	.040	.042	.043
$1.52 < \eta < 1.81$	.009	.020	.024	.025	.026	.026	.026
$1.81 < \eta < 2.01$	.013	.024	.027	.029	.029	.029	.029
$2.01 < \eta < 2.37$	.015	.030	.035	.037	.038	.038	.038
$2.37 < \eta < 2.47$	.015	.034	.041	.044	.045	.046	.046
$2.47 < \eta < 5.00$	.015	.040	.049	.054	.056	.057	.056

Table 5.4: Corrections applied to EtCone variables, for electrons, to correct for E_{T} leakage outside of the subtracted core.

to material upstream of the calorimeter, and thus depend more strongly on the details of the detector simulation.[28]

5.3.3 Corrections for Pileup and Non-Perturbative Effects

As described in Section 2.6, previous experiments have dealt with the issue of pileup and non-perturbative effects in a variety of ways. CDF applies an explicit correction to their isolation measurement based on the number of reconstructed vertices; CMS and D∅ apply no corrections for pileup. Both CMS and CDF estimate the impact of the underlying event by use of `PYTHIA` Monte Carlo samples, and use that estimate to correct the parton-level predictions in `JETPHOX` to the particle level.

In ATLAS, the procedure for estimating the size of the non-perturbative effects is fundamentally different, though elements of the approaches described above do survive. The procedure used to account for both the underlying event and pileup is based on ideas first presented in [58], and expanded on in [19]. The procedure is designed to extract an estimate of the ambient transverse energy density on an event-by-event basis, rather than applying an average correction to all events. This has the benefit of naturally accounting for potentially large event-to-event variations in the amount of activity from the underlying event and in-time pileup.

The ambient energy in each event is estimated by exploiting the concept of "jet areas", which can be computed by the jet-finding program `FastJet`. [59] In this case, a $k_\perp$ algorithm [60, 61], with size parameter 0.5, is run on noise-suppressed, three-dimensional topological clusters in the calorimeters (`TopoClusters`, described in [62]) and used to reconstruct

[28] An updated set of corrections, implemented after the inclusive analyses presented in this document, make several improvements on the results described here. The primary changes are that separate corrections are defined for converted and unconverted photons, and that the single-particle simulation data used to derive the corrections are updated with an improved geometrical detector description. The differences between the new and old corrections are small (at the percent level) and have little effect for objects below $E_{\mathrm{T}} \approx$100 GeV.

all jets in the event. There is no explicit cut on the transverse energy of the jets, except that the total jet E_{T} must be positive. The `TopoCluster`s that seed the jet reconstruction are required to have one cell with a 4σ (or larger) deviation from the baseline noise rate.[29] The 4σ requirement does not correspond to a fixed value in transverse energy, but typically sets a lower jet E_{T} bound at around 100 MeV. During reconstruction, each jet is assigned an area via a Voronoi tessellation [63] of the $\eta - \phi$ space. According to the algorithm, every point within a jet's assigned area is closer to the axis of that jet than of any other jet. The transverse energy density for each jet is then computed from the ratio of the jet transverse energy to its area.

The distribution of jet E_{T} densities within an event can be very broad. Leading jets can have transverse energies of tens, hundreds, or thousands of GeV for typical photon-jet events. (The photon itself is also reconstructed as a jet, and is included in this distribution; it usually has the largest jet-E_{T}-density in a photon-jet event.) The bulk of the distribution, meanwhile, is found at low E_{T}-densities, corresponding to the very soft jets that populate the $\eta - \phi$ space of a typical pp collision. The mean of the E_{T}-density distribution for a given event is therefore strongly correlated with the E_{T} of the photon, and in a way that tends to overestimate the ambient E_{T} density for the event as a whole. On the other hand, the median jet E_{T} density is less influenced by transverse energies of the leading jets.

The ambient transverse energy density for the event is taken to be the median jet E_{T} density. The distribution of the median jet E_{T} densities for true prompt photon events, along with the corresponding distributions for signal and background from `PYTHIA`, is shown in Fig. 5.9.

The estimated ambient E_{T} density is multiplied by the active area of the isolation cone to

[29] The definition of the noise width is primarily driven by noise in the electronics. At high luminosities, however, the nominal noise width can be increased to take in-time pileup into account, effectively raising the threshold for `TopoCluster` creation.

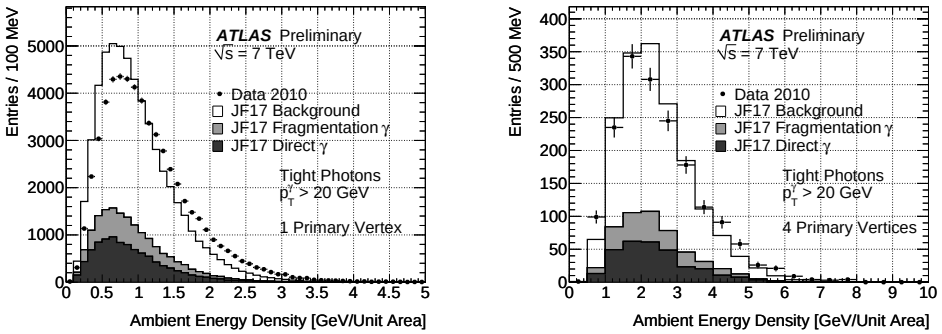

(a) 1 Primary Vertex (b) 4 Primary Vertices

Figure 5.9: The energy density as computed by the area correction technique, for events containing tight photon candidates, and only one (a) or four (b) reconstructed primary vertices with three or more tracks. In both figures, the fractions of signal and background events in the simulated samples are as predicted by `PYTHIA`, and the sum of the simulated samples is normalized to the data.

compute I_{pileup}, the correction to $E_{\text{T}}^{\text{iso}}$ that accounts for both the underlying event and pileup.

5.3.4 Corrected Calorimeter Isolation

With the values of I_{leakage} and I_{pileup} derived in the previous sections, the "fully corrected" isolation energy I is computed as in Eq. (5.10). An example distribution of this variable for simulated prompt photons is shown in Fig. 5.10a. An example of the same distribution, calculated for electrons from simulated Z decays, is shown in Fig. 5.10b. The distributions for both photons and electrons, after all of the corrections, are now E_{T}-independent, and centered close to zero. The width of the distribution is primarily driven by calorimeter noise. The E_{T}-independence of the distributions allows a single cut to be applied on photons over a wide range of energies while maintaining a constant efficiency.

The final selection requirement for prompt photons used for the inclusive and isolated cross section measurement is $E_{\text{T}}^{\text{iso}} < 3$ GeV, where $E_{\text{T}}^{\text{iso}}$ is the corrected calorimeter isolation.

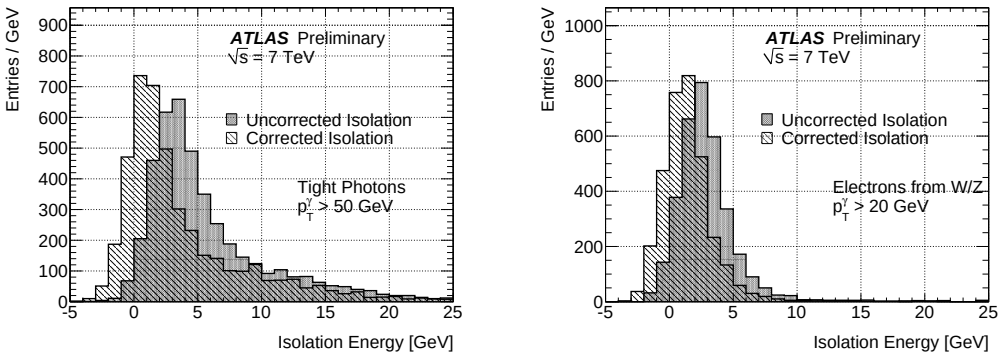

(a) High p_{T} Photons

(b) Electrons from W and Z Decays

Figure 5.10: The isolation energies of high p_{T} photons (a) and electrons from W and Z decays (b), before and after the isolation corrections are applied, measured in collision events. The total shift for the high-p_{T} photons is dominated by the corrections for out-of-core leakage.

5.3.5 Monte Carlo Truth Information

In addition to the isolation requirement made in the experimental measurement, an isolation requirement must be made when calculating the expected cross section in order to make a valid comparison between the two. In this case, the prediction is made by the `JETPHOX` program, which calculates the cross section (and the isolation energy) at the parton level. `PYTHIA` photon+jet samples are used to determine the correspondence between an isolation cut after reconstruction and a cut on the parton or particle-level (after hadronization, but before detector simulation) isolation energy. The parton-level isolation is defined as the sum of partonic energy in a cone around the prompt photon axis, excluding any activity not associated with the hard scattering process that produced the photon.[30] The particle-level isolation energy is similarly defined as the E_{T} sum of all particles in a cone around the photon axis. At the particle level, however, the distinction between particles from the hard interaction and those from the underlying event is not physically meaningful, as it depends on unphysical

[30] This definition is motivated by the limitations of the `JETPHOX` program, which does not model the underlying event.

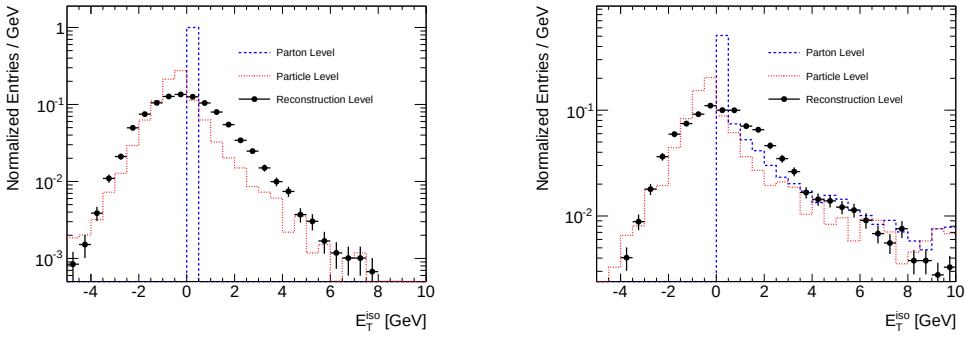

(a) Direct Photons (b) Fragmentation Photons

Figure 5.11: The reconstructed, particle, and parton isolation energies for direct (a) and fragmentation (b) photons from PYTHIA. The particle- and reconstructed-level isolation distributions are corrected using the jet-area correction method.

parameters used to tune the model of the hadronization process.[31] To remove the effects of the underlying event, the same jet area subtraction technique used for the reconstructed isolation energy is applied at the particle-level, using jets composed of true particles from the generator.

All three isolation distributions (reconstructed, particle, and parton level) are shown in Fig. 5.11, for a sample of true prompt photons from PYTHIA. For direct photons, which are produced back-to-back with a jet, the parton isolation has a well-defined peak at 0. The long tail in the parton isolation distribution is due to the fragmentation photons, which are modeled in PYTHIA as hard radiation off of final-state partons. The particle-level isolation energies are more similar in nature to those after reconstruction, as many of the direct photons acquire some non-zero isolation energy during the hadronization of jets from the hard process, the underlying event, or pileup.

The truth-level isolation cut that corresponds to the cut after reconstruction is chosen as the cut that gives the same efficiency for accepting photons from fragmentation as a cut on the reconstructed isolation energy. Direct photons are not considered because of their sharp peak

[31] This is certainly true in fixed-order Monte Carlo programs like PYTHIA and HERWIG.

at zero in the parton isolation distribution, and because the actual ratio of direct photons to fragmentation photons is not necessarily modeled correctly in PYTHIA. For a reconstruction-level cut at $E_{\mathrm{T}}^{\mathrm{iso}} < 3$ GeV, the equivalent cuts at both the particle-level and parton-level are 4 GeV. This requirement at the particle level is therefore used to compute the NLO prediction of the cross section in JETPHOX, as well as being used to define the denominator of the prompt photon efficiency measurements in the following chapter.

Chapter 6

Measurement of the Reconstruction, Identification, and Trigger Efficiencies

This chapter discusses the extraction of the reconstruction, identification, and trigger efficiencies for prompt photons. The reconstruction efficiency is evaluated using Monte Carlo samples. The identification efficiency is evaluated for reconstructed photons using Monte Carlo samples modified by the observed differences with data. A data-driven method, using electrons from W decays, is also discussed. The trigger efficiency is estimated using collision data with a boot-strap method, using a series of triggers with different thresholds. Finally, the systematic uncertainties affecting the efficiency measurements are estimated.

6.1 Reconstruction Efficiency

The total reconstruction efficiency for isolated prompt photons, as a function of the pseudo-rapidity interval k and the photon transverse energy E_{T}^{γ}, is defined as:

$$\varepsilon^{\mathrm{reco,k}}(E_{\mathrm{T,true}}^{\gamma}) \equiv \frac{dN^{\gamma}(\eta_{k,1} \leq |\eta_{\mathrm{reco}}^{\gamma}| < \eta_{k,2}, E_{\mathrm{T,reco}}^{\mathrm{iso}} < 3 \text{ GeV})/dE_{\mathrm{T,true}}^{\gamma}}{dN^{\gamma}(\eta_{k,1} \leq |\eta_{\mathrm{true}}^{\gamma}| < \eta_{k,2}, E_{\mathrm{T,true}}^{\mathrm{iso}} < 4 \text{ GeV})/dE_{\mathrm{T,true}}^{\gamma}} \tag{6.1}$$

Here the true isolation is defined at the particle level, after jet-area corrections are applied on truth jets. The efficiency is calculated using `PYTHIA` γ+jet samples, including both direct

E_{T} min [GeV]	E_{T} max [GeV]	$0.00 \leq \lvert\eta^{\gamma}\rvert < 0.60$ [%]	$0.60 \leq \lvert\eta^{\gamma}\rvert < 1.37$ [%]	$1.52 \leq \lvert\eta^{\gamma}\rvert < 1.81$ [%]
15.0	20.0	83.1	83.5	79.2
20.0	25.0	83.7	84.4	78.7
25.0	30.0	84.2	84.7	78.8
30.0	35.0	84.3	85.1	78.5
35.0	40.0	84.3	84.2	78.2
40.0	50.0	84.1	83.9	76.3
50.0	60.0	83.5	83.7	76.1
60.0	100.0	83.9	82.7	73.8

Table 6.1: The total reconstruction efficiency for prompt photons, based on PYTHIA signal samples. The efficiency is estimated after conversion recovery, and includes both acceptance losses and losses due to the isolation criterion.

and fragmentation photons in the ratio predicted by PYTHIA. The extracted efficiencies are shown in Table 6.1. The reconstruction efficiency includes acceptance losses, primarily from dead front-end modules in the EM calorimeter (an 11% effect). The isolation cut is also applied here, and accounts for 3-4% of the efficiency loss in the first two η regions (11% in the third η region).

The η resolution of the EM calorimeter is at the 10^{-4} level, good enough that bin-to-bin migrations in η have a negligible effect on the efficiencies calculated in this chapter. The effects of the finite energy resolution of the EM calorimeter will be discussed in Section 8.2.

6.2 Identification Efficiency

The identification efficiency is defined as the fraction of reconstructed isolated prompt photons that also pass the tight selection criteria (described in Section 5.2.3) within a pseudorapidity interval k:

$$\varepsilon^{\mathrm{off},k}(E^{\gamma}_{\mathrm{T},reco}) \equiv \frac{dN^{\gamma}(\eta_{k,1} \leq |\eta^{\gamma}_{\mathrm{reco}}| < \eta_{k,2}, E^{\mathrm{iso}}_{\mathrm{T,reco}} < 3 \text{ GeV}, \text{tight-ID})/dE^{\gamma}_{\mathrm{T,reco}}}{dN^{\gamma}(\eta_{k,1} \leq |\eta^{\gamma}_{\mathrm{reco}}| < \eta_{k,2}, E^{\mathrm{iso}}_{\mathrm{T,reco}} < 3 \text{ GeV})/dE^{\gamma}_{\mathrm{T,reco}}} \tag{6.2}$$

As with the reconstruction efficiency, the identification efficiency is calculated from PYTHIA

γ+jet samples including both direct and fragmentation photons. The shower-shape distributions from the simulated samples are corrected by the observed differences between data and MC, and the efficiency is calculated from the shifted distributions.

A second extraction of the efficiency is made using electrons from $W \to e\nu$ decays, where the electrons are tagged using kinematic selection criteria, and re-calibrated as photons. While the small number of $W \to e\nu$ candidates prohibits a precise measurement of the efficiency, this method is a useful data-driven cross-check of the nominal (simulation-based) approach.

The shower shape distributions for photons in data, after applying the loose selection criteria, are shown in Fig. 6.1, along with the expected signal and background shapes from Monte Carlo. Some variables, most notably R_η and w_2, show significant deviations from MC expectations, motivating the need for a data-driven estimation of the identification efficiency.

6.2.1 Shower Shape Correction Factors

The first investigations of photon shower shapes in 2010 collision data indicated that the photon showers had more lateral spread in η than expected from simulation. This particularly affects the distributions of variables like R_η, w_2, and F_{side}, which are directly sensitive to the lateral shower profile. To first order, such data/MC discrepancies for a variable ξ are well modeled by a simple shift of the mean (μ_ξ) along the x-axis, calculated in each region of E_{T}^γ and $|\eta^\gamma|$:

$$\Delta\mu_\xi \left(E_{\text{T}}^\gamma, \eta^\gamma\right) = \langle \xi_{\text{data}} \rangle \left(E_{\text{T}}^\gamma, \eta^\gamma\right) - \langle \xi_{\text{MC}} \rangle \left(E_{\text{T}}^\gamma, \eta^\gamma\right) \tag{6.3}$$

The value of $\Delta\mu_\xi$ is then used to correct the value of ξ on an event-by-event basis in the MC samples:

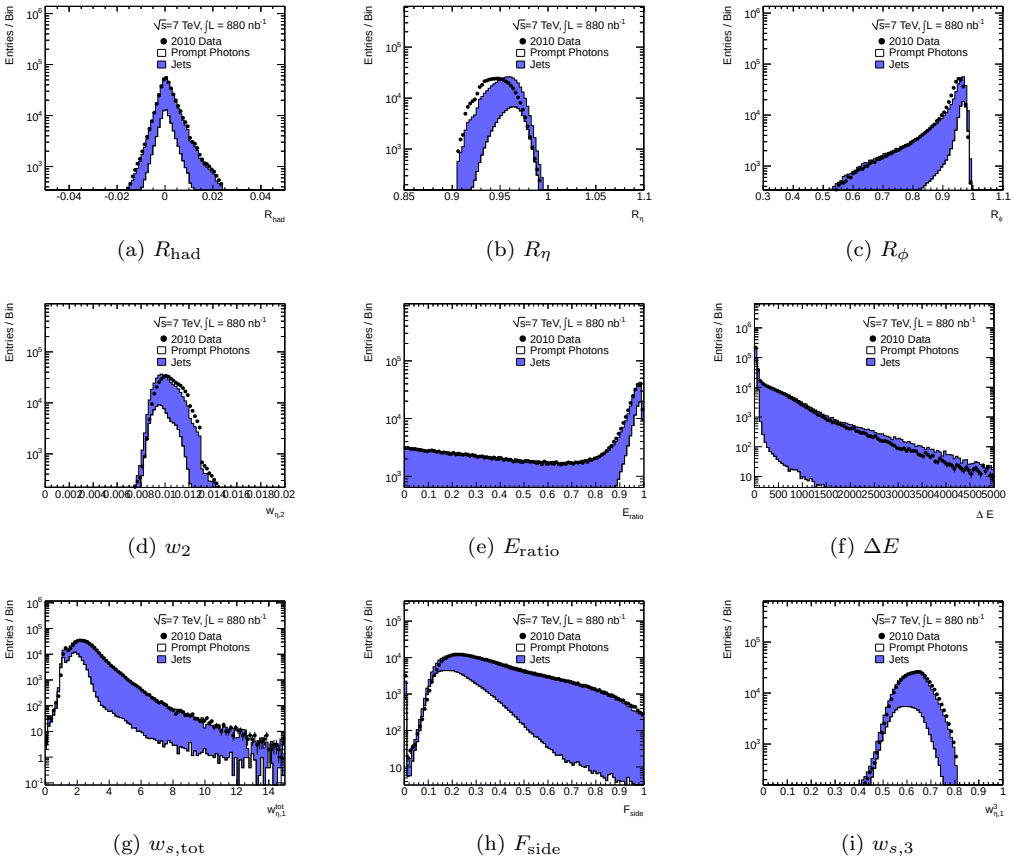

(a) R_{had} (b) R_{η} (c) R_{ϕ}

(d) w_2 (e) E_{ratio} (f) ΔE

(g) $w_{s,\mathrm{tot}}$ (h) F_{side} (i) $w_{s,3}$

Figure 6.1: Photon identification variables, shown for photon candidates satisfying the loose photon selection criteria. The signal and background distributions, in white and blue, are taken from PYTHIA. The signal distribution is scaled using the expected prompt photon cross section (as estimated by PYTHIA), while the background is scaled so that the sum of signal and background are normalized to the data.

$$\xi' = \xi - \Delta\mu_{\xi} \tag{6.4}$$

Ideally the extraction of $\Delta\mu_{\xi}$ would be made by using only true signal events from data and MC, to avoid the possible effects of background mis-modeling in the MC. However, especially at low-E_{T}, a pure sample of photons in data does not exist. Any sample used to extract the corrections will have a non-trivial background component, the amount of which is driven by the selection criteria used to define the sample. The corrections are calculated by applying

the tight selection criteria, excluding cuts on the variable under study and other variables that are highly correlated with it. A second set of corrections is computed applying the loose criteria, and the efficiencies are recomputed. The differences in efficiencies when using $\Delta\mu_{\xi}^{\text{tight}}$ compared to $\Delta\mu_{\xi}^{\text{loose}}$ range from 0% to 5%, depending on η and E_{T}, and are taken as systematic uncertainties on the method.

The identification efficiencies before and after the shower-shape corrections are shown in Fig. 6.2. In the first three pseudorapidity regions, the shower-shape shifts cause changes in the efficiencies of only a few percent. In the final pseudorapidity region, however, the differences are closer to 10% (absolute). In that region the cuts are too tight both in the offline reconstruction and in the trigger selection. These large efficiency losses make an evaluation of the trigger and offline efficiencies in that region very difficult, and thus that region is not considered when evaluating the final cross sections.

The identification efficiencies evaluated after the shower shape corrections are applied are shown in Table 6.2 for the three remaining pseudorapidity regions. The efficiencies range from 63% at low E_{T} to almost 95% in the highest E_{T} bin.

6.2.2 Extrapolation from Electrons

Prompt photons and prompt electrons induce a similar response in the EM calorimeter, especially when the electrons do not lose a significant amount of energy to bremsstrahlung before showering. This similarity can be exploited to determine the efficiency of the photon selection criteria by applying the shower-shape cuts on an unbiased sample of electrons.

One way to obtain a pure sample of unbiased electrons is with a tag-and-probe technique applied on $Z \to ee$ candidates: one electron is used as the tag, and has all tight selection criteria applied, while the other electron, the probe, is only required to be kinematically consistent with being the second leg of a $Z \to ee$ decay. Since the probe has no requirements

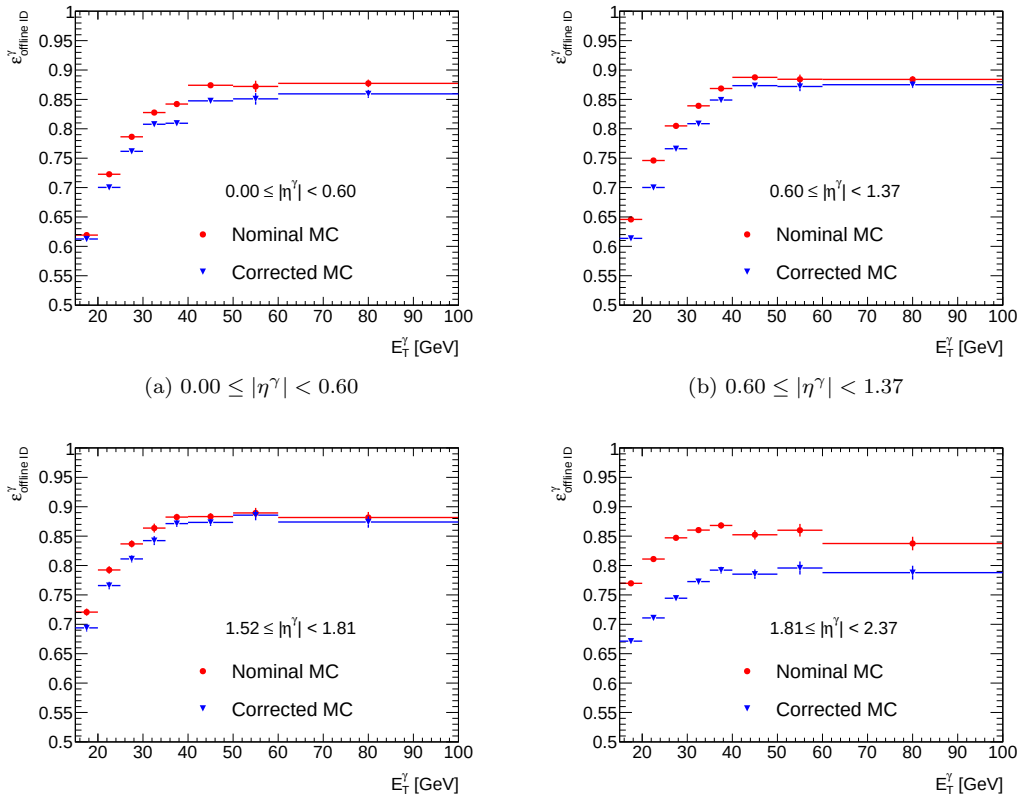

(a) $0.00 \le |\eta^{\gamma}| < 0.60$

(b) $0.60 \le |\eta^{\gamma}| < 1.37$

(c) $1.52 \le |\eta^{\gamma}| < 1.81$

(d) $1.81 \le |\eta^{\gamma}| < 2.37$

Figure 6.2: The offline tight identification efficiencies for prompt photons, as a function of E_{T}^{γ}, for each of four pseudorapidity regions. The efficiencies taken directly from Monte Carlo (red circles) are larger than the efficiencies computed after shifting the MC distributions by the observed differences between MC and data (blue triangles). The large differences in the last pseudorapidity region are due to selection cuts that are too tight, substantially reducing the overall efficiency in that region.

made on its shower shapes, the corresponding distributions remain unbiased, and an efficiency can be extracted with small uncertainties. However, the $Z \to ee$ cross section times branching ratio at the LHC is only 0.75 nb, [64] yielding too few $Z \to ee$ candidates in an 880 nb^{-1} sample to make a statistically meaningful measurement of the photon identification efficiency.

A similar technique can be applied to select electrons from $W \to e\nu$ decays, using the $E_{\mathrm{T}}^{\mathrm{miss}}$ as the tag. The $W \to e\nu$ cross section times branching ratio is more than ten times larger than that of $Z \to ee$, and thus provides a greater statistical reach (albeit at some cost

E_{T} range $[\mathrm{G}eV]$	$0 \leq \lvert\eta^{\gamma}\rvert < 0.6$ [%]	$0.6 \leq \lvert\eta^{\gamma}\rvert < 1.37$ [%]	$1.52 \leq \lvert\eta^{\gamma}\rvert < 1.81$ [%]	$1.81 \leq \lvert\eta^{\gamma}\rvert < 2.37$ [%]
unconverted γ				
$[15, 20)$	64.24	64.48	71.34	77.57
$[20, 25)$	73.85	73.70	80.19	81.21
$[25, 30)$	80.40	80.35	85.51	83.71
$[30, 35)$	85.51	84.35	89.67	86.29
$[35, 40)$	85.30	88.71	91.72	86.92
$[40, 50)$	89.17	91.59	91.90	88.86
$[50, 60)$	90.76	93.30	92.66	87.28
$[60, 100)$	91.44	93.67	92.61	90.18
converted γ				
$[15, 20)$	57.27	60.86	73.64	61.44
$[20, 25)$	71.42	72.89	83.85	70.02
$[25, 30)$	79.14	81.77	88.63	74.31
$[30, 35)$	85.25	87.61	91.43	78.55
$[35, 40)$	84.75	90.65	93.01	82.17
$[40, 50)$	89.13	93.24	95.74	83.05
$[50, 60)$	93.40	95.67	95.50	87.40
$[60, 100)$	95.22	97.13	96.17	88.03
all γ				
$[15, 20)$	63.29	63.55	72.15	69.90
$[20, 25)$	73.46	73.47	81.59	75.70
$[25, 30)$	80.18	80.78	86.74	78.91
$[30, 35)$	85.46	85.35	90.41	82.25
$[35, 40)$	85.20	89.33	92.28	84.44
$[40, 50)$	89.16	92.11	93.53	85.73
$[50, 60)$	91.29	94.08	93.90	87.34
$[60, 100)$	92.24	94.85	94.18	89.03

Table 6.2: Isolated prompt photon identification efficiency $\varepsilon_k^{\mathrm{offl}}(E_{\mathrm{T}}^{\gamma})$, defined as the fraction of true prompt photons reconstructed in a certain interval k of pseudorapidity, passing e/γ object quality criteria, with reconstructed isolation energy lower than 3 GeV, that pass tight photon identification criteria.

to the electron purity). To further improve the statistics, an additional 2.3 pb^{-1} of data are used to collect $W \to e\nu$ candidates.[32]

The electrons are selected by requiring that the track properties and event kinematics are consistent with a W boson decaying to an electron and a neutrino. The track must have $p_{\mathrm{T}} > 20$ GeV, and must pass the standard E/p and cluster matching requirements for tight electrons.[33] It is also required to have a high ratio of high threshold hits in the TRT portion of the track (to reject charged pion backgrounds). The event must have $E_{\mathrm{T}}^{\mathrm{miss}} > 25$ GeV, and a ϕ separation between the $E_{\mathrm{T}}^{\mathrm{miss}}$ and all jets with $p_{\mathrm{T}} > 15$ GeV (including the jet associated with the electron) of greater than 2.5 radians.[34] The E_{T} spectrum of electron candidates passing these cuts falls off sharply after 50 GeV, limiting the E_{T} range over which the electrons can be directly compared with prompt photons of equivalent E_{T}. With the 3.1 pb^{-1} sample, the efficiency measurements with electrons are only made up to E_{T}=50 GeV.

After selection, the electrons are re-clustered, calibrated, and have their shower shape profiles recomputed as though they were converted or unconverted photon candidates. This allows the same selection criteria normally applied to photons to be applied to the electrons.

The shower-shape variables for converted photons and electrons are very similar. This means that the identification efficiency for converted photons can be taken directly from applying the tight selection criteria to electrons reconstructed as converted photons. The difference between the true converted photon efficiency and the efficiency extracted from electrons in simulated events is shown in Fig. 6.3. The precision of this method is roughly 2% (absolute), with some small variations in E_{T} and η.

[32] These data were collected immediately after the 880 nb^{-1} sample, under similar conditions. Several aspects of the photon triggers changed after the 880 nb^{-1}sample was collected, motivating the cutoff for the photon sample. For the electron sample, there is no apparent bias introduced by the additional data.

[33] The tight electron identification criteria are similar to the tight criteria for photons, but include some additional variables related to the electron track. For more details on the electron selection criteria, see [54].

[34] This is equivalent to a transverse mass requirement of 42 GeV for events that just satisfy the track-p_{T} and $E_{\mathrm{T}}^{\mathrm{miss}}$ requirements.

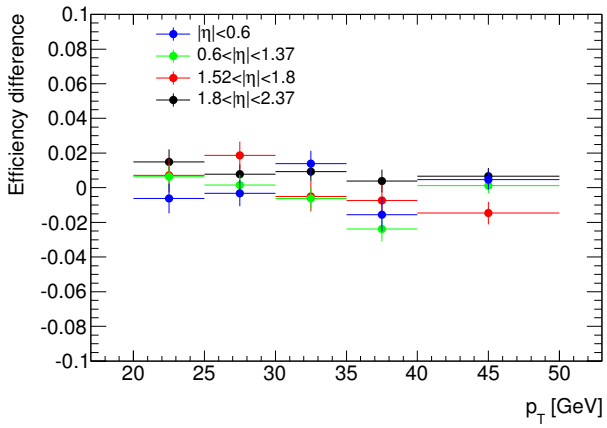

Figure 6.3: The difference of the converted prompt photon efficiency derived from electrons from W decays and the true prompt photon efficiency for a simulated sample of converted photons in photon+jet events, as a function of E_{T}^{γ}, for four different regions of pseudorapidity. The electron extrapolation method reproduces the true efficiency with an uncertainty of roughly 2%, with little apparent bias as a function of E_{T} or η.

Finally, the method is applied on electrons from data, and the results are compared with the converted photon efficiencies described in Section 6.2.1. The comparisons are shown in Fig. 6.4. While the estimates from the electrons have large statistical and systematic uncertainties, they are in reasonable agreement with the results from the nominal method.

The comparison between electrons and unconverted photons is not as straightforward. In this case, the shower profiles can differ significantly, leading to large changes in the shapes of discriminating variables like R_{ϕ} (which is sensitive to bremsstrahlung effects, and to ϕ bending of the electron from the magnetic field). Simulated samples of $W \rightarrow e\nu$ electrons and unconverted prompt photons are used to derive electron→photon transforms in MC. The transforms are modeled as simple shifts of the distrbution along the variable's axis, and are applied to electrons in data to approximate the distributions of photons in data. The identification criteria for unconverted photons are then applied on these transformed distributions, and the resulting efficiencies (again compared with the nominal efficiencies extracted in Section 6.2.1) are shown in Fig. 6.5.

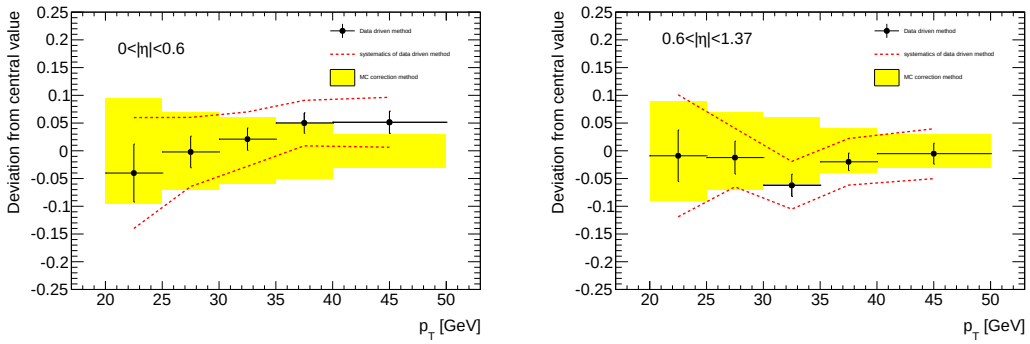

(a) $0.00 \leq |\eta| < 0.60$ (b) $0.60 \leq |\eta| < 1.37$

(c) $1.52 \leq |\eta| < 1.81$ (d) $1.81 \leq |\eta| < 2.37$

Figure 6.4: The difference of the converted prompt photon efficiency derived from electrons from W decays and the same quantity derived with the shifted-shower-shape approach, as a function of E_{T}^{γ}, for four different regions of pseudorapidity. The electron extrapolation method has large systematic and statistical uncertainties, but is in reasonable agreement with the results of the nominal method.

The selection criteria provide a relatively pure sample of electrons whose shower shapes are unbiased. The purity of the sample is assessed with a 2-D sideband technique applied on the R_{η} and isolation distributions of the electrons. (For a description of the 2-D sideband method, see Section 7.3.) The background contamination ranges from less than 2% to almost 20%, depending on E_{T} and η, and is taken into account when estimating systematic uncertainties on the method.

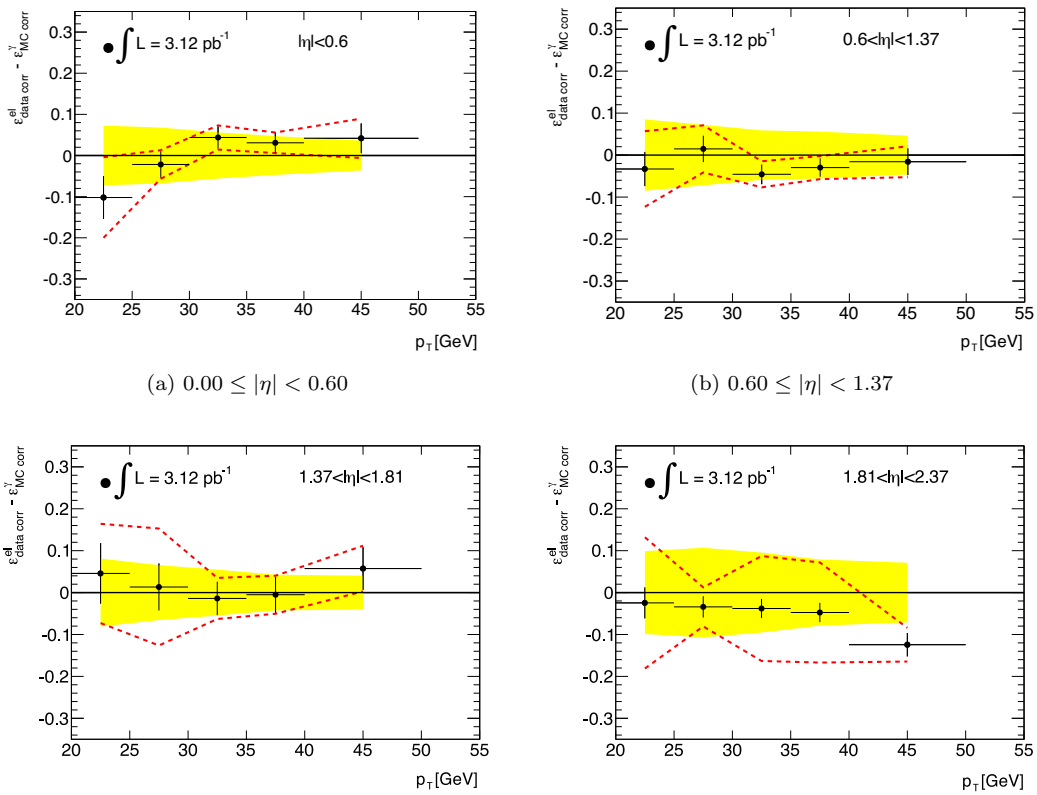

(a) $0.00 \leq |\eta| < 0.60$

(b) $0.60 \leq |\eta| < 1.37$

(c) $1.52 \leq |\eta| < 1.81$

(d) $1.81 \leq |\eta| < 2.37$

Figure 6.5: The difference of the unconverted prompt photon efficiency derived from electrons from W decays and the same quantity derived with the shifted-shower-shape approach, as a function of E_{T}^{γ}, for four different regions of pseudorapidity. The electron extrapolation method has large systematic and statistical uncertainties, but is in reasonable agreement with the results of the nominal method.

6.3 Trigger Efficiency

The trigger used in this analysis, called g10_loose, has a nominal E_{T} threshold of 10 GeV, and applies a modified set of selection criteria compatible with the loose selection defined in Section 5.2.2. It is seeded from a first level trigger with an E_{T} threshold of 5 GeV.

The efficiency of the calorimeter trigger is defined relative to the photon reconstruction and offline selection. It is the probability of a true prompt photon to pass the g10_loose trigger selection, after having been reconstructed as an isolated photon that passes the tight selection

criteria.

$$\varepsilon^{\mathrm{trig},k}(E^{\gamma}_{\mathrm{T,reco}}) \equiv \frac{dN^{\gamma}(\eta_{k,1} \leq |\eta^{\gamma}_{\mathrm{reco}}| < \eta_{k,2}, E^{\mathrm{iso}}_{\mathrm{T,reco}} < 3 \text{ GeV}, \text{tight-ID}, \text{trigger})/dE^{\gamma}_{\mathrm{T,reco}}}{dN^{\gamma}(\eta_{k,1} \leq |\eta^{\gamma}_{\mathrm{reco}}| < \eta_{k,2}, E^{\mathrm{iso}}_{\mathrm{T,reco}} < 3 \text{ GeV}, \text{tight-ID})/dE^{\gamma}_{\mathrm{T,reco}}} \tag{6.5}$$

The efficiency is estimated with a bootstrapping method, where a low-threshold trigger with high efficiency is used as a reference for the nominal trigger. In this case the efficiency of a L1-calorimeter trigger with a nominal threshold of 3.5 GeVis computed relative to a prescaled sample of minimum bias triggers. The measured efficiency of the low-threshold trigger is 100% for photon candidates with reconstructed E_{T} above 15 GeV passing tight identification criteria. The effiicency of `g10_loose` is then measured with respect to the low-threshold trigger. The extracted efficiencies are shown in Fig. 6.6. The trigger efficiency is roughly 99.5% over the full range of E^{γ}_{T} considered in this analysis.

6.4 Systematic Uncertainties

There are several sources of potential bias in the efficiency measurements, many of which are common to both the reconstruction and identification efficiencies. Wherever possible, the systematic uncertainties are evaluated for both efficiencies simultaneously, to take any correlations into account.

6.4.1 MC Sample Composition

The Monte Carlo samples used for the extraction of the nominal efficiencies were generated with `PYTHIA`, which makes some assumptions concerning the amount of soft activity in the event, as well as making assumptions about the fractions of direct and fragmentation photons. To test these generator effects, a `HERWIG` photon+jet sample is used to evaluate the reco+ID

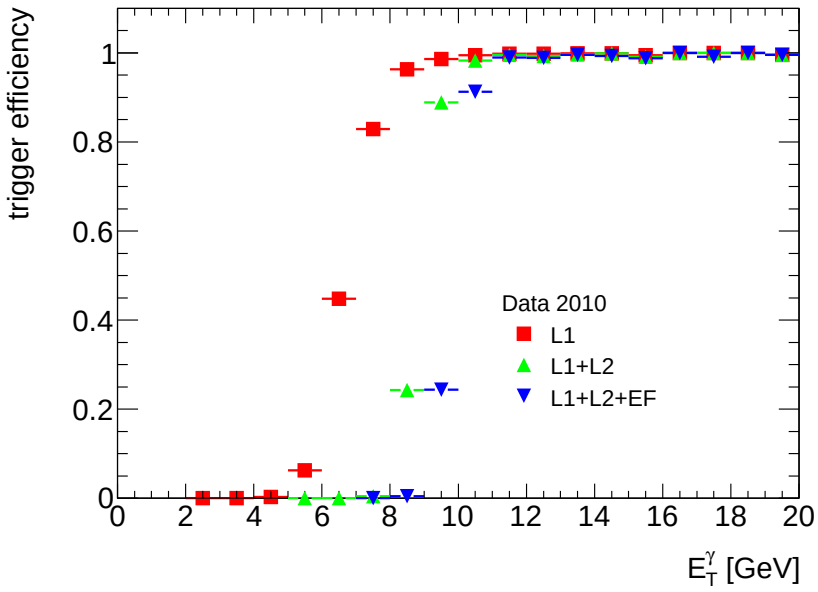

Figure 6.6: Photon trigger efficiency with respect to the offline photon selection as measured in data for the three levels of the g10_loose trigger chain, on photon candidates passing the tight identification criteria and with isolation energy lower than 3 GeV.

efficiencies. In both the PYTHIA and HERWIG samples, the direct and fragmentation components are varied from 20% to 80%, and the efficiencies re-evaluated. The case where the sample is divided equally between direct and fragmentation photons is taken for the central value; the variations around that value for both PYTHIA and HERWIG are within 1.5%. The difference between PYTHIA and HERWIG adds an additional 1% to the systematic uncertainty.

6.4.2 EM Calorimeter Effects

6.4.2.1 EM Scale

The uncertainty on the EM calorimeter energy scale used for this measurement is 3%.[65] The energies of the photon candidates, as well as any discriminating variables sensitive to changes in the scale (like R_{had}), are re-calculated and used to extract the final efficiencies after varying the scale by 3% above and below the nominal value. The effect on the final efficiency is at the

0.1% level. (The EM scale has a much larger effect in the unfolding of the final E_{T} spectrum, discussed in Section 8.2.)

6.4.2.2 Gain Corruption

Some fraction of events in collision data suffer from a problem with the data recorded by the LAr RODs from the front end electronics. The LAr RODs can, under certain conditions, over-write the front-end data near the end of a data buffer, causing the recorded energy to be a factor of ten different from what was actually seen at the front-end. This can either reduce the energy of a very energetic cluster, or increase the energy of a soft cluster, in a more-or-less random way. The effect on the efficiency is estimated with a dedicated MC sample that simulates this corruption. The total effect is calculated for each E_{T} bin separately in the barrel and endcap regions, and ranges from 0.2% to 3.1%.[35]

6.4.2.3 Acceptance Losses

Most of the acceptance losses are due to dead front-end transmitters in the EM calorimeter. The effect of these losses is estimated by using a map of the dead cells to veto candidates in both data and simulation that overlap with the dead regions. The difference in the total acceptance loss seen between data and MC is 0.7%, and is taken as a systematic uncertainty.

6.4.3 Inner Tracker Material Effects

One of the largest sources of uncertainty is on the amount of material in the inner tracker, which will affect the rate of photon conversions, and which will further affect the energy loss of photons that do convert. The impact of the upstream material on the efficiency is evaluated with dedicated samples of photon+jet events that use modified descriptions of the inner tracker

[35] This problem has since been corrected, and does not affect the data collected in 2011.

	$\Delta\varepsilon$ [%]					
	Reco+PID		Reco		PID	
E_{T}[GeV]	Barrel	Endcap	Barrel	Endcap	Barrel	Endcap
unconverted γ						
$[15, 20)$	$4.1 \pm .6$	$3.9 \pm .9$	$1.4 \pm .4$	$2 \pm .7$	$3.6 \pm .6$	$2.7 \pm .8$
$[20, 25)$	$3.6 \pm .2$	$2.6 \pm .3$	$0.1 \pm .1$	$0.6 \pm .2$	$3.6 \pm .2$	$2.2 \pm .3$
$[25, 30)$	$2.7 \pm .3$	$1.5 \pm .4$	$0.0 \pm .1$	$0.6 \pm .3$	$2.8 \pm .3$	$1.1 \pm .4$
$[30, 35)$	$2 \pm .3$	$1.2 \pm .6$	$0.0 \pm .1$	$0.1 \pm .4$	$2.0 \pm .3$	$1.4 \pm .5$
$[35, 40)$	$1.7 \pm .4$	$0.0 \pm .8$	$0.0 \pm .2$	$0.5 \pm .6$	$1.8 \pm .4$	$0.5 \pm .6$
$[40, 50)$	$1.3 \pm .4$	$0.6 \pm .8$	$0.4 \pm .2$	$1.0 \pm .6$	$1.0 \pm .4$	$1.6 \pm .6$
$[50, 60)$	$0.3 \pm .6$	2 ± 1	$0.1 \pm .3$	$2 \pm .1$	$0.4 \pm .5$	$0.9 \pm .9$
$[60, 100)$	$0.6 \pm .6$	$0 \pm .1$	$0.2 \pm .3$	$1 \pm .1$	$0.4 \pm .5$	$1.1 \pm .9$
converted γ						
$[15, 20)$	$7.7 \pm .9$	$7.6 \pm .9$	$6.2 \pm .9$	$3.2 \pm .9$	8 ± 1	$9 \pm .1$
$[20, 25)$	$5.4 \pm .3$	$8.1 \pm .3$	$0.8 \pm .3$	$1.4 \pm .3$	$6.1 \pm .4$	$8.9 \pm .3$
$[25, 30)$	$4.7 \pm .5$	$6.9 \pm .4$	$1.1 \pm .4$	$0.9 \pm .4$	$4.8 \pm .4$	$7.6 \pm .4$
$[30, 35)$	$4.0 \pm .6$	$6.0 \pm .6$	$0.5 \pm .5$	$0.8 \pm .5$	$4.3 \pm .5$	$6.5 \pm .5$
$[35, 40)$	$4.3 \pm .8$	$5.5 \pm .8$	$1.9 \pm .7$	$1.1 \pm .7$	$3.2 \pm .6$	$5.6 \pm .7$
$[40, 50)$	$3.6 \pm .8$	$5.3 \pm .8$	$1.5 \pm .7$	$1.8 \pm .7$	$2.7 \pm .6$	$4.7 \pm .6$
$[50, 60)$	1 ± 1	4 ± 1	1 ± 1	2 ± 1	$0.6 \pm .7$	$3.2 \pm .9$
$[60, 100)$	3 ± 1	5 ± 1	2 ± 1	3 ± 1	$1.6 \pm .7$	$2.5 \pm .8$
all γ						
$[15, 20)$	$5.8 \pm .5$	$7.5 \pm .7$	$3.6 \pm .4$	$4.0 \pm .6$	$4.4 \pm .6$	$6.3 \pm .7$
$[20, 25)$	$4.6 \pm .2$	$6.8 \pm .2$	$0.7 \pm .1$	$1.8 \pm .2$	$4.4 \pm .2$	$6.4 \pm .2$
$[25, 30)$	$3.7 \pm .2$	$5.6 \pm .3$	$0.7 \pm .1$	$1.5 \pm .3$	$3.4 \pm .2$	$5.0 \pm .3$
$[30, 35)$	$3.0 \pm .3$	$4.8 \pm .4$	$0.6 \pm .2$	$1.1 \pm .4$	$2.7 \pm .3$	$4.5 \pm .4$
$[35, 40)$	$2.9 \pm .4$	$4 \pm .6$	$1.0 \pm .3$	$1.2 \pm .5$	$2.2 \pm .3$	$3.5 \pm .5$
$[40, 50)$	$2.3 \pm .4$	$4.1 \pm .6$	$1.0 \pm .3$	$1.3 \pm .5$	$1.5 \pm .3$	$3.4 \pm .5$
$[50, 60)$	$0.34 \pm .5$	$4.1 \pm .9$	$0.5 \pm .4$	$2.4 \pm .8$	$0.17 \pm .4$	$2.2 \pm .7$
$[60, 100)$	$0.8 \pm .6$	$3.3 \pm .9$	$0.8 \pm .4$	$2.8 \pm .8$	$0.13 \pm .4$	$0.9 \pm .6$

Table 6.3: Uncertainties on photon reconstruction ("Reco") and offline identification extracted from a photon+jet sample with an artificially inflated material distribution in the inner tracker.

geometry. In one of these distorted material samples, the inner tracker material is inflated by 5% everywhere; in another, the total material is inflated by 10%, and by up to 20% in specific areas where the material estimates are less certain. The resulting systematic uncertainties for different E_{T} and η regions are shown separately for converted and unconverted photons in Table 6.3, for the simulated sample with the most extreme changes to the detector geometry. The effects are largest at low E_{T}, while at high E_{T} even large changes in the material have less than a 1% effect on the total efficiency.

6.4.4 Conversion Classification

The cuts for unconverted photons are generally tighter than those for converted photons, so the failure of the reconstruction to identify a photon as being a conversion will generally lead to a loss in the identification efficiency. The impact of this is estimated by reducing the efficiency of classifying a photon as a conversion by 10%. This results in a drop in the total efficiency of roughly 1% in the barrel region, and a drop of roughly 2% in the endcap.

6.4.5 Pileup Effects

The Monte Carlo samples used for the bulk of the systematic studies have only a single proton-proton interaction per event. A separate simulated sample of photon+jet events with additional minimum bias events overlaid on top of the primary hard interaction is used to estimate the impact of in-time pileup on the combined efficiency.[36] The MC sample is weighted so that the distribution of the number of reconstructed primary vertices in MC is identical to that in data. The total impact on the efficiency is less than 0.5% in the barrel calorimeter, and 1.2% in the endcap.

6.4.6 Uncertainties on the Shifted-Shower-Shape Method

Finally, the uncertainties related to the method of shifting the shower shapes in MC to better match those in data are evaluated. The procedure is tested with the distorted material samples used to estimate the impact of additional material in the inner tracker. The shower shapes from the nominal MC sample are shifted to match those of the distorted sample (using the same technique described in Section 6.2.1, and the extracted efficiencies are then compared with the true efficiencies for the distorted sample. For unconverted photons, the efficiencies

[36] There is no out-of-time pileup present in the 880 nb^{-1} data sample used in this measurement.

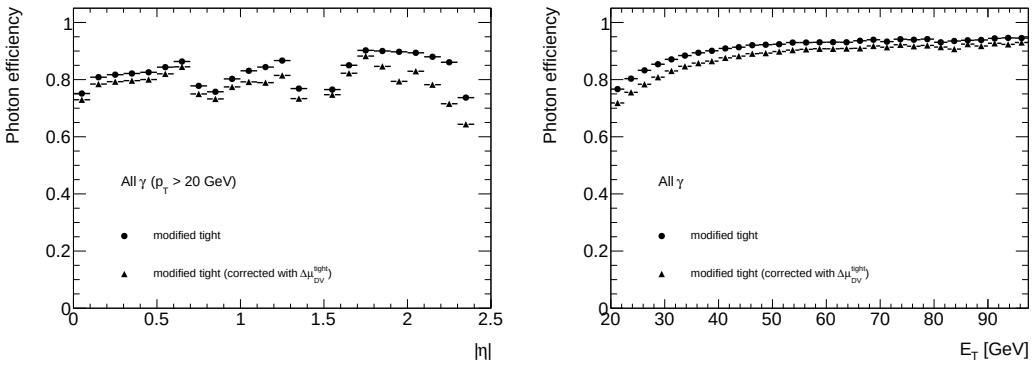

(a) Efficiency vs. η (b) Efficiency vs. E_{T}

Figure 6.7: The corrected photon identification efficiencies, using two different photon subsamples to derive the shower shape shifts between data and MC. The baseline case uses a sample of loose photons, while the modified subsample ("corrected with $\Delta\mu_{\mathrm{DV}}^{\mathrm{tight}}$") uses tight photons. The efficiencies for both types of corrections are shown vs (a) true $|\eta|$ and (b) true E_{T}.

always agree within 3%, while for converted photons, the efficiencies can differ by up to 6% at low E_{T}.

When extracting the data/MC shower-shape shifts, some of the photon identification criteria are applied to reduce the background contamination of the subsamples. Applying the loose criteria will allow more background into the subsample than applying the tight criteria, and the difference in the extracted efficiency due to this choice is an indication of the impact of background contamination on the method. Figure 6.7 shows the differences in the efficiencies for all photons when using the loose and tight criteria to define the photon samples; photons in the outer endcap show the largest uncertainties (further motivating the decision to exclude this region from the final measurement), while the other $|\eta|$ regions have smaller uncertainties. These differences are taken as additional systematic uncertainties on the method.

6.4.7 Final Efficiency Systematics

The final systematic uncertainties are determined from the uncertainties described above, and summarized in Table 6.4. In most cases, the largest contribution to the total uncertainty comes from the distorted material studies, though there are non-negligible uncertainties associated with the shower-shape correction technique itself. In the future, a large sample of electrons from W and Z decays in data will help reduce these uncertainties significantly (or eliminate them altogether).

E_T GeV	$\sigma^{\text{MC corr}}$	$\sigma^{\text{material}}_{\text{Reco+PID}}$	$\sigma^{\text{LAr gain}}_{\text{Reco+PID}}$	$\sigma^{\text{hard/brem}}_{\text{Reco+PID}}$	$\sigma^{\text{Pythia/Herwig}}_{\text{Reco+PID}}$	$\sigma^{\text{pile-up}}_{\text{Reco+PID}}$	σ^{OTx}	$\sigma^{\text{worse conv reco}}$	$\sigma^{\text{total}}_{\varepsilon^{\text{reco}}\varepsilon^{\text{offl}}}$
$\lvert\eta\rvert < 0.6$									
[15, 20)	4.5 %	5.8 %	0.5 %	1.5 %	1.0 %	0.4 %	0.7 %	0.6 %	7.6 %
[20, 25)	3.6 %	4.6 %	0.5 %	1.5 %	1.0 %	0.4 %	0.7 %	1.0 %	6.3 %
[25, 30)	3.5 %	3.7 %	0.5 %	1.5 %	1.0 %	0.4 %	0.7 %	1.1 %	5.6 %
[30, 35)	2.9 %	3.0 %	0.5 %	1.5 %	1.0 %	0.4 %	0.7 %	1.1 %	4.8 %
[35, 40)	2.4 %	2.9 %	0.5 %	1.5 %	1.0 %	0.4 %	0.7 %	1.0 %	4.4 %
[40, 50)	1.9 %	2.3 %	0.5 %	1.5 %	1.0 %	0.4 %	0.7 %	1.2 %	3.8 %
[50, 60)	2.1 %	0.3 %	0.5 %	1.5 %	1.0 %	0.4 %	0.7 %	1.3 %	3.2 %
[60, 100)	1.1 %	0.8 %	0.5 %	1.5 %	1.0 %	0.4 %	0.7 %	1.3 %	2.8 %
$0.6 < \lvert\eta\rvert < 1.37$									
[15, 20)	4.8 %	5.8 %	0.5 %	1.5 %	1.0 %	0.4 %	0.7 %	1.2 %	7.9 %
[20, 25)	4.7 %	4.6 %	0.5 %	1.5 %	1.0 %	0.4 %	0.7 %	1.3 %	7.0 %
[25, 30)	4.0 %	3.7 %	0.5 %	1.5 %	1.0 %	0.4 %	0.7 %	1.2 %	5.9 %
[30, 35)	3.2 %	3.0 %	0.5 %	1.5 %	1.0 %	0.4 %	0.7 %	1.3 %	5.0 %
[35, 40)	3.0 %	2.9 %	0.5 %	1.5 %	1.0 %	0.4 %	0.7 %	1.1 %	4.8 %
[40, 50)	2.5 %	2.3 %	0.5 %	1.5 %	1.0 %	0.4 %	0.7 %	0.9 %	4.1 %
[50, 60)	1.9 %	0.3 %	0.5 %	1.5 %	1.0 %	0.4 %	0.7 %	0.8 %	2.9 %
[60, 100)	1.7 %	0.8 %	0.5 %	1.5 %	1.0 %	0.4 %	0.7 %	0.5 %	2.8 %
$1.52 < \lvert\eta\rvert < 1.81$									
[15, 20)	4.6 %	7.5 %	1.0 %	1.5 %	1.0 %	1.2 %	0.7 %	2.0 %	9.4 %
[20, 25)	4.5 %	6.8 %	1.0 %	1.5 %	1.0 %	1.2 %	0.7 %	1.7 %	8.7 %
[25, 30)	2.7 %	5.6 %	1.0 %	1.5 %	1.0 %	1.2 %	0.7 %	1.6 %	6.9 %
[30, 35)	2.4 %	4.8 %	1.0 %	1.5 %	1.0 %	1.2 %	0.7 %	1.7 %	6.1 %
[35, 40)	2.1 %	4.0 %	1.0 %	1.5 %	1.0 %	1.2 %	0.7 %	1.5 %	5.4 %
[40, 50)	1.5 %	4.1 %	1.0 %	1.5 %	1.0 %	1.2 %	0.7 %	1.2 %	5.2 %
[50, 60)	0.8 %	4.1 %	1.0 %	1.5 %	1.0 %	1.2 %	0.7 %	1.2 %	5.0 %
[60, 100)	1.3 %	3.3 %	1.0 %	1.5 %	1.0 %	1.2 %	0.7 %	0.1 %	4.3 %

Table 6.4: Contributions to the overall systematic uncertainty on the photon reconstruction and offline identification efficiency used for the inclusive photon cross section measurement, and total systematic uncertain in the different η and E_T bins used in the study.

Chapter 7

Background Estimation

The tight photon selection criteria described in Chapter 5 exploit shower profiles in the EM calorimeter to separate signal from background. The separation, however, is not perfect, and non-prompt photons still form a large part of the candidate sample, especially at low E_{T}^{γ}. An estimate of this residual contamination is an important part of the measurement of the final cross section.

The residual background is estimated using calorimeter isolation measurements. The primary backgrounds, from light meson decays to photon pairs, will have isolation energies that are larger than those of prompt photons. The separation is not good enough to achieve perfect event-by-event discrimination of signal from background, but the shape differences are large enough that a statistical estimation of the background is possible.

The first section of this chapter describes a technique for extracting the isolation profile of background photons from data. The next two sections describe different ways of using the background template, along with some information on the signal shapes taken from data and Monte Carlo samples, to estimate the residual background for tight, isolated prompt photon candidates. The final section discusses other sources of backgrounds, including electrons that fake photons, and non-collision backgrounds.

7.1 Background Models

The prompt photon background is dominated by jets with a leading π^0 that then decays to two photons. The remainder of the QCD background is primarily due to η and ω mesons, which also decay to photon pairs. The discriminating variables that use the calorimeter strips are designed to be sensitive to exactly these types of photon candidates by looking for the presence of two peaks with small separation in η. In addition, these variables are not strongly correlated with the calorimeter isolation variables, which exclude from their sum the cells in the center of the cluster over which most of the strip variables are defined. A model of the isolation distribution for background photons can therefore be extracted by reversing the cuts on one or more of the strip variables.

Four strip variables are used to define the enriched background sample (or the "reverse cuts" sample): $F_{\rm side}$, $w_{s,3}$, ΔE, and $E_{\rm ratio}$. (The fifth strip variable, $w_{s,\rm tot}$, is defined over a larger region in η, and has a non-negligible correlation with $E_{\rm T}^{\rm iso}$.) The reverse cuts sample is composed of all photon candidates that fail any one (or more) of these four cuts, but which satisfy all of the other tight selection criteria. The isolation distribution of the reverse cuts sample, compared with the isolation of true background from Monte Carlo (where the photon candidates are not matched to a true prompt photon) passing the tight criteria, is shown in Figs. 7.1 to 7.4 for all $E_{\rm T}$ and η bins. The reverse-cuts sample in MC has a similar distribution to the true background, confirming the weak correlation between the reverse-cuts criteria and the isolation profile. The isolation profile of the reverse-cuts sample in data does not always agree with either the true or reverse-cuts backgrounds in MC, motivating the need for a data-driven technique.

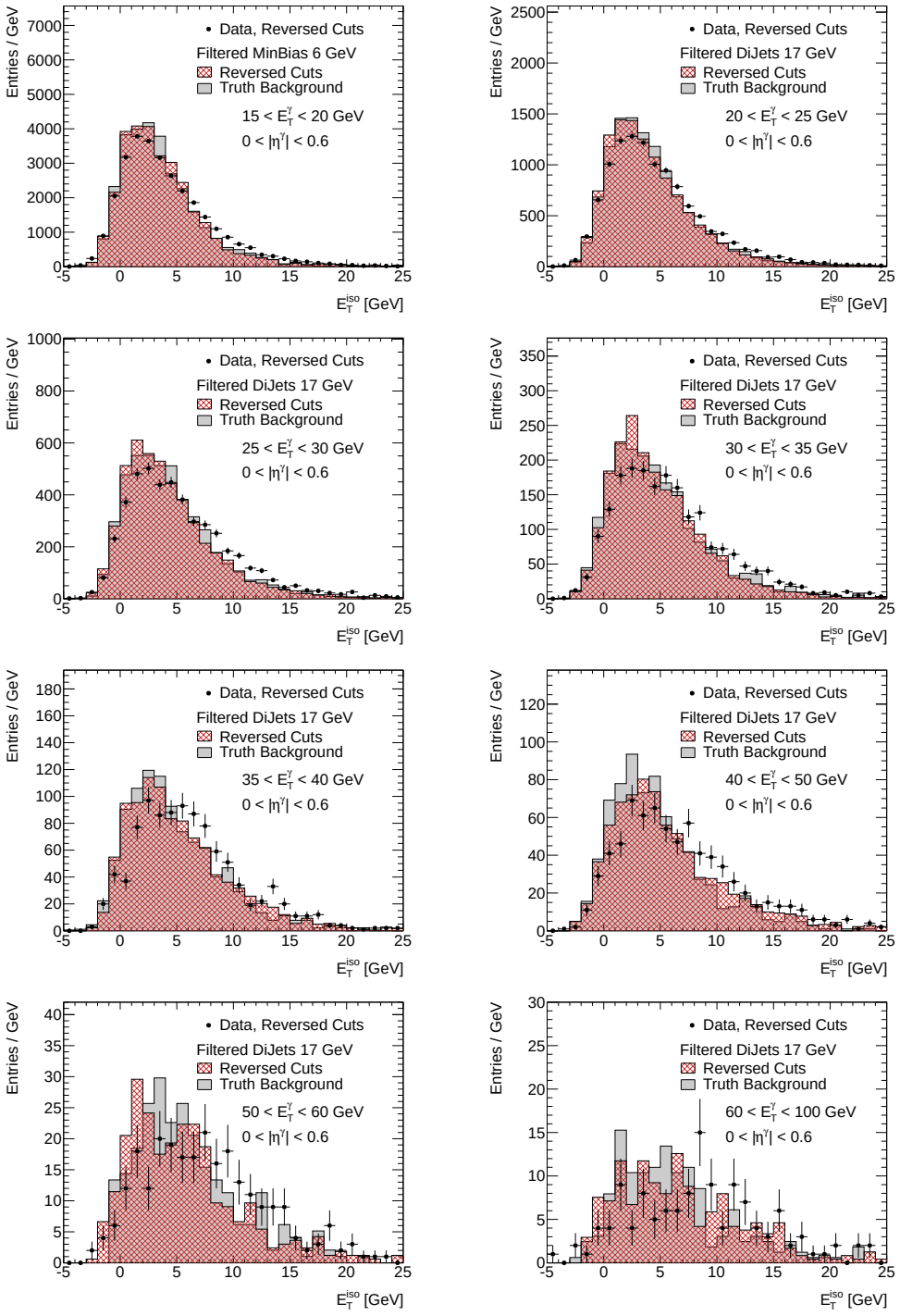

Figure 7.1: Enriched, reverse-cuts background $E_{\mathrm{T}}^{\mathrm{iso}}$ distributions from data and MC, compared with true $E_{\mathrm{T}}^{\mathrm{iso}}$ background distributions from MC, for the pseudorapidity region $0.0 \leq \eta^{\gamma} < 0.6$.

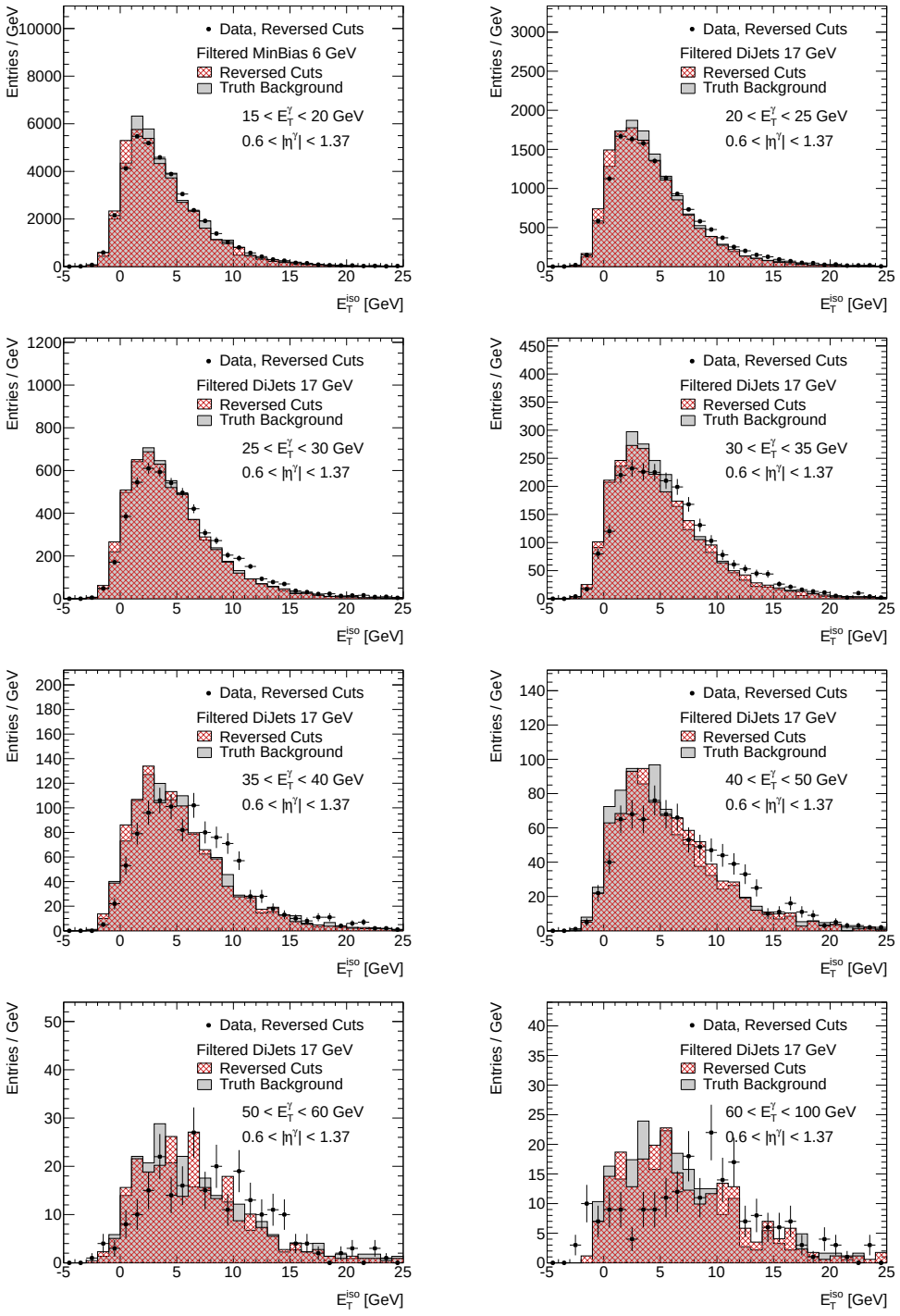

Figure 7.2: Enriched, reverse-cuts background $E_{\mathrm{T}}^{\mathrm{iso}}$ distributions from data and MC, compared with true $E_{\mathrm{T}}^{\mathrm{iso}}$ background distributions from MC, for the pseudorapidity region $0.6 \leq \eta^{\gamma} < 1.37$.

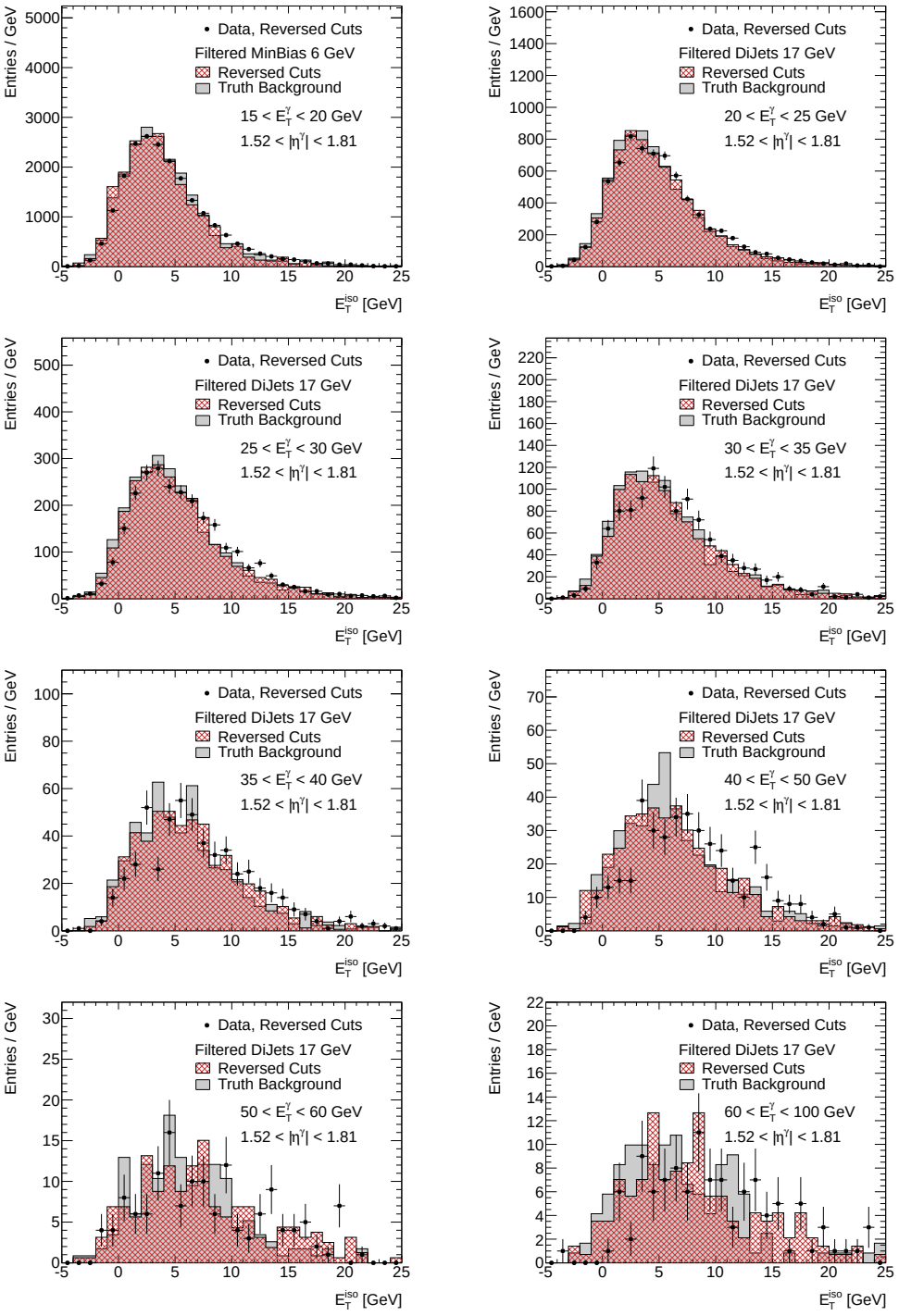

Figure 7.3: Enriched, reverse-cuts background $E_{\mathrm{T}}^{\mathrm{iso}}$ distributions from data and MC, compared with true $E_{\mathrm{T}}^{\mathrm{iso}}$ background distributions from MC, for the pseudorapidity region $1.52 \leq \eta^{\gamma} < 1.81$.

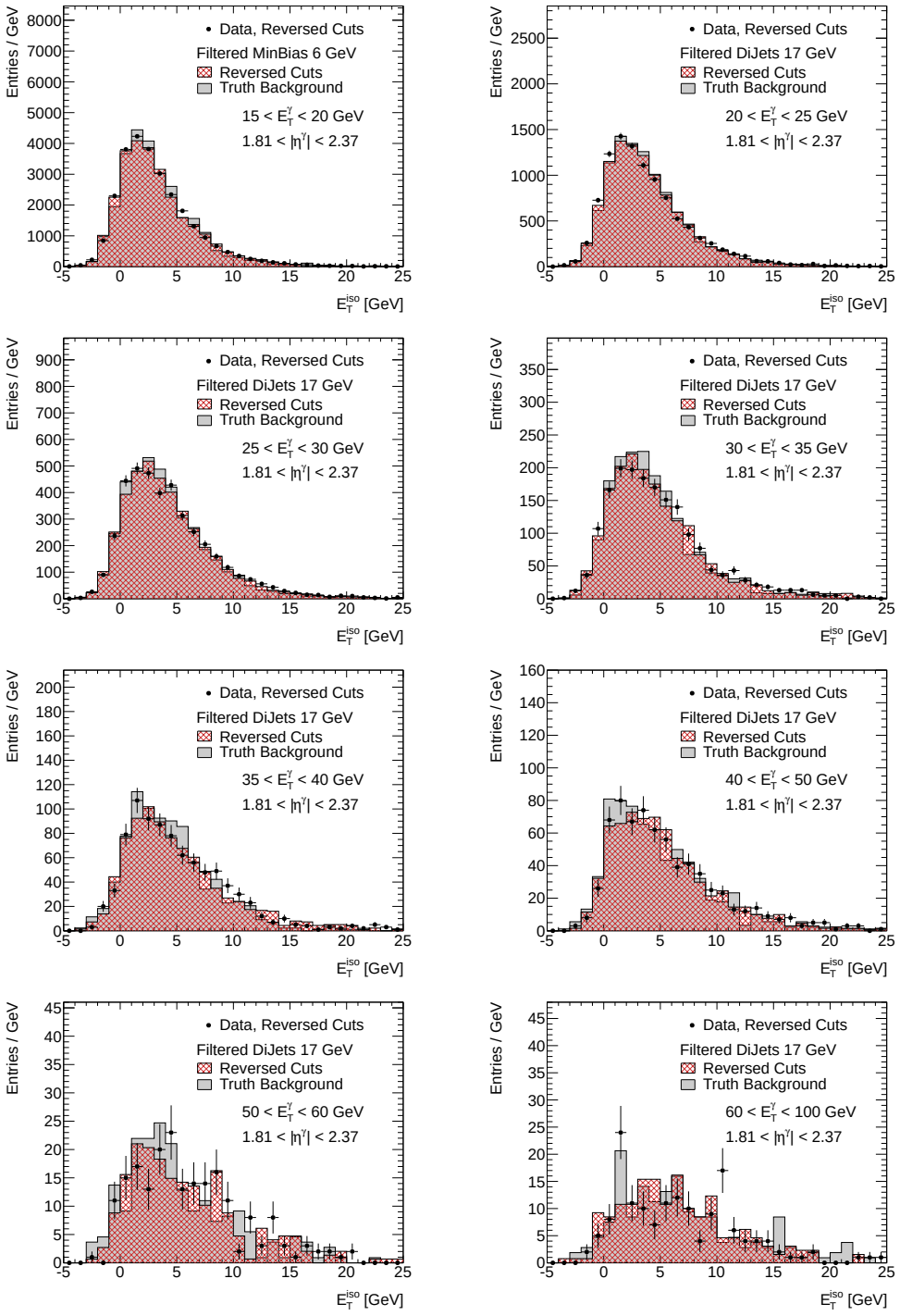

Figure 7.4: Enriched, reverse-cuts background $E_{\mathrm{T}}^{\mathrm{iso}}$ distributions from data and MC, compared with true $E_{\mathrm{T}}^{\mathrm{iso}}$ background distributions from MC, for the pseudorapidity region $1.81 \leq \eta^{\gamma} < 2.37$.

7.2 Isolation Template Fits

In the isolation template fit method, the $E_{\mathrm{T}}^{\mathrm{iso}}$ distribution of photon candidates in data is fit to a sum of signal and background templates. The background templates are taken from the reverse-cuts samples, while the signal templates come from pure electron samples. Both the signal and background templates are extracted from data, to minimize the dependence of the method on the event generator or detector simulation.

7.2.1 Extraction of the Templates

The background templates are taken from the $E_{\mathrm{T}}^{\mathrm{iso}}$ distributions of the reverse-cuts samples defined above. A template is extracted for each (E_{T}, η) bin.

The signal templates are taken from a sample of $W \to e\nu$ and $Z \to ee$ electrons. The W selection requires an event to have $E_{\mathrm{T}}^{\mathrm{miss}} > 25$ GeV, $m_{\mathrm{T}} > 40$ GeV, and an electron with $p_{\mathrm{T}} > 20$ GeV that satisfies the tight electron selection criteria. The Z selection requires two opposite-charge electrons with an invariant mass within 25 GeV of the Z mass, both of which have $p_{\mathrm{T}} > 20$ GeV and satisfy the medium electron selection criteria.

The $E_{\mathrm{T}}^{\mathrm{iso}}$ distribution of well-isolated electrons and photons is designed to be E_{T}-independent (by virtue of the corrections described in Section 5.3.2). The signal templates are therefore not binned in E_{T}, and are only binned in η. This has the advantage of providing well-populated signal templates even in the highest E_{T} bins, where there would normally be relatively few electrons satisfying the W or Z selection criteria.

Electrons from W and Z decays appear to be slightly less well-isolated than prompt photons; a comparison of their isolation distributions in `PYTHIA` is shown in Fig. 7.5. The signal templates are shifted by the observed difference in each η bin.

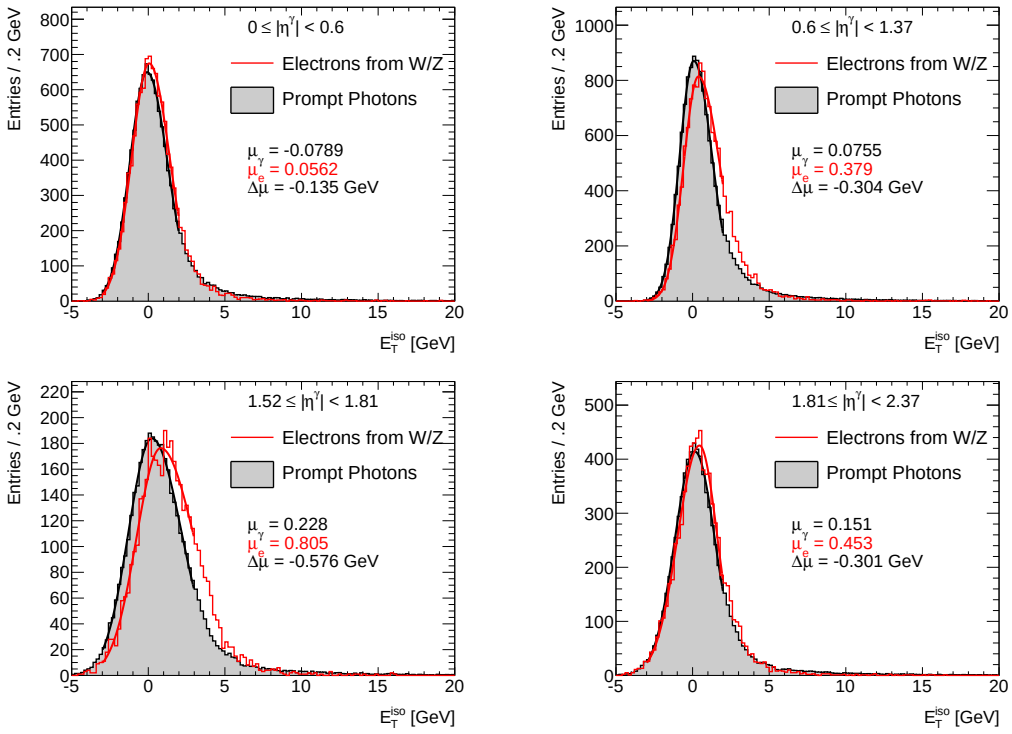

Figure 7.5: A comparison of the $E_{\mathrm{T}}^{\mathrm{iso}}$ distributions of electrons from simulated $W \rightarrow e\nu$ decays with those of prompt photons in `PYTHIA` Monte Carlo. The distributions are fit to an asymmetric Gaussian distribution (a Gaussian function defined by a single mean, with different widths on either side of the mean) in a restricted range around the peak. The difference, $\Delta\mu$, between the electron and photon distributions are used to shift the signal templates derived from electron in data.

7.2.2 Extraction of the Signal Yield

The fit is performed separately for each (E_{T}, η) bin as a binned extended maximum likelihood fit [66] with the `RooFit` [67] package. The data are fit to a sum of the signal and background templates, producing an estimated signal yield and purity for the region $E_{\mathrm{T}}^{\mathrm{iso}} < 3$ GeV. As a test of the fit procedure, an example of a fit in one bin of E_{T}^{γ} and η^{γ} for a sample of `PYTHIA` dijet events (with a cross-section-weighted mixture of signal and background) is shown in Fig. 7.6. The difference between the estimated and true purities for all bins in the `PYTHIA` dijet sample is shown in Fig. 7.7. The estimated purities are always within 10% of truth.

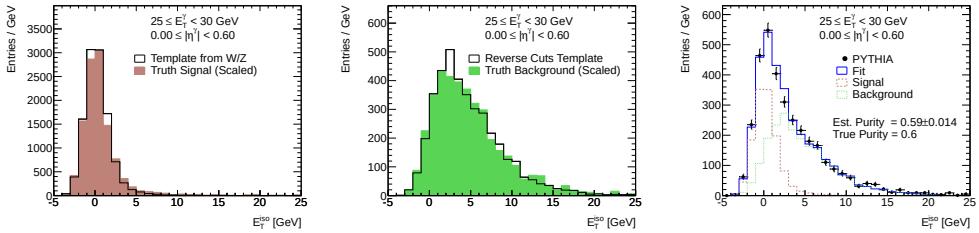

(a) Signal (b) Background (c) Test Data

Figure 7.6: A fit for the signal and background components of a test distribution derived from PYTHIA Monte Carlo. The left plot shows the signal template from electrons, along with the $E_{\mathrm{T}}^{\mathrm{iso}}$ distribution of true prompt photons from the test sample (normalized to the integral of the template). The middle plot shows the background template from the reversed-cut sample, along with the $E_{\mathrm{T}}^{\mathrm{iso}}$ distribution of true background photons from the test sample (normalized to the integral of the template). The right plot shows the fit of the test sample to a sum of the signal and background templates.

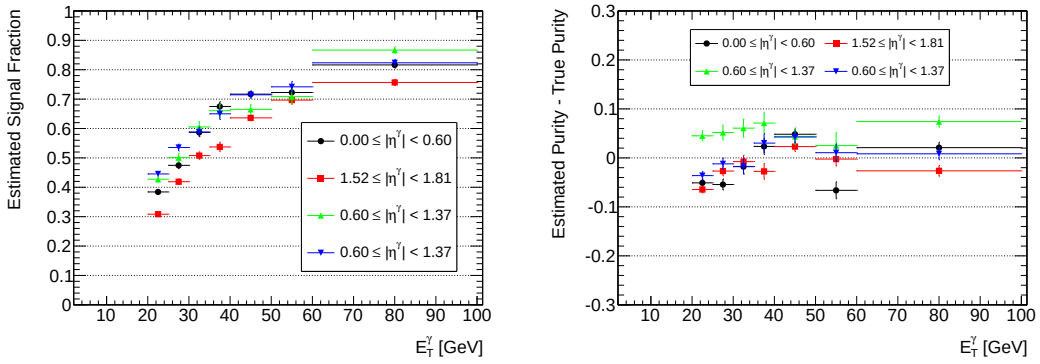

(a) Estimated Purities (b) Comparison with Truth

Figure 7.7: A comparison of the estimated purities with the true purities for a sample of PYTHIA filtered dijet events containing a cross-section weighted mixture of signal and background events.

7.2.3 Systematic Uncertainties

The main sources of systematic uncertainty for this method of extracting the purity and signal yield arise from the definitions of the signal and background templates. Most of the following studies of systematic uncertainties are carried out with Monte Carlo samples. These studies rely on the assumption that, given templates that perfectly describe the true $E_{\mathrm{T}}^{\mathrm{iso}}$ distributions in data, the method will accurately return the true purity. This assumption is found to hold for all E_{T}^{γ} and η^{γ} bins to within 1%.

7.2.3.1 Signal Template

The primary uncertainty associated with the signal template is whether electrons from W and Z decays are truly reasonable proxies for prompt photons. To test this assumption, the signal template used in the fit is replaced with the $E_{\mathrm{T}}^{\mathrm{iso}}$ distribution of true prompt photons in the test sample, which represents the case where the signal template is a perfect model for prompt photons. The differences of the estimated purities from the true purities are always less than 3% (absolute) under these conditions, indicating that variations in the signal template have a small overall impact on the final purity.

7.2.3.2 Background Template

The dominant uncertainty in the templates is in the shape of the background, which is difficult to determine from data. Two checks are done to estimate systematics on the background shape. The first is carried out with simulated samples of signal and background photons. The background template from the reverse-cuts sample is replaced with the $E_{\mathrm{T}}^{\mathrm{iso}}$ distribution of true background candidates in the test sample. A comparison of the resulting purities with the purities in the normal case reveals that almost all of the variation seen in Fig. 7.7 is due to the differences between the derived and the true background $E_{\mathrm{T}}^{\mathrm{iso}}$ distributions. These

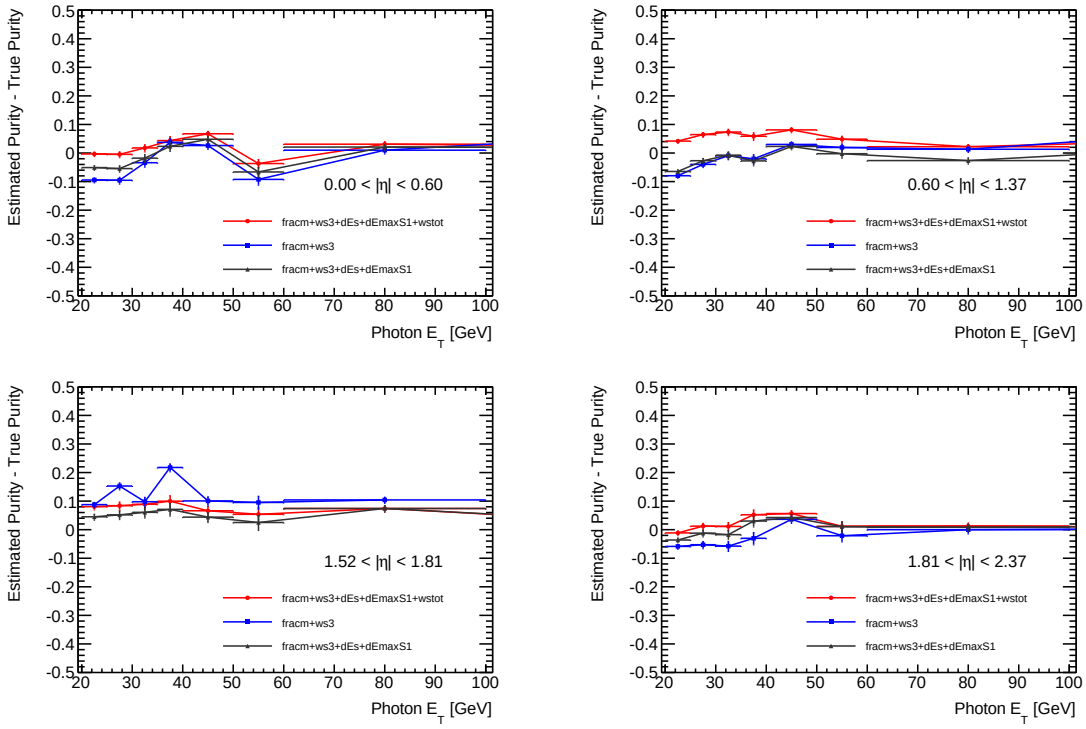

Figure 7.8: The difference between the estimated and true purities for three variations of the reverse-cuts background templates. The nominal case is shown in black triangles, where photon candidates are required to fail one or more of four different cuts. The other cases correspond to reversing more (red circles) or fewer (blue squares) cuts.

differences are taken as systematics.

In the second test, the procedure for constructing the background template is varied when evaluating the purities in data. The construction of the background template relies on a certain choice of photon identification cuts to reverse. Changing this collection of cuts can cause the background template to change shape, resulting in different purities. The difference between the estimated and true purities for three different variations of the reverse-cuts prescription are shown in Fig. 7.8. The largest variation is generally seen at low E_{T}^{γ}, where the total amount of true background is high.

Finally, there is some amount of leakage of signal events into the background templates, as the cuts that are reversed are not 100% efficient for true prompt photons. The impact of

this on the final purity is checked by explicitly removing signal photons from the background templates in Monte Carlo samples, and re-evaluating the purity. Removing signal events from the background templates results in an upward shift of all purities by roughly 2% (absolute); these shifts are used to correct the final purities from data.

7.2.4 Results

The signal and background templates, as well as the fit results, for the photon candidates from collision data are shown in Figs. 7.9 to 7.12, and the estimated purities are shown in Fig. 7.13. The purities in data are generally higher than those seen in MC (ranging from roughly 20% at low E_{T}^{γ} to 5% at high E_{T}^{γ}), for equivalent E_{T}^{γ} and η^{γ} bins.

The final purities estimated with the template fit, including all systematic uncertainties, are shown in Fig. 7.14 for the three pseudorapdity regions considered in the final measurement of the cross section.

7.2.4.1 Background-Only Template Fits

Finally, some systematic studies are carried out with a modified form of the template fit method, in which the background template is fit to the data in the region $E_{\mathrm{T}}^{\mathrm{iso}} > 5$ GeV. The normalized template is then subtracted from the data, and the remainder is considered signal. This technique is similar to the technique discussed in the following section, but uses the shape of the background template to derive data-driven $E_{\mathrm{T}}^{\mathrm{iso}}$ distributions for signal photons. The extracted signal $E_{\mathrm{T}}^{\mathrm{iso}}$ distributions are shown together with the distributions from electrons in Figs. 7.15 to 7.18. As the distributions are derived completely separately, the good agreement is an argument for the use of the electron distributions as a model for the prompt photon signal in the template fits.

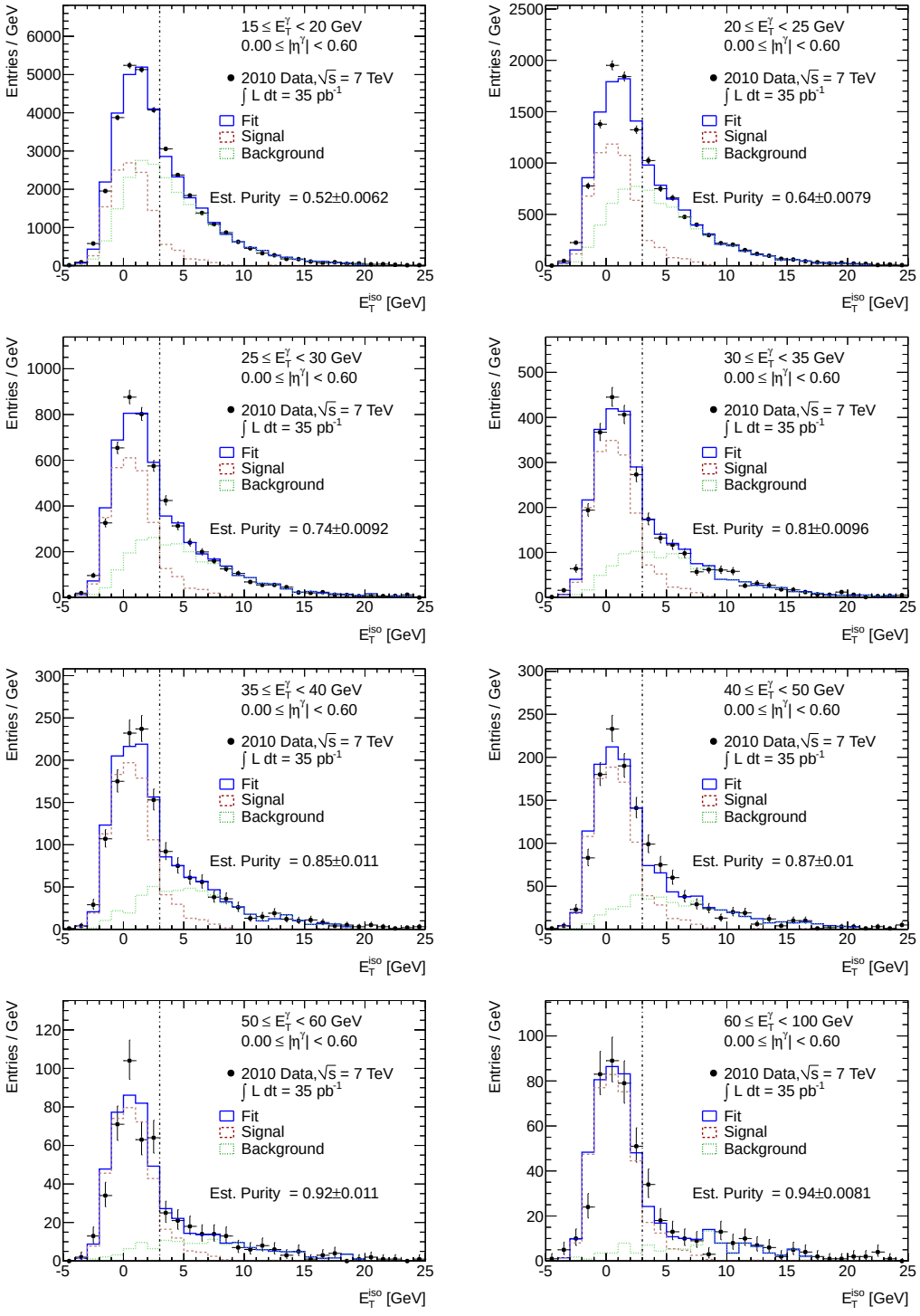

Figure 7.9: Template fits for $0.00 \leq |\eta^{\gamma}| < 0.60$.

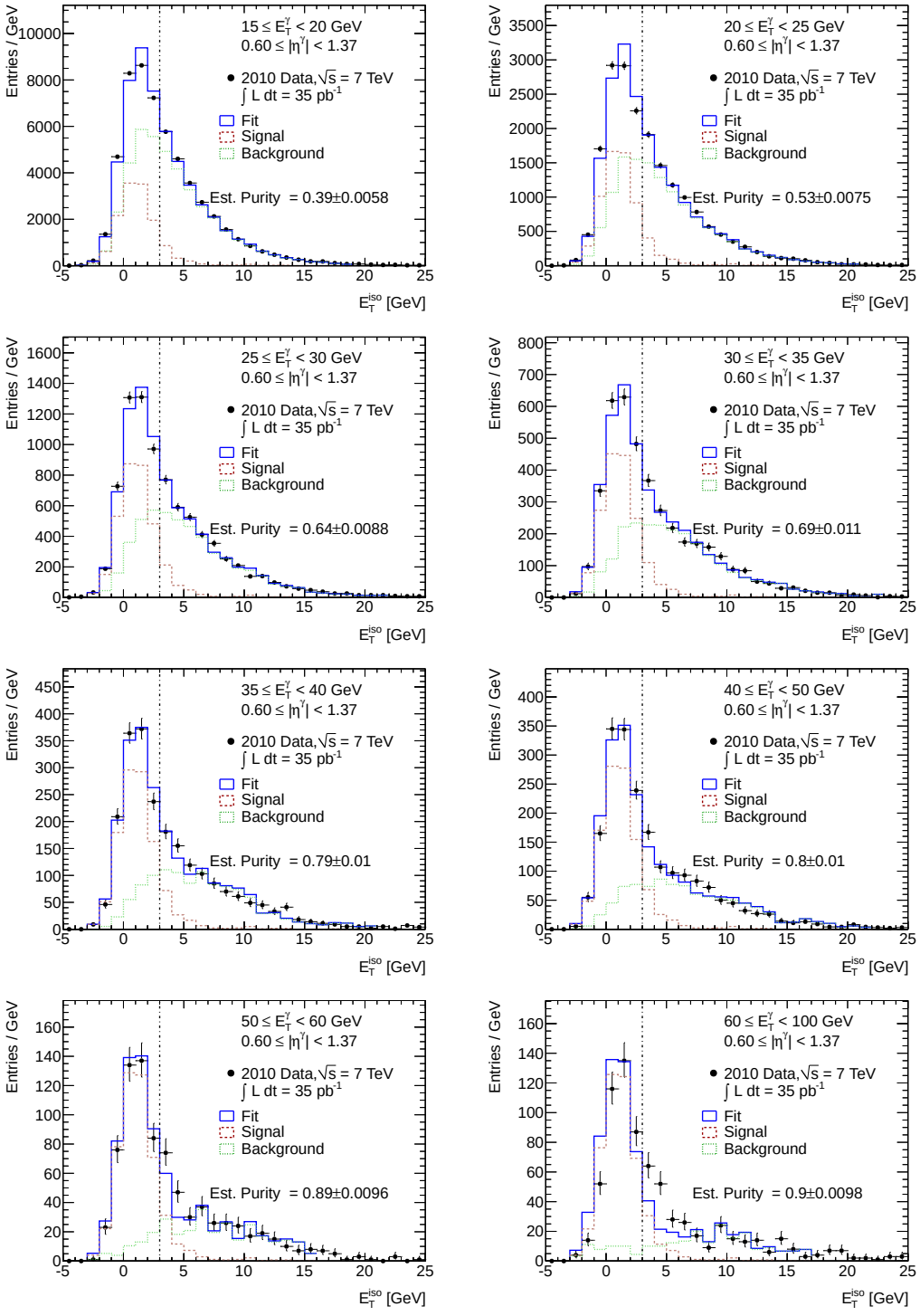

Figure 7.10: Template fits for $0.60 \leq |\eta^{\gamma}| < 1.37$.

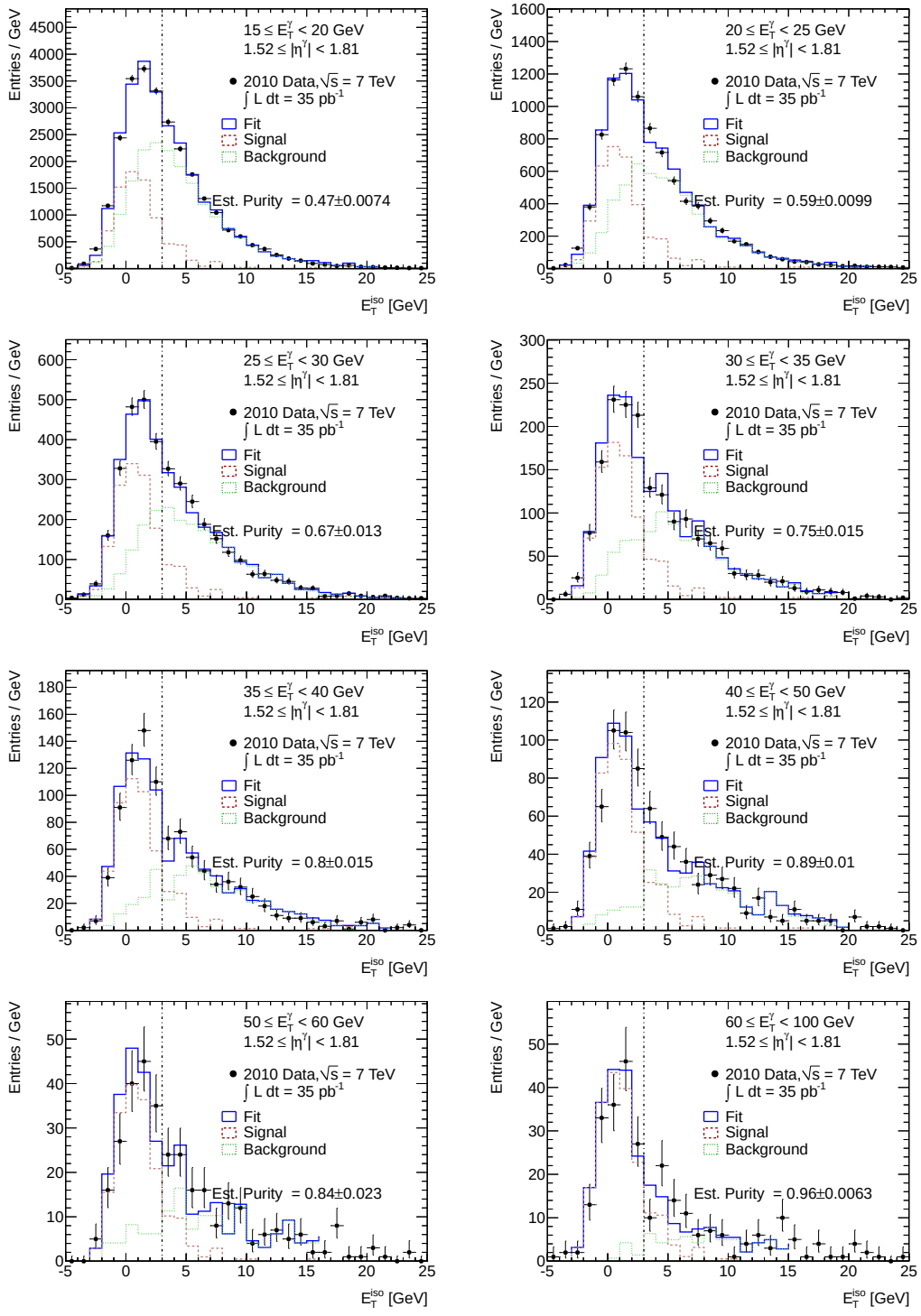

Figure 7.11: Template fits for $1.52 \leq |\eta^{\gamma}| < 1.81$.

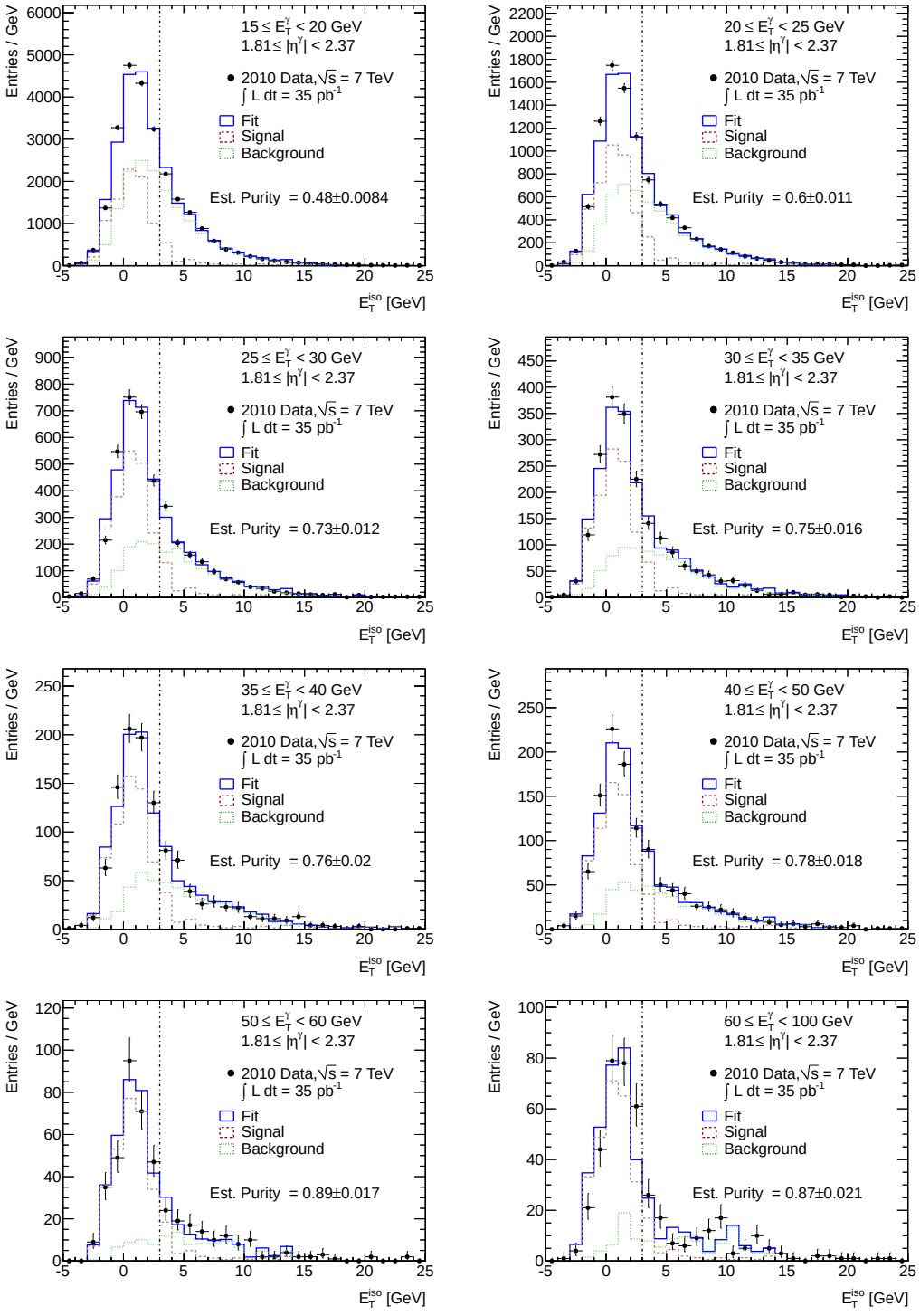

Figure 7.12: Template fits for $1.81 \leq |\eta^{\gamma}| < 2.37$.

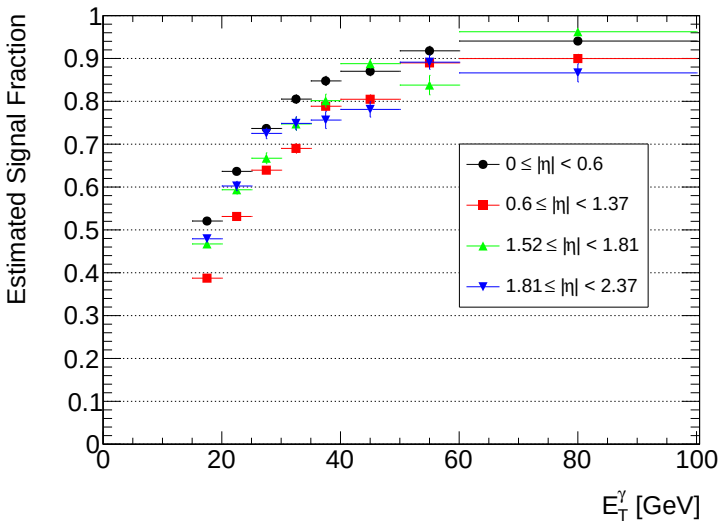

Figure 7.13: The estimated purity of photon candidates from collision data in bins of E_{T}^{γ} for each of the four pseudorapdity regions under study. The uncertainties are statistical only.

7.3 Sideband Approach

As an alternative to a full template fit, a two-dimensional sideband technique can also be used to estimate the amount of background in the signal sample. The purity is estimated by extrapolating from control regions, which are composed primarily of background, into the signal region, where the fractions of signal and background are unknown. A two-dimensional plane is constructed, with the isolation energy on the x-axis, and the tightness of the photon on the y-axis. The isolation axis is continuous, while the tightness axis has two bins, one for photons that pass all of the tight criteria, and another for photons that satisfy the reverse-cuts criteria described in Section 7.1. This technique benefits from fewer assumptions about the shape of the signal distribution, and may also be useful in regions where the statistics are not sufficient for a full template fit.

A pictorial representation of the technique is shown in Fig. 7.19. The method defines four regions:

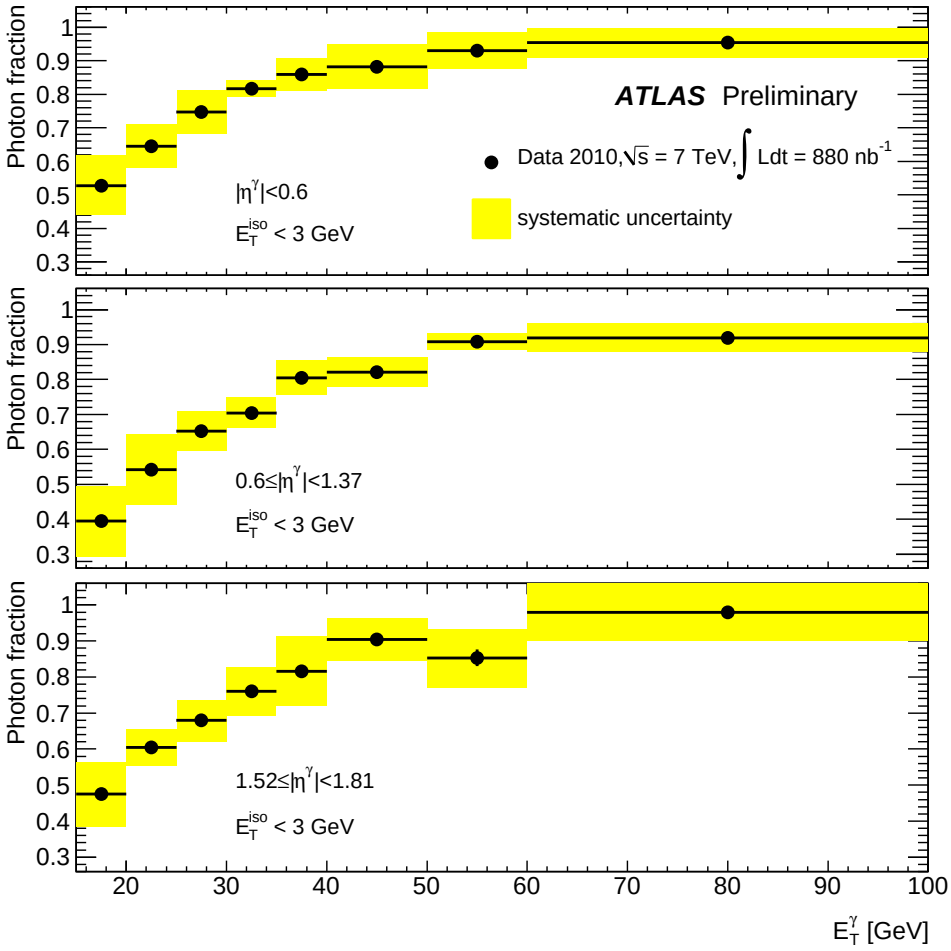

Figure 7.14: Fraction of isolated prompt photons as a function of the photon transverse energy, as obtained with the template fit method.

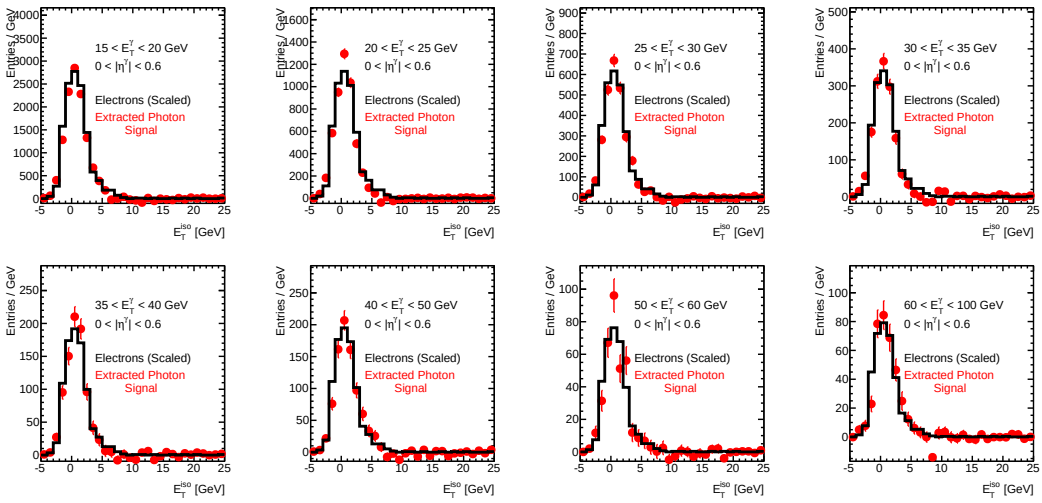

Figure 7.15: The $E_{\mathrm{T}}^{\mathrm{iso}}$ distributions for background-subtracted photons, compared with the signal templates used in the template fits, for the region $0 \leq |\eta^{\gamma}| < 0.6$.

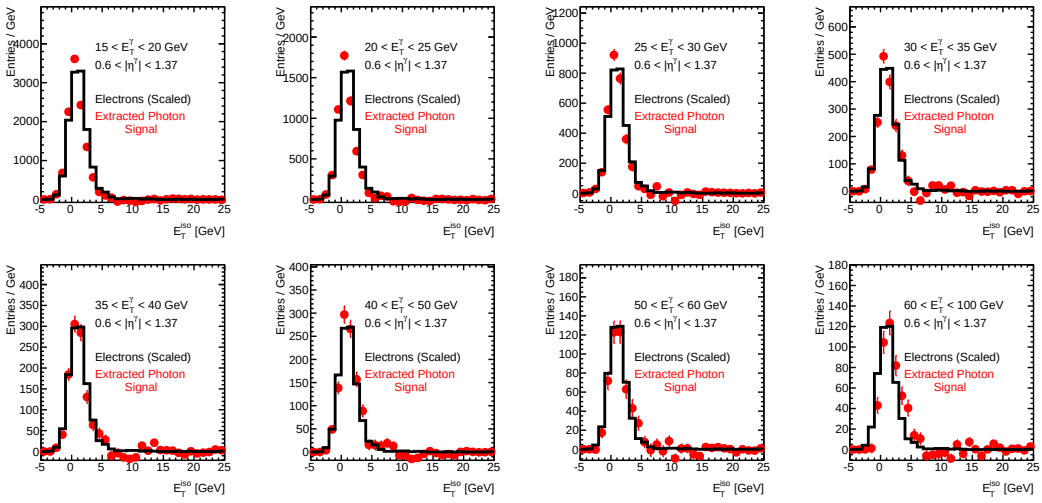

Figure 7.16: The $E_{\mathrm{T}}^{\mathrm{iso}}$ distributions for background-subtracted photons, compared with the signal templates used in the template fits, for the region $0.6 \leq |\eta^{\gamma}| < 1.37$.

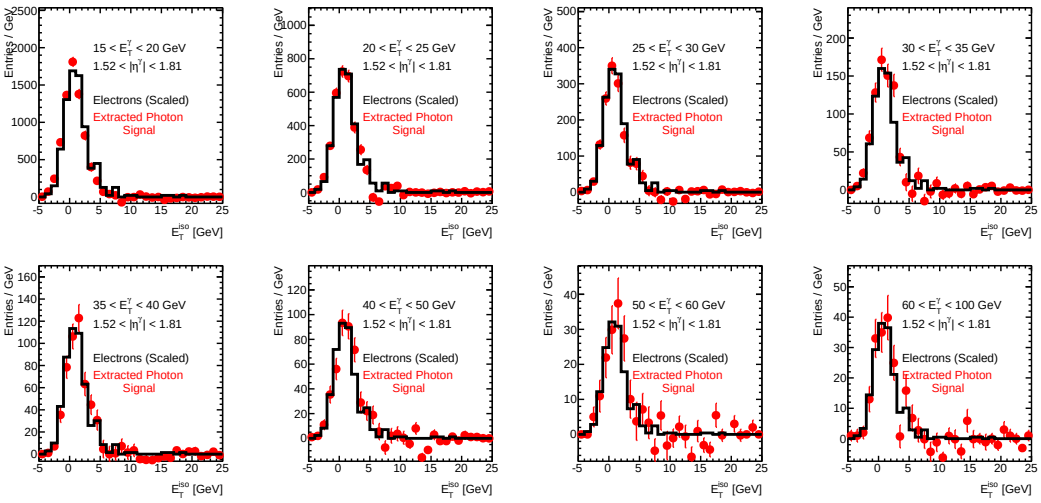

Figure 7.17: The $E_{\mathrm{T}}^{\mathrm{iso}}$ distributions for background-subtracted photons, compared with the signal templates used in the template fits, for the region $1.52 \leq |\eta^{\gamma}| < 1.81$.

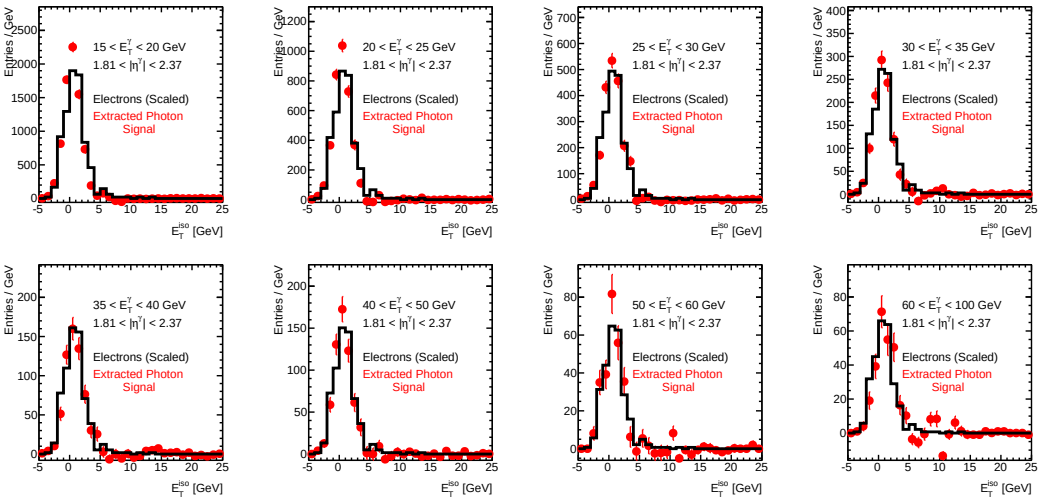

Figure 7.18: The $E_{\mathrm{T}}^{\mathrm{iso}}$ distributions for background-subtracted photons, compared with the signal templates used in the template fits, for the region $1.81 \leq |\eta^{\gamma}| < 2.37$.

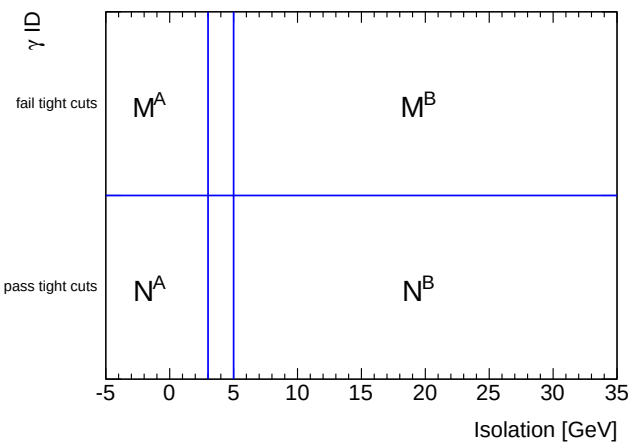

Figure 7.19: The two-dimensional sideband technique used to estimate the background contamination of the prompt photon signal sample. Region A contains the majority of signal candidates, while regions B, C, and D are dominated by background. The number of background events in region A is determined by counting the number of events in regions B, C, and D, and extrapolating into the signal-like region.

- **Region** A: photon candidates pass the tight identification criteria, and have $E_{\mathrm{T}}^{\mathrm{iso}} < 3$ GeV.
- **Region** B: photon candidates pass the tight identification criteria, and have $E_{\mathrm{T}}^{\mathrm{iso}} > 5$ GeV.
- **Region** C: photon candidates pass the reverse-cuts identification criteria, and have $E_{\mathrm{T}}^{\mathrm{iso}} < 3$ GeV.
- **Region** D: photon candidates pass the reverse-cuts identification criteria, and have $E_{\mathrm{T}}^{\mathrm{iso}} > 5$ GeV.

Region A is the signal-like region, in which the method will estimate the background, while regions B, C, and D are the control regions. Two assumptions are made about the contents of these regions. First, the control regions are assumed to be composed almost entirely of background, and have very little (if any) signal present; *i.e.* $N_X = N_X^{BG}$, where N_X is the

number of events in region X, and N_X^{BG} is the number of background events in region X, for $X \in \{B, C, D\}$. Second, the variables used to define the axes are assumed to be uncorrelated, so that $N_A^{BG}/N_B^{BG} = N_C^{BG}/N_D^{BG}$. If these assumptions hold, then the number of background events in region A can be extracted simply by counting the candidates in each of the three control regions:

$$N_A^{BG} = \frac{N_B^{BG} N_C^{BG}}{N_D^{BG}} = \frac{N_B N_C}{N_D} \tag{7.1}$$

The number of signal events in region A, N_A^{Sig}, is then simply $N_A - N_A^{BG}$.

7.3.1 Accounting for Correlations

The assumptions made in the previous section are valid enough to justify the use of this method, but they leave room for bias in cases where they are not perfectly satisfied. In particular, is is certainly the case that some fraction of prompt photons will leak into the control regions. The amount of leakage is estimated using prompt photon Monte Carlo samples, and quantified in three coefficients, c_B, c_C, and c_D, where $c_X = N_X^{Sig}/N_A^{Sig}$. Using these fractions to correct for the signal leakage, Eq. (7.1) then becomes:

$$N_A^{Sig} = N_A - N_A^{BG} = N_A - \frac{\left(N_B - c_B N_A^{Sig}\right)\left(N_C - c_C N_A^{Sig}\right)}{N_D - c_D N_A^{Sig}} \tag{7.2}$$

This can then be solved as a quadratic equation for N_A^{Sig}.

The second assumption, that there is no correlation between the variables used to define the x and y axes, is also evaluated using Monte Carlo. The residual correlation is summarized by one parameter, $R_{MC} \equiv (N_A^{BG} N_D^{BG})/(N_B^{BG} N_C^{BG})$. In cases where $R_{MC} < 1$, the non-tight regions have an isolation profile that is more signal-like than the true background, and N_A^{BG} will be overestimated by a factor of $1/R_{MC}$. The final equation for the signal yield is then:

$$N_A^{Sig} = N_A - R_{MC} N_A^{BG} = N_A - R_{MC} \frac{\left(N_B - c_B N_A^{Sig}\right)\left(N_C - c_C N_A^{Sig}\right)}{N_D - c_D N_A^{Sig}} \tag{7.3}$$

7.3.2 Extraction of the Signal Yield

The signal yield is extracted using Eq. (7.3) in each (E_{T}, η) bin. The c_X coefficients are extracted separately for each bin from PYTHIA Monte Carlo; their values are listed in Table 7.1. R_{MC} is assumed to be 1.0, and is varied to derive systematic uncertainties rather than to correct the central value of the signal yield.

E_{T} range	$\eta \in [0.00; 0.60)$			$\eta \in [0.60; 1.37)$			$\eta \in (1.52; 1.81)$			$\eta \in [1.81; 2.37)$		
[GeV]	$c_{\mathbf{B}}$	$c_{\mathbf{C}}$	$c_{\mathbf{D}}$	$c_{\mathbf{B}}$	$c_{\mathbf{C}}$	$c_{\mathbf{D}}$	$c_{\mathbf{B}}$	$c_{\mathbf{C}}$	$c_{\mathbf{D}}$	$c_{\mathbf{B}}$	$c_{\mathbf{C}}$	$c_{\mathbf{D}}$
$[15; 20)$	0.03	0.12	0.00	0.03	0.14	0.00	0.04	0.07	0.01	0.03	0.14	0.01
$[20; 25)$	0.04	0.08	0.00	0.05	0.09	0.01	0.06	0.06	0.01	0.04	0.10	0.01
$[25; 30)$	0.05	0.06	0.00	0.05	0.06	0.01	0.08	0.05	0.01	0.05	0.08	0.01
$[30; 35)$	0.06	0.04	0.00	0.06	0.05	0.01	0.08	0.04	0.01	0.07	0.07	0.01
$[35; 40)$	0.07	0.04	0.01	0.08	0.04	0.01	0.10	0.04	0.01	0.07	0.06	0.01
$[40; 50)$	0.08	0.03	0.00	0.10	0.03	0.01	0.11	0.03	0.02	0.08	0.05	0.01
$[50; 60)$	0.10	0.03	0.01	0.12	0.03	0.01	0.17	0.05	0.01	0.11	0.05	0.01
$[60; 100)$	0.14	0.02	0.01	0.14	0.03	0.01	0.17	0.03	0.05	0.14	0.04	0.02

Table 7.1: Fractions of signal leaking into the three control regions, as predicted by PYTHIA, for all η and E_{T} regions.

7.3.3 Systematic Uncertainties

There are several sources of potential systematic bias in this technique.

- **Definition of the non-tight control regions:** The non-tight control regions are defined by selecting photon candidates which fail at least one of the cuts on four strip variables: F_{side}, $w_{s,3}$, ΔE, and E_{ratio}. Changing the set of cuts to be reversed causes the shape of the isolation distribution in the non-tight regions to change, so it's possible that the choice of these four cuts is causing some amount of bias. To check the effect on the signal yield, the four-cut case is compared to a two-cut case (only reversing F_{side}

and $w_{s,3}$, which use the smallest number of strips) and a five-cut case (adding $w_{s,\mathrm{tot}}$ to the normal four cuts). The signed maximum deviation from the four-cut case is taken as the uncertainty.

- **Definition of the non-isolated control regions:** The choice of 5 GeV as the starting point for the non-isolated control region is motivated by the desire to reduce the signal leakage into the non-isolated region while still providing enough events in the non-isolated region to make a statistically meaningful purity estimate. The minimum value of $E_{\mathrm{T}}^{\mathrm{iso}}$ for the non-isolated region is varied from 4 to 6 GeV, and the maximum value of $E_{\mathrm{T}}^{\mathrm{iso}}$(normally infinite) is allowed to vary down to 10 GeV.

- **Definition of the signal leakage coefficients:** The estimate of the signal leakage into the non-tight regions is taken from MC. However, it was shown in Chapter 6 that the MC does not necessarily reproduce the efficiency of the data by default. The efficiency used to extract c_C is therefore varied by 5% to estimate this possible bias.

- **Correlation of the non-tight and isolation axes:** The values of R_{MC} taken from `PYTHIA` samples are mostly consistent with 1, but vary from bin-to-bin with large uncertainties. A plot of the R_{MC} values is shown in Fig. 7.20. The signal yield is extracted taking these coefficients into account, and the variation from the nominal case (with R_{MC}=1) is used as a systematic uncertainty.

7.3.4 Results

The purities estimated with the two-dimensional sideband technique are shown in Fig. 7.21 for the three pseudorapidity regions considered in the cross section measurement.

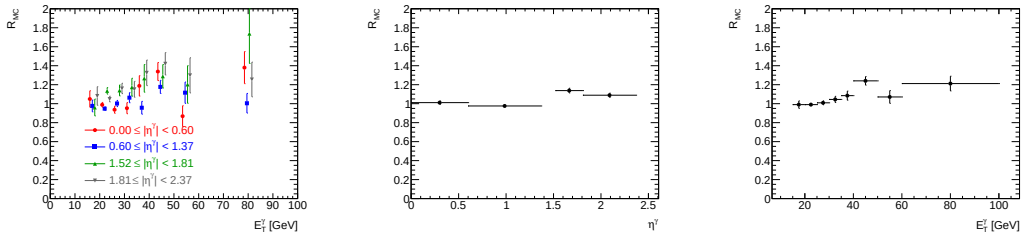

(a) (b) (c)

Figure 7.20: The R_{MC} correlation coefficients extracted from PYTHIA Monte Carlo samples, for different bins of E_{T} and η. The E_{T}^{γ} values in (a) are offset within each bin to allow all values to be seen with their uncertainties.

7.4 Comparison of Template-Fit and Sideband Techniques

The 2-D sideband and template-fit results are compared in Fig. 7.22. The extracted purities are almost entirely within the uncertainties for both methods, with only a few exceptions.

7.5 Electron and Non-Collision Backgrounds

7.5.1 Mis-Identified Electrons

In addition to the high rate of fakes from light mesons within jets, some additional background is due to electrons. When electrons are mis-identified as photons, they are frequently (though not always) reconstructed as converted photons that have a single track, and can be very difficult to distinguish from photons based solely on shower profiles in the EM calorimeter. Electrons which fake tight photons with no isolation requirement are primarily produced by heavy flavor (c and b quark) decays. Generally speaking, the $E_{\mathrm{T}}^{\mathrm{iso}}$ distributions of such candidates are similar to the same distributions for π^0 and other light meson fakes, and are properly handled by the sideband and template-fit methods described above. Electrons that fake tight, isolated photons are typically produced by W, Z, and τ decays, and these require special treatment to remove, as they have $E_{\mathrm{T}}^{\mathrm{iso}}$ distributions that are similar to prompt

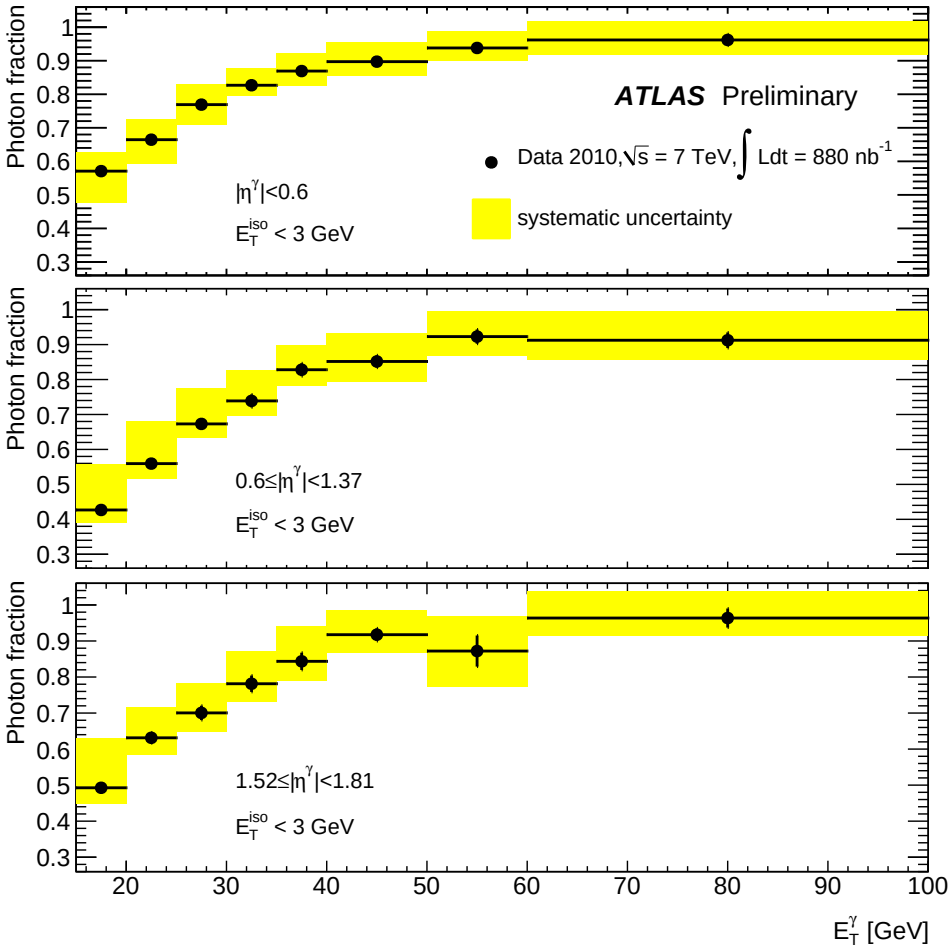

Figure 7.21: Fraction of isolated prompt photons as a function of the photon transverse energy, as obtained with the 2D sideband method.

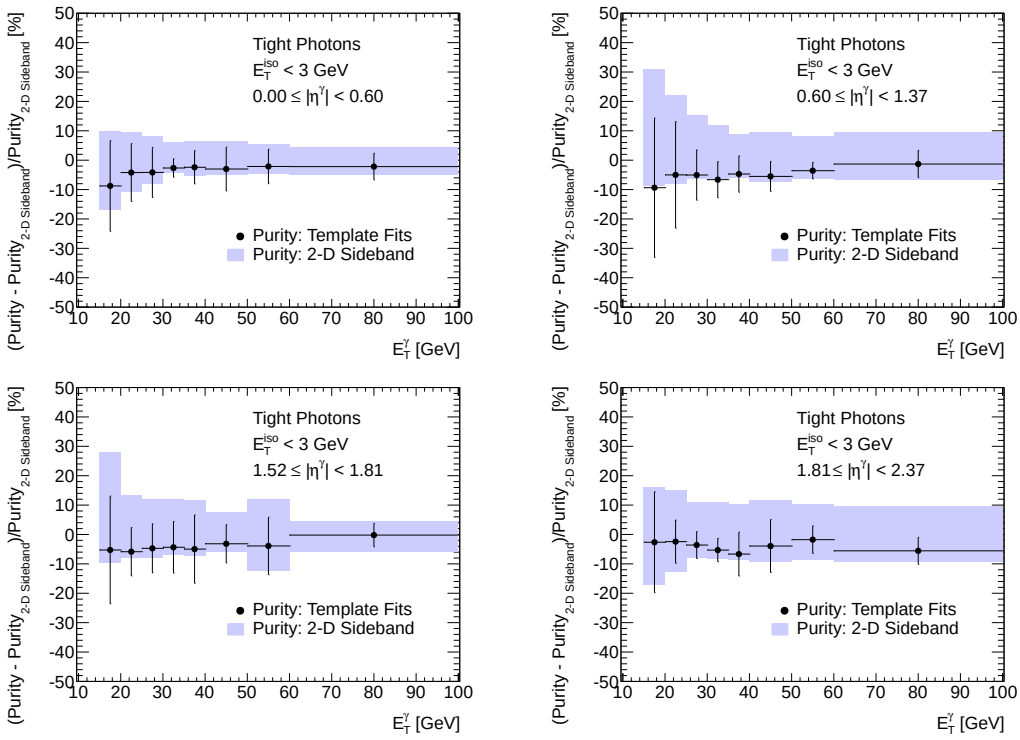

Figure 7.22: Comparison of the purities extracted with the template fit and 2-D sideband methods, as a function of E_{T}^{γ}, for each of the pseudorapidity regions under study. The error bars (blue fill) for the template (2-D sideband) data include both systematic and statistical uncertainties.

photons.

Two methods were used to estimate the contribution from electrons in the prompt photon sample. The first is a Monte Carlo based method, which extracts the fake rate by counting the number of photon candidates that survive the nominal photon selection criteria in a pure sample of electrons. The second is based on data, and uses the number of events that have an electron and a photon with an invariant mass close to the Z mass to estimate the fake rate. The electron misidentification rate, ρ, is shown in Fig. 7.23 as a function of E_{T}. Both methods give similar results, with the overall fraction of photon candidates due to electrons peaking at roughly 2.5% in the E_{T} bins from 40 to 50 GeV. The estimated contribution from these

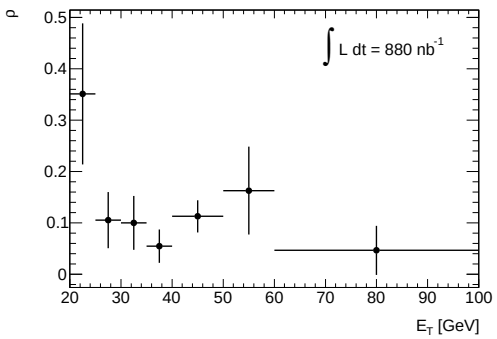

Figure 7.23: The rate, ρ, at which electrons from W, Z, and τ decays fake prompt photons, as a function of E_{T}^{γ}. Most electrons→photon fakes are the result of $W \to e\nu$ decays.

electrons is removed from the final signal yields before the calculation of the cross section.

7.5.2 Cosmic Rays

Cosmic ray muons that deposit some energy in the EM calorimeter can also fake prompt photons, and will tend to be very well isolated compared to other backgrounds. The size of this background is estimated by looking at events that fire a special empty trigger, during events in which no proton beams crossed the interaction point. The trigger also requires the presence of a cluster in the EM calorimeter with some low E_{T} threshold (roughly 5 GeV). Ignoring the empty requirement, the trigger is 100% efficient for prompt photon candidates with $E_{\mathrm{T}}^{\gamma} > 15$ GeV. The rate of prompt photon candidates that fire this trigger (with the empty requirement) is shown in Fig. 7.24a, and is at a low level for the entire E_{T}^{γ} range under study. This source of background is therefore considered negligible.

7.5.3 Beam Gas and Beam Halo

Finally, there are additional backgrounds from beam-induced non-collision sources, such as beam-gas and beam-halo interactions. These are studied with events in which only one beam passes through the interaction point, but which still produce a cluster in the EM calorimeter

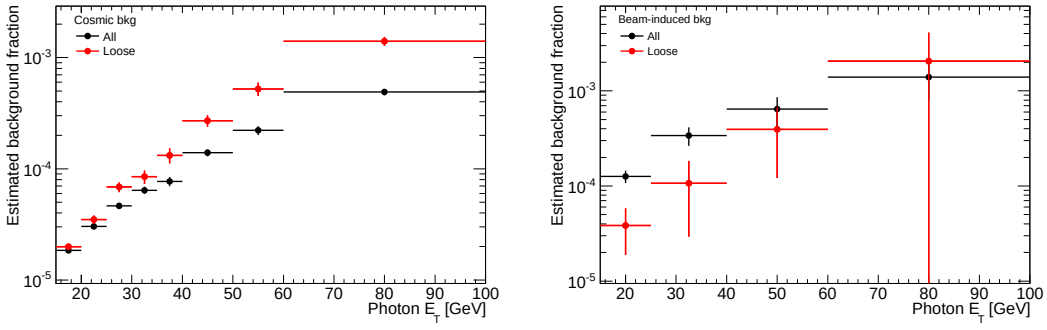

(a) Cosmic Ray Background

(b) Beam Induced Background

Figure 7.24: (a) Fraction of candidate signal events originating from cosmic rays, as a function of E_{T}^{γ}. (b) Fraction of candidate signal events originating from beam-induced non-collision sources, as a function of E_{T}^{γ}. The black dots are for all photon candidates after reconstruction, while the red dots correspond to photon candidates after the loose identification criteria.

that seeds a photon candidate. The rate of fake photons from such processes is shown in Fig. 7.24b, and is at or below the 0.1% level for the entire E_{T}^{γ} range under study. Even this small fraction is significantly reduced by the primary vertex requirement, which is sufficient to reject nearly all such events. This source of background is therefore also considered negligible.

Chapter 8

Measurement of the Inclusive Isolated Prompt Photon Cross Section and Evaluation of Systematic Uncertainties

This chapter presents the way in which the E_{T}-differential cross section is estimated, along with all the relevant systematic uncertainties.

8.1 Definition of the Cross Section

The differential cross section for each E_{T}^{γ} bin, within a single pseudorapidity region, is calculated according to the following equation:

$$\frac{d\sigma}{dE_{\mathrm{T}}^{\gamma}} = \frac{N_{\mathrm{yield}}\ U}{\left(\int \mathcal{L}dt\right)\ \Delta E_{\mathrm{T}}^{\gamma}\ \varepsilon_{\mathrm{trigger}}\ \varepsilon_{\mathrm{reco}}\ \varepsilon_{\mathrm{ID}}} \tag{8.1}$$

The observed signal yield (N_{yield}) is divided by the widths of the E_{T}^{γ}-intervals ($\Delta E_{\mathrm{T}}^{\gamma}$) and by the product of the photon identification efficiency ($\varepsilon_{\mathrm{ID}}$, determined in Section 6.2) and of the trigger efficiency relative to photon candidates satisfying the identification criteria ($\varepsilon_{\mathrm{trigger}}$, determined in Section 6.3). The spectrum obtained this way, which depends on the reconstructed transverse energy of the photon candidates, is then corrected for detector energy resolution and energy scale effects using bin-by-bin correction factors (the unfolding coeffi-

cients U) evaluated using simulated samples of photon+jet events. The corrected spectrum, which is then a function of the true photon energy, is divided by the photon reconstruction efficiency $\varepsilon_{\text{reco}}$ (Section 6.1) and by the integrated luminosity of the data sample, $\int \mathcal{L}dt$.

8.2 Unfolding the Observed Spectrum

Simulated prompt photon samples are used to unfold detector effects from the observed E_{T} spectrum. The detector has finite E_{T} resolution, and has an energy scale that can distort the observed E_{T} spectrum. The expected bin-to-bin migrations due to such effects are encapsulated in the unfolding coefficients, U_{ij}, which give the probability for a true photon with $E_{\text{T}}^{i} \leq E_{\text{T,true}}^{\gamma} < E_{\text{T}}^{i+1}$ to be reconstructed with $E_{\text{T}}^{j} \leq E_{\text{T,reco}}^{\gamma} < E_{\text{T}}^{j+1}$, where i and j represent indices over the E_{T}^{γ} bins. In principle the η resolution should be unfolded in the same way; in practice, the η resolution is at the 10^{-4} level (see Section 3.2.3.1), and has a negligible impact on the final cross section (or its systematic uncertainties).

The statistical and physical issues surrounding the unfolding of an observed spectrum back to the particle (or parton) level are many and varied; a good discussion of such issues, and solutions to some common problems, can be found in [68]. In this measurement, the bin sizes are large relative to the experimental resolution, which keeps the number of bin-to-bin migrations small. This is most directly seen in the response matrices shown in Fig. 8.1, which are derived from prompt photon MC, and which show the migration of photons with some true E_{T} into various bins of reconstruced E_{T} for the different pseudorapidity regions. The off-diagonal elements of those matrices are very small, and are almost zero for migrations of more than a single bin.

A bin-by-bin unfolding technique is used to extract the final unfolding coefficients. This technique makes the approximation that any off-diagonal elements in the response matrices

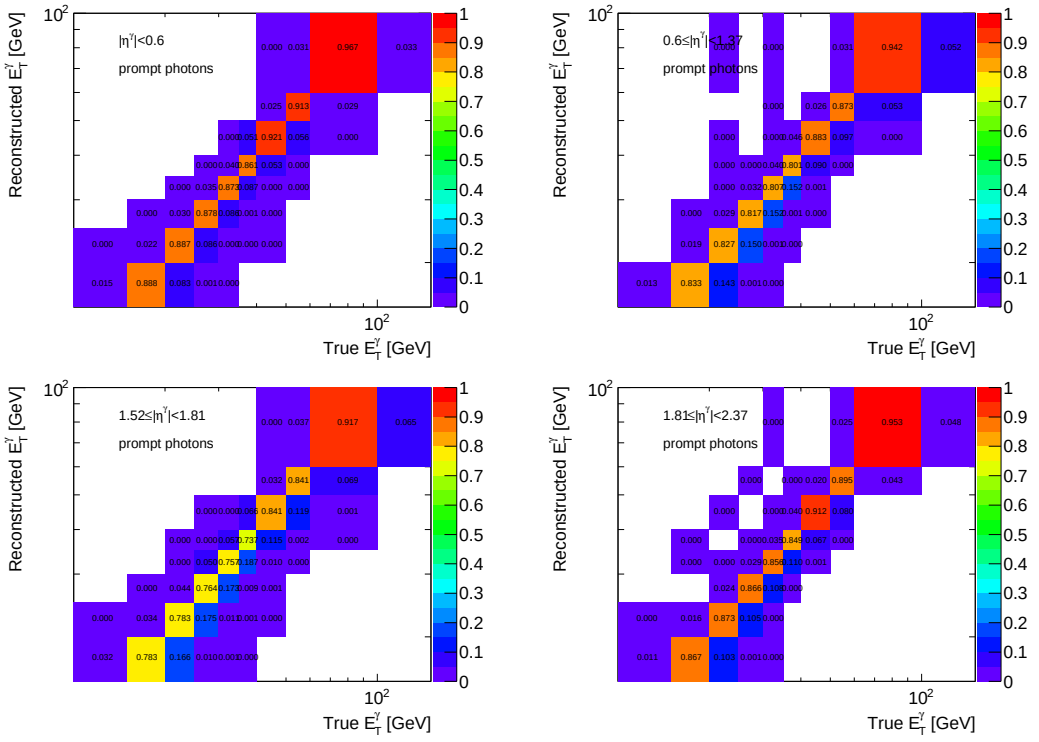

Figure 8.1: Transverse energy response matrices as determined from a simulation of prompt photons. Top left: $0.00 \leq |\eta^{\gamma}| < 0.60$. Top right: $0.60 \leq |\eta^{\gamma}| < 1.37$. Bottom left: $1.52 \leq |\eta^{\gamma}| < 1.81$. Bottom right: $1.81 \leq |\eta^{\gamma}| < 2.37$.

are equivalent to acceptance losses, and that it is enough to simply compute the coefficients as:

$$U_i = \frac{N^{\gamma}\left(E_{\mathrm{T},i} \leq E^{\gamma}_{\mathrm{T,reco}} < E_{\mathrm{T},i+1}\right)}{N^{\gamma}\left(E_{\mathrm{T},i} \leq E^{\gamma}_{\mathrm{T,true}} < E_{\mathrm{T},i+1}\right)} \tag{8.2}$$

Prompt photon MC samples are used to extract these coefficients, which are listed in Table 8.1.

To cross-check this assumption, an iterative Bayesian method is also used to extract the unfolding coefficients. In this method, the initial E_{T} spectra (both before and after reconstruction) are taken from simulation, and the response matrices are used to evolve the reconstructed spectrum iteratively until it is stable (and converges on the initial spectrum). The unfolding

E_{T} range [GeV]	$0.00 \leq \lvert\eta^{\gamma}\rvert < 0.60$	$0.60 \leq \lvert\eta^{\gamma}\rvert < 1.37$	$1.52 \leq \lvert\eta^{\gamma}\rvert < 1.81$	$1.81 \leq \lvert\eta^{\gamma}\rvert < 2.37$
$[15, 20)$	1.021 ± 0.003	1.066 ± 0.004	1.031 ± 0.007	1.055 ± 0.004
$[20, 25)$	1.018 ± 0.001	1.052 ± 0.002	1.046 ± 0.003	1.035 ± 0.001
$[25, 30)$	1.016 ± 0.002	1.046 ± 0.002	1.054 ± 0.005	1.028 ± 0.002
$[30, 35)$	1.009 ± 0.003	1.051 ± 0.004	1.035 ± 0.007	1.028 ± 0.004
$[35, 40)$	1.007 ± 0.005	1.037 ± 0.005	1.049 ± 0.011	1.019 ± 0.005
$[40, 50)$	1.004 ± 0.004	1.029 ± 0.004	1.043 ± 0.008	1.013 ± 0.004
$[50, 60)$	1.006 ± 0.007	1.017 ± 0.007	1.017 ± 0.012	1.022 ± 0.008
$[60, 100)$	0.991 ± 0.006	1.017 ± 0.006	1.037 ± 0.011	1.009 ± 0.006

Table 8.1: Isolated prompt photon transverse energy bin-by-bin unfolding coefficients. They are defined as the ratio between the number of true prompt photons reconstructed in a certain interval k of pseudorapidity, passing e/γ object quality criteria and with reconstructed isolation energy lower than 3 GeV, with true E_{T} in a certain bin i, and the number of true prompt photons (passing the same pseudorapidity and isolation requirements) with reconstructed transverse energy in the same bin.

coefficients are then taken from the solution of the final iteration. The coefficients extracted from the Bayesian method agree with those from the bin-by-bin method to within 2% for all E_{T} and η bins; the differences are taken as systematic uncertainties in the final cross section.

The unfolding factors also correct for the inefficiency of the reconstructed isolation requirement to retain photons that are truly isolated. To check the impact of applying the isolation requirement at the parton- or particle-level, the cross section is computed separately for each case. Figure 8.2 shows the ratio of the measured differential cross section computed using a particle-level isolation requirement to that using a parton-level isolation requirement. The differences in all regions of transverse energy and pseudorapidity are small, at the 1% level, which indicates the robustness of the isolation prescription to the effects of hadronization.

8.2.1 Systematic Uncertainties

The systematic uncertainties that enter in the unfolding procedure include:

- The uncertainty associated with the assumptions made by the bin-by-bin technique

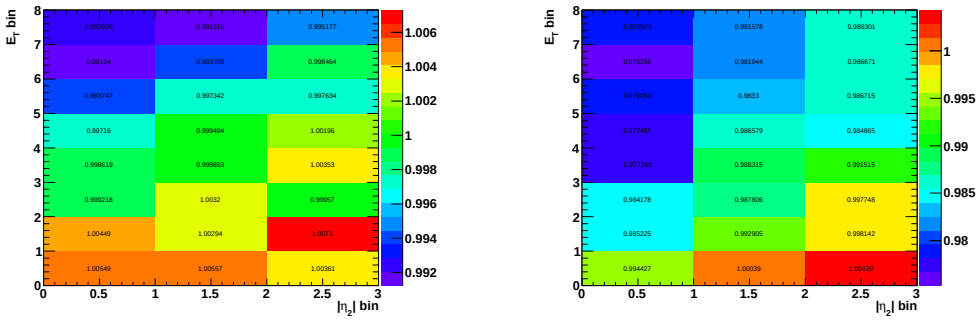

(a) PYTHIA (b) HERWIG

Figure 8.2: Ratio of the measured differential cross section using a parton-level isolation requirement of 4 GeV to that using a particle-level isolation cut at 4 GeV, with unfolding factors computed using prompt photons from PYTHIA (left) and HERWIG (right). In all cases the differences are less than 1% for PYTHIA, and less than 3% for HERWIG.

- The dependence on the simulated E_{T} spectrum provided by the MC generator
- The energy scale uncertainty
- The energy resolution uncertainty

The first uncertainty is addressed in the previous section by comparing the results with a Bayesian unfolding technique, which gives results consistent with the bin-by-bin technique to within 2%.

The uncertainty on the MC generator, in this case PYTHIA, is assessed with a variation of the iterative unfolding procedure. In this case, the initial reconstructed E_{T} spectrum is taken from PYTHIA, but subsequent iterations use the reconstructed background-subtracted spectrum from data as the input. The unfolding coefficients are extracted after the same number of iterations used in the all-PYTHIA technique, and the differences in the resulting cross section from the nominal cross section are taken as systematic uncertainties.

The energy-scale uncertainty is taken from test beam studies, where it is quoted as 3%. Preliminary studies with data indicate that the energy scale uncertainty is smaller than this [49],

so this should be a conservative bound on the efficiency. Its effect on the final cross section is shown in Fig. 8.3, and it represents one of the largest systematic uncertainties for photons with large transverse energies.[37]

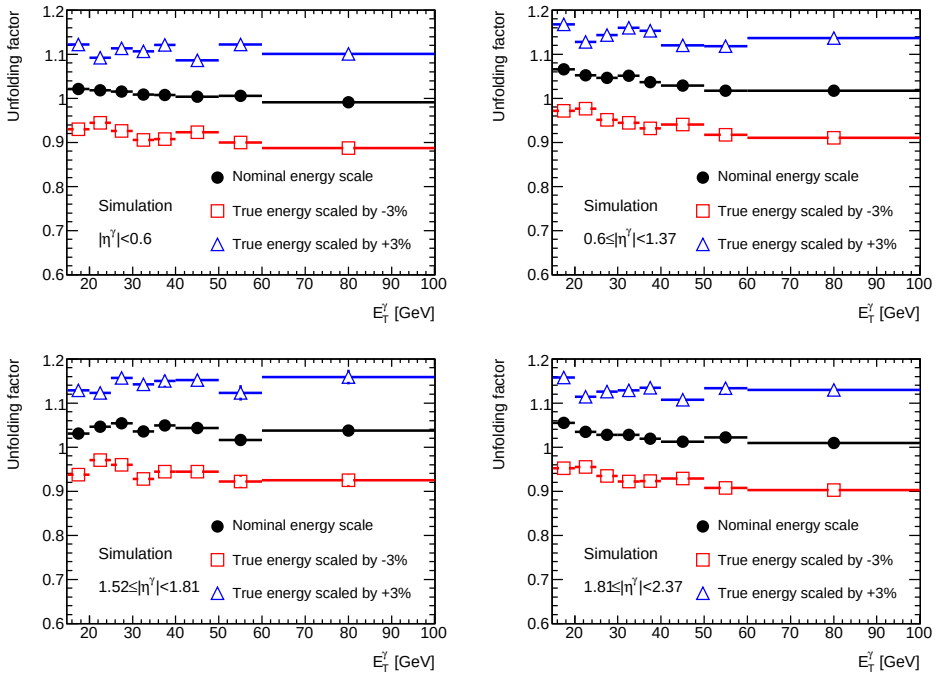

Figure 8.3: Bin-by-bin transverse energy unfolding factors as determined from a simulation of prompt photons: nominal energy scale (full black dots), and after shifting the true photon energy by -3% (red open squares) or $+3\%$ (blue open triangles).

The energy resolution in the EM calorimeter is nominally $\sigma_E/E = 10\%/\sqrt{E} \oplus 0.7\%$. Variations of either the sampling ($10\%/\sqrt{E}$) or constant (0.7%) terms will have a direct impact on the final energy resolution, and therefore on the observed E_{T} spectrum. To estimate the systematic uncertainty associated with this, the sampling term is increased by $2\%/\sqrt{E}$, the constant term is increased by 1.3% (2.9%) in the barrel (endcap), and the unfolding coefficients are recomputed after smearing the initial E_{T} spectrum with the degraded resolution terms.

[37] Subsequent improvements in the energy-scale have significantly reduced the associated uncertainties in more recent measurements.

The effect on the unfolding coefficients is less than 1%. A sample of simulated prompt photons with increased material in the inner tracker is used to estimate the impact of non-Gaussian tails in the energy resolution; these effects are also small, below 1% for all E_{T} and η.

8.3 Additional Sources of Systematic Uncertainty

8.3.1 Luminosity Uncertainty

The integrated luminosities are calculated during runs as described in Section 3.2.5. The relative systematic uncertainty on the luminosity measurement is estimated to be 11% [69] and translates directly into a 11% relative uncertainty on the cross-section.[38]

8.3.2 Signal Yield Stability Over Different Run Periods

Figure 8.4 shows the estimated signal yield for each run used in this analysis, divided by the integrated luminosity for that run. The estimated signal yield is computed by scaling each isolated, tight photon candidate in a given run by the average purity for all photons (in all runs) in the same bin of (E_{T}, $|\eta|$). The signal yield per inverse nanobarn appears stable over the entire run range, with allowances for large uncertainties in runs with poor statistics.

8.4 Total Sytematic Uncertainty

The total systematic uncertainty has contributions from the uncertainties on the signal yield, the efficiency measurements, the energy scale, the unfolding factors. Some systematic uncertainties are evaluated using the same MC samples, such as the components of the efficiency and signal yield uncertainties that are evaluated by using a `HERWIG` sample to estimate the dependence on `PYTHIA`; these uncertainties are treated as fully correlated, and are added lin-

[38] Updates to the luminosity estimation will reduce this uncertainty to approximately 3.5%.

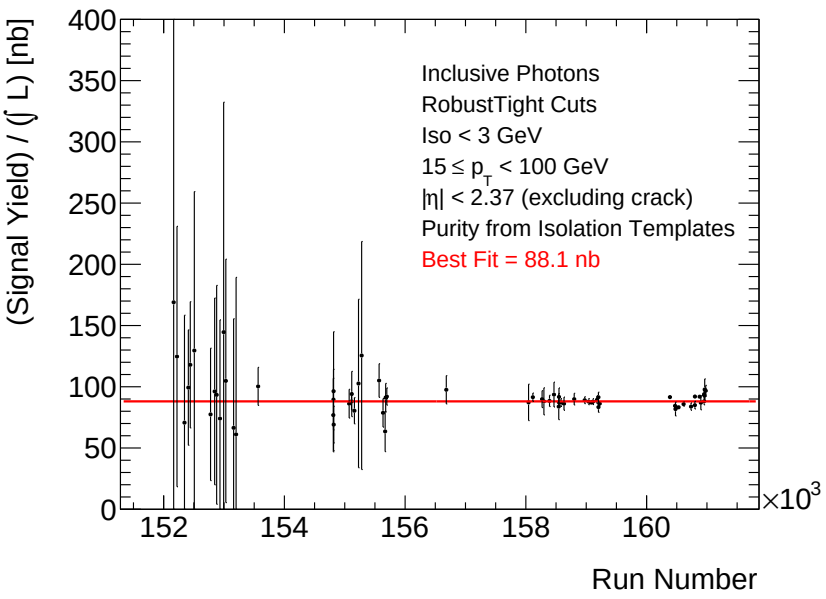

Figure 8.4: Background-subtracted estimates of signal candidates plotted by run number. The signal yield is computed with the isolation template method. The "best fit" cross section does not take into account any efficiency losses, and does not represent a measurement of the total cross section.

early. The remaining uncertainties are treated as uncorrelated. The different uncertainties, as well as the total uncertainty, are shown for each pseudorapidity region as a function of E_{T}^{γ} in Fig. 8.5. At low E_{T}^{γ}, the total uncertainty is dominated by uncertainties in the efficiency and signal yield; at high E_{T}^{γ}, the energy scale becomes the largest source of uncertainty.

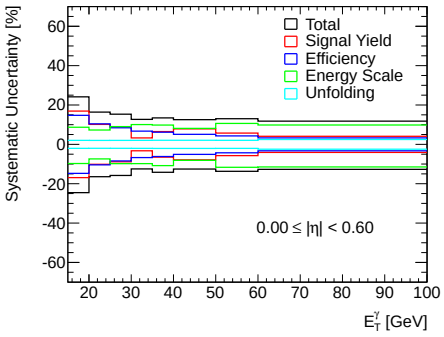

(a) Central Barrel

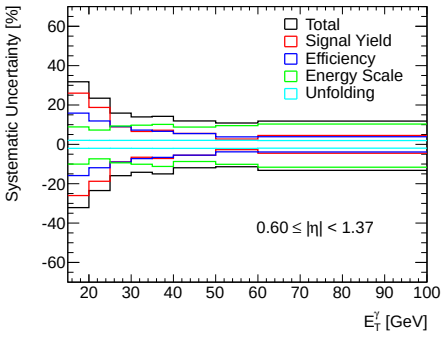

(b) Outer Barrel

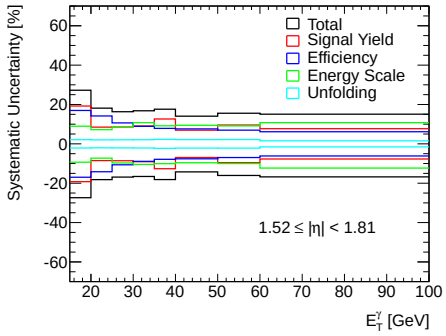

(c) Endcap

Figure 8.5: The total systematic uncertainty for all η^γ regions, as a function of E_{T}^{γ}. Some individual systematic uncertainties are correlated, and are added linearly; the rest are added in quadrature to produce the total systematic uncertainty. This uncertainty does not include the uncertainty on the luminosity estimate, which is a constant 11% for all E_{T} and η.

Chapter 9

Results of the Measurement and Comparison with Predictions

This chapter presents the final measured cross section with all uncertainties, and compares it against predictions from the JETPHOX Monte Carlo generator.

9.1 JETPHOX Predictions

The JETPHOX Monte Carlo generator [26] is used to calculate the expected cross section for inclusive photon production. JETPHOX version 1.2.2 is used here, and is available on the web [70]. The PDF used in this calculation is CTEQ 6.6. The fragmentation functions are from Bourhis *et al.* [71]. The renormalization, fragmentation, and factorization scales are set to $\mu_R = \mu_f = \mu_F = \mu = E_{\mathrm{T}}^{\gamma}$. The isolation requirement is $E_{\mathrm{T}}^{\mathrm{iso}} < 4$ GeV for an isolation cone of radius 0.4 in the $\eta - \phi$ plane. The E_{T}-differential cross section, $d\sigma/dE_{\mathrm{T}}^{\gamma}$, is predicted separately in each of the three pseudorapidity regions, assuming perfect symmetry across $\eta = 0$.

The prediction provided by JETPHOX is made at the parton level, while the measurement is made after reconstruction and unfolded to the particle level. To account for the difference between the parton and particle levels, it is customary for a measurement to include some

correction factor to be applied to the parton-level result based on the observed differences between the parton and particle levels in simulation. In the case of prompt photons, the only significant effect of the parton→particle transition is in the isolation energy; differences in the reconstruction and identification efficiencies are negligible, and there is very little smearing of the energy or position resolution due to hadronization or the underlying event. However, in this measurement, the isolation energy is calculated with a technique that actively removes many of the effects of soft (non-perturbative) physics, defining an observable that is less sensitive to the parton/particle distinction. As discussed in Section 8.2, changing the isolation requirement from the parton to the particle level results in less than a 1% change in the final cross section. Therefore, no scale factor is applied to the predicted parton-level cross section.

9.1.1 Systematic Uncertainties

9.1.1.1 Isolation Requirement

The isolation requirement $E_{\mathrm{T}}^{\mathrm{iso}} < 4$ GeV is based on studies discussed in Section 5.3.5, which determined that an isolation cut at 3 GeV after reconstruction is roughly equivalent to an isolation cut of 4 GeV at the parton level. This choice, however, relies on an implicit assumption that `JETPHOX` and `PYTHIA` have similar models of how partonic energy will be distributed near the photon. That assumption may be reasonable for direct photons (where photons are typically well-separated from hard jets), but photons from fragmentation are poorly understood theoretically, and their implementation in `PYTHIA` is different from the full NLO treatment in `JETPHOX`. To allow for these differences, the isolation cut in `JETPHOX` is varied from 2 GeV to 6 GeV, with the corresponding spread in the predicted cross section taken as systematic uncertainties. The results of this variation are shown in Fig. 9.1; the total uncertainty due to this choice is never more than 3%.

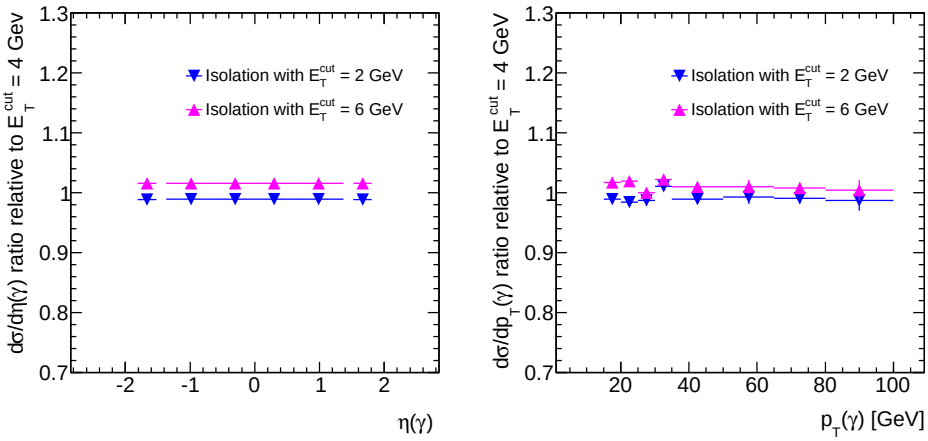

Figure 9.1: The ratio of the differential cross section after altering the $E_{\mathrm{T}}^{\mathrm{iso}}$ cut by ± 2 GeVto the cross section with the nominal isolation cut at 4 GeV, as a function of E_{T}^{γ} (left) and η (right).

9.1.1.2 Choice of Scales

As described in Section 2.1.4, the uncertainty due to the choice of scale parameters is assessed by varying each scale parameter (μ_R, μ_f, and μ_F) independently from $0.5E_{\mathrm{T}}^{\gamma}$ to $2E_{\mathrm{T}}^{\gamma}$. The effects of these variations on the predicted cross section are shown in Fig. 9.2. The renormalization scale is the source of the largest uncertainty, especially at low E_{T}^{γ}. The case where all three scales are varied coherently is shown in the blue shaded regions; there, the effects of the renormalization and factorization scales cancel each other, leading to a smaller uncertainty at low E_{T}^{γ} than at high E_{T}^{γ}. The outer envelope of the results after the independent scale variations is taken as the systematic uncertainty.

9.1.1.3 PDF Uncertainty

The PDF set provides eigenvectors which quantify the uncertainty on each of the parameters used in the global PDF fit. Deviations in the predicted cross section due to variations of the fit parameters are used to determine the total uncertainty associated to the PDF. The

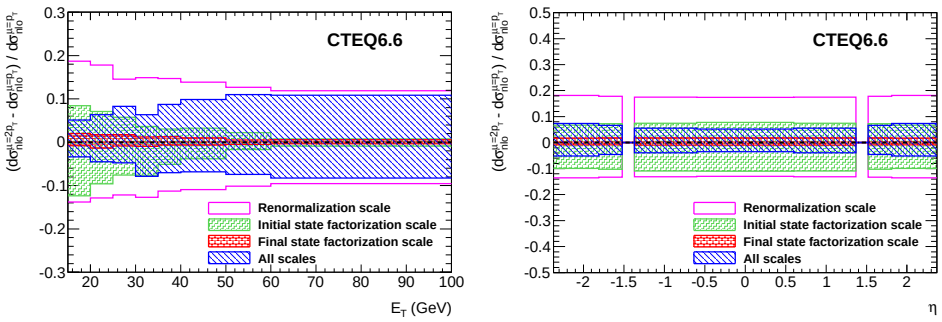

(a) E_{T} dependence (b) η dependence

Figure 9.2: Scale variation as a function of p_{T} and η obtained varying the scales independently as well as coherently. The final state factorization scale, also called the fragmentation scale, consistently has the smallest contribution to the overall uncertainty, while the renormalization scale dominates for all E_{T}^{γ} and η.

(signed) maximum deviations seen by varying each of the eigenvector components are summed in quadrature to extract the total uncertainty. The PDF4LHC group [72] recommends using the uncertainty band associated with the 68% confidence-level (CL) eigenvectors; however, the CTEQ 6.6 PDF only contains 90% CL eigenvectors. To determine the 68% CL bands, the 90% CL band is divided by a factor of 1.645. The total PDF uncertainty is shown in Fig. 9.3, along with the total scale uncertainty from Section 9.1.1.2.

9.2 Measured Cross Section

The measured E_{T}-differential cross sections for inclusive isolated prompt photon production at $\sqrt{s} = 7$ TeV are shown in Figs. 9.4 to 9.6, along with a comparison to the corresponding theoretical predictions from `JETPHOX`. The ratio of the measured cross section to the predicted cross section is also shown. The uncertainties on the measured values include all systematic and statistical uncertainties except for the uncertainty on the luminosity, which is shown separately. The uncertainties on the `JETPHOX` predictions are plotted as yellow bands.

In general, the measured cross sections are in agreement with the theoretical predictions

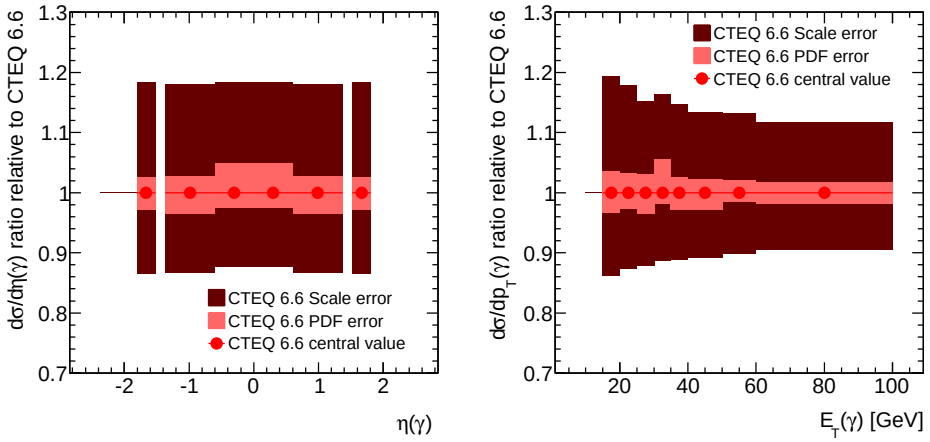

Figure 9.3: The PDF and scale as functions of η (left) and E_{T}^{γ} (right). The total scale uncertainty dominates the total systematic uncertainty.

for $E_{\mathrm{T}}^{\gamma} > 25$ GeV. The large-E_{T}^{γ} regions are easier to probe experimentally, as the signal to background ratios after the tight selection criteria are substantially better. This leads to smaller relative systematic uncertainties, which should become even smaller in future measurements as an improved understanding of the detector allows for better estimates of both the efficiencies and signal yields.

For $E_{\mathrm{T}}^{\gamma} < 25$ GeV, in the two pseudorapidity regions covered by the electromagnetic calorimeter barrel ($|\eta^{\gamma}| < 0.6$ and $0.6 \leq |\eta^{\gamma}| < 1.37$) the data seem to favor lower values of the cross section than those predicted by `JETPHOX`. Such low transverse energies at the LHC correspond to small values of $x_T = E_{\mathrm{T}}^{\gamma}/\sqrt{s}$, where NLO theoretical predictions are less well understood. For instance, in such a regime the appropriate values of the different scales are far from clear, and the uncertainties associated with these scales in the theoretical predictions may not be well modeled by simple variations of any one scale about the default value of E_{T}^{γ} [73]. As the low-E_{T}^{γ} region is exactly where the fragmentation component has the most significant impact on the total cross section, the total uncertainty associated with NLO predictions at low E_{T}^{γ} may be underestimated. Additionally, the authors of [74] claim that

prompt photon production in the low-x_T range requires a k_T factorization approach, and such predictions are more consistent with the low-η^γ, low-E_{T}^{γ} measurements presented here than those made by JETPHOX. A full comparison of the ATLAS measurements with the predictions by JETPHOX, SHERPA, and the k_T factorization approach will be an interesting test of much of what is currently known about prompt photon physics at hadron colliders.

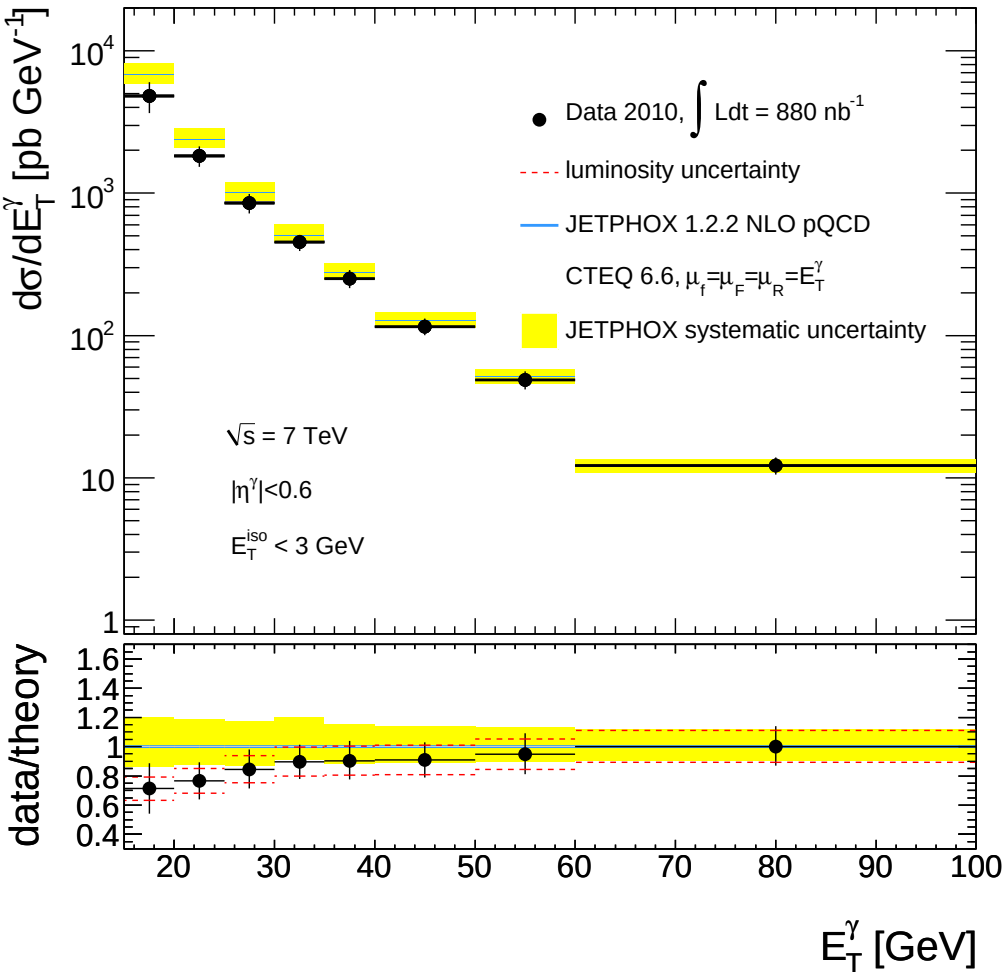

Figure 9.4: Measured vs expected inclusive prompt photon production cross section, for photons with transverse energies above 15 GeV and in the pseudorapidity range $|\eta^{\gamma}| < 0.6$. Results with the template fit method.

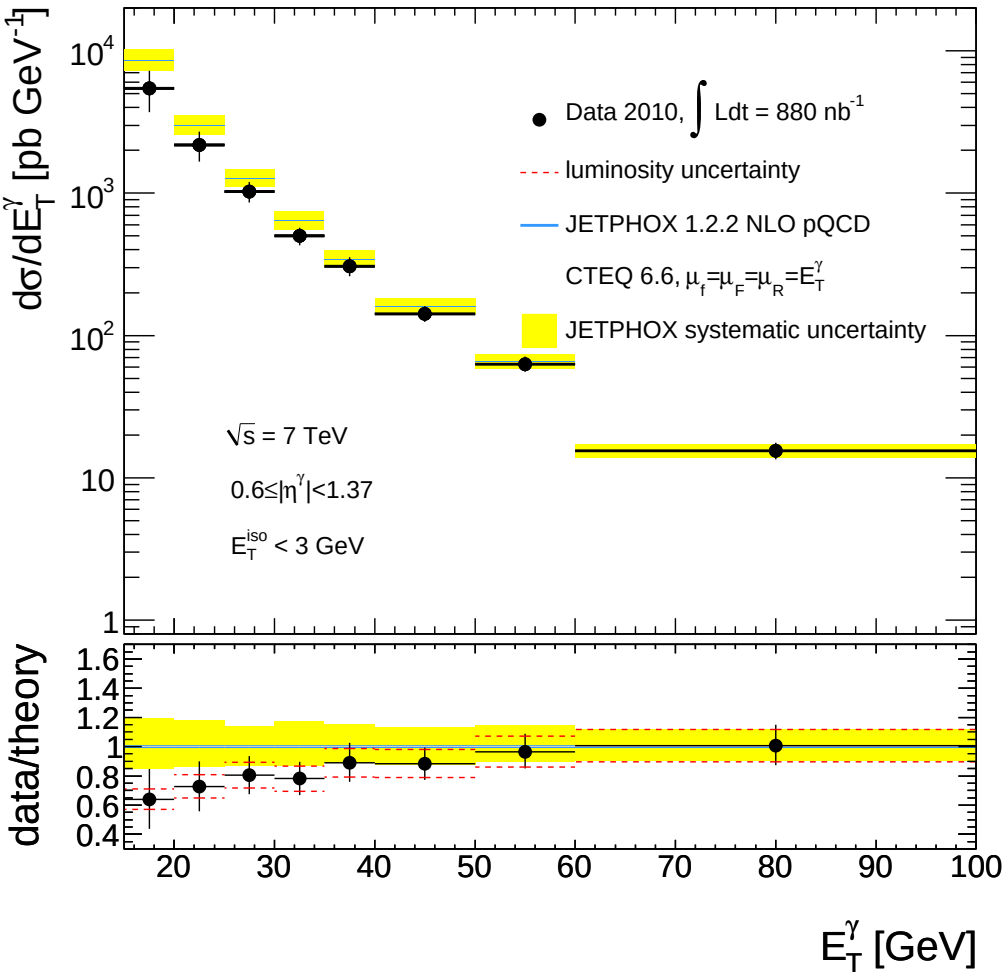

Figure 9.5: Measured vs expected inclusive prompt photon production cross section, for photons with transverse energies above 15 GeV and in the pseudorapidity range $0.6 \leq |\eta^{\gamma}| < 1.37$. Results with the template fit method.

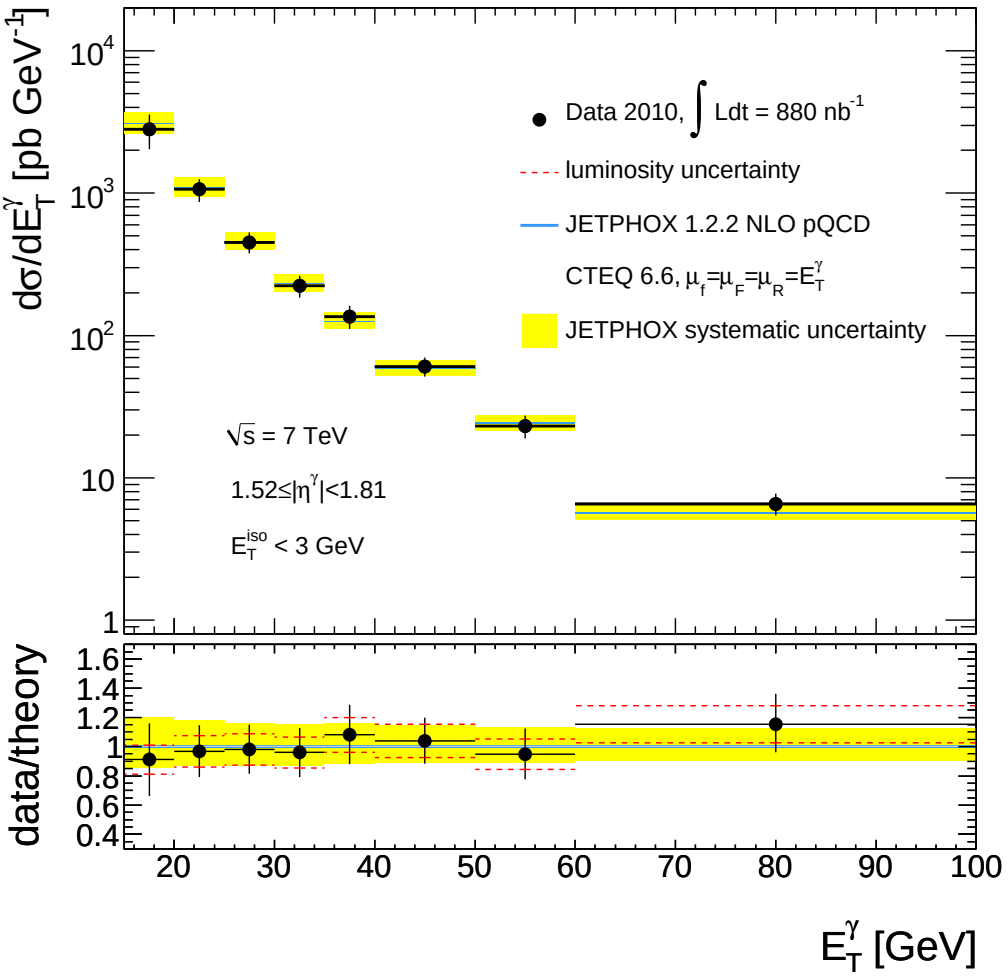

Figure 9.6: Measured vs expected inclusive prompt photon production cross section, for photons with transverse energies above 15 GeV and in the pseudorapidity range $1.52 \leq |\eta^{\gamma}| < 1.81$. Results with the template fit method.

Chapter 10

Extending the Measurement with a Larger Data Set

This chapter presents an extension of the measurement discussed in the previous chapters, this time exploiting the majority of the 2010 dataset and extending the upper E_{T}^{γ} reach to 400 GeV. The final measurement is made in eight bins of E_{T}^{γ}: 45-55 GeV, 55-70 GeV, 70-85 GeV, 85-100 GeV, 100-125 GeV, 125-150 GeV, 150-200 GeV, and 200-400 GeV. By improving the selection criteria applied by the trigger and offline reconstruction algorithms, the pseudorapidity region $1.81 \leq |\eta| < 2.37$ is also included in the measurement, in addition to the three pseudorapidity regions used in the 880 nb^{-1} analysis.

The data used in this update have an increased amount of in-time pileup compared to the 880 nb^{-1} dataset. The average number of reconstructed primary vertices per crossing is roughly 2.5, compared to less than 1.5 previously. In addition, the majority of the integrated luminosity was collected when the LHC was running with collisions closely grouped in time, meaning that out-of-time pileup is also a factor. The colliding bunches were separated by a minimum of 150 ns, and came in "trains" of eight bunches, with successive trains separated by as little as 225 ns.

Most aspects of the analysis proceed in the same way as the 880 nb^{-1} measurement. The

main differences are highlighted in the next sections, followed by the measured cross section compared with JETPHOX predictions.

10.1 Data Samples

The analysis presented in this chapter uses data collected by the ATLAS detector between August and November of 2010. The dataset corresponds to 35 pb^{-1} of integrated luminosity. Events used for this analysis are triggered using the g40_loose high level calorimeter trigger, which differs from the g10_loose trigger used in the 880 nb^{-1} analysis in two important ways. First, the nominal E_{T} threshold is 40 GeV, instead of 10 GeV. Second, the selection criteria, which use shower-shape information, are modified to improve the signal efficiency, most notably in the outer endcap.

The simulated samples used in the analysis are the same, at the generator level, as those used for the 880 nb^{-1} analysis. Some additional signal and background samples are used to investigate the high-E_{T} region of the photon spectrum; these differ from similar low-E_{T} samples only in the energy threshold. In order to account for the increase in in-time pileup, as well as the presence of out-of-time pileup, the samples are simulated with additional min-bias interactions (a mean of 2.2 interactions per crossing), and with a beam structure corresponding to two bunch trains of eight colliding bunches each, with a minimum collision separation of 150 ns, and a bunch train separation of 225ns.

10.2 Event Selection

Photons are reconstructed as described in Chapter 5, and the identification criteria differ only in the relaxing of several cuts that were found to be too restrictive in collision data. Photons are still required to have no overlap with bad calorimeter cells. An additional quality cut

is included to reject noise bursts in the calorimeter, and requires that jets associated with photons with less than 5% of their energy in the EM calorimeter have a low "quality factor" (indicating that they are not overly pathological). This requirement is nearly 100% efficient for true photons in simulation, and rejects less than 0.1% of photon candidates that satisfy the fiducial requirements in collision data.

The isolation energy is calculated as described in Section 5.3. The nominal isolation energy is corrected for out-of-core leakage based on simulated samples of single photons, which eliminates the E_{T} dependence of true photons in Monte Carlo samples, and significantly reduces it in collision data. Collision data, however, show clear signs of an increase in the lateral spread of electromagnetic showers in the EM calorimeter relative to simulated data. An additional set of leakage corrections are derived to compensate for this effect. The corrections are extracted from plots of the mean value of $E_{\mathrm{T}}^{\mathrm{iso}}$ vs. E_{T}, for each of the four pseudorapidity regions under study. For prompt photons, the isolation profile used for the data-driven corrections is defined as the difference between the isolation distribution for tight photons and the background template normalized to the tight distribution for $E_{\mathrm{T}}^{\mathrm{iso}} > 8$ GeV (where the background template is extracted as described in Section 7.1). This distribution is then fit with a Gaussian around the peak, and the mean is extracted from the fit. For the electron distributions, the isolation profile is taken from electrons from W decays, which are identified as described in Section 7.2.1. The distribution is fit with a Gaussian, and the mean is extracted. The trends of these means, as a function of the photon or electron E_{T}, are shown in Figs. 10.1 and 10.2. The additional corrections are between 0.1% and 0.45% of the photon E_{T}, and thus have a small effect for all but the highest-energy candidates. To cover any uncertainty on the exact value of the additional leakage corrections, the data-driven correction is varied by 20% around the values quoted in Fig. 10.1.

Finally, the increased instantaneous luminosity of the 35 pb^{-1} dataset allows for a more

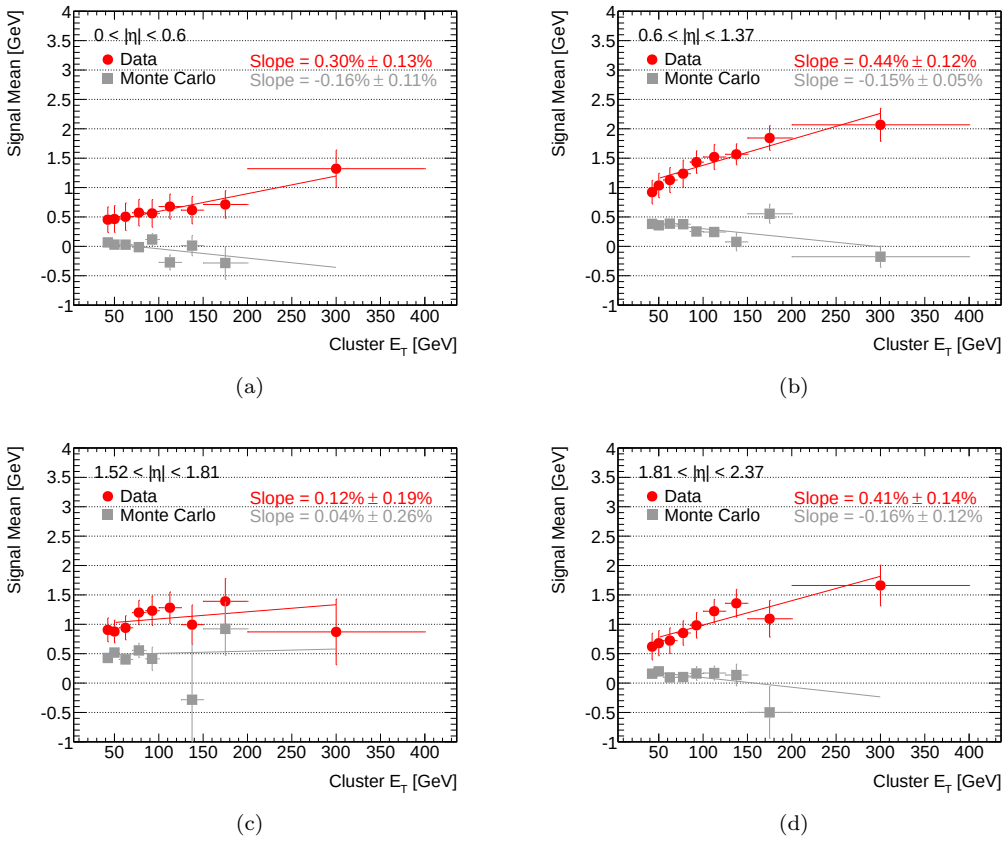

Figure 10.1: Trend of the corrected isolation distribution as a function of E_{T}^{γ} for photons. The y-axis represents the mean of a Gaussian fit to the core of the background-subtracted isolation distributions for prompt photon candidates.

careful study of the effectiveness of the jet-area corrections in the presence of in-time pileup. The corrected isolation values of electrons from W decays are plotted in bins of the number of reconstructed primary vertices in the event, and the individual isolation distributions are fit as described above. The results are shown in Fig. 10.3, where there is evidence of some residual effects from pileup even after the jet-area corrections are applied. In most pseudorapidity regions the effect is not large, and is reasonably well reproduced by Monte Carlo. The difference is therefore treated as a systematic uncertainty by varying the size of the jet-area correction to the isolation energy by a factor of two, which is sufficient to reduce the slopes

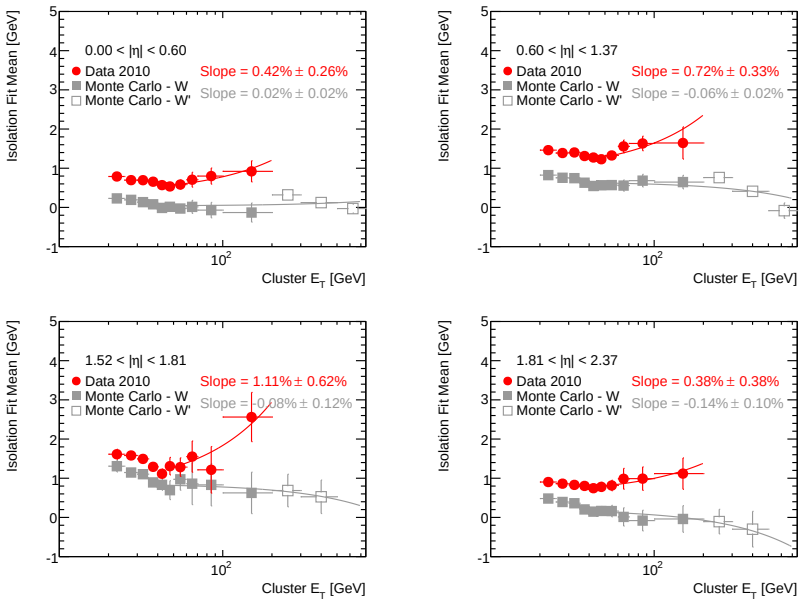

Figure 10.2: Trend of the corrected isolation distribution as a function of E_{T}^{γ} for electrons. The y-axis represents the mean of a Gaussian fit to the core of the isolation distributions for electrons from W decays.

of all of the data points to zero or negative values.

10.3 Measurement of the Cross Section

10.3.1 Efficiency

The trigger, reconstruction, and identification efficiencies are calculated as described in Chapter 6, making use of the simulated samples containing in-time and out-of-time pileup described above. The systematic uncertainties on the efficiency measurements are similar in nature to those presented earlier, but as the updated measurement avoids the low-E_{T} region where the uncertainties were the largest, the overall uncertainties are significantly smaller. The identification efficiency measurements, and their uncertainties, are shown in Fig. 10.4.

The plateau of the identification efficiency is over 95% for the first three pseudorapidity

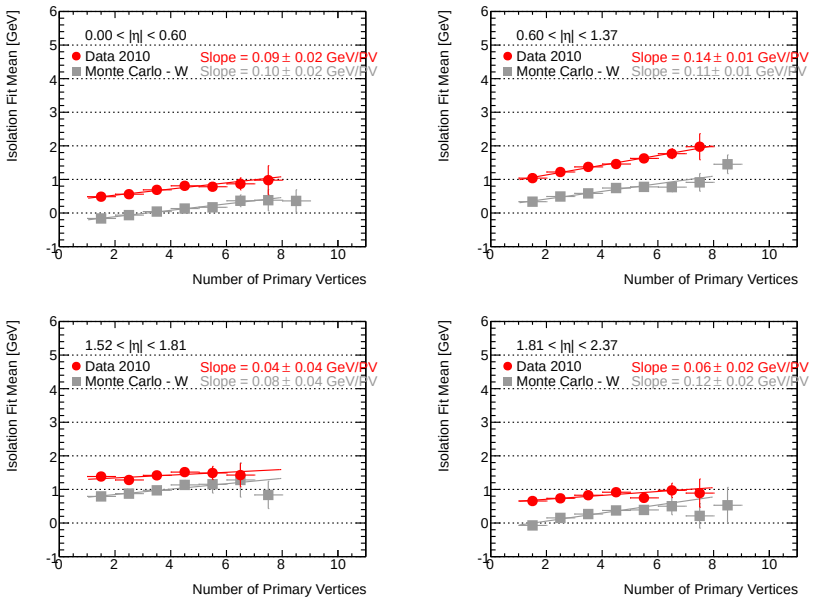

Figure 10.3: Trend of the corrected isolation distribution as a function of the number of reconstructed primary vertices for electrons. The y-axis represents the mean of a Gaussian fit to the core of the isolation distributions for electrons from W decays.

regions. In the last pseudorapidity region the plateau is closer to 90%, indicating that the identification criteria are still not perfectly optimized.

10.3.2 Signal Yield

The signal yield is calculated using a modified form of the isolation template method described in Chapter 7. To construct the signal template, the $E_{\mathrm{T}}^{\mathrm{iso}}$ distribution from $W \to e\nu$ electrons is fit to a Crystal Ball distribution, which consists of a Gaussian core with a power law tail, and is defined as:

$$f_{CB}(x;\sigma,\alpha,n,\mu) = N \cdot \begin{cases} \exp\left(-\frac{(x-\mu)^2}{2\sigma^2}\right) & \text{for } \frac{x-\mu}{\sigma} > -\alpha \\ \left(\frac{n}{n-\alpha^2-\sigma^{-1}(|\alpha|(x-\mu))}\right)^n \exp\left(-\frac{\alpha^2}{2}\right) & \text{for } \frac{x-\mu}{\sigma} \leq -\alpha \end{cases} \tag{10.1}$$

where x represents $E_{\mathrm{T}}^{\mathrm{iso}}$, μ is the Gaussian mean, σ the Gaussian width, and α and n control

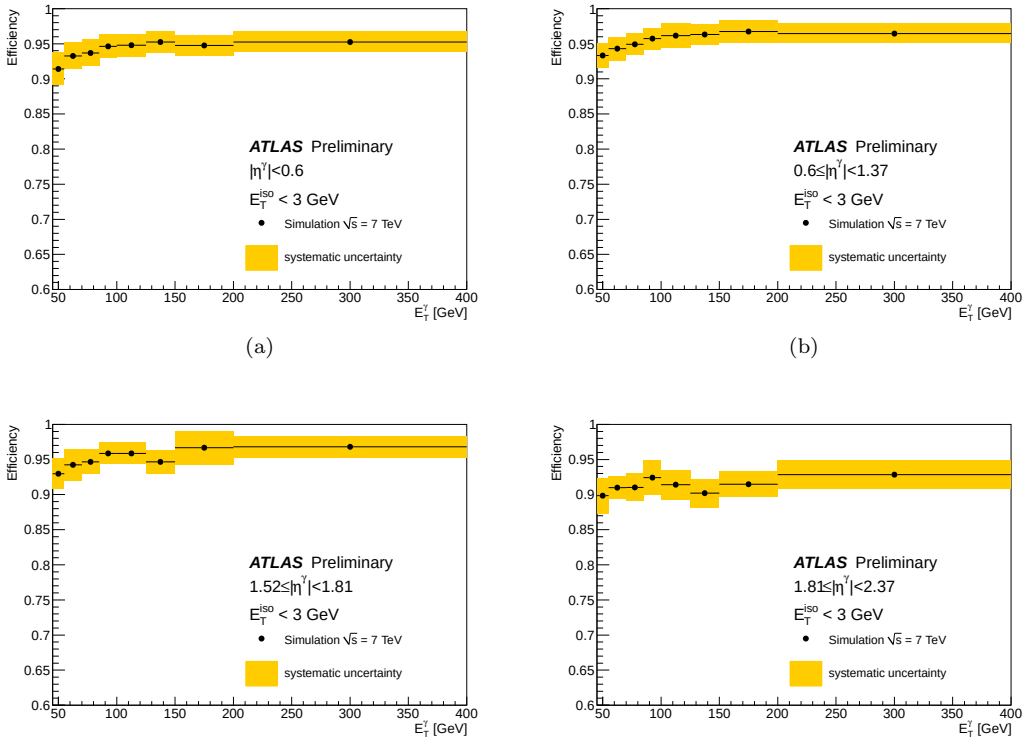

Figure 10.4: Estimated identification efficiencies for the different η^{γ} regions, as a function of E_{T}^{γ}. Shower shape distributions in Monte Carlo are shifted to better agree with those in data, and the identification efficiencies are estimated using the modified Monte Carlo samples.

the power-law tail. As before, a single signal template is constructed for each pseudorapidity region, exploiting the E_{T}-invariance of the isolation energy after the leakage corrections. The four signal templates are shown in Fig. 10.5.

For the first three pseudorapidity regions, the background template is derived from a fit of the reverse-cuts background sample to a Novosibirsk function, defined as:

$$f_{NB}(x;\sigma,\tau,x_0) = N \cdot \exp\left[-\frac{1}{2}\left(\frac{\ln^2\left(1+\frac{\sinh\left(\tau\sqrt{\ln 4}\right)}{\sigma\sqrt{\ln 4}}\left(x-x_0\right)\right)}{\tau^2}+\tau^2\right)\right] \tag{10.2}$$

Here, x_0 represents the peak of the distribution, σ the Gaussian width, and τ the parameter

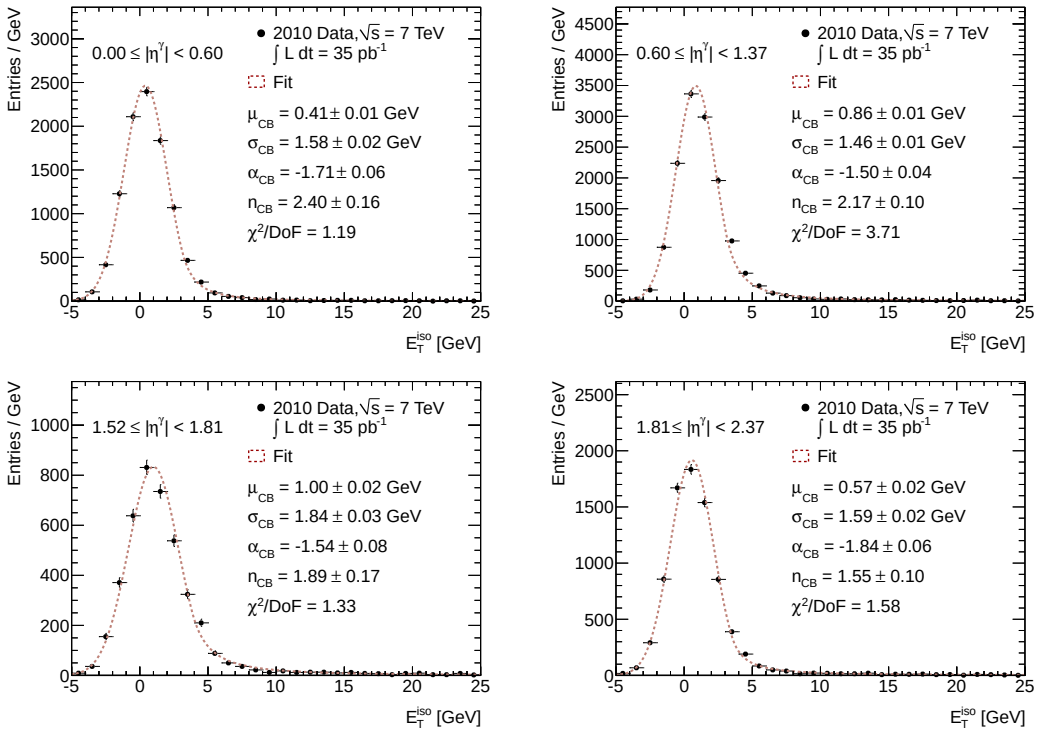

Figure 10.5: The $E_{\mathrm{T}}^{\mathrm{iso}}$ distribution of electrons from $W \to e\nu$ decays, fit to a Crystal Ball function, for each of the four pseudorapidity regions under study.

that parametrizes the behavior of the non-Gaussian tail. The fit is performed in bins of E_{T} and η up to the E_{T} bin beginning at 150 GeV, at which point the low statistics in the reverse-cuts background samples lead to poor fits. In the final two E_{T} bins, therefore, the fit parameters are taken from a linear extrapolation of the fit parameters in the lower bins. The reverse-cuts samples, and the results of the fits, for the first three pseudorapidity regions can be seen in Figs. 10.6 to 10.8. The parameters of the Novosibirsk fits for all of the E_{T} and η regions are shown in Fig. 10.10.

In the last pseudorapidity region, a significant amount of signal leaks into the reverse-cuts background sample. This signal leakage can be inferred from Fig. 10.4, where the identification efficiency plateaus at 92-93%, as opposed to roughly 97% for other pseudorapidity regions.

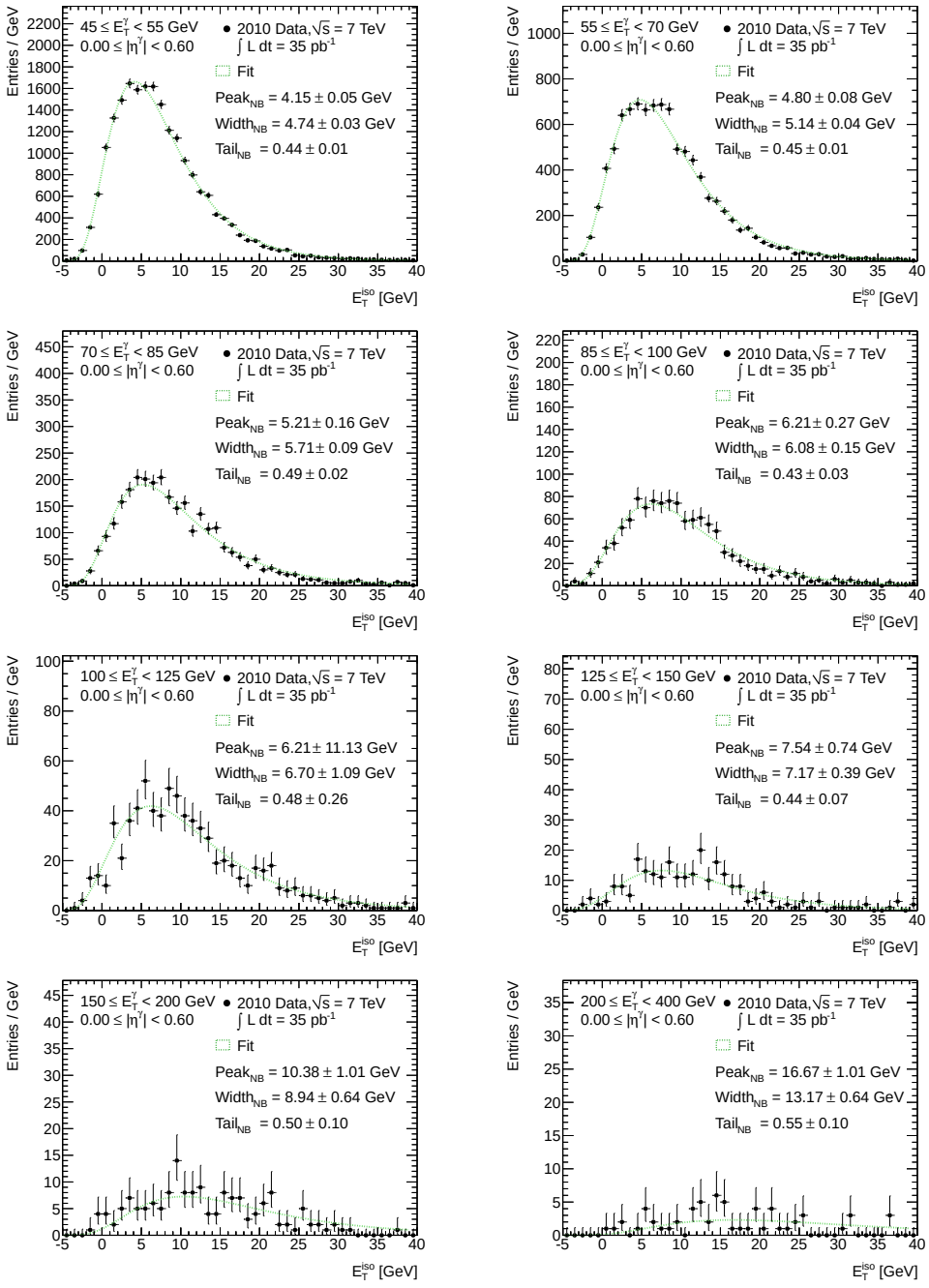

Figure 10.6: Background templates and fits for $0.0 \leq |\eta^{\gamma}| < 0.6$. The data are composed of photon candidates which satisfy the reverse cuts criteria. A Novosibirsk function is fit to the data for the first six E_{T} bins, while the functional parameters for the last two E_{T} bins are determined from a linear extrapolation of the fit parameters in the first six bins to their expected values in the last two bins.

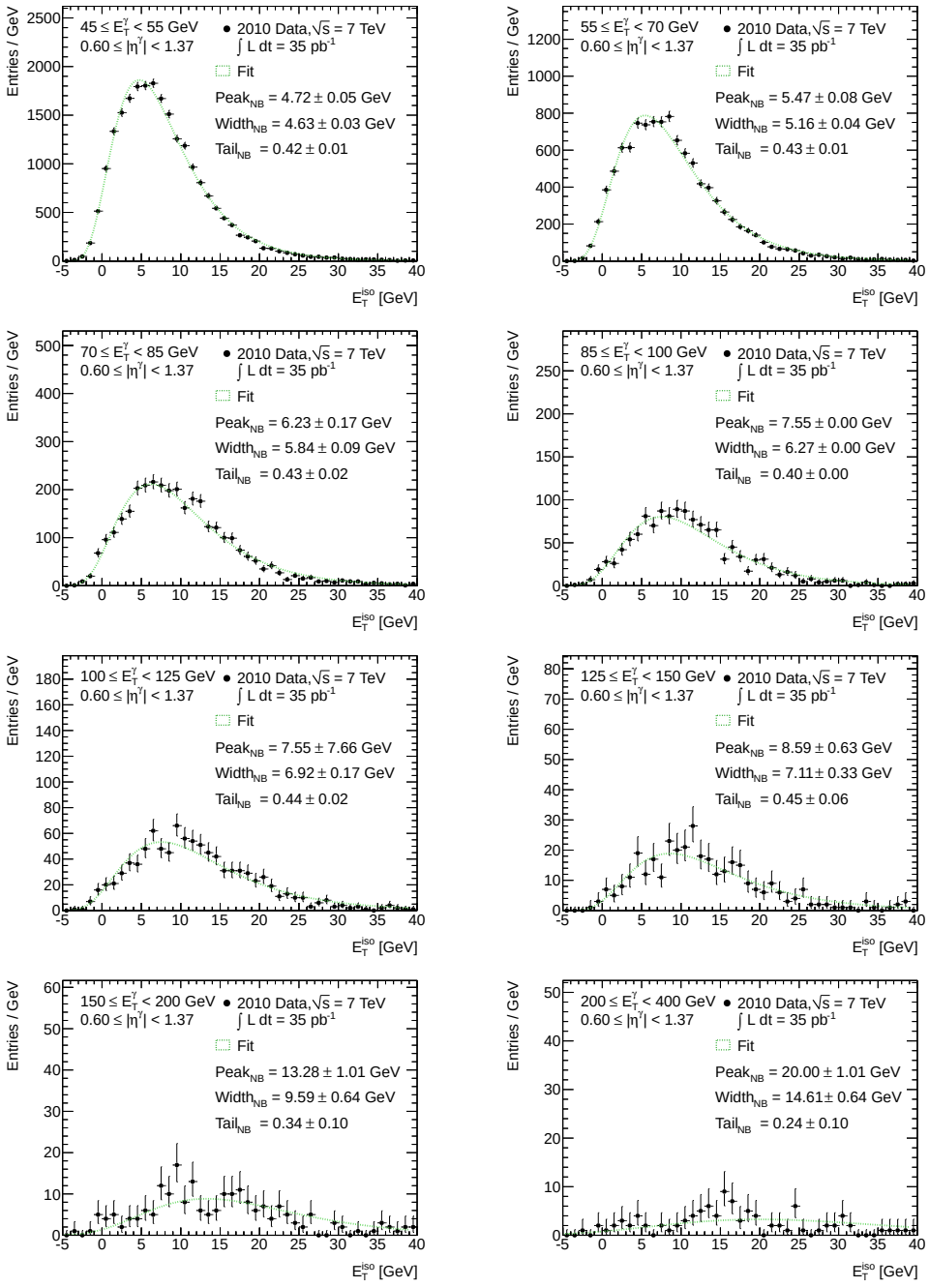

Figure 10.7: Background templates and fits for $0.6 \leq \eta^{\gamma} < 1.37$. The data are composed of photon candidates which satisfy the reverse cuts criteria. A Novosibirsk function is fit to the data for the first six E_{T} bins, while the functional parameters for the last two E_{T} bins are determined from a linear extrapolation of the fit parameters in the first six bins to their expected values in the last two bins.

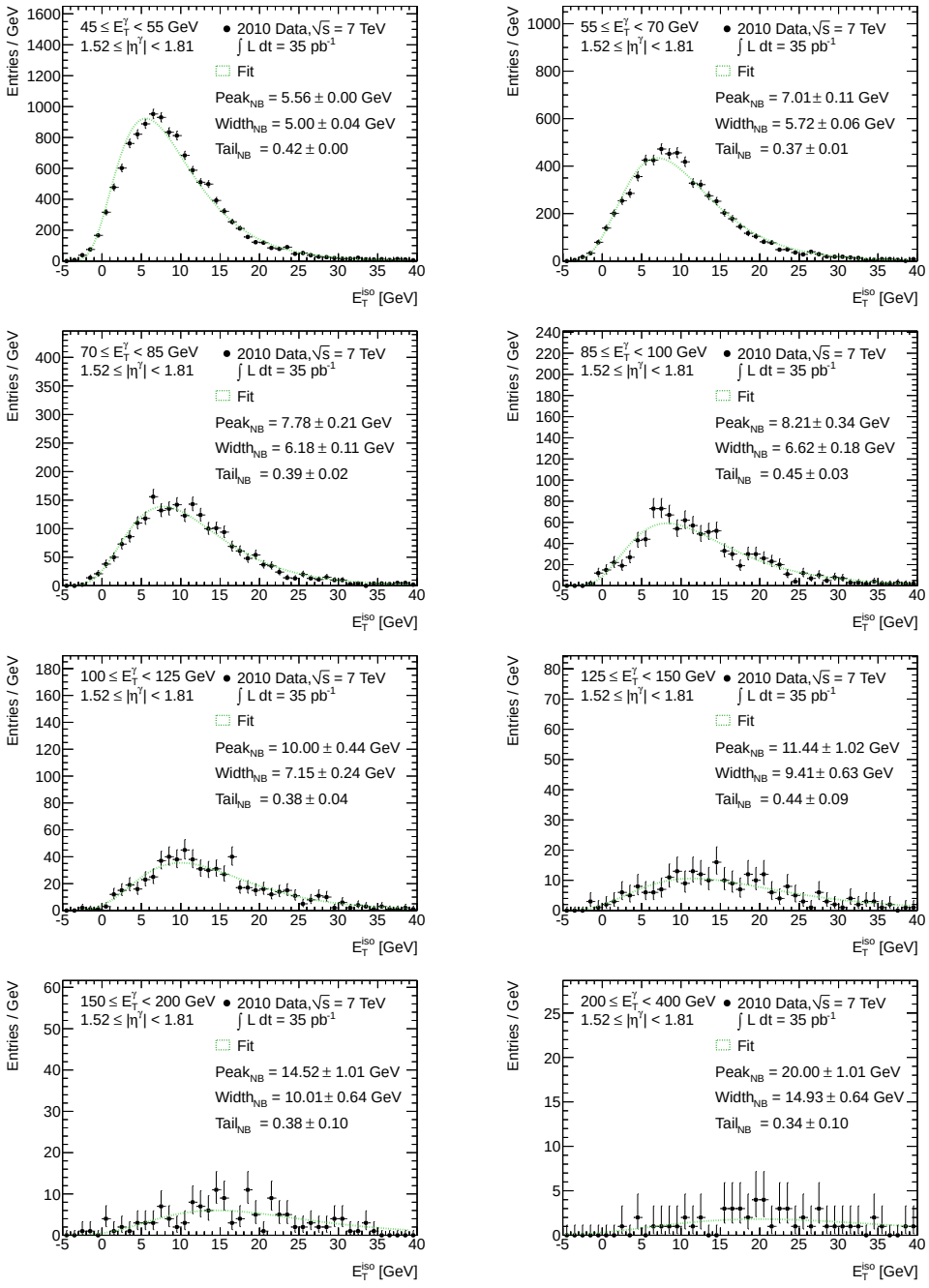

Figure 10.8: Background templates and fits for $1.52 \leq |\eta^{\gamma}| < 1.81$. The data are composed of photon candidates which satisfy the reverse cuts criteria. A Novosibirsk function is fit to the data for the first six E_{T} bins, while the functional parameters for the last two E_{T} bins are determined from a linear extrapolation of the fit parameters in the first six bins to their expected values in the last two bins.

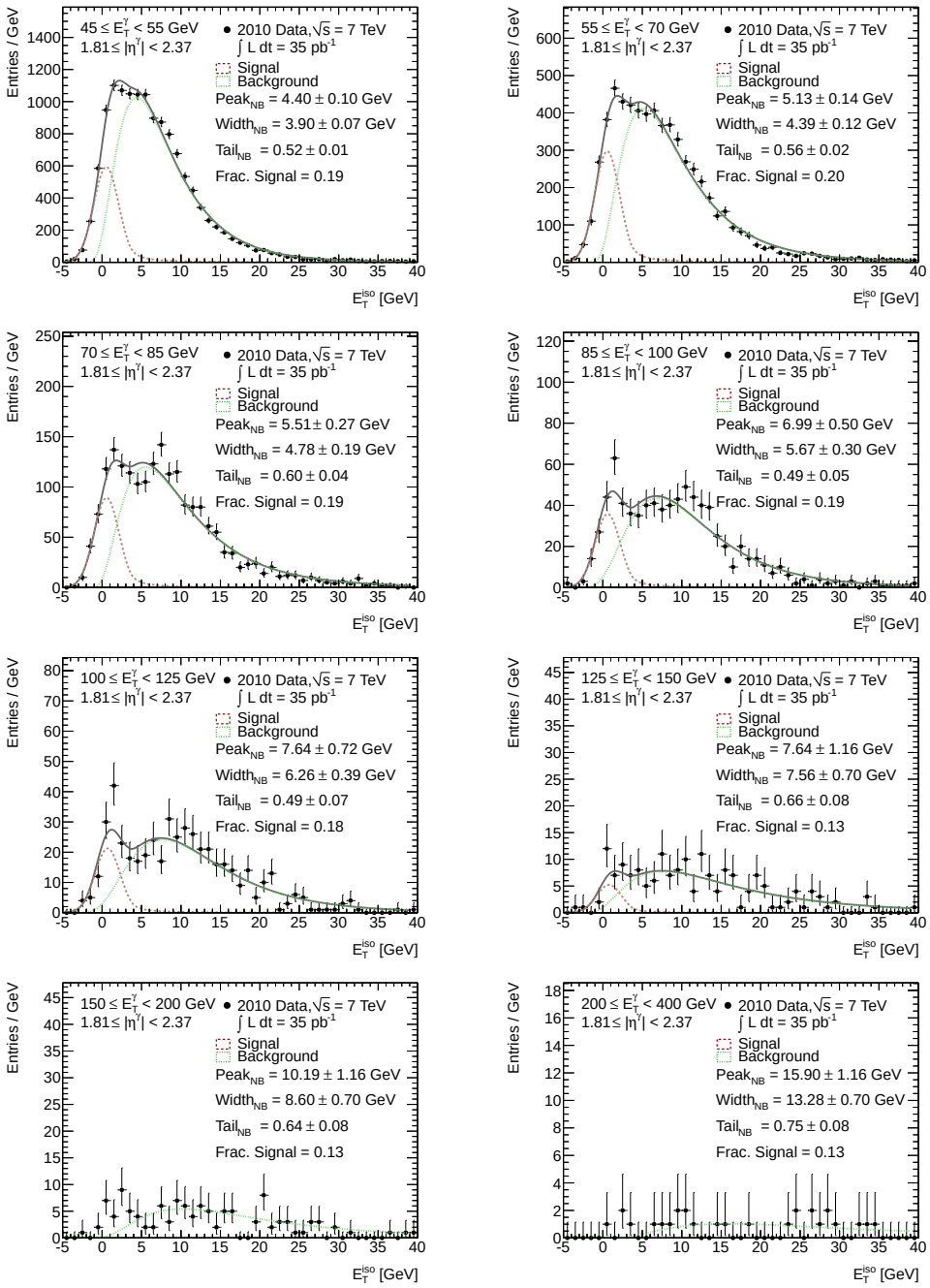

Figure 10.9: Background templates and fits for $1.81 \leq |\eta^{\gamma}| < 2.37$. The data are composed of photon candidates which satisfy the reverse cuts criteria. In the first six E_{T} bins, a sum of the signal template for this pseudorapidity region and a Novosibirsk function is fit to the data, to account for the relatively large amount of signal present in these samples. The Novosibirsk parameters for the last two E_{T} bins are determined from a linear extrapolation of the fit parameters in the first six bins to their expected values in the last two bins.

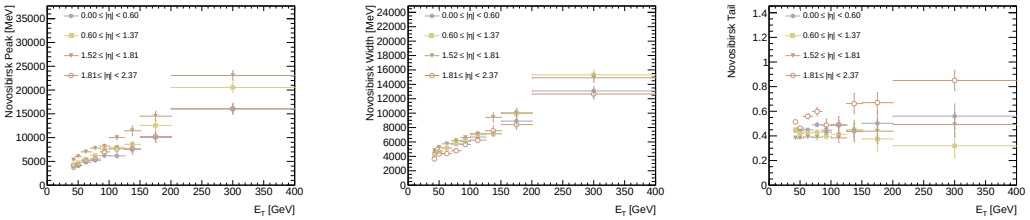

(a) Peak (b) Width (c) Tail

Figure 10.10: Background template parameters

This signal leakage results in a bias of the Novosibirsk fit parameters, primarily pushing x_0 towards lower values, and increasing the width (σ). To compensate for this effect, the reverse-cuts sample in this bin is fit to a sum of the Crystal Ball signal template (with all fit parameters fixed) and a Novosibirsk function (without any constraints). The Novosibirsk parameters taken from this fit are then used in the background template. As with the other pseudorapidity regions, the background template parameters for the final two E_{T}-bins are taken from a linear extrapolation of the fit parameters in the lower-E_{T} bins. The results of these fits are shown in Fig. 10.8. The Novosibirsk fit parameters are shown with the other pseudorapidity regions in Fig. 10.10.

After the extraction of the signal and background templates from the control samples, the photon candidate sample is fit to a sum of the signal and background templates with an unbinned extended maximum likelihood fit. The mean of the signal template, μ, is allowed to float in the final fit, removing the need for an explicit correction for the differences between electrons and photons (as done in the 880 nb^{-1} measurement). The fits are shown in Figs. 10.11 to 10.14, along with the signal and background templates normalized to the yields expected from the fit.

The purity and signal yield of each sample are extracted from the fits. The purities are shown in Fig. 10.15, along with the purities measured using the template method in the 880 nb^{-1} sample.

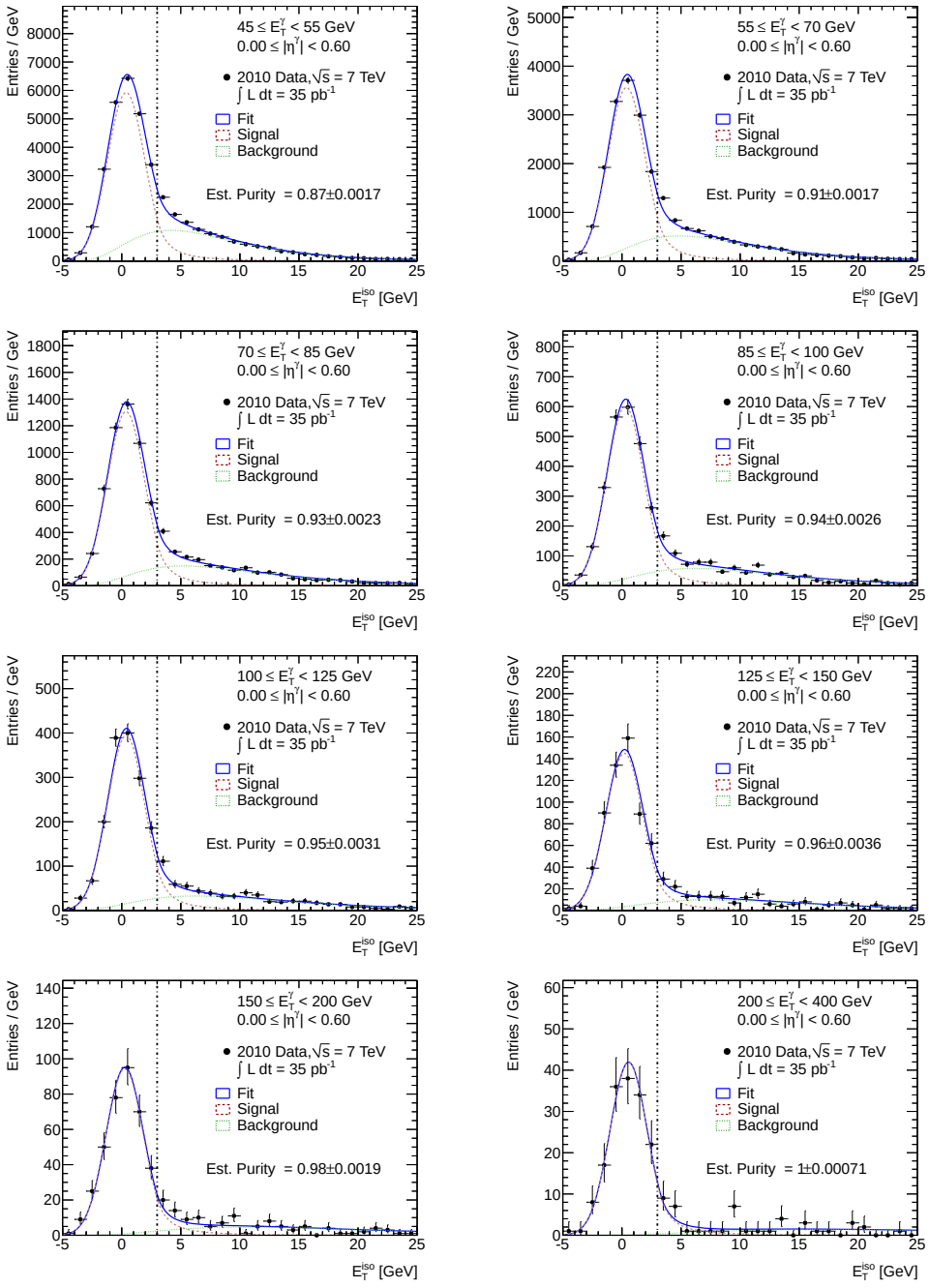

Figure 10.11: Fits for $0 \leq |\eta^{\gamma}| < 0.6$. The data are composed of tight photon candidates. The signal PDF is a Crystal Ball function, with parameters defined by a fit to the equivalent distribution from $W \to e\nu$ electrons, with a floating mean. The background PDF is a Novosibirsk function fit to the reverse-cuts background sample. The purity quoted in the plot corresponds to the fraction of data below the isolation cut estimated to be composed of signal.

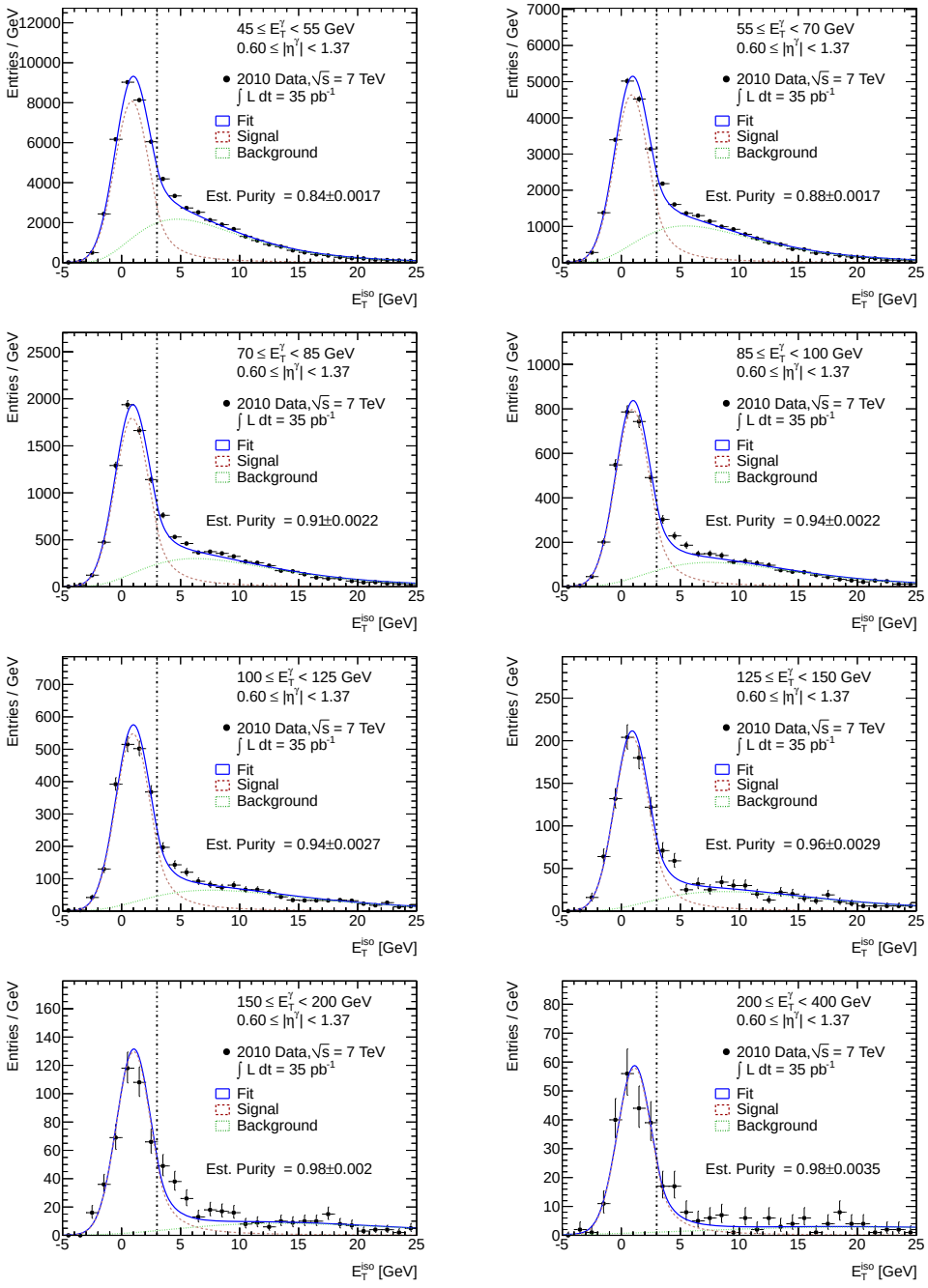

Figure 10.12: Fits for $0.6 \leq |\eta^{\gamma}| < 1.37$. The data are composed of tight photon candidates. The signal PDF is a Crystal Ball function, with parameters defined by a fit to the equivalent distribution from $W \rightarrow e\nu$ electrons, with a floating mean. The background PDF is a Novosibirsk function fit to the reverse-cuts background sample. The purity quoted in the plot corresponds to the fraction of data below the isolation cut estimated to be composed of signal.

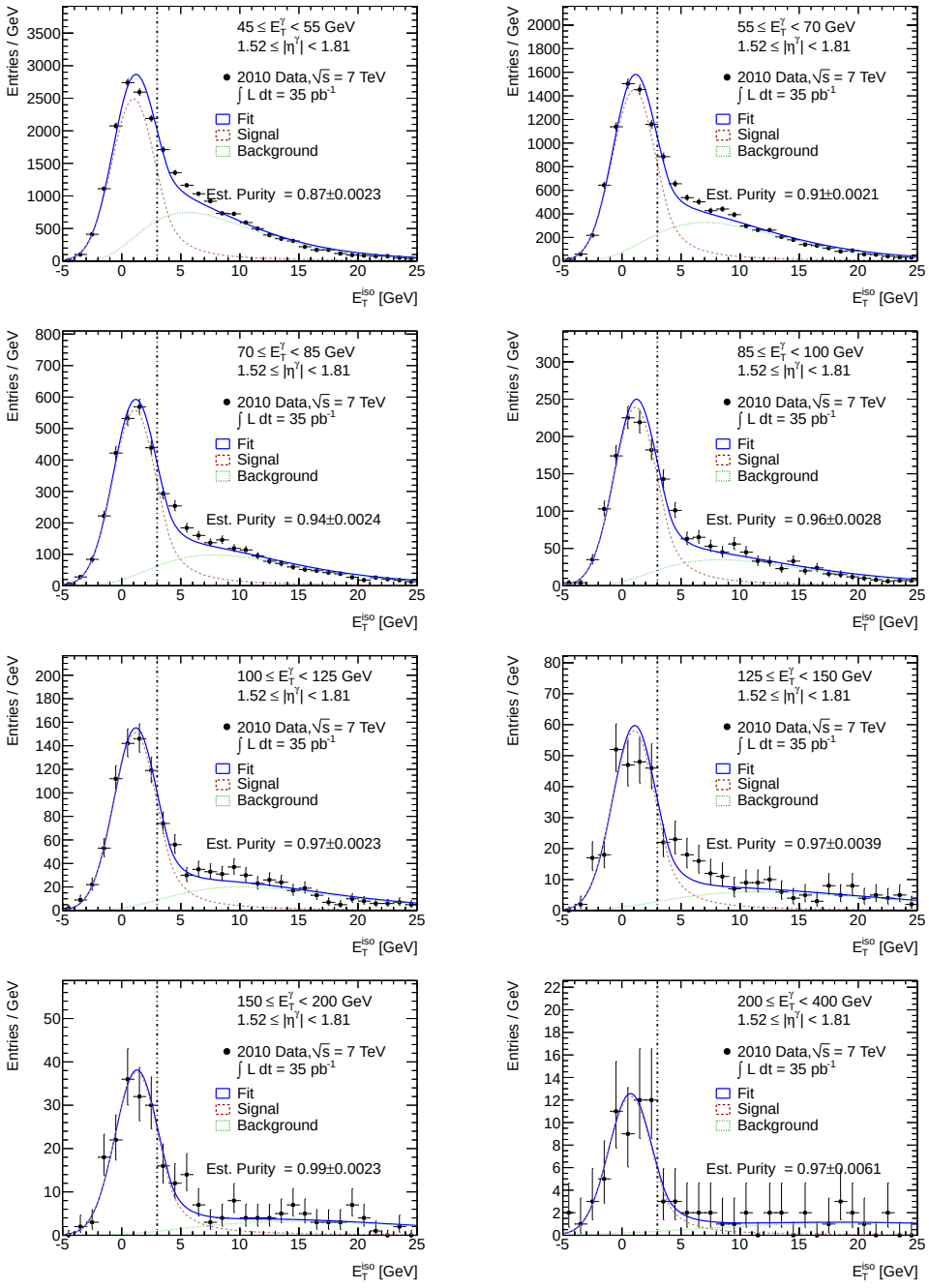

Figure 10.13: Fits for $1.52 \leq |\eta^{\gamma}| < 1.81$. The data are composed of tight photon candidates. The signal PDF is a Crystal Ball function, with parameters defined by a fit to the equivalent distribution from $W \rightarrow e\nu$ electrons, with a floating mean. The background PDF is a Novosibirsk function fit to the reverse-cuts background sample. The purity quoted in the plot corresponds to the fraction of data below the isolation cut estimated to be composed of signal.

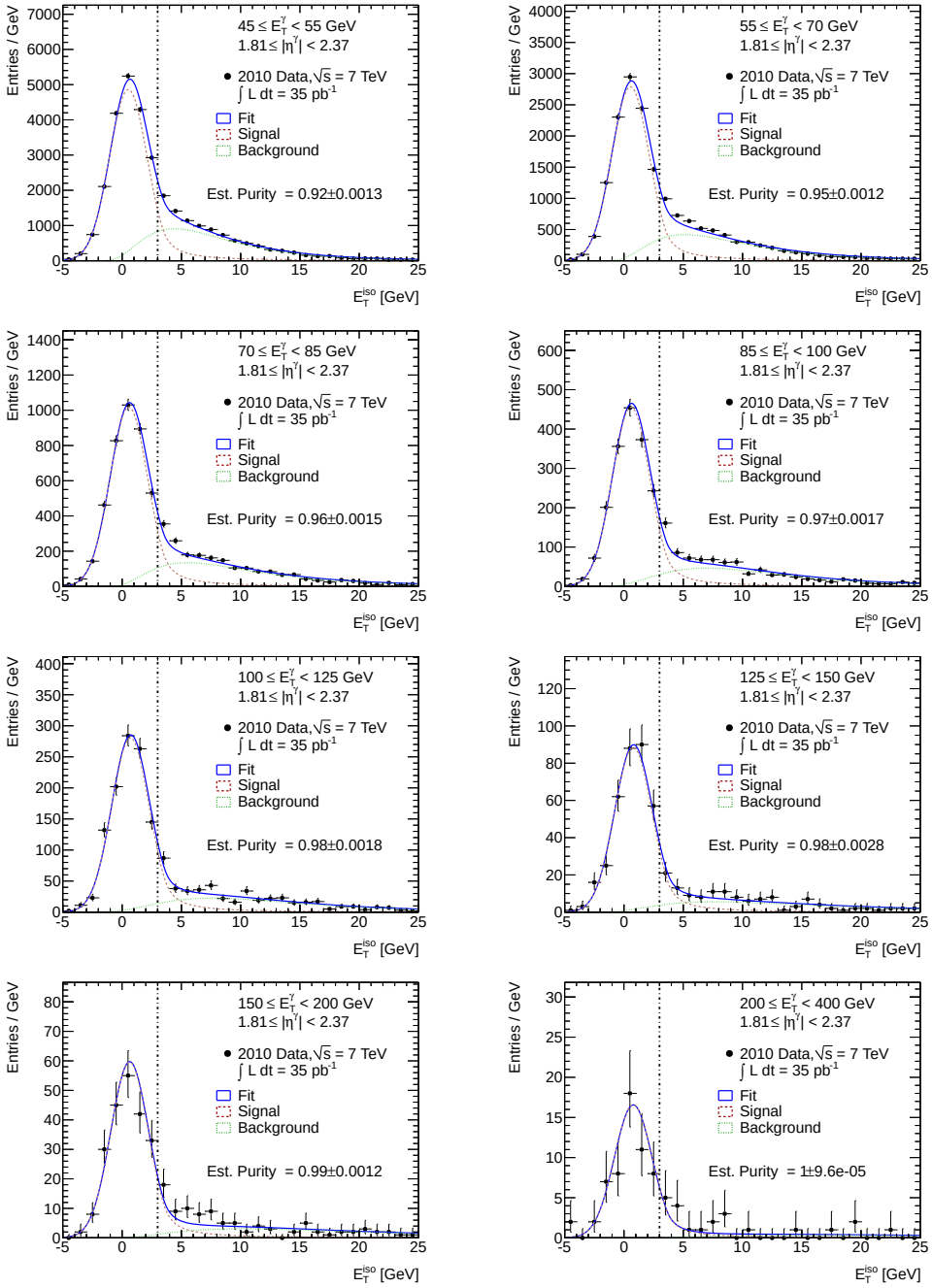

Figure 10.14: Final fits for $1.81 \leq |\eta^{\gamma}| < 2.37$. The data are composed of tight photon candidates. The signal PDF is a Crystal Ball function, with parameters defined by a fit to the equivalent distribution from $W \to e\nu$ electrons, with a floating mean. The background PDF is a Novosibirsk function fit to the reverse-cuts background sample. The purity quoted in the plot corresponds to the fraction of data below the isolation cut estimated to be composed of signal.

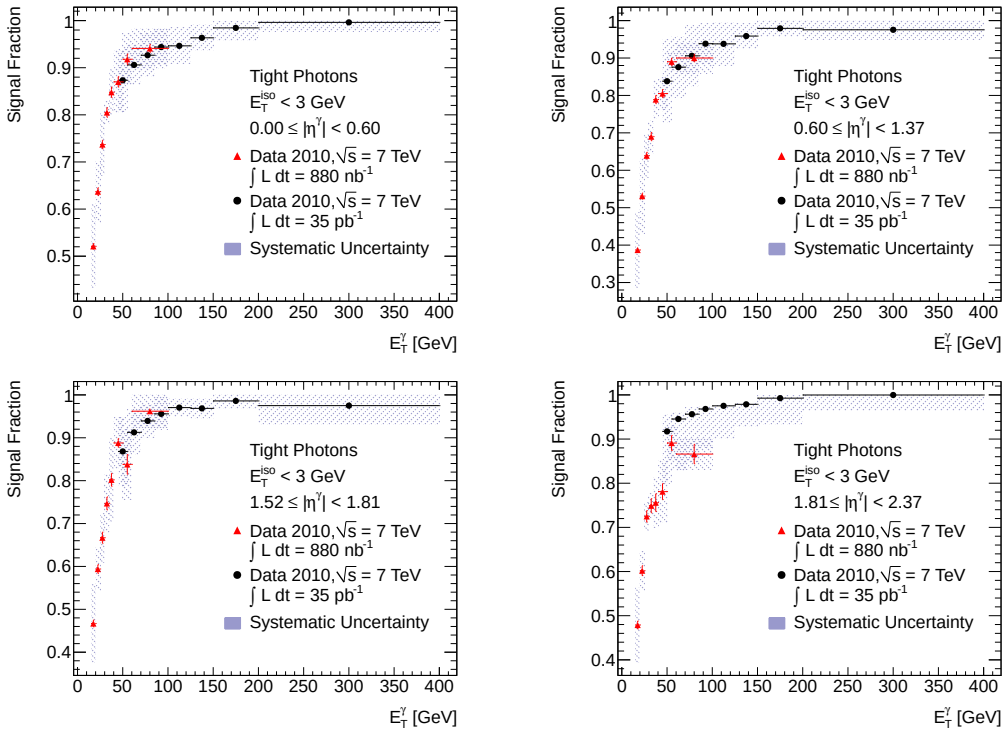

Figure 10.15: The measured purities for the 880 nb^{-1} and 35 pb^{-1} datasets, along with the associated statistical and systematic uncertainties.

10.3.3 Unfolding

The unfolding procedure uses a singular value decomposition (SVD) method to diagonalize the detector response matrix. [75] This method smooths the raw dN/dE_{T} distribution through a discrete minimization of the curvature of the ratio of the measured spectrum to a spectrum from Monte Carlo. This process, also called regularization, injects some amount of bias from the Monte Carlo sample. The effects of this bias, as estimated by using different Monte Carlo generators to derive the unfolding factors, are absorbed into the systematic uncertainties. The results of this method are also consistent with the results of a bin-by-bin unfolding procedure, as described in Section 8.2.

10.4 Total Sytematic Uncertainty

The total systematic uncertainty, along with its principle components, for each pseudorapidity region is shown in Fig. 10.16. The trends of the systematics with E_{T} are generally consistent with those of the 880 nb^{-1} measurement, and do not exceed 10% except for the third pseudorapidity region. In addition to the systematics discussed in the 880 nb^{-1} measurement, additional systematics considered in this measurement include the effects of in-time pileup on $E_{\mathrm{T}}^{\mathrm{iso}}$, the uncertainty on the data-driven leakage corrections to $E_{\mathrm{T}}^{\mathrm{iso}}$, and the uncertainties associated with the SVD unfolding procedure.

The choice of parametrized models for the signal and background templates in the purity fits also has associated systematic uncertainties. The differences of the results for the parametrized template fits with the results from the histogram-based approach described in Chapter 7 are taken as systematic uncertainties, as are the differences between the signal yield measured with the composite background model (where the reverse-cuts background data are fit to a sum of signal and background templates) and the background model assuming zero signal contamination. These uncertainties are typically on the order of 8% (relative).

The total systematic uncertainty, along with its principle components, is shown as a function of E_{T}^{γ} in Fig. 10.16 for each pseudorapidity region.

10.5 Results

The final measured cross sections with the 2010 dataset are shown in Fig. 10.17, along with the results of the 880 nb^{-1} measurement and the predicted cross sections from `JETPHOX`. The two measurements together span almost six orders of magnitude, and come close to reaching the upper E_{T}-range of prompt photons measured at the Tevatron. The data tend to favor slightly higher cross sections at high-E_{T} than predicted by `JETPHOX`, though the central values

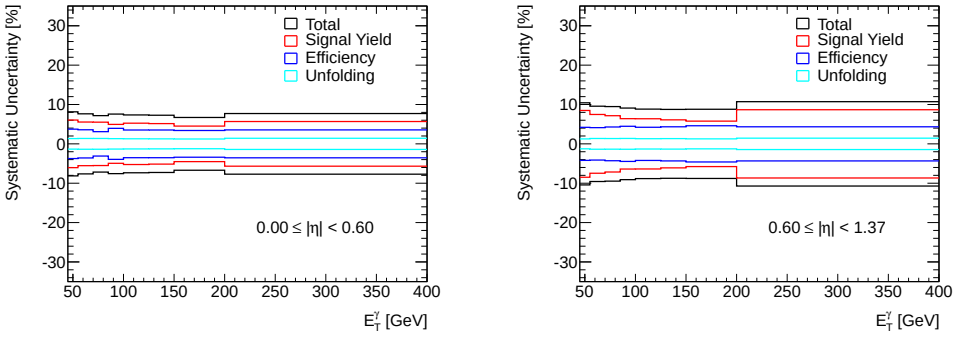

(a) Central Barrel

(b) Outer Barrel

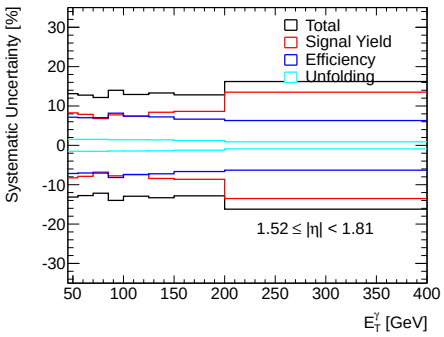

(c) Inner Endcap

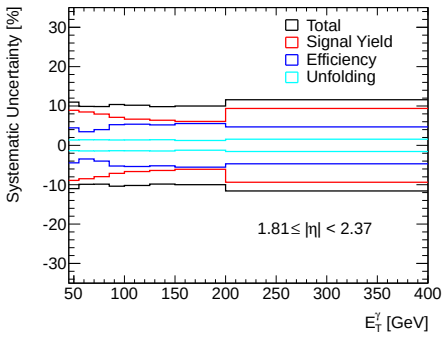

(d) Outer Endcap

Figure 10.16: The total systematic uncertainty for all η^γ regions, as a function of E_{T}^γ. Some individual systematic uncertainties are correlated, and are added linearly; the rest are added in quadrature to produce the total systematic uncertainty. This uncertainty does not include the uncertainty on the luminosity estimate, which is a constant 3.4% for all E_{T} and η. The energy scale uncertainty, which was large for the 880 nb^{-1} measurement, is significantly smaller in the extended measurement, and is not shown here.

typically lie within uncertainties of each other.

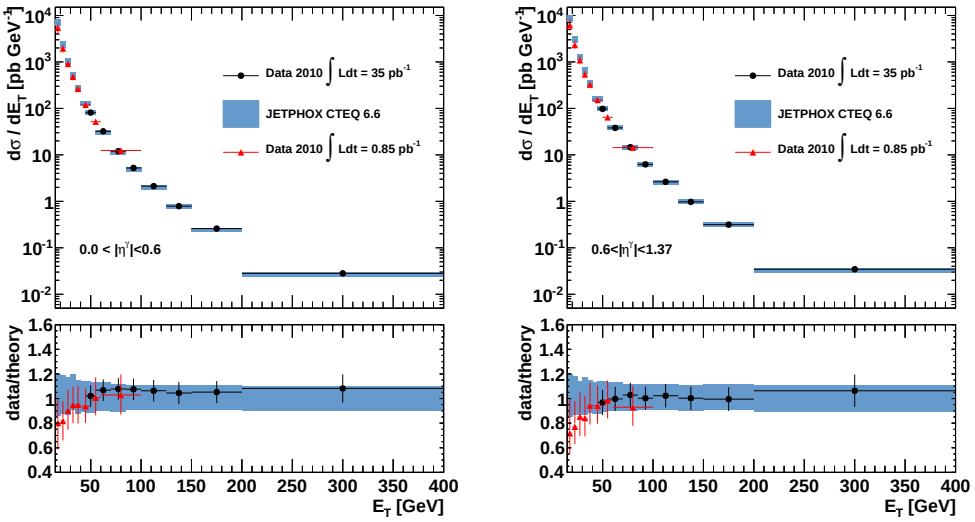

(a) Central Barrel

(b) Outer Barrel

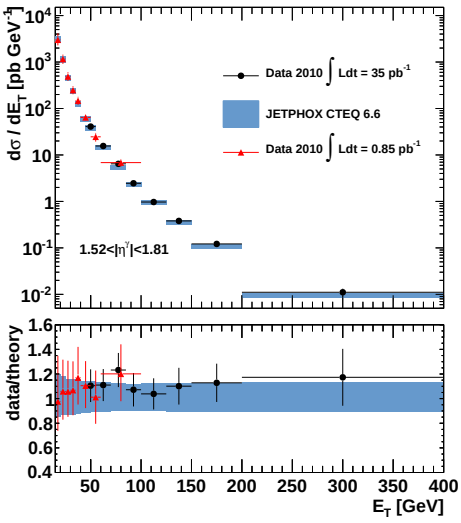

(c) Inner Endcap

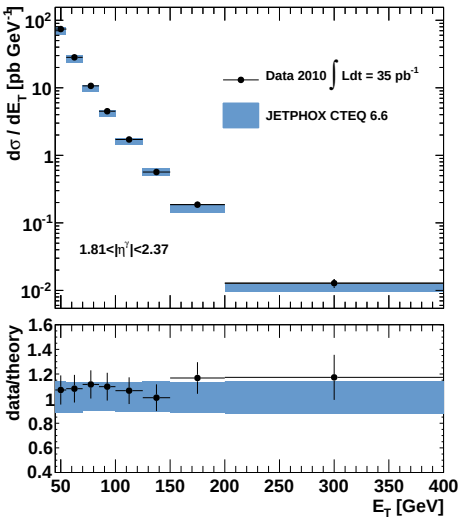

(d) Outer Endcap

Figure 10.17: The measured inclusive isolated prompt photon cross section using the full 2010 data sample, for each of four η^γ regions, as a function of E_{T}^{γ}. The results are compared with JETPHOX predictions. For the first three η^γ regions, the corresponding measurements from the 880 nb^{-1} sample are also shown.

Chapter 11

Conclusion

This thesis has presented two measurements of the inclusive isolated prompt photon cross section at $\sqrt{s} = 7$ TeV with the ATLAS detector. The first measurement is based on 880 nb^{-1} of data, and evaluated $d\sigma/dE_{\mathrm{T}}^{\gamma}$ in three pseudorapidity regions, over the range 15 GeV $\leq E_{\mathrm{T}}^{\gamma} <$ 100 GeV. The second is based on 35 pb^{-1} of data and was made in four pseudorapidity regions over the range 45 GeV $\leq E_{\mathrm{T}}^{\gamma} <$ 400 GeV. The measurements are generally consistent with theoretical predictions made by the `JETPHOX` program, though the data at low values of E_{T}^{γ} and η^{γ} seem to favor smaller cross sections than predicted by theory.

The measurements presented here represent some of the first probes of prompt photons at LHC energies, and hopefully will not be the last of their kind. Precision measurements of the prompt photon cross section should allow for improved constraints on parton distribution functions, specifically those which predict the gluon content of the proton. They also provide a clean probe of QCD at increasingly large Q^2.

Future measurements of the inclusive prompt photon cross section at the LHC will certainly extend the E_{T}^{γ} range far beyond that presented here, likely nearing the 1 TeV mark before the end of 7 TeV running in 2012. Measurements of the γ+jet (including the measurements of the angular separation of the photon and jet) and diphoton cross sections will also be important steps in understanding prompt photon production at hadron colliders. The γ+jet cross section

measurement made at D∅ [76], for instance, shows large deviations of data with respect to theoretical predictions, which will be interesting to probe at LHC energies.

There are additional improvements to the inclusive analysis that have interested theorists and experimentalists in recent years. They primarily revolve around modifications to the isolation prescription that will help to remove a larger portion of both the fragmentation and non-prompt components of the candidate sample. The most popular example is an isolation prescription first proposed by Frixione in [77]. In this formulation, a relatively loose requirement is made on the isolation energy in a large cone, and progressively tighter requirements are made on smaller and smaller cone sizes, culminating in a requirement of zero isolation energy in a cone with zero radius.[39] The function which relates the isolation cut with the cone size is required to be smooth, and usually of the form:

$$E_{\mathrm{T}}^{\mathrm{iso}}(R) < \varepsilon E_{\mathrm{T}}^{\gamma} \left(\frac{1-\cos(R)}{1-\cos(R_0)} \right)^n \tag{11.1}$$

where R is the cone radius, R_0 is some maximum cone radius (of order 1.0), $\varepsilon E_{\mathrm{T}}^{\gamma}$ is the amount of isolation energy allowed in a cone of radius R_0, and n is a shape parameter that is required to be positive, and is typically of order 1.0. Examples of the isolation profiles as functions of R and n are shown in Fig. 11.1.

For appropriate choices of ε, R_0, and n, this technique has the advantage of removing all photons from fragmentation when applied at the parton level. This is appealing to some theorists, as it would allow a measurement of the direct component of the prompt photon cross section without any contribution from the fragmentation part. Experimentally, however, this prescription is difficult to implement. The size of a reconstructed photon in the ATLAS calorimeter, for instance, is not zero, and thus a cut on the isolation energy in a cone with a

[39] This strategy was one of the initial motivations for the implementation of the jet-area technique to remove the effects of the underlying event - if direct photons are required to have zero isolation energy, then the effects of the underlying event need to be removed before the cuts are applied.

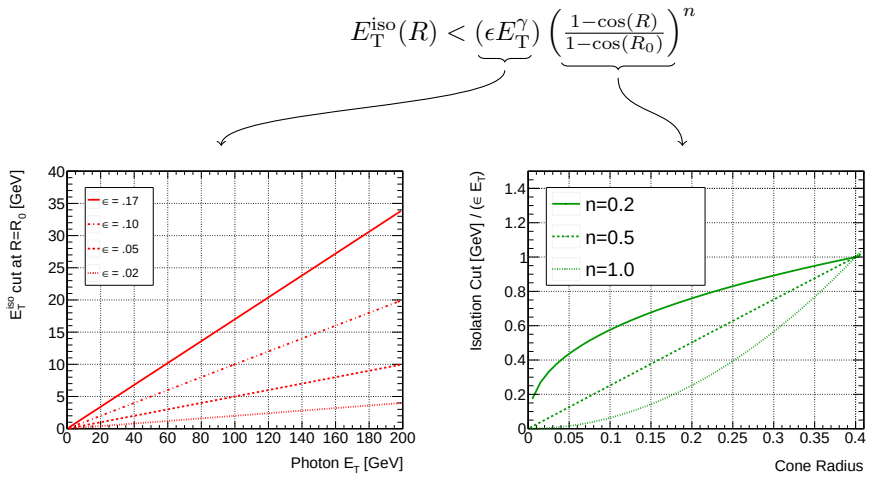

Figure 11.1: The effects of the different pieces of the Frixione isolation prescription on the isolation cut applied as a function of E_{T}^{γ} (left) and cone radius R (right).

smaller radius than the typical size of a photon cluster (around $\Delta R = 0.05$) makes little sense. Furthermore, energy deposits in calorimeters are made in cells of discrete size, meaning that a continuous cut in R will be discontinuous in $E_{\mathrm{T}}^{\mathrm{iso}}$. Some contributors of [78] therefore proposed a discrete form of this technique, where an isolation cut is made in several steps in R, with a minimum value of $R \approx 0.10$. This reduces the power of the Frixione isolation prescription to remove fragmentation photons, but is still a marked improvement over the simple prescriptions used to date by experimentalists. A generalized form of Eq. (11.1), implemented in such discrete steps, has been implemented in `JETPHOX`, and is shown in Eq. (11.2). The addition of several new parameters allows more fine-tuning of the isolation cut as a function of E_{T}^{γ} (see Fig. 11.2), and it will be interesting to investigate the effects of such a technique in an experimental context.

$$E_{\mathrm{T}}^{\mathrm{iso}}(R) < \left(\left(E_{\mathrm{T}}^{\mathrm{iso}}(R_0)\right)^m + (\varepsilon E_{\mathrm{T}}^{\gamma})^m \right)^{1/m} \left(\frac{1-\cos(R)}{1-\cos(R_0)}\right)^n \tag{11.2}$$

Finally, the techniques developed in the course of the inclusive analyses have been used

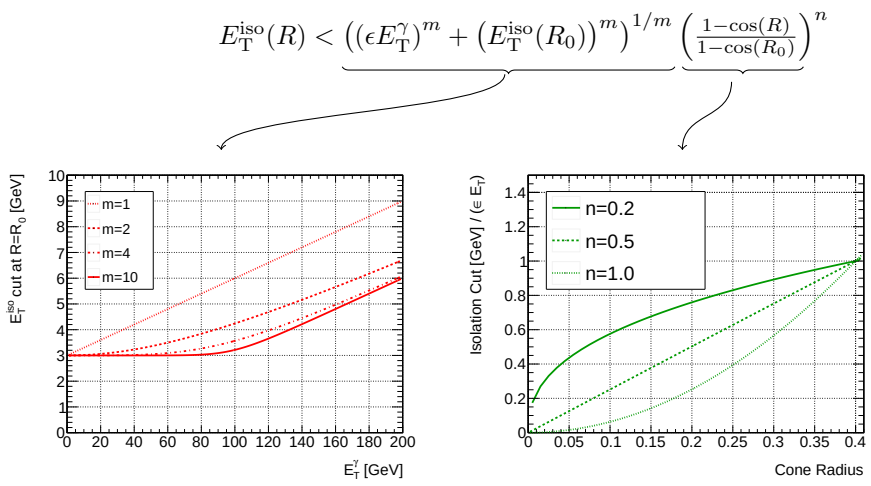

Figure 11.2: The effects of the different pieces of the generalized Frixione isolation prescription on the isolation cut applied as a function of E_{T}^{γ} (left) and cone radius R (right). The addition of the m parameter, and the minimum $E_{\mathrm{T}}^{\mathrm{iso}}$ cut $E_{\mathrm{T}}^{\mathrm{iso}}(R_0)(= E_{\mathrm{T}}^{\mathrm{iso}}(0.4) = 3$ GeV), allows for a shallower turn-on of the allowed isolation energy at low E_{T}^{γ}, while still allowing the isolation energy to grow at higher E_{T}^{γ}.

heavily in other ATLAS searches for new physics. The most prominent example is the search for Higgs bosons decaying to two photons. The most recent ATLAS results on the $H \to \gamma\gamma$ search [79] make heavy use of the techniques for efficiency and purity estimates developed in the inclusive analyses. The $H \to \gamma\gamma$ search requires both photons to be tight and well-isolated, but as with the analyses described here, a non-trivial amount of background remains in the final candidate sample. A form of the two-dimensional sideband technique, modified to look at two two-dimensional planes (one for each photon), has been used to evaluate the γ-jet and jet-jet backgrounds to the $\gamma\gamma$ signal. The resulting decomposition of the sample, shown as a function of the invariant mass, is shown in Fig. 11.3.[40]

In that analysis, the γ-jet and jet-jet backgrounds are assumed to have a smooth exponential shape, with the total normalization given by the sideband technique. Additional improvements to the final purity estimates for $H \to \gamma\gamma$ candidate events may come from a

[40] This work was pioneered by colleagues at LPNHE (Paris), and extended by James Saxon (Penn).

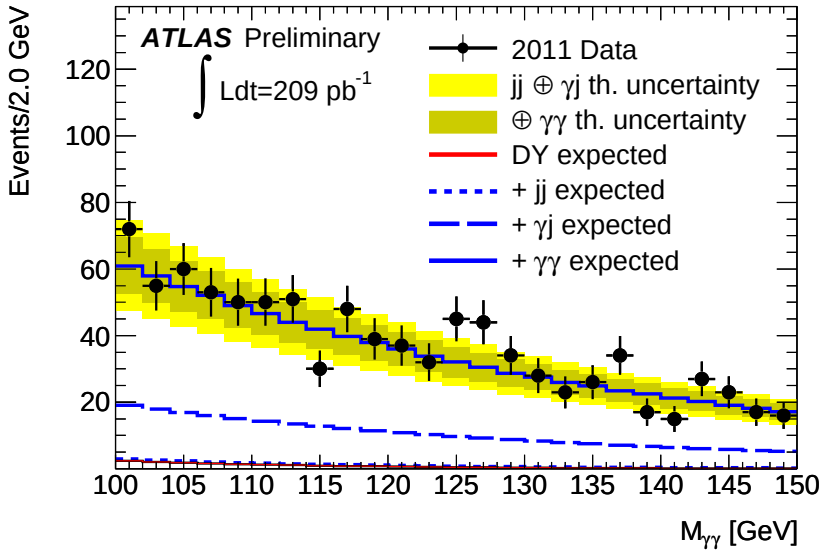

Figure 11.3: The diphoton invariant mass spectrum measured at ATLAS with 209 pb^{-1} of integrated luminosity. The blue-dashed and red lines indicate the estimated backgrounds, which are small compared with the $\gamma\gamma$ component in blue.

form of the template fits, where the individual templates for leading and subleading photons, for both signal and background, are used to estimate the total $\gamma\gamma$ signal yield. The candidate events in which both the leading and subleading photons pass the tight selection criteria are used to populate a two-dimensional plane, with $E_{\text{T}}^{\text{iso}}$ of the leading photon on the x-axis, and $E_{\text{T}}^{\text{iso}}$ of the subleading photon on the y-axis. Four distributions can be used to construct the four different two-dimensional templates:

A. The leading signal photon distribution is taken from the leading electron in $Z \to ee$ decays, fit to a Crystal Ball function,

B. The subleading signal photon distribution is taken from the subleading electron in $Z \to ee$ decays, fit to a Crystal Ball function,

C. The leading fake photon distribution is taken from a sample of diphoton candidates in which the leading photon satisfies the reverse-cuts criteria, and the subleading pho-

ton satisfies the loose identification criteria. The distribution is fit with a Novosibirsk function,

D. The subleading fake photon distribution is taken from a sample of diphoton candidates in which the leading photon satisfies the tight identification criteria, and the subleading photon satisfies the reverse-cuts identification criteria. The distribution is fit with a Novosibirsk function.

The templates containing signal photons are then:

$$\gamma - \gamma \quad = \mathrm{A} \times \mathrm{B} \tag{11.3}$$

$$\gamma\text{−jet} \quad = \mathrm{A} \times \mathrm{C} \tag{11.4}$$

$$\text{jet}-\gamma \quad = \mathrm{B} \times \mathrm{D} \tag{11.5}$$

In this example, the fourth template, for jet-jet events, is a two-dimensional adaptive kernel estimation [80] of the product of $E_{\mathrm{T}}^{\mathrm{iso}}$ distributions used to construct C and D. All four templates are shown in Fig. 11.4.

The data are then fit to a sum of all four distributions: $\gamma\gamma$, γ-jet, jet-γ, and jet-jet. The results are shown projected onto the one-dimensional $E_{\mathrm{T}}^{\mathrm{iso}}$ distributions of the leading and subleading photons in Fig. 11.5. The total number of $\gamma\gamma$ events is estimated to be 637±33, in excellent agreement with the 643±45 events quoted in [79] (where all uncertainties are statistical only). Such a technique could then be extended to parametrize the signal and background components as functions of E_{T}^{γ} or of the invariant mass, eliminating the need to assume fixed shapes for the background components, and allowing each to be inferred individually.

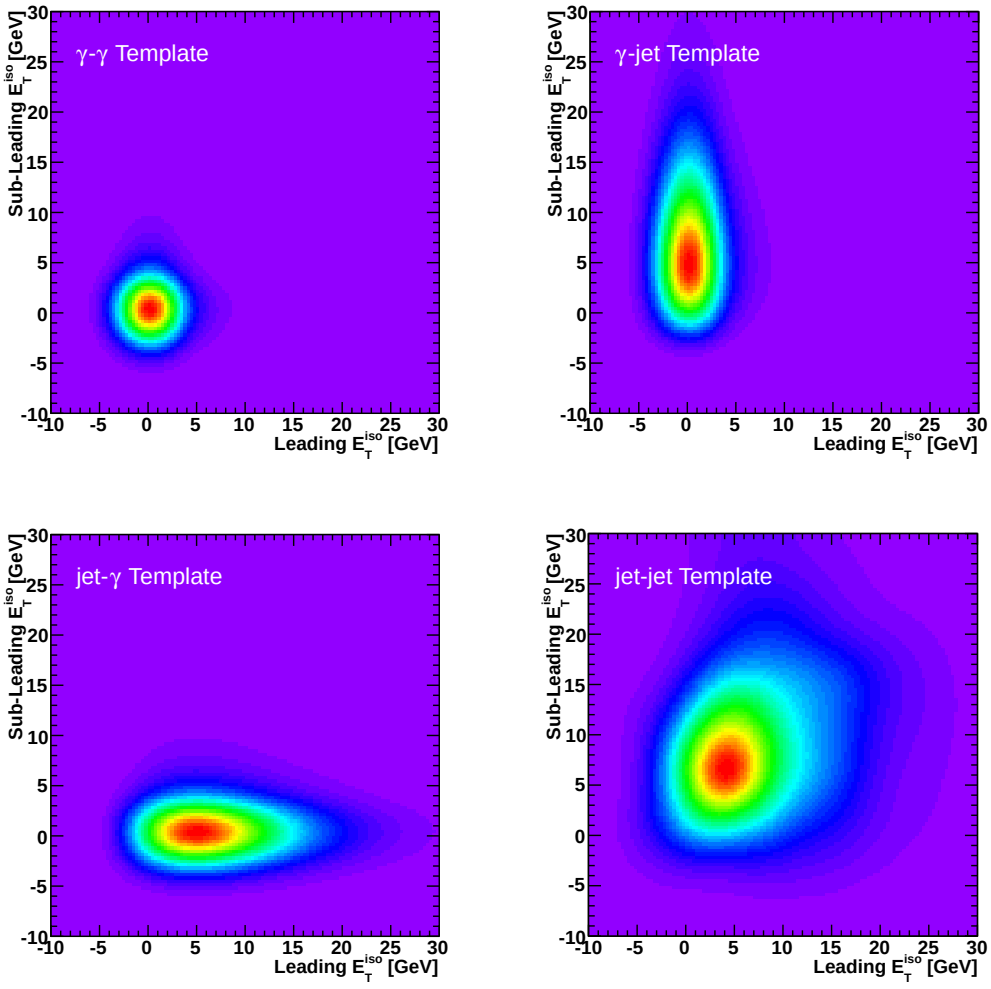

Figure 11.4: Two-dimensional functional templates for $\gamma\gamma$ (upper left), γ-jet (upper right), jet-γ (lower left) and jet-jet (lower right).

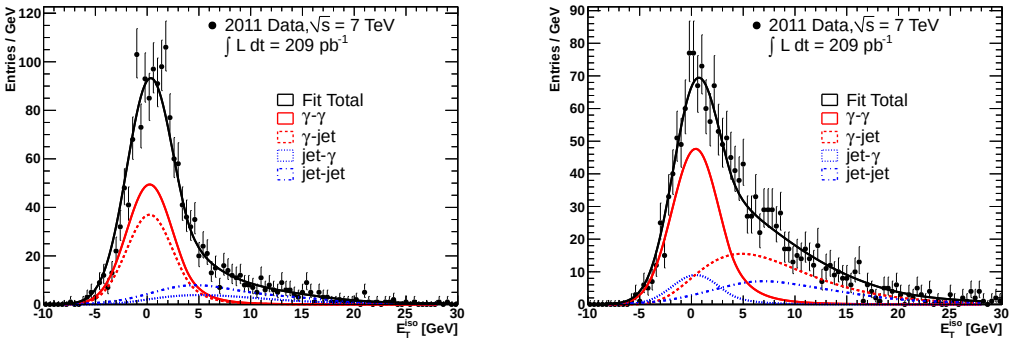

(a) Leading Photon (b) Sub-Leading Photon

Figure 11.5: The projection of two-dimensional $E_{\mathrm{T}}^{\mathrm{iso}}$ fits to a sample of candidate diphoton candidates with invariant masses between 100 and 150 GeV. The $\gamma\gamma$ contribution is roughly 68% of the total yield with $E_{\mathrm{T}}^{\mathrm{iso}} < 5$ GeV.

The ever increasing luminosity of the LHC will present many opportunities to extend the measurements made here, and to apply the techniques developed in these analyses in other searches for new physics. The search for the Higgs may well conclude before the end of 7 TeV running in 2012; if it does, it is likely that the $H \to \gamma\gamma$ channel will play a significant role in the understanding of the lower end of the invariant mass spectrum.

Bibliography

[1] ATLAS Collaboration, *ATLAS inner detector: Technical design report. Vol. 2*, . CERN-LHCC-97-17.

[2] E. Abat et al., *The ATLAS TRT electronics*, J. Instrum. **3** (2008) P06007.

[3] S. L. Glashow, *Partial-symmetries of weak interactions*, Nuclear Physics **2**2 (1961) no. 4, 579 – 588.

[4] S. Weinberg, *A Model of Leptons*, Phys. Rev. Lett. **1**9 (1967) no. 21, 1264 – 1266.

[5] A. Salam, *in Elementary Particle Theory, p. 367*. Almqvist and Wiksell, Stockholm, 1968.

[6] (Super-Kamiokande Collaboration) Collaboration, Y. Fukuda et al., *Evidence for Oscillation of Atmospheric Neutrinos*, Phys. Rev. Lett. **8**1 (1998) no. 8, 1562–1567.

[7] R. Davis, *Solar neutrinos. II: Experimental*, Phys. Rev. Lett. **1**2 (1964) 303–305.

[8] SNO Collaboration, Q. R. Ahmad et al., *Measurement of the charged current interactions produced by B-8 solar neutrinos at the Sudbury Neutrino Observatory*, Phys. Rev. Lett. **8**7 (2001) 071301, arXiv:nucl-ex/0106015.

[9] J. D. Bjorken and E. A. Paschos, *Inelastic Electron-Proton and γ-Proton Scattering and the Structure of the Nucleon*, Phys. Rev. **1**85 (1969) no. 5, 1975 – 1982.

[10] R. P. Feynman, *The behavior of hadron collisions at extreme energies*, . Invited paper at the Third Conference on High-Energy Collisions, Stony Brook, New York, 5-6 Sep 1969.

[11] D. J. Gross and F. Wilczek, *Ultraviolet Behavior of Non-Abelian Gauge Theories*, Phys. Rev. Lett. **3**0 (1973) no. 26, 1343–1346.

[12] R. Feynman and J. Robbins, *The pleasure of finding things out: the best short works of Richard P. Feynman*. Helix book. Perseus Books, 2000.

[13] J. M. Campbell, J. W. Huston, and W. J. Stirling, *Hard Interactions of Quarks and Gluons: A Primer for LHC Physics*, Rept. Prog. Phys. **7**0 (2007) 89, arXiv:hep-ph/0611148.

[14] V. N. Gribov and L. N. Lipatov, *Deep inelastic e p scattering in perturbation theory*, Sov. J. Nucl. Phys. **1**5 (1972) 438–450.

[15] G. Altarelli and G. Parisi, *Asymptotic Freedom in Parton Language*, Nucl. Phys. **B**126 (1977) 298.

[16] Y. L. Dokshitzer, *Calculation of the Structure Functions for Deep Inelastic Scattering and e+ e- Annihilation by Perturbation Theory in Quantum Chromodynamics*, Sov. Phys. JETP **4**6 (1977) 641–653.

[17] J. Pumplin et al., *New Generation of Parton Distributions with Uncertainties from Global QCD Analysis*, JHEP **0**7 (2002) 012.

[18] A. D. Martin, W. J. Stirling, R. S. Thorne, and G. Watt, *Parton Distributions for LO Generators*, Eur. Phys. J. C **6**3 (2009) 189–285.

[19] M. Cacciari, G. P. Salam, and S. Sapeta, *On the characterisation of the underlying event*, JHEP **0**4 (2010) 065.

[20] M. Cacciari, G. P. Salam, and G. Soyez, *The anti-k_t jet clustering algorithm*, JHEP **0**4 (2008) 063, arXiv:0802.1189 [hep-ph].

[21] L. Randall and R. Sundrum, *A large mass hierarchy from a small extra dimension*, Phys. Rev. Lett. **8**3 (1999) 3370–3373.

[22] N. Arkani-Hamed, S. Dimopoulos, and G. Dvali, *The hierarchy problem and new dimensions at a millimeter*, Physics Letters B **4**29 (1998) no. 3-4, 263 – 272.

[23] M. Dine, W. Fischler, and M. Srednicki, *Supersymmetric Technicolor*, Nucl. Phys. B **1**89 (1981) 575–593.

[24] S. Dimopoulos and S. Raby, *Supercolor*, Nucl. Phys. B **1**92 (1981) 353.

[25] C. R. Nappi and B. A. Ovrut, *Supersymmetric Extension of the SU(3) x SU(2) x U(1) Model*, Phys. Lett. B **1**13 (1982) 175.

[26] S. Catani et al., *Cross section of isolated prompt photons in hadron-hadron collisions*, JHEP **0**5 (2002) 028.

[27] T. Sjöstrand et al., *High-Energy-Physics Event Generation with PYTHIA 6.1*, Computer Phys. Commun. **1**35 (2001) 238.

[28] B. Andersson, G. Gustafson, G. Ingelman, and T. Sjöstrand, *Parton Fragmentation and String Dynamics*, Phys. Rept. **9**7 (1983) 31–145.

[29] A. Sherstnev and R. S. Thorne, *Parton distributions for LO generators*, Eur. Phys. J. C **5**5 (2008) 553.

[30] ATLAS Collaboration, G. Aad et al., *ATLAS Monte Carlo tunes for MC09*, ATL-PHYS-PUB-2010-002 (2010) . http://cdsweb.cern.ch/record/1247375.

[31] GEANT4 Collaboration, S. Agostinelli et al., *GEANT4 - a simulation toolkit*, Nucl. Instrum. Methods A **5**06 (2003) 250.

[32] ATLAS Collaboration, G. Aad et al., *The ATLAS Simulation Infrastructure*, Eur. Phys. J. C **70** (2010) 823.

[33] G. Corcella et al., *Herwig 6.5*, JHEP **01** (2001) 010.

[34] J. M. Butterworth, J. R. Forshaw, and M. H. Seymour, *Multiparton Interactions in Photoproduction at HERA*, Z. Phys. C **72** (1996) 637.

[35] S. Hoeche, S. Schumann, and F. Siegert, *Hard photon production and matrix-element parton-shower merging*, Phys. Rev. **D81** (2010) 034026, arXiv:0912.3501 [hep-ph].

[36] E. Anassontzis et al., *High p(t) Direct Photon Production in p p Collisions*, Z. Phys. C **13** (1982) 277–289.

[37] CMOR Collaboration, A. L. S. Angelis et al., *DIRECT PHOTON PRODUCTION AT THE CERN ISR*, Nucl. Phys. B **327** (1989) 541.

[38] UA2 Collaboration, J. A. Appel et al., *DIRECT PHOTON PRODUCTION AT THE CERN anti-p p COLLIDER*, Phys. Lett. B **176** (1986) 239.

[39] UA1 Collaboration, C. Albajar et al., *Direct photon production at the CERN proton-antiproton Collider*, Phys. Lett. B **209** (1988) 385.

[40] UA6 Collaboration, M. Werlen et al., *A New determination of α_s using direct photon production cross-sections in pp and $\bar{p}p$ collisions at $S^{(1/2)} = 24.3$-GeV*, Phys. Lett. B **452** (1999) 201–206.

[41] D0 Collaboration, V. M. Abazov et al., *Measurement of the isolated cross section in $p\bar{p}$ collisions at $\sqrt{s} = 1.96$ TeV*, Phys. Lett. B **639** (2006) 151.

[42] CDF Collaboration, T. Aaltonen et al., *Measurement of the inclusive isolated prompt photon cross section in $p\bar{p}$ collisions at $\sqrt{s} = 1.96$ TeV using the CDF detector*, Phys. Rev. D **80** (2009) 111106(R).

[43] CMS Collaboration, *Measurement of the Isolated Prompt Photon Production Cross Section in pp Collisions at sqrt(s) = 7 TeV*, arXiv:1012.0799 [hep-ex].

[44] A. Breskin and R. Voss, *The CERN Large Hadron Collider: Accelerator and Experiments*. CERN, Geneva, 2009.

[45] G. Aad et al., *The ATLAS Experiment at the CERN Large Hadron Collider*, J. Instrum. **3** (2008) S08003. 437 p. Also published by CERN Geneva in 2010.

[46] E. Abat et al., *The ATLAS TRT Barrel Detector*, J. Instrum. **3** (2008) P02014.

[47] E. Abat et al., *The ATLAS TRT end-cap detectors*, J. Instrum. **3** (2008) P10003.

[48] ATLAS Collaboration, *Electron and photon reconstruction and identification in ATLAS: expected performance at high energy and results at 900 GeV*, ATLAS-CONF-2010-005 (2010) . http://cdsweb.cern.ch/record/1273197.

[49] T. A. Collaboration, *Calibrated $Z \to ee$ Invariant Mass*, ATL-COM-PHYS-2010-734 (2010) .

[50] ATLAS Collaboration, G. Aad et al., *Luminosity Determination in pp Collisions at $\sqrt{s} = 7$ TeV Using the ATLAS Detector at the LHC*, arXiv:1101.2185 [hep-ex]. Submitted to Eur. Phys. J. C.

[51] T. A. Collaboration, *Updated Luminosity Determination in pp Collisions at root(s)=7 TeV using the ATLAS Detector*, Tech. Rep. ATLAS-CONF-2011-011, CERN, Geneva, Mar, 2011.

[52] W. Lampl et al., *Calorimeter Clustering Algorithms: Description and Performance*, Tech. Rep. ATL-LARG-PUB-2008-002. ATL-COM-LARG-2008-003, CERN, Geneva, Apr, 2008.

[53] D. D. Ryutov, *Using Plasma Physics to Weigh the Photon*, Plasma Phys. Control. Fusion **4**9 (2007) B429.

[54] ATLAS Collaboration, G. Aad et al., *Expected Performance of the ATLAS Experiment, Detector, Trigger and Physics*, CERN-OPEN-2008-020 (2008) , arXiv:0901.0512 [hep-ex].

[55] T. A. Collaboration, *ATLAS liquid argon calorimeter: Technical design report*, . CERN-LHCC-96-41.

[56] A. Collaboration, *Expected photon performance in the ATLAS experiment*, Tech. Rep. ATL-PHYS-PUB-2011-007, CERN, Geneva, Apr, 2011.

[57] D. Green, *At the leading edge: the ATLAS and CMS LHC experiments*. World Scientific, 2009.

[58] M. Cacciari, G. P. Salam, and G. Soyez, *The Catchment Area of Jets*, JHEP **0**4 (2008) 005.

[59] M. Cacciari and G. P. Salam, *Dispelling the N^3 myth for the k_t jet-finder*, Phys. Lett. B **6**41 (2006) 57–61.

[60] S. D. Ellis and D. E. Soper, *Successive combination jet algorithm for hadron collisions*, Phys. Rev. D **4**8 (1993) 3160–3166.

[61] S. Catani, Y. L. Dokshitzer, M. H. Seymour, and B. R. Webber, *Longitudinally invariant K_t clustering algorithms for hadron hadron collisions*, Nucl. Phys. B **4**06 (1993) 187–224.

[62] T. Barillari et al., *Local Hadronic Calibration*, Tech. Rep. ATL-LARG-PUB-2009-001-2, CERN, Geneva, 2008.

[63] G. Voronoi, *Nouvelles applications des paramtres continus la thorie des formes quadratiques.*, Journal für die Reine und Angewandte Mathematik **1**33 (1907) 97–178.

[64] ATLAS Collaboration, G. Aad et al., *Measurement of the production cross section for W-bosons in association with jets in pp collisions at sqrt(s) = 7 TeV with the ATLAS detector*, Phys. Lett. **B**698 (2011) 325–345, arXiv:1012.5382 [hep-ex].

[65] M. Aleksa et al., *ATLAS Combined Testbeam: Computation and Validation of the Electronic Calibration Constants*, ATL-LARG-PUB-2006-003 (2006) . `http://cdsweb.cern.ch/record/942528`.

[66] R. Barlow, *Extended maximum likelihood*, Nuclear Instruments and Methods **2**97 (1990) no. 3, 496 – 506.

[67] *The RooFit Toolkit for Data Modeling*, http://roofit.sourceforge.net.

[68] R. Barlow, *SLUO Lectures on Statistics and Numerical Methods in HEP Lecture 9: Unfolding*, http://www-group.slac.stanford.edu/sluo/Lectures/stat_lecture_files/sluolec9.pdf.

[69] ATLAS Collaboration, *Luminosity determination using the ATLAS detector*, ATLAS-CONF-2010-060 (2010) . http://cdsweb.cern.ch/record/1281333.

[70] *The JetPhox Monte Carlo Programme*, http://lapth.in2p3.fr/PHOX_FAMILY/jetphox.html.

[71] L. Bourhis, M. Fontannaz, J. P. Guillet, and M. Werlen, *Next-to-leading order determination of fragmentation functions*, Eur. Phys. J. C **1**9 (2001) 89–98.

[72] *PDF4LHC recomendation*, http://www.hep.ucl.ac.uk/pdf4lhc.

[73] J. P. Guillet and E. Pilon. Private communication, 2010.

[74] A. V. Lipatov, M. A. Malyshev, and N. P. Zotov, *Testing for kt-factorization with inclusive prompt photon production at LHC*, Phys. Lett. **B**699 (2011) 93–97, arXiv:1102.1134 [hep-ph].

[75] A. Höcker and V. Kartvelishvili, *SVD Approach to Data Unfolding*, Nucl. Instrum. Meth. **A**372 (1996) 469–481, hep-ph/9509307.

[76] D0 Collaboration, A. Kumar, *Measurement of triple differential photon plus jet cross-section by D0*, J. Phys. Conf. Ser. **1**10 (2008) 022025, arXiv:0710.0415 [hep-ex].

[77] S. Frixione, *Isolated photons in perturbative QCD*, Phys. Lett. **B**429 (1998) 369–374, arXiv:hep-ph/9801442.

[78] SM and NLO Multileg Working Group Collaboration, J. R. Andersen et al., *The SM and NLO multileg working group: Summary report*, arXiv:1003.1241 [hep-ph].

[79] *Search for the Higgs Boson in the Diphoton Channel with the ATLAS Detector using 209 pb-1 of 7 TeV Data taken in 2011*, Tech. Rep. ATLAS-CONF-2011-085, CERN, Geneva, Jun, 2011.

[80] K. S. Cranmer, *Kernel estimation in high-energy physics*, Comput. Phys. Commun. **1**36 (2001) 198–207, arXiv:hep-ex/0011057.